Richard M. Bateman

Cased-Hole Log Analysis and Reservoir Performance Monitoring

Second Edition

Springer

Cased-Hole Log Analysis and Reservoir Performance Monitoring

Richard M. Bateman

Cased-Hole Log Analysis and Reservoir Performance Monitoring

Second Edition

Springer

Richard M. Bateman
Lubbock, TX, USA

ISBN 978-1-4939-2067-9 ISBN 978-1-4939-2068-6 (eBook)
DOI 10.1007/978-1-4939-2068-6
Springer New York Heidelberg Dordrecht London

Library of Congress Control Number: 2014951359

Printed on acid-free paper

Springer is part of Springer Science+Business Media (www.springer.com)

This book is dedicated to the memory of three gentlemen and scholars: Rex Cantrell and John Aitken, who awakened my interest in the subject matter, and Rex Curtis who instructed me so wisely in its practice.

Preface to the Second Edition

Since the first publication of this work, our industry has progressed. Whereas formerly production of hydrocarbons was from predominantly conventional reservoirs using vertical wells, it is now more common to produce from unconventional reservoirs using high angle or horizontal wells. This has resulted in a need for innovative methods for conveying measurement devices to the ends of the non-vertical wells. It has also called for design changes to the measurement devices themselves in order to properly monitor segregated flow regimes in non-vertical pipes.

Our industry has also progressed in the design of new measurement devices that considerably enhance our ability to perform formation evaluation through casing and to monitor tri-phasic flow in production strings. Data recording methods have also progressed and now offer a number of alternatives to conventional real-time wireline logging methods. In particular it is now common to leave permanent sensors in wells to provide continuous measurements of key parameters of reservoir performance.

Hopefully this revised second edition of *Cased-Hole Log Analysis and Reservoir Performance Monitoring* will bring the reader some useful insights to assist in day-to-day improvement in the task of economical hydrocarbon production. It is sobering to note that the time taken to drill and complete a new well is measured in weeks or months but the life of a producing well is measured in years or decades. Every year the number of old wells in need of remediation grows and worldwide is numbered in the millions.

The tools and techniques described in this work constitute a vital, but often underrated, resource for tapping hydrocarbons that have already been found and they deserve to be more widely understood and used.

Lubbock, TX, USA — Richard M. Bateman

Acknowledgments

This book is largely based on the courses I have taught to engineers and geologists whose most urgent need was for a basic understanding of production logging tools and an effective, practical method for analyzing their measurements. In collecting materials for such courses, I have received invaluable help from many individuals, service companies, oil companies, and authors who have published materials in technical journals such as ***Petrophysics*** (formerly ***The Log Analyst***), the ***Journal of Petroleum Technology***, and others. In many cases it has been difficult, if not impossible, to trace the source of the materials used in this book. The logging fraternity is a closely knit one and, in the interests of getting the job done, tends to share publication materials rather freely. Wherever possible I have given credit to my sources, and where not possible I thank the many dedicated friends who have provided me with figures, charts, and log examples. I also owe a debt of gratitude to the hundreds of students who have given me valuable feedback on both the content and style of my presentations. I particularly thank the students, staff, and faculty of Texas Tech University who have provided valuable help and advice in the preparation of this Second Edition. In particular Dr. M.Y. Soliman, Dr. M. Shahri, and H. A. Carter have been of inestimable help in bringing the work to completion.

Contents

Introduction 1

Objectives of Production Logging

The objectives of production logging can be categorized as follows:

1. Monitoring of reservoir performance
2. Diagnosis of completion problems
3. Delineating production and injection profiles
4. Gauging treatment effectiveness

Reservoir Performance

Monitoring reservoir performance is an important aspect of production logging. It allows an operator to establish the overall behavior of a reservoir and hence make intelligent decisions regarding fieldwide production or injection strategies. In particular, the information sought includes details concerning:

Water breakthrough
Water coning
Gas breakthrough
Abnormal formation pressures
Thief zones
Pressure maintenance

In this book, methods of making measurements in a completed well to gather the needed data will be discussed.

R.M. Bateman, *Cased-Hole Log Analysis and Reservoir Performance Monitoring*,
DOI 10.1007/978-1-4939-2068-6_1

Completion Problems

Completion problems may arise due to the mechanical state of the completion string. Relatively simple measurements can be made to pinpoint such problems as:

Casing leaks
Packer leaks
Bad cement jobs
Plugged perforations
Corrosion

Many different tools and techniques may be used in the search for mechanical problems and each will be discussed later in the text.

Production and Injection Profiles

An important diagnostic tool for both producing and injecting wells is the ability to derive flow profiles from production logging devices. These devices seek to answer the questions, (1) How much of what comes from where? and (2) How much goes where? In most wells a production or injection profile will be a surprise to the operator. In few cases does the flow come from, or go to, the expected reservoir unit.

Gauging Treatment Effectiveness

Finally, productive logging can be used to establish the effectiveness of well treatments such as frac jobs and/or secondary and tertiary floods.

Petroleum Reservoirs

In order to place these production/injection problems in perspective and illustrate the conditions that may arise during the life of a well or field, it is worthwhile to recall the four principal types of petroleum reservoirs:

1. Solution–gas drive
2. Gas-cap expansion
3. Water drive
4. Gravity drainage (segregation)

Gas problems may be expected with solution–gas drive and gas-cap expansion reservoirs as illustrated in Figs. 1.1 and 1.2. Gas problems may be caused by:

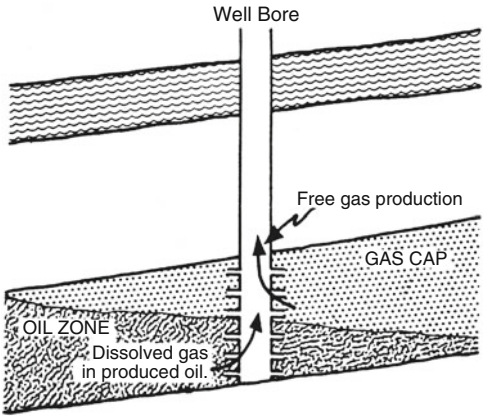

Fig. 1.1 Gas produced with oil from associated gas-cap and solution in the oil. Reprinted with permission of the Petroleum Engineer International *from Cesak and Schultz* (1956)

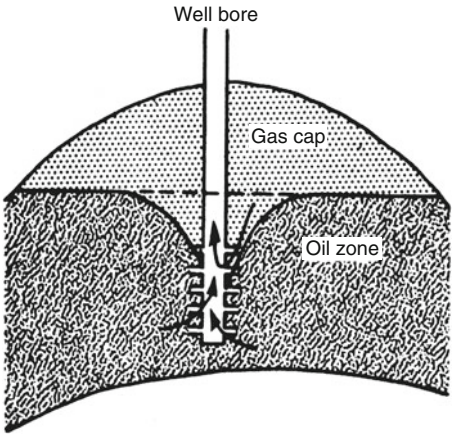

Fig. 1.2 Coning of free gas into a well across bedding planes. Reprinted with permission of the Petroleum Engineer International *from Cesak and Schultz* (1956)

Gas breakthrough
Inadequate pressure maintenance
Production rate too high
Formation pressure below bubble point
Incorrect completion

Water problems may be expected with water drive and gravity drainage reservoirs as illustrated in Figs. 1.3, 1.4, and 1.5—and can be traced to the following causes:

Coning of water
Permeability problems
Completion problems

Modern Production Logging Tools

Modern production logging tools may be categorized in three general groups as making measurements of:

Formation properties through casing and/or tubing
Fluid type, flow rate, and movement within the casing/tubing vicinity
The status of the completion string

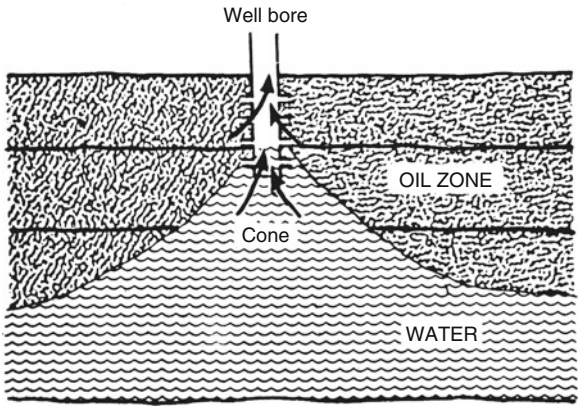

Fig. 1.3 Water coning across bedding planes. Reprinted with permission of the Petroleum Engineer International *from Cesak and Schultz* (1956)

Tools for Formation Properties

Tools that measure formation properties from within a completed well include:

Pulsed neutron logs: (TDT, NLL, TMD)
Gamma ray logs: (GR)
Natural gamma spectra logs: (NGT)
Inelastic gamma logs: (IGT)
Carbon/oxygen logs: (C/O, GST)

All have a common characteristic; they depend on interactions of nuclear particles (neutrons) and/or radiation (gamma rays) that have the ability to pass through steel casing.

Tools for Fluid Typing and Monitoring

Tools that distinguish oil from gas and water and monitor their flow rates include:

Flowmeters: packer, basket, and continuous
Temperature: absolute, differential, and radial
Fluid density: gradiomanometer and gamma–gamma
Radioactive tracers
Noise logs

Each of these devices will be discussed and their uses illustrated with field examples.

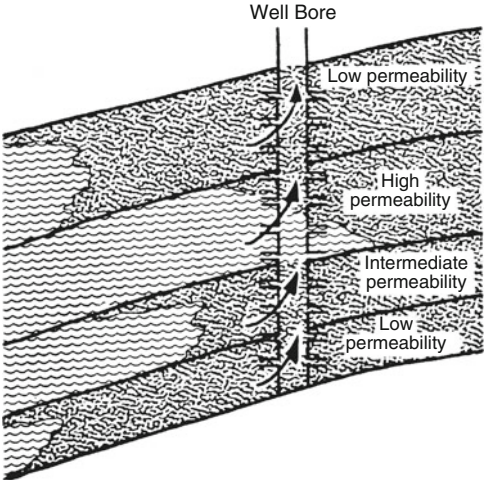

Fig. 1.4 Irregular water encroachment and early breakthrough in high-permeability layers. Reprinted with permission of the Petroleum Engineer International *from Cesak and Schultz* (1956)

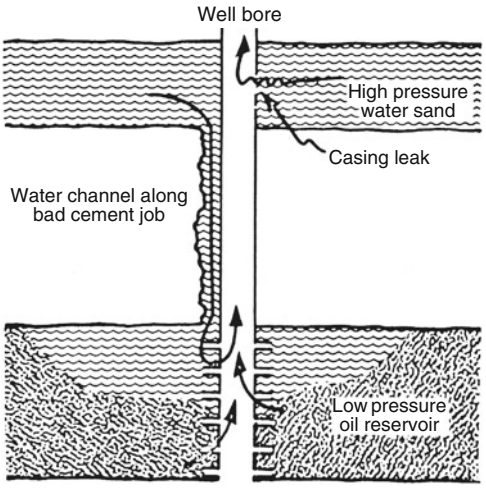

Fig. 1.5 Water production through casing leak and channel leak. Reprinted by permission of the Petroleum Engineer International *from Cesak and Schultz* (1956)

Tools for Completion Inspection

Tools for monitoring the mechanical status of the completion string include:

Cement bond logs: (CBL, CET)
Casing-collar logs: (CCL)
Casing inspection logs: (ETT, PAL, calipers)
Casing potential logs

In addition to these direct measurements of the status of the completion string, all the fluid typing and monitoring tools may be used to infer completion problems. For example, a temperature log may indicate a tubing leak.

Quick Reference to Production Logging Tools

Table 1.1 summarizes the majority of the common production logging tools and their spheres of measurement. Examples of each type of log will be shown in the chapters that follow.

Table 1.1 Common PL devices

	Sphere of measurement		
Tool name	Formation properties	Fluid type of flow	Status of tubulars
Pulsed neutron	X		
Gamma ray	X		
GR Spectra	X		
Inelastic gamma	X		
Carbon/oxygen	X		
Flowmeters		X	X
Temperature		X	X
Fluid density		X	
Gadiomanometer		X	
Radioactive tracers		X	X
Noise logs		X	X
Cement bond log			X
Casing-collar locator			X
Electromagnetic thickness tool			X
Pipe-analysis log			X
Calipers			X

Bibliography

Cesak NJ, Schultz WP. Time analysis of problem wells. Pet Eng Intl. 1956:13–30.

Fertl WH. Well logging and its application in cased hole. In: Paper SPE 10034 presented at the 1982 international petroleum exhibition and technical symposium, Beijing, China; 1982.

Raymer LL, Burgess KA. The role of well logs in reservoir modeling. In: Paper SPE 9342 presented at the SPE 55th annual technical conference and exhibition, Dallas; 21–24 Sept 1980.

Timur A. Open hole well logging. In: Paper SPE 10037 presented at the 1982 international petroleum exhibition and technical symposium, Beijing, China; 1982.

Cased-Hole Logging Environment

2

Planning a Production Logging Job

Planning is an important part of a production logging job. Frequently these jobs can only be done in safety during daylight. Thus, the correct type of equipment must be available for the expected well conditions. Before attempting any production logging job the following checklist should be consulted:

1. Full well-completion details
2. Full production history
3. All open-hole logs
4. PVT data

Lack of any part of this data will result in delays that may jeopardize the entire job.

Pressure-Control Equipment

Practical details should not be forgotten. In particular, considerable care and attention should be given to the matter of working on a well that has pressure at the wellhead. It is a good idea to plan well in advance with the logging-service company using the following checklist:

1. Wellhead connection
2. Riser requirements
3. Tubing restrictions (minimum ID)

R.M. Bateman, *Cased-Hole Log Analysis and Reservoir Performance Monitoring*,
DOI 10.1007/978-1-4939-2068-6_2

4. Tubing-head pressure
5. Safety (H_2S/pressure/temperature ratings)

In general, when working against wellhead pressure the logging cable will be a single-conductor armored cable about 1/4 in. in diameter. To seal the wellhead assembly against well fluids, a stuffing box or hydraulic packing gland will be used. For high pressures, a "grease-seal" assembly will be used. In order to get logging tools into and out of the well in a safe and efficient manner, a section of riser will be needed. A typical setup is illustrated in Fig. 2.1. Note that, above the wireline blow-out preventer, this pressure-control assembly has (l) a tool trap, (2) multiple sections of riser, and (3) the pressure sealing equipment. When retrieving a tool from the well, it is sometimes difficult to gauge exactly where the cable head is in the riser. If it is pulled up against the pressure sealing assembly too briskly, the tool may shear off the end of the cable and drop back into the well. To prevent this undesirable event, the tool trap catches the tool at the base of the riser.

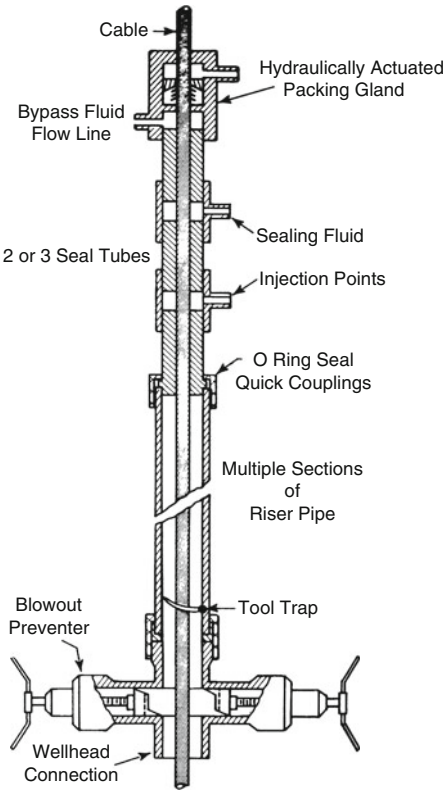

Fig. 2.1 Production logging wellhead pressure-control assembly. Courtesy Schlumberger

The cable itself is at all times subject to an extrusion force, since the portion inside the riser experiences wellhead pressure, while the portion outside the riser experiences atmospheric pressure. The upward force is thus the difference in pressure multiplied by the cross-sectional area of the cable itself. Sometimes this upward force can be surprisingly large and tools will not go down the well unless "ballasted" with additional weights.

Question #2.1
Tubing head pressure is 4,986 psi. The logging cable OD is 7/32 in. The tool weighs 20 lb and is 16 ft long.

(a) Calculate the upward force on the cable.
(b) If weights are available, each 4 ft long and weighing 26 lb, how many are needed to make the tool go down the well?
(c) In that case, how long a riser is required?
(d) If the top of the BOP is 10 ft above ground level, the grease-seal equipment measures 10 ft, and the sheave assembly requires 6 ft of clearance, how tall must the workover rig be in order to log this well?

It is also important to plan the arrangement of the Christmas tree—the objective being to be able to log the well without disturbing the dynamic behavior of the production or injection process. Sometimes this consideration is forgotten in the planning with the result that the only way to get production logging tools into and out of the well is by shutting in the well. This is undesirable, since a well may take hours or days to reach equilibrium again after being shut in. Figure 2.2 illustrates an ideal Christmas-tree setup. Note the numbered items in the figure:

#1 Valve on the riser side of the production line
#2 Valve on the production line
#3 Valve on the well side of the production line
#4 Pressure gauge on the riser
#5 Bleed-off valve on the riser

Question #2.2
(a) What happens if item # 1 is missing?
(b) What happens if item #3 is missing?
(c) Why are items #4 and #5 needed?

The Borehole Environment

In many of the problems that arise in completed wells, quantitative analysis will require detailed knowledge of flow rates, casing and tubing sizes and weights, as well as the types of flow that are occurring. For example, in the analysis of

flowmeter data, fluid speed needs to be related to volumetric flow rate. Conversion from one set of units to another can be facilitated by using:

Appendix A: Conversion factors between metric, API, and customary (US) measures
Appendix B: Average fluid velocity vs. tubing size
Appendix C: Average fluid velocity vs. casing size

Question #2.3
Use Appendix C to find the flow rate in 7-in., 26-lb casing if the fluid speed is 9.1 ft/min.

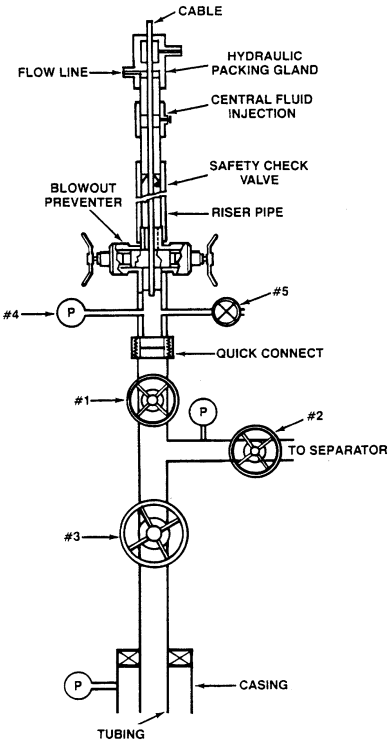

Fig. 2.2 Correct Christmas-tree arrangement for production logging

Choosing Production Logs

Depending on the type of problem encountered, a choice will exist regarding the correct tool or logging technique to be used. The following suggestions are offered as a quick guide. A more informed choice can be made after studying the individual tools in the chapters that follow.

Flow rates	
Low (0 and up)	Radioactive tracer log
Low to medium (10–1,900 B/D)	Packer or diverter flowmeter
Medium to high (50–5,000 B/D)	Full-bore flowmeter
High (3,000 B/D and up)	Continuous flowmeter

Fluid type	
Oil/water	Gradiomanometer
Oil/gas	Gradiomanometer or densimeter/vibrator
Gas/water	Densimeter/vibrator or gamma–gamma log

Formation content	
High-salinity water	Pulsed neutron log
Low-salinity water	Carbon/oxygen log
General	Elemental concentration log
	Spectral gamma ray
	Resistivity through casing

Casing/tubing inspection	Electromagnetic thickness tool
	Flux-leakage-type tool
	Multi-fingered caliper
	Ultrasonic imaging
	Optical imaging

Cement/channeling	Cement bond log
	Radial differential thermometer
	Temperature log
	Noise log
	Radioactive tracer log

Conveyance Methods

The conveyance of a production logging tool string to the required depth in a well can present challenges when the well is not vertical. Where the well is deviated from the vertical problems can arise since the tool string (lowered on a conductive wireline) may not slide down the well path past a certain angle of deviation. More challenging yet is the task of conveying the production logging tools to the end of a horizontal well. To overcome these difficulties the logging industry has evolved a number of conveyance mechanisms that strive to overcome such mechanical difficulties.

Combinations of techniques can be used to ensure that the tools get to where they need to be and the data is recorded. These can be classified as:

- *Conventional wireline*: Tool string is gravity fed to TD and data is recorded in real time as the wireline conductor cable is reeled up.
- *Wired coiled tubing*: Tool is "pushed" down-hole with coiled tubing and data is recorded in real time as the coiled tubing is retrieved.
- *Assisted wireline*: Tool string is equipped with a motorized "tractor" that pulls the tool string to the end of the well. Data is recorded as the tool is extracted from the well in a conventional manner.
- *Wireless conveyance*: Tools are "pushed" via plain coiled tubing or heavy "slick line" and data is recorded in a digital memory format for downloading later when the tool is retrieved back at surface. In this case depth control is managed by recoding the logging signals as a function of time which can then be keyed to a known depth vs. time recording made at surface as the coiled tubing or nonconducting line is recovered.

Figure 2.3 illustrates a motorized tractor that can be added to the lowered production logging string and activated to mechanical crawl along the low side of the casing to pull the tool string to the required depth even in horizontal holes. The spring loaded drive wheels can be activated from surface to open up and engage the pipe walls and then can be turned as drive wheels to propel the logging tool string along the well path.

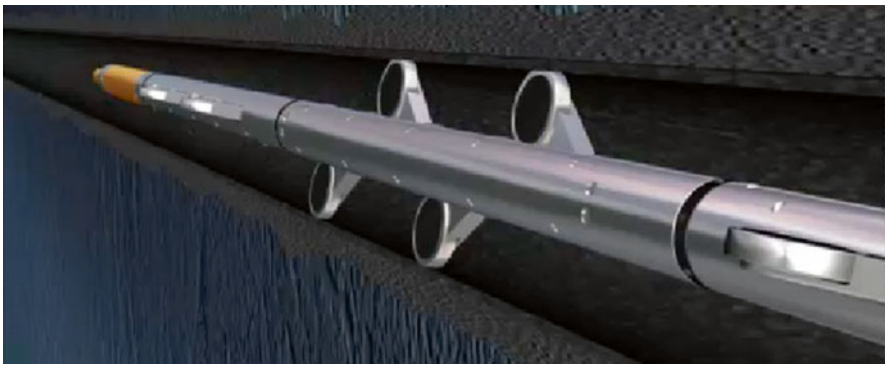

Fig. 2.3 Wireline tractor for production logging in highly deviated pipe. Courtesy Welltec®

Answers to Text Questions

Question #2.1

Cable area = $\pi/4 \times (7/32)^2 = 0.03758$ sq in.

Differential pressure = 4,986 psi.

(a) Upward force = $4{,}986 \times 0.03758 = 187.4$ lb.
(b) Weights required = $(187.4 - 20)/26 = 6.44$.
(c) So use seven weights.
(d) Riser requirements = 16-ft tool + $(7 \times 4$ ft) = 44 ft.
(e) Rig height = $10 + 44 + 10 + 6 = 70$ ft.

Question #2.2

(a) The well must be shut in before tools can be run in or out of the well.
(b) No effect on ability to log well.
(c) To bleed off pressure in the riser before undoing the quick-connect riser connection.

Question #2.3

500 B/D

Reservoir Fluid Properties

3

PVT Refresher Course

For a complete understanding of the behavior of producing wells, it is necessary to keep in mind the fundamental principles that govern the properties of hydrocarbon liquids and gases. Only then can downhole flow rates be accurately found from surface flow rates. The correct choice of a flowmeter tool depends on the expected flow rate and whether or not free gas is present will influence the choice of a fluid-typing tool. In order to keep clear the different sets of conditions of pressure, volume, and temperature, subscripts will be used in this text as follows:

b	Bubble-point
bc	Brine concentration
g	Gas
o	Oil
s	Solution
sc	Standard conditions
w	Water
wf	Well flowing conditions (at depth)

Additionally, the following symbols will be used:

C	Concentration
ρ	Density
q	Flow rate
B	Formation volume factor
R	Gas/oil ratio or solubility
p	Pressure
γ	Specific gravity
T	Temperature
μ	Viscosity

R.M. Bateman, *Cased-Hole Log Analysis and Reservoir Performance Monitoring*,
DOI 10.1007/978-1-4939-2068-6_3

and the following abbreviations:

BFPD	Barrels of fluid per day
BGPD	Barrels of gas per day
BOPD	Barrels of oil per day
BWPD	Barrels of water per day
cf/B	Cubic feet per barrel
scf/D	Standard cubic feet per day

Single-Component Hydrocarbon System

The behavior of a single-component hydrocarbon system is illustrated in Fig. 3.1. On the graph, pressure is plotted against volume, and the resulting curve is called the *vapor–pressure curve*. As the pressure on a fixed mass of hydrocarbon liquid is reduced, its volume increases slightly until the *bubble-point* is reached. Further increasing the volume available leaves the pressure constant and more and more of the liquid hydrocarbon converts to the gaseous phase. As the volume continues to increase, eventually the *dew-point* is reached and no further liquid hydrocarbon is present; from then on, further increases in volume result in reductions in pressure. The PV diagram shown in Fig. 3.1 is for a fixed temperature. The effects of temperature can be understood by reference to Fig. 3.2. Note that at high

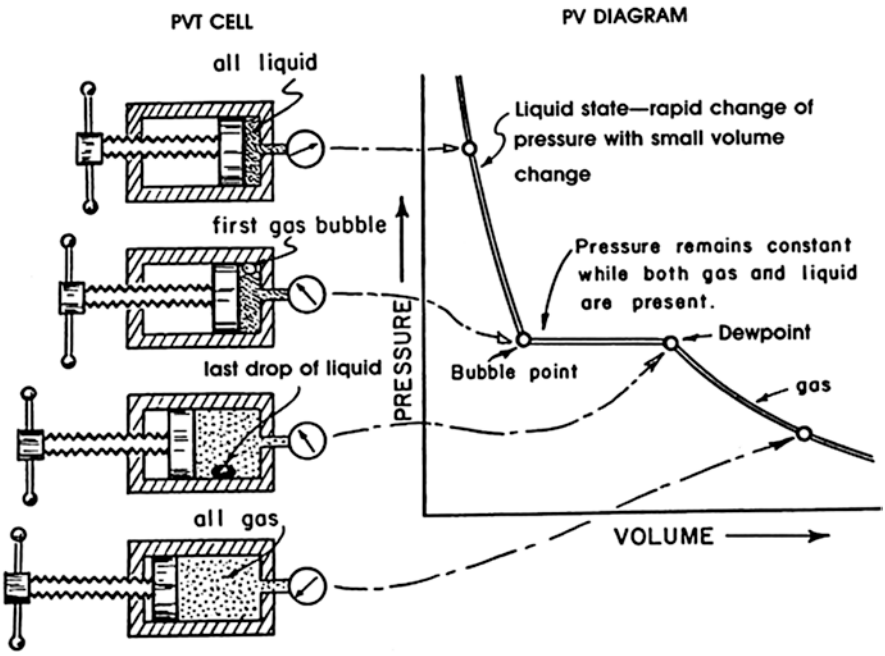

Fig. 3.1 Phase behavior of a single-component hydrocarbon. Courtesy Schlumberger

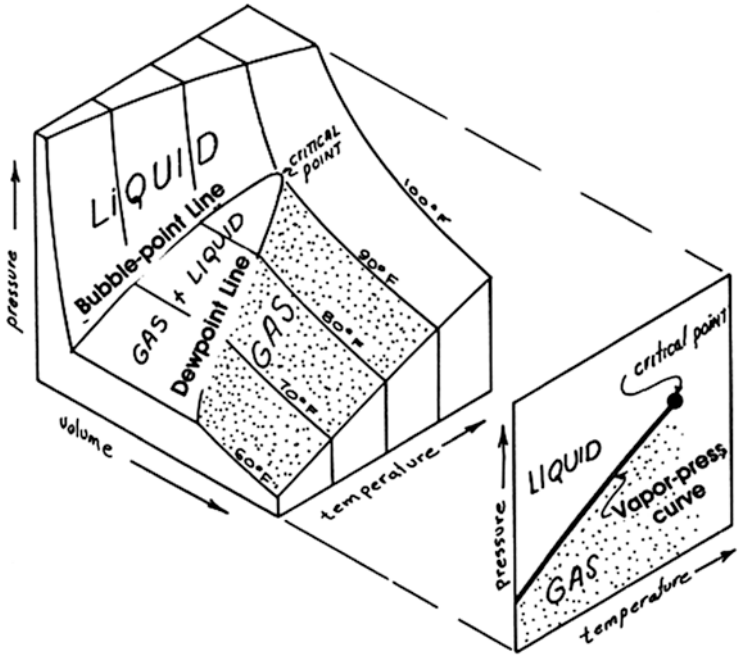

Fig. 3.2 Three-dimensional diagram of a single-component system. Courtesy Schlumberger

temperature the dew-point line and the bubble-point line coincide at the *critical point*. In summary, a single-component hydrocarbon (methane, ethane, etc.) can exist as a gas, a liquid, or a gas–liquid mixture depending on the pressure and temperature to which it is subjected.

Multicomponent Hydrocarbon System

In actual reservoirs, the hydrocarbons found are never single-component systems. Rather, they are mixtures of several different hydrocarbons and the behavior of the mix is different from that of any single component. In particular, there is no single vapor–pressure line. Rather, an envelope exists between the bubble-point line and the dewpoint line within which gas and liquid coexist. Figure 3.3 illustrates this concept. Note that on the PV plane the bubble-point and the dew-point are found as discontinuities and no straight-line portion exists on the PV graph (see Fig. 3.4). What, therefore, distinguishes one type of reservoir from another? What kind of production may be expected from a multicomponent hydrocarbon system? The answers lie in the starting and ending points on a pressure–temperature plot and their positions relative to the envelope between the bubble-point and dew-point lines.

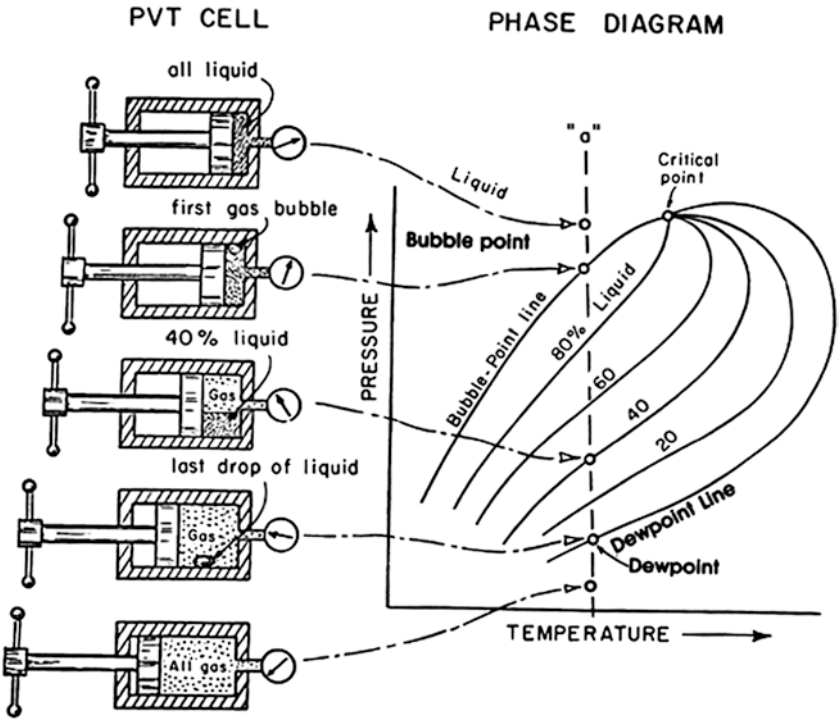

Fig. 3.3 Phase behavior of a multicomponent system. Courtesy Schlumberger

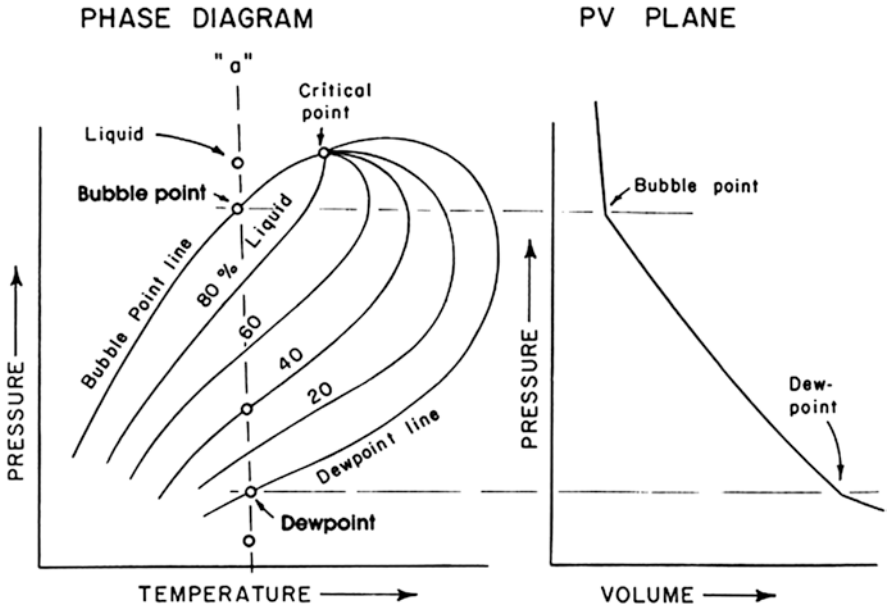

Fig. 3.4 Bubble-point and dew-point determination for a multicomponent system. Courtesy Schlumberger

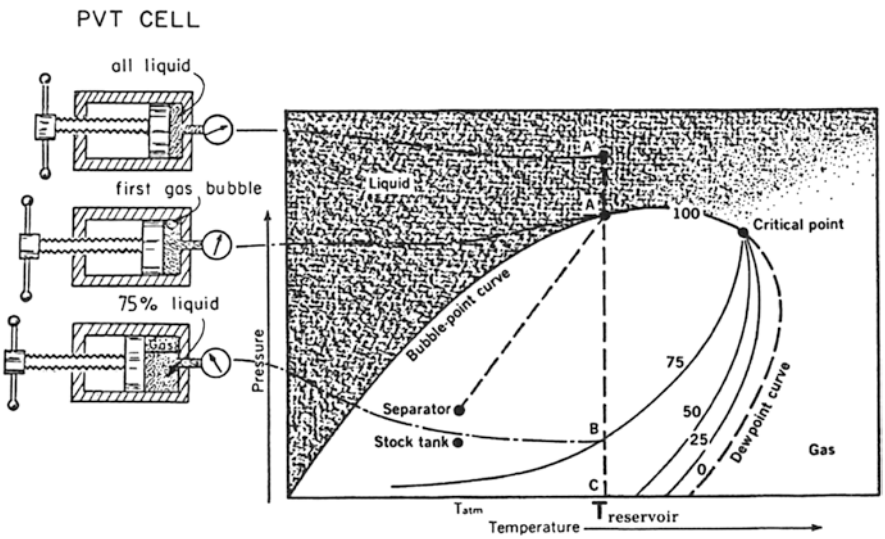

Fig. 3.5 Phase diagram of a normal GOR well. Courtesy Schlumberger

Oil Reservoirs

Figure 3.5 shows a plot of pressure vs. temperature for an oil-producing reservoir. At formation conditions, pressure and temperature are such as to place point A′, representing the original conditions, above the critical pressure. The multicomponent hydrocarbon therefore exists as an undersaturated liquid. As the pressure in the reservoir is drawn down by the production process, point A—the bubble-point—is reached. Some gas can now start to come out of solution. The path from the producing horizon up the production string to the separator is illustrated by the dashed line. The final step to the stock tank leaves a point that falls on a line representing some percentage of oil and some percentage of gas. Typically, 80–90 % of the original fluid is recovered in the form of liquid (oil).

Condensate Reservoirs

Figure 3.6 illustrates a reservoir where the starting point A' is above the critical temperature. Thus, all of the multicomponent system exists as a gas. During the production process, however, the temperature and pressure fall sufficiently to place point B, for example, back inside the bubble-point-line-dewpoint-line envelope. Thus, although in the reservoir the hydrocarbon exists as gas, by the time it reaches the separator, some of it exists as liquid oil. This process is known as retrograde condensation. Typically, 25 % of the hydrocarbon may be recovered as oil at the separator and somewhat less in the stock tank.

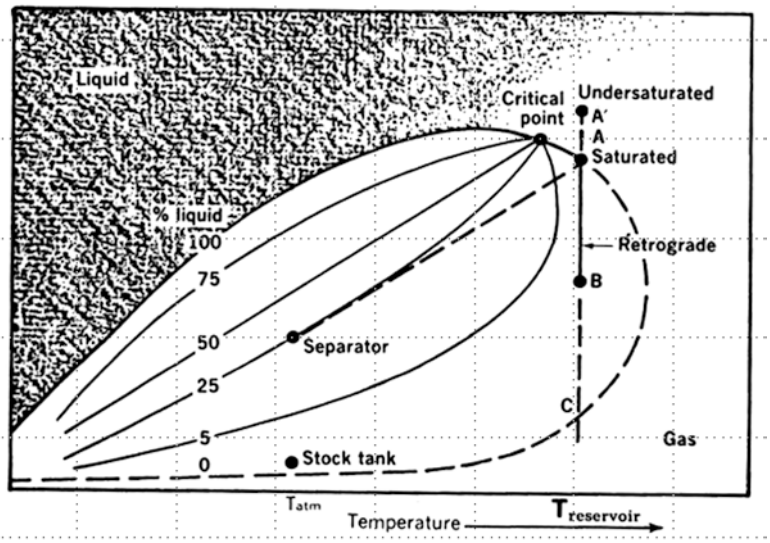

Fig. 3.6 Phase diagram of a retrograde condensate-gas well. Courtesy Schlumberger

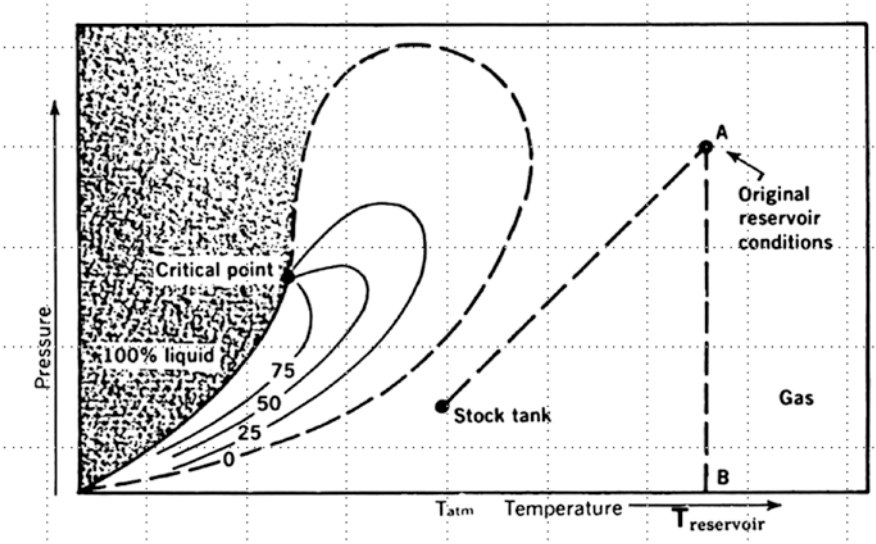

Fig. 3.7 Phase diagram of a dry-gas reservoir. Courtesy Schlumberger

Dry-Gas Reservoir

Figure 3.7 illustrates a dry-gas reservoir. Note that both starting and ending points are outside the envelope and hence no liquid recovery is possible.

Table 3.1 Composition of natural gases

Field	Hugoton	Austin	Leduc Gas Cap D-3	Viking, Kinsella	West Cameron, Blk 149
State	Oklahoma, Texas	Michigan	Alberta	Alberta	Louisiana (Gulf)
Formation	Permian Dolomite	Stray Sand	Devonian	Cretaceous Sand	Miocene Sand
Depth (ft)	3,000	1,200	5,000	–	7,150
Mole percentage					
Nitrogen, N_2	15.5	7.3	7.41	0.24	–
Carbon dioxide, CO_2	–	–	0.72	2.26	0.3
Helium, He	0.58	0.4			–
Methane, CH_4	71.51	79.74	72.88	88.76	96.95
Ethane, C_2H_6	7	9.1	9.97	4.76	2.05
Propane, C_3H_8	4.4	2.8	5.09	2.67	0.47
Isobutane, C_4H_{10}	0.29	0.1	0.72	0.42	0.08
n-Butane, C_4H_{10}	0.7	0.4	1.76	0.21	0.09
Isopentane, C_5H_{12}	0.02 }	0.1	0.99	0.38 {	0.03
n-Pentane, C_5H_{12}	– }				0.02
Hexane, C_6H_{14}	–	0.05	0.46	0.3	0.31
Heptane+	–	0.01			
	100	*100*	*100*	*100*	*100*

Note: Reprinted with permission, from Donald Katz et al.: *Handbook of Natural Gas Engineering* (New York: McGraw-Hill, 1959)

Composition of Natural Oils and Gases

The exact behavior of any particular reservoir is thus a function of the components of the hydrocarbon mixture placed there by nature and, to a small extent, of the way in which the multicomponent system is produced. By varying the temperature and pressure at various separator stages it is sometimes possible to increase slightly the liquid (oil) recovery. The range of hydrocarbon types commonly found is given in Tables 3.1 and 3.2.

Fluid Properties

Downhole flow rates can differ quite markedly from surface-recorded flow rates. For example, water is compressible, thus less water flows at downhole conditions than at surface. This can be expressed as:

$$q_{\mathrm{wwf}} = q_{\mathrm{wsc}} * B_{\mathrm{w}}$$

where B_{w} is the water formation volume factor (FVF). By contrast, oil flow rates downhole are greater than oil flow rates at surface. Although oil too is compressible, it can also accept greater volumes of dissolved gas at reservoir conditions and therefore expands. This can be expressed as:

$$q_{\mathrm{owf}} = q_{\mathrm{osc}} * B_{\mathrm{o}}$$

where B_{o} is the oil formation volume factor. Gas is highly compressible, hence downhole gas flow rates will be much smaller than those recorded on surface at standard conditions. Thus we have:

$$q_{\mathrm{gwf}} = q_{\mathrm{gsc}} * B_{\mathrm{g}}$$

However, the fact must also be taken into account that there are really three sources of the gas seen at the surface. Some will have come out of solution in the oil and/or water and some will be free gas at reservoir conditions (assuming reservoir pressure is below the bubble-point). Hence,

$$\text{gas at surface} = \text{free gas} + \text{solution gas}$$

Figure 3.8 illustrates these concepts. In order to calculate downhole flow rates from the surface rates a series of charts may be used. Computer software is also widely available for this task.

Table 3.2 Analysis of reservoir oils containing dissolved gases

Field	Leduc D-2	Leduc D-3	Paloma	Oklahoma City, Wilcox	Rodessa	Keokuk	Schuler (Jones Sand)
State or Province	Alberta	Alberta	California	Oklahoma	Louisiana	Oklahoma	Arkansas
Reservoir							
Depth (ft)	5,000	5,300	10,600	6,200	5,950	4,026	7,600
Pressure (psia)	1,774	1,908	4,663	2,630	2,600	1,455	3,520
Temperature (°F)	149	153	255	132	192	130	198
Mole percentage							
Nitrogen, N_2	–	–	–	–	–	–	1
Carbon dioxide, CO_2	–	–	–	–	–	–	0.8
Methane, CH_4	28.6	30.3	55.8	37.7	40.88	25.6	42.85
Ethane, C_2H_6	10.9	13.1	5.81	8.7	4.53	8.88	6.6
Propane, C_3H_8	9.4	9.4	6.42	6.3	2.6	12.41	4.1
Isobutane, C_4H_{10}	2.5	1.8	1.31	1.4	1.25	1.93	3.64
n-Butane, C_4H_{10}	4.4	4.9	3.97	3	1.82	7.56	
Pentane, C_5H_{12}							
Hexane, C_6H_{14}	4.8	4.5	3.67	3.3	3.48	5.53	3.1
Heptane+	39.4	36	2.61	39.6	4.43	38.09	3.83
	–	–	20.41	–	41.01		34.08
	100	*100*	*100*	*100*	*100*	*100*	*100*
Molecular weight							
Heptanes+	201	193	237	225	220	195	243
Specific gravity as							
Liquid heptanes+	0.840	0.840	0.891	0.840	0.824	0.839	0.876

Note: Reprinted with permission, from Donald Katz et al.: *Handbook of Natural Gas Engineering* (New York: McGraw-Hill, 1959)

Water

Formation Volume Factor. The properties of water are determined by the amount of salt dissolved in it and by pressure and temperature. Figure 3.9 relates these three variables. Note that increasing temperature tends to expand a given volume of water, whereas increasing pressure tends to contract it. Thus, values of B_w tend to be close to 1.0. B_w can be expressed in a number of equivalent forms, e.g.,

$$B_w = V_{wwf} / V_{wsc}$$
$$B_w = q_{wwf} / q_{wsc} \quad \text{or}$$
$$B_w = \rho_{wsc} / \rho_{wwf}$$

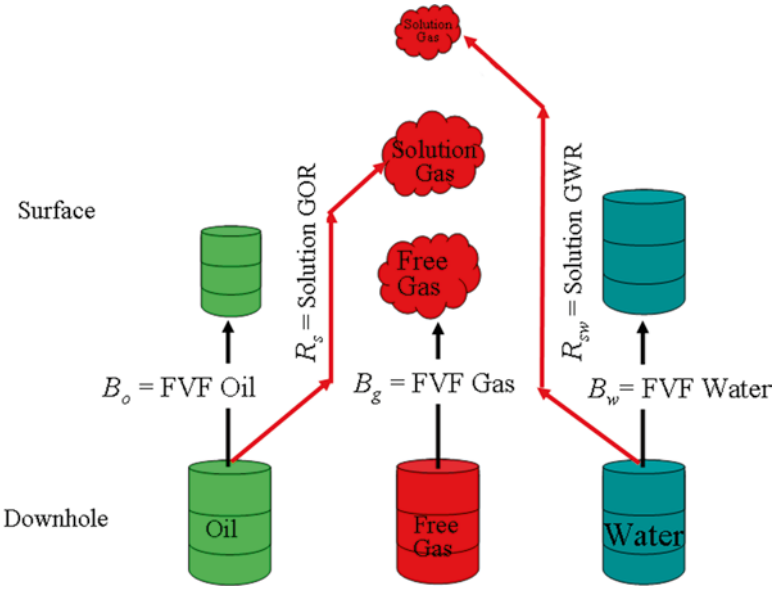

Fig. 3.8 Relation between surface and downhole volumes. Courtesy Schlumberger

As an example Fig. 3.9 can be used to find the downhole water density, ρ_{wwf}.
Given: $C_{NaCl} = 90{,}000$ ppm, $T_{wf} = 200$ °F and $P_{wf} = 2{,}000$ psia

1. Locate Point **a** by a line from $C_{NaCl} = 90{,}000$ through $T_{wf} = 200$ to **a**
2. Draw a line from $p_{wf} = 2{,}000$ through point **a** and extend it to the ρ_{wf} vertical line
3. Read $\rho_{wwf} = 1.038$ g/cm^3

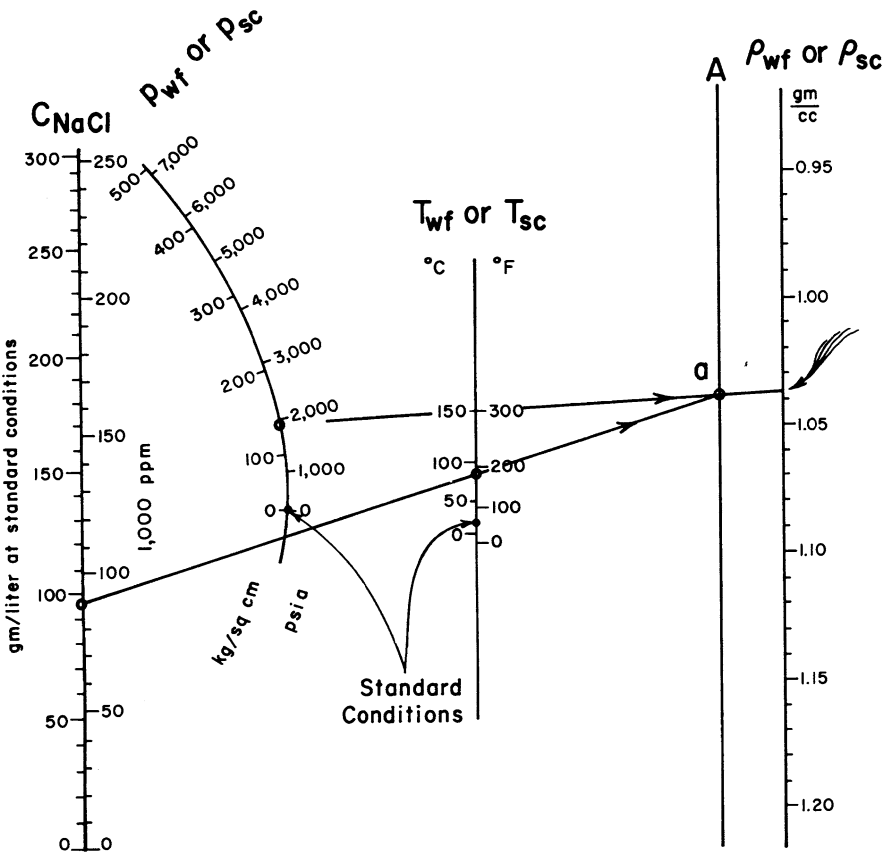

Fig. 3.9 Densities of NaCl solutions. Courtesy Schlumberger

Question #3.1 B_w and q_{wwf}
Flowing pressure = 3,000 psi, flowing temperature = 200 °F, water salinity = 150,000 ppm NaCl, and surface flow rate = 300 BWPD (barrels of water per day).

a. Find ρ_{wsc} = ___ g/cm^3
b. Find ρ_{wwf} = ___ g/cm^3
c. Hence B_w = ___, and
d. q_{wwf} = ___ BWPD

Gas Solubility in Water. Gas is soluble in water; the solubility is a function of temperature and water salinity. Figure 3.10 gives a means of finding R_{sw}. An example on how to use Fig. 3.10 to find gas solubility in water for a given set of input parameters is given here below:

$T_{wf} = 180$ °F, $p_{wf} = 3{,}400$ psia, $C_{NaCl} = 20{,}000$ ppm.

1. (Top) Enter the abscissa at $T_{wf} = 180$ °F
2. Go up to $p_{wf} = 3{,}400$ psia
3. Read $R'_{sw} = 16$ cf/B
4. (Bottom) Enter the abscissa at 20 (20,000 ppm)
5. Go up to $T = 180$
6. Read $F_{bc} = 0.91$
7. $R_{sw} = R'_{sw} \times F_{bc} = 16 \times 0.91 = 15$ cf/B

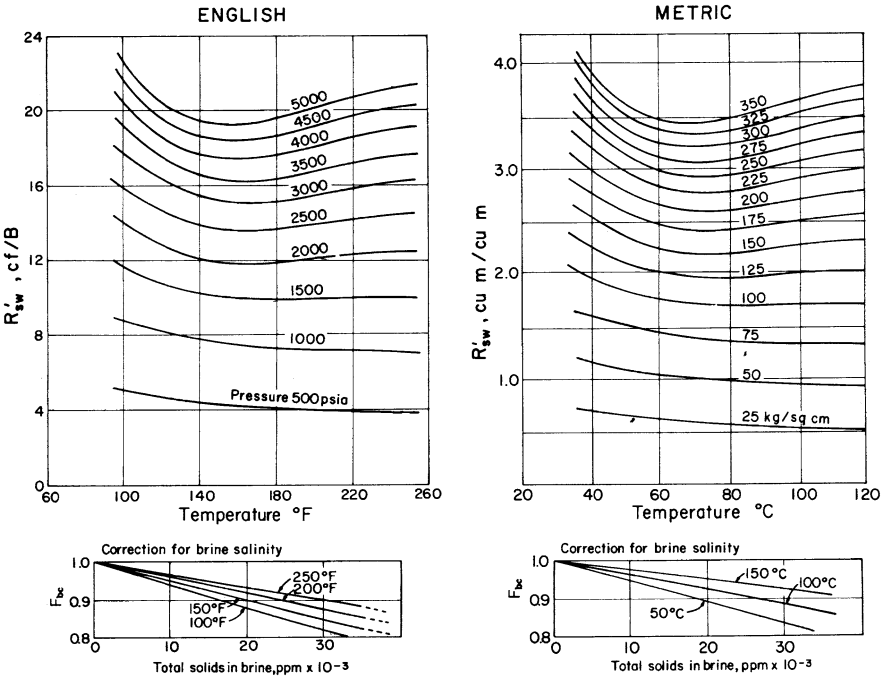

Fig. 3.10 Solubility of gas in water. Courtesy Schlumberger (after Dodson and Standing 1944)

Question #3.2 R_{sw}
Flowing pressure = 2,000 psi.
Flowing temperature = 200 °F.
Water salinity = 25,000 ppm NaCl.

a. Find R'_{sw} from the upper chart
b. Find F_{bc} from the lower chart
c. Find $R_{sw} = R'_{sw} \times F_{bc} =$ ___ cf/B

Water Viscosity. The viscosity of water can be an important item of data when interpreting spinner (flowmeter) surveys and repeat formation tester permeability tests. Water viscosity can be determined from Fig. 3.11. By way of example Fig. 3.11 may be used to find water viscosity, μ_{wwf} as follows:
Given: $C_{NaCl} = 150{,}000$ ppm and $T_{wf} = 200$ °F

1. Enter abscissa at $T_{wf} = 200$
2. Go up to $C_{NaCl} = 150{,}000$
3. Read $\mu_{wwf} = 0.43$ cp

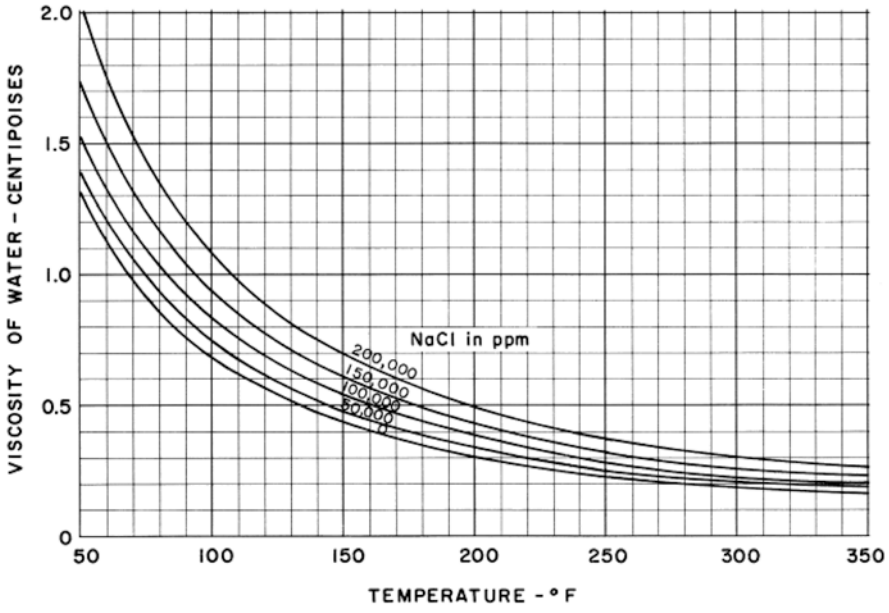

Fig. 3.11 Water viscosity. Courtesy Schlumberger

Question #3.3 μ_{wwf}
Temperature = 190 °F
Water salinity = 100,000 ppm NaCl
Find μ_{wwf} = ___ cp

Gas

Gas Formation Volume Factor B_g. The behavior of natural gases is non ideal. Thus, the ideal gas law needs a "fudge factor" to make it truly reflect the behavior of natural hydrocarbon gases. This fudge factor is given the symbol Z and is known as the *supercompressibility factor*.

The ideal gas law can then be re-written as:

$$\frac{1}{B_g} = \frac{V_{sc}}{V_{wf}} = \frac{1}{Z} \times \frac{T_{sc}}{T_{wf}} \times \frac{p_{wf}}{p_{sc}}$$

If the Z factor is known for the conditions encountered and the gas in question, then B_g may be found by direct solution of this equation. However, Z is not normally known. A short-cut method uses Fig. 3.12, which requires only temperature, pressure, and gas gravity as inputs; $1/B_g$ may be read directly as output.

An example of how to use the "quick look" chart to find $1/B_g$ and hence V_{gwf} is straightforward.

If V_{gsc} = 400 cubic ft, γ_g = 0.70, T_{wf} = 200 °F and P_{wf} = 2,000 psia.

Then select the γ_g = 0.70 section and enter the abscissa at 2,000 psia. From there go vertically to 200 °F and then left to $1/B_g$ = 125.

Remembering that $1/B_g = 125 = V_{gac}/V_{gwf}$ it follows that V_{gwf} = 3.2 cubic ft.

Question #3.4 B_g
Pressure = 3,000 psi
Temperature = 200 °F
Gas gravity = 0.7
Find $1/B_g$ = ___

When more accurate results are required, the Z factor must be determined. This is a more laborious task and involves:

1. finding the pseudo-critical pressure (p_{pc})
2. finding the pseudo-critical temperature (T_{pc})
3. finding the pseudo-reduced pressure (p_{pr})

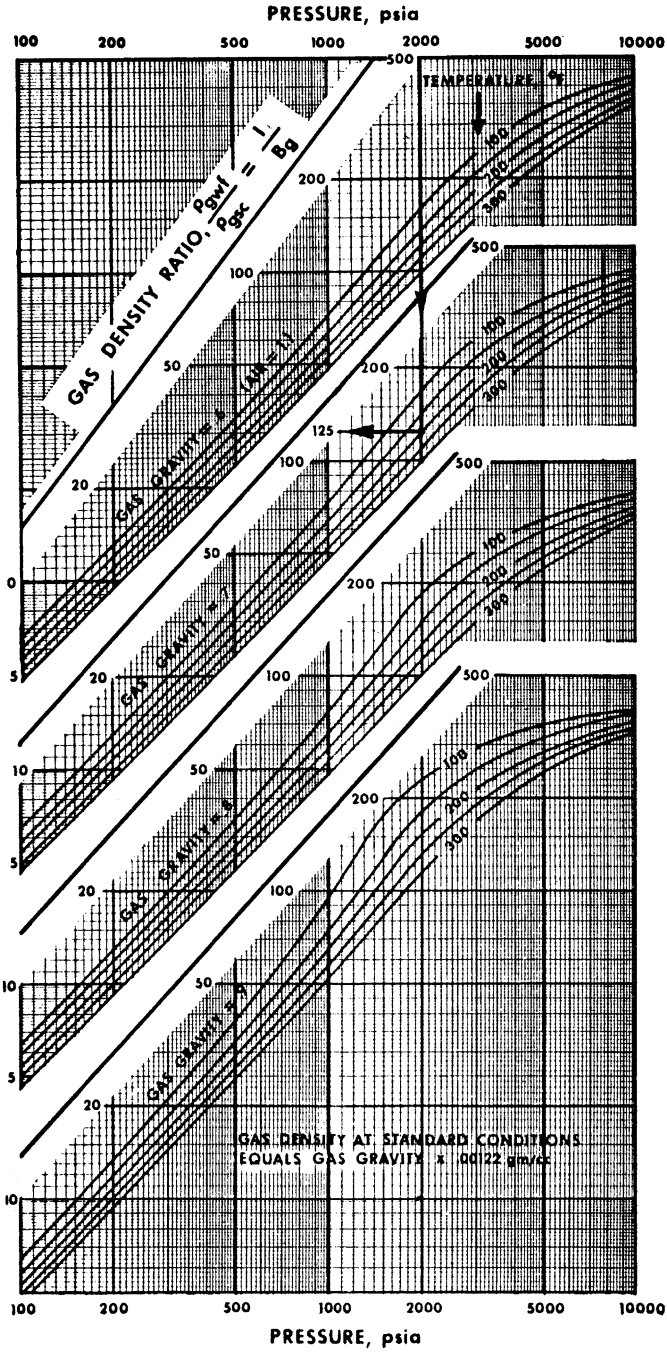

Fig. 3.12 Quick solution for B_g. Courtesy Schlumberger; after Standing and Katz 1942

4. finding the pseudo-reduced temperature (T_{pr}), and
5. using the latter two to find Z.

Figure 3.13 may be used to find p_{pc} and T_{pc} as a function of gas gravity to air and gas type. Using this Fig. 3.13 to find T_{pc} and p_{pc} is straightforward. For example if $\gamma_g = 0.75$ then enter the abscissa at 0.75 and go up to read (on the "Miscellaneous gases" line) that $T_{pc} = 406°R$ and $p_{pc} = 664$ psia. T_{pc} and P_{pc} may be converted to pseudo-reduced values depending on the flowing-well conditions:

$$p_{pr} = p_{wf} / p_{pc} \quad \text{and} \quad T_{pr} = T_{wf} / T_{pc}$$

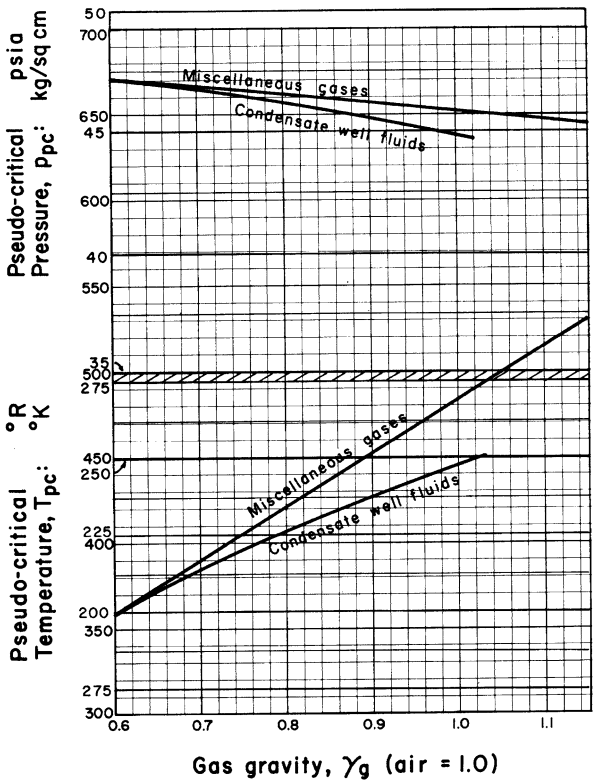

Fig. 3.13 Pseudo-critical natural gas parameters. Courtesy Schlumberger; after Brown and Katz 1948

Question #3.5 T_{pc} and p_{pc}
Given that gas gravity to air is 0.8 assume "Miscellaneous gas" and:

a. Find T_{pc} = ___ °F
b. Find p_{pc} = ___ psi

The values of p_{pr} and T_{pr} thus found can be entered in Fig. 3.14 to find the Z factor. By way of example the value of Z can be found starting with the given values:
p_{wf} = 2,000 psia, p_{pc} = 650 psia, T_{wf} = 200 °F (660 °R), T_{pc} = 410 °R then,

1. Find $p_{pr} = p_{wf}/p_{pc} = 2{,}000/650 = 3.07$
2. Find $T_{pr} = T_{wf}/T_{pc}$ 660/410 = 1.61
3. Enter abscissa (top) at 3.07 (p_{pr})
4. Go down to T_{pr} of 1.61, between 1.6 and 1.7 lines
5. Read Z = 0.828

Question #3.6 p_{pr}, T_{pr}, and Z
Given:
T_{pc} = 420 °F, p_{pc} = 662 psi, T_{wf} = 149 °F (°R = °F + 460), p_{wf} = 2,913 psi

a. Find p_{pr} = ___
b. Find T_{pr} = ___
c. Find Z = ___

Once Z is established, $1/B_g$ can be calculated either from the equation:

$$\frac{1}{B_g} = \frac{1}{Z} \times \frac{T_{sc}}{T_{wf}} \times \frac{p_{wf}}{p_{sc}}$$

or by use of the nomogram given in Fig. 3.15. Note that values for T in the above equation must be in degrees Rankin (°R). To convert from Fahrenheit to Rankin, use °R = °F + 460. By way of example $1/B_g$ can be found graphically given that p_{wf} = 140 kg/cm^2, T_{wf} = 93 °C, and Z = 0.828 by the following steps:

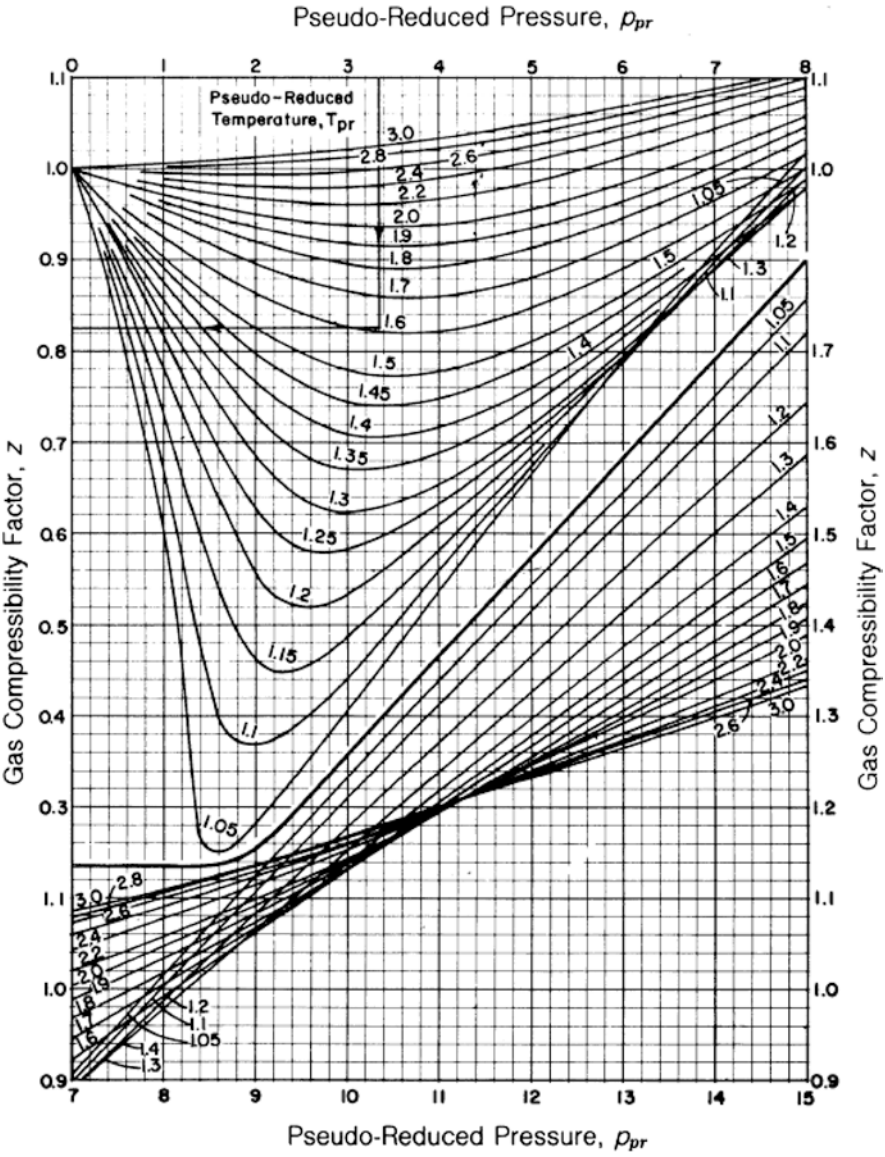

Fig. 3.14 Natural gas deviation factor. Courtesy Schlumberger; after Standing and Katz 1942

1. Enter p_{wf} scale at 140 kg/cm^2
2. Draw a **First Line** to the T_{wf} value of 93 °C. This will define a "pivot point" on the vertical line **A**
3. Draw a **Second Line** from the pivot point defined in Step 2 to the Z value of 0.828
4. Read $1/B_g = 135$

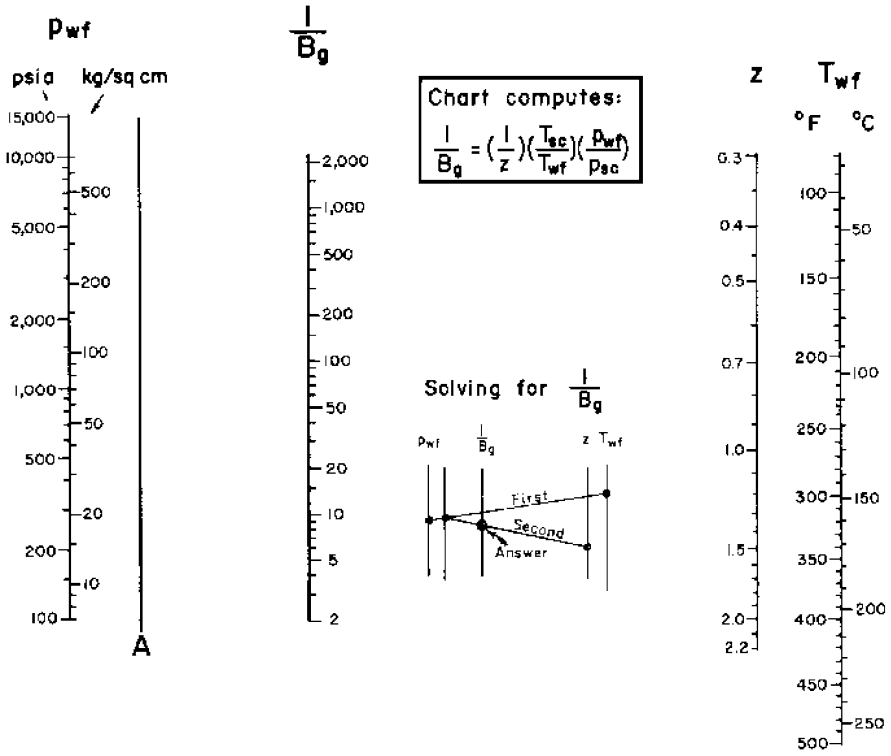

Fig. 3.15 Gas formation volume factor. Courtesy Schlumberger

Question #3.7 $1/B_g$ and q_{gwf}
Given: $p_{wf} = 2{,}913$ psi, $T_{wf} = 149$ °F, $Z = 0.76$

a. Find $1/B_g$
b. If the well flows 1 MMscf/ D, what is q_{gwf}?

Bottom Hole Gas Density. The bottomhole gas density is an important item of data for correct interpretation of gradiomanometer surveys. It may be calculated directly using the equation:

$$\rho_{gwf} = \gamma_g \times 0.001223 \times 1 / B_g \, g / cm^3$$

Figure 3.16 offers a nomogram that performs the same calculation. By way of example, if the gas density to air (γ_g) is 0.75 a line is drawn from this point, on the left of the chart, to the $1/B_g$ value of 140, on the right of the chart (as shown in the small diagram). Where this line intersects the ρ_{Fgwf}. vertical axis the answer can be read at 0.13 g/cm^3.

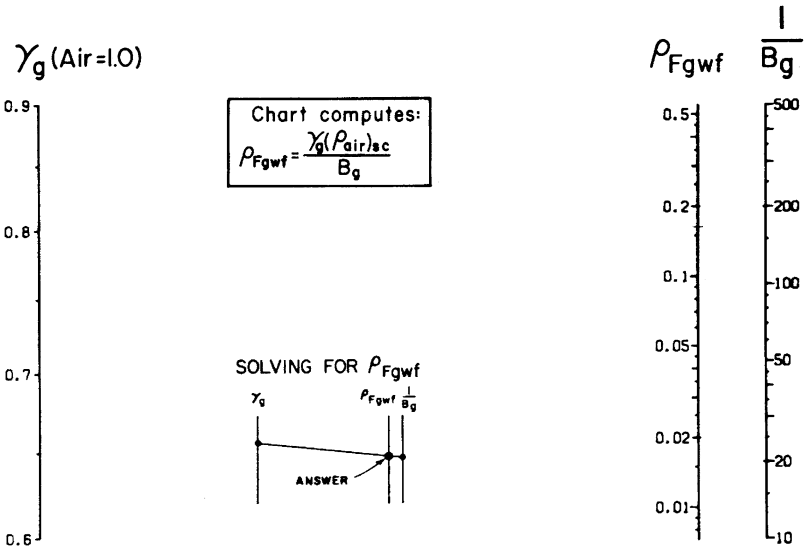

Fig. 3.16 Gas density. Courtesy Schlumberger

Question #3.8 ρ_{gwf}
Given: $1/B_g = 100$, $\gamma_g = 0.7$ (to air)
Find ρ_{gwf}=___g/cm^3

Gas Viscosity. Gas viscosity is a function of gas gravity, temperature, and pressure. Figure 3.17 offers a means of finding μ_g. By way of example the gas viscosity at well flowing conditions μ_{gwf} can be found given that $\gamma_g = 0.70$, $p_{wf} = 2{,}000$ psia, and $T_{wf} = 200$ °F by following the steps:

1. Enter $\gamma_g = 0.70$ chart at $p_{wf} = 2{,}000$ psia
2. Go up to $T_{wf} = 200$ °F
3. Read $\mu_{gwf} = 0.018$ cp

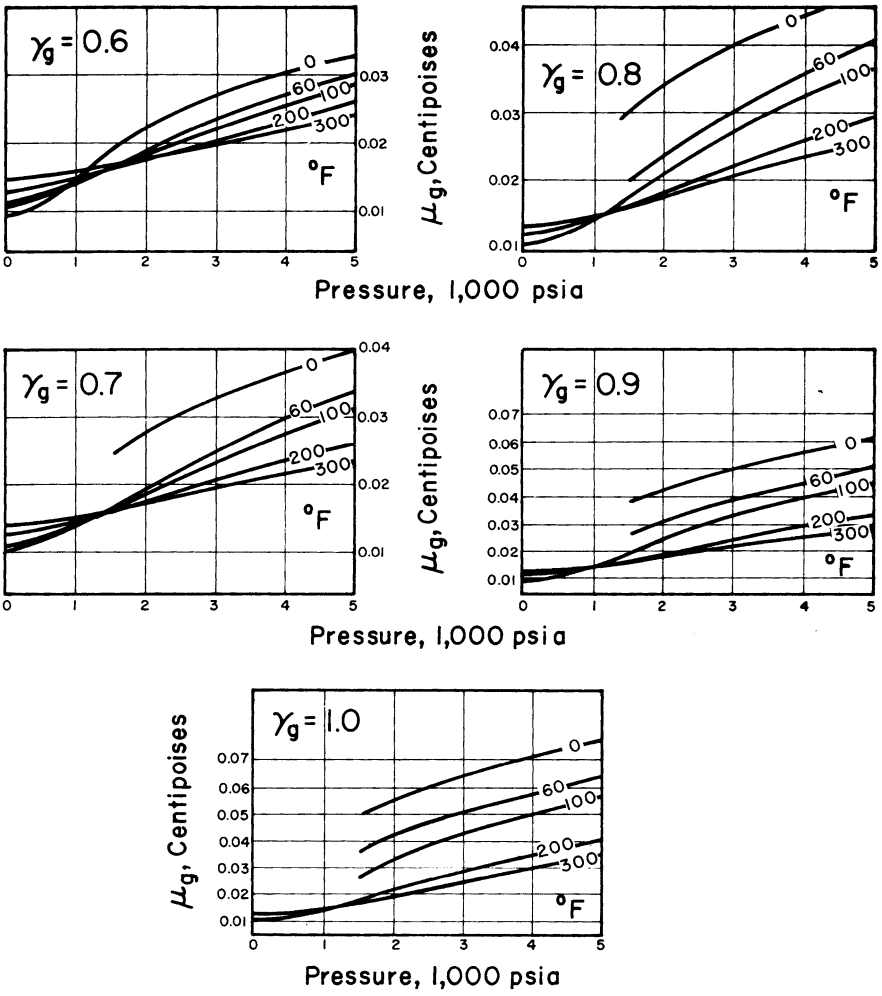

Fig. 3.17 Gas viscosity. Reprinted with permission of the Oil and Gas Journal (from May 12, 1949)

Question #3.9 μ_g
Given: $\gamma_g = 0.6$, $T_{wf} = 200$ °F, $p_{wf} = 3{,}000$ psi
Find $\mu_g =$ ___cp

Oil

Bubble-Point Pressure. The bubble-point pressure is a critical item of data. It is used to make many of the estimates necessary for correct prediction of downhole conditions during the planning of production logging and/or interpretation of the results. Bubble-point pressure (p_b) depends on T_{wf}, R_s, p_{wf}, γ_o, and γ_g. Figure 3.18 combines all these factors on one chart.

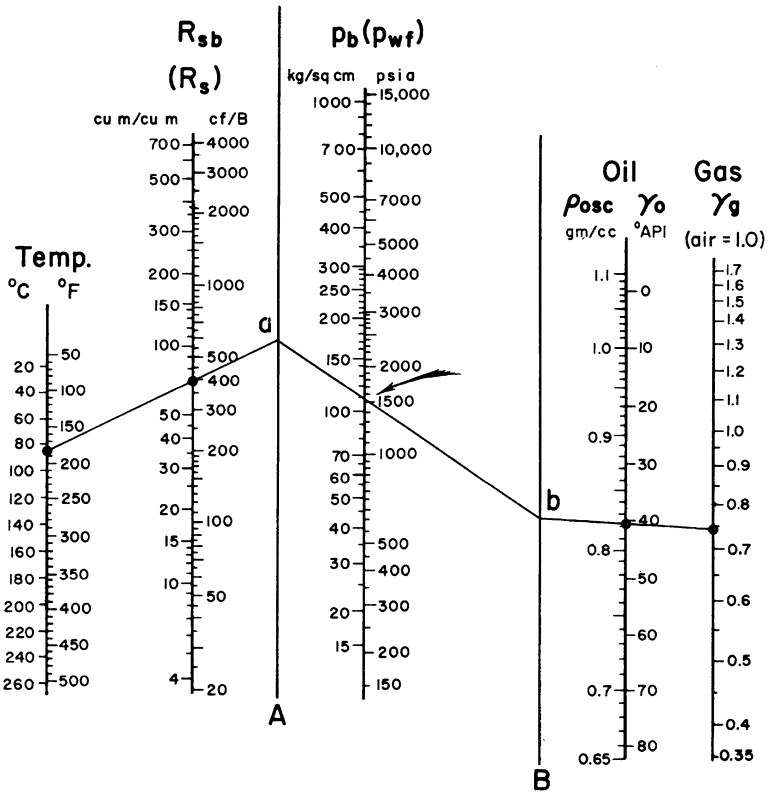

Fig. 3.18 Bubble-point pressure. Courtesy Schlumberger

An example of how to use Fig. 3.18 in order to find P_b will use the following given starting points: $T_{wf}=180$ °F, $q_{osc}=600$ B/D, $q_{gac}=240$ Mcf/D, $\gamma_g=0.75$ and $\gamma_o=40°$ API.

1. $R=\dfrac{240{,}000\text{cf / D}}{600\text{B / D}}=400\text{cf / B}$
2. $R_{sb}=R$, since the field-usage definition of P_b stipulates given flow rates of oil and gas, taken here to be q_{osc} and q_{gac} (above)
3. On the nomograph, locate Point **a** by a line through $T_{wf}=180$ °F and $R_{sb}=400$
4. Locate Point **b** by a line through $\gamma_g=0.75$ and $\gamma_o=40°$ API
5. Connect **a** and **b** to read $P_b=1{,}560$ psia

Question #3.10 p_b
Given: $\gamma_g=0.7$, $\gamma_o=40°$ API, $T_{wf}=200$ °F, $R_{sb}=1{,}000$ cf/B
Find $p_b=$___psi

Oil Formation Volume Factor

By definition, $B_o=V_{owf}/V_{osc}$ or $B_o=q_{owf}/q_{osc}$. The oil formation volume factor is a function of γ_g, R_{sb}, and T. Its value at the bubble-point pressure can be estimated from Fig. 3.19.

By way of example the value of the oil formation volume factor at the bubble-point pressure B_{ob} may be estimated from the given starting parameters:

$R_{sb}=400$ cf/B, $T_{wf}=180$ °F, $\gamma_g=0.65$, $\gamma_o=45°$ API

1. Locate Point **a** by drawing a line through $\gamma_g=0.65$ and $R_{sb}=400$
2. Draw a line from Point **a** through $T_{wf}=180$ °F, to B_{ob}
3. Read $B_{ob}=1.24$

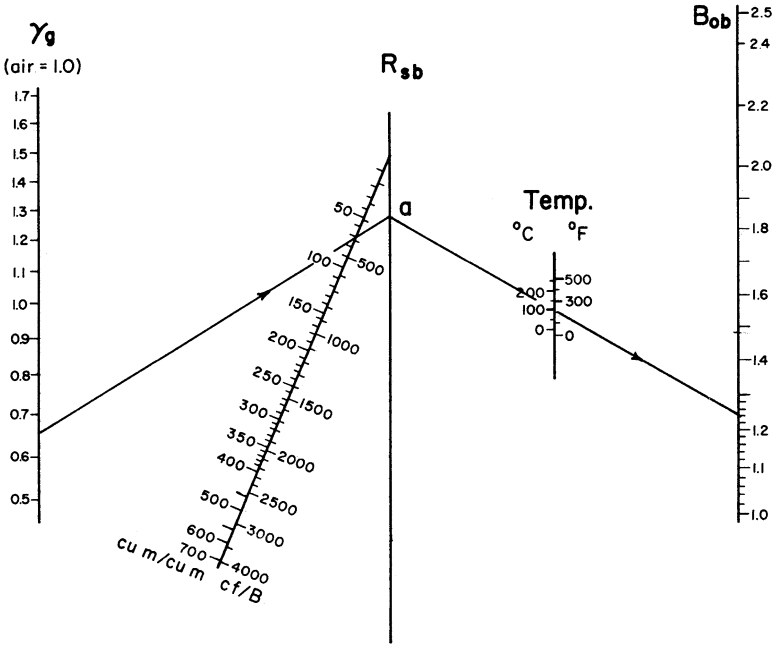

Fig. 3.19 Oil formation volume factor at P_b, Courtesy Schlumberger

Question #3.11 B_{ob} and q_{owf}
Given: $\gamma_g = 0.8$, $R_{sb} = 1{,}500$ cf/B, $T = 200$ °F

a. Find B_{ob} = _____
b. If $q_{osc} = 1{,}000$ BOPD,
find q_{owf} = _____BOPD

The nomogram in Fig. 3.19 holds only for conditions at bubble-point pressure. At well flowing pressures above and below the bubble-point, it is necessary to apply the following algorithms: (1) for undersaturated oils (above bubble-point pressure),

$$B_o = B_{ob}\left[1 - C_o\left(p_{wf} - p_b\right)\right]$$

where C_o is the oil compressibility, a function of ρ_{ob}; and (2) for saturated oils (below bubble-point pressure),

$$B_o = 1 + k\left(B_{ob} - 1\right)$$

where k is a function of p_{wf}/p_b. Figure 3.20 serves to find the values of C_o (upper portion) and k (lower portion).

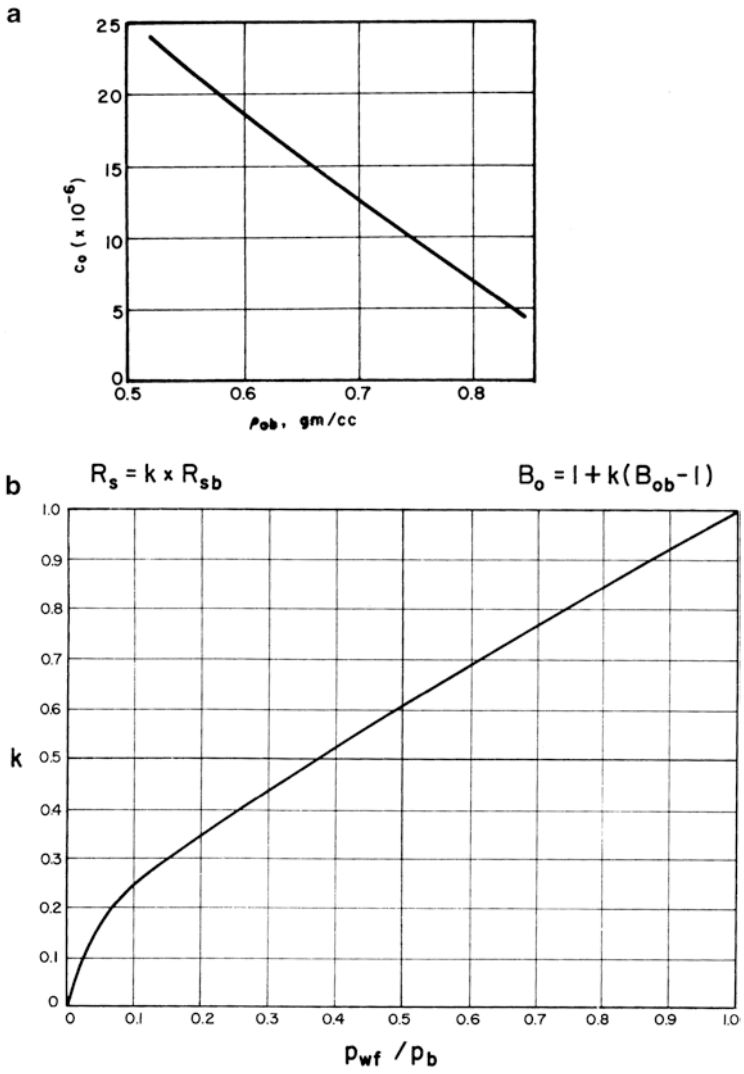

Fig. 3.20 Finding C_o and k. Courtesy Schlumberger

Question #3.12 C_o and k

a. If $\rho_{ob} = 0.745$,
   find $C_o =$ ___
b. If $p_{wf}/p_b = 0.375$,
   find $k =$ ___

Question #3.13 B_o

Using the answers from Question 3.12, find B_o for the following conditions:

a. Undersaturated oil, where
   $B_{ob} = 1.44$, $p_b = 3{,}800$, and $p_{wf} = 4{,}800$
   $\therefore B_o =$ ____
b. Saturated oil, where
   $B_{ob} = 1.44$, and $p_{wf}/p_b = 0.375$
   $\therefore B_o =$ ____

Oil Density. Oil density at well flowing conditions is another vital piece of data for interpretation of gradiomanometer surveys. It is a function of γ_g, R_s, B_o, and γ_o. Figure 3.21 combines all the appropriate data on one chart and gives ρ_{owf} as a result.

Oil density at well flowing conditions (ρ_{owf}) may be estimated using the chart by following an example calculation. If the inputs given are:

$\gamma_o = 30°$ API, $\gamma_g = 0.75$, $R_s = 350$ cf/B, $B_o = 1.21$

1. Locate Point **a** by a line from $\gamma_g = 0.75$ through $R_s = 350$
2. Locate Point **b** by a line from Point **a** to $\gamma_o = 30°$ API
3. Draw a line from Point **b** through $B_o = 1.21$ and read $\rho_{owf} = 0.77$ g/cm^3

ρ_{owf} may also be calculated directly using the equation:

$$\rho_{owf} = \frac{\dfrac{141.5}{(131.5 + \gamma_o)} + 0.0002178 \times \gamma_g \times R_s}{B_o}$$

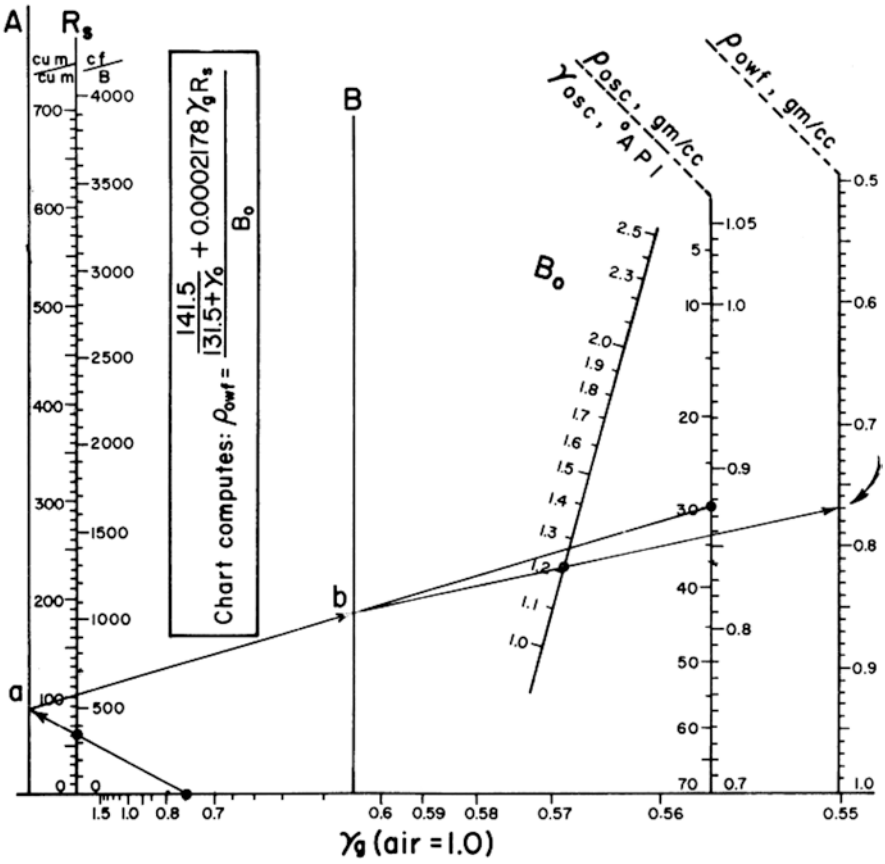

Fig. 3.21 Oil density at well conditions. Courtesy Schlumberger

Question #3.14 ρ_{owf}
Given: $\gamma_g = 0.7$, $R_s = 1{,}000$ cf/B, $B_o = 1.44$, $\gamma_o = 40°$ API
Find $\rho_{owf} =$ ___ g/cm^3

Oil Viscosity. Oil viscosity is a function of γ_{osc}, T_{wf}, R_{sb} and Δp, the incremental pressure above the bubble-point pressure. It can be determined using Fig. 3.22, which is built in two parts. The first part gives μ_{ob}, the oil viscosity at the bubble-point pressure. For conditions above p_b, μ_o increases by a factor, $\Delta\mu$, given by the second part of the chart.

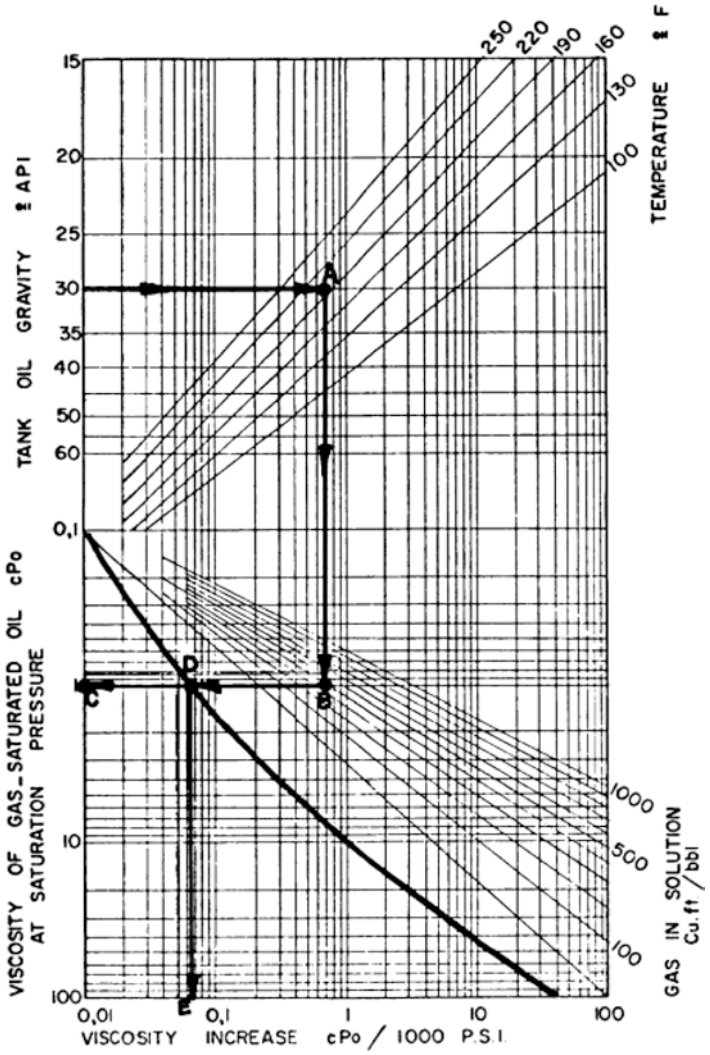

Fig. 3.22 Oil viscosity. Courtesy Schlumberger

Oil viscosity at downhole well flowing conditions (μ_{owf}) can conveniently be derived using this chart. For example, if the starting points are:

$\gamma_o = 30°$ API, $T_{wf} = 200$ °F, $p_b = 1{,}700$ psia, $p_{wf} = 2{,}700$ psia, $R_{sb} = 400$ cf/B

Then:

1. Enter ordinate at $\gamma_{osc} = 30°$ API
2. Go right to $T_{wf} = 200$ °F (Point **A**)
3. Go down to $R_{sb} = 400$ (Point **B**)
4. Go left to answer, locating Point **D** on the way: $\mu_{ob} = 1.0$ cp (Point **C**)
5. Since $p_{wf} > p_b$, $\mu_{owf} > \mu_{ob}$. From Point **D**, go down to read: viscosity increase = 0.07 cp/1,000 psi (Point **E**)
6. $\mu_{owf} = \mu_{ob} + \Delta\mu(p_{wf} - p_b)/1{,}000 = 1.0 + 0.07(2{,}700 - 1{,}700)/1{,}000 = 1.07$ cp

Question #3.15 μ_{ob} and μ_{owf}

Given: $\gamma_{osc} = 40°$ API, $T_{wf} = 190$ °F, $R_{sb} = 1{,}000$ cf/B, $\Delta p = 1{,}000$ psi

a. Find $\mu_{ob} =$ _____ cp
b. Find $\mu_{owf} =$ _____ cp

Practical Applications

The whole purpose of this section has been to equip the analyst with a practical tool for actual field cases where decisions must be made regarding tool rating and interpretation techniques. A few examples should serve to guide the user in the analysis of day-to-day problems. Before planning a production logging survey, the production history of the well should be examined. Typically, production rates may be quoted as:

900 BFPD
GOR 500 cf/B
Water cut 15 %

The first job is to translate those figures into the three components:

$q_{wsc} = 900 \times 0.15 = 135$ BWPD
$q_{osc} = 900 - 135 = 765$ BOPD
$q_{gsc} = 765 \times 500 = 382.5$ Mcf/D

The next question is, "what will be the downhole flow rate?" In order to answer that question, the values of the formation volume factors must be found. For example, given $B_w = 1.1$, $B_o = 1.3$, and $1/B_g = 150$, the downhole flow rate can be estimated as:

$$q_{wwf} = 135 \times 1.1 = 148.5 \text{ BWPD}$$
$$q_{owf} = 765 \times 1.3 = 994.5 \text{ BOPD}$$
$$q_{gwf} = \frac{382.5}{150} \times \frac{1000}{5.615} = 454.1 \text{ BGPD}$$

for a total downhole rate of 1597.1 barrels of fluid per day.

The next question will be "can free gas be expected to flow downhole at well flowing conditions?" If $p_{wf} < p_b$, then the answer is a definite "yes." However, there remains the question "how much free gas will be flowing downhole?" To answer this question, it is necessary to find the solubility of the gas in oil at pressures below the bubble-point. This may be done by applying the equation:

$$R_s = k \times R_{sb}$$

where k can be found as a function of p_{wf}/p_b from Fig. 3.20. For example, a well has the following characteristics:

$\gamma_g = 0.7$, $\gamma_o = 40°$ API, $T_{wf} = 200$ °F, $P_b = 3{,}800$ psi, $P_{wf} = 2{,}800$ psi, $R_{sb} = 1{,}000$ cf/B

From Fig. 3.20, k is found to be 0.8. Therefore, $R_s = 800$ cf/B. This means that there are 200 cubic ft of gas flowing free (1,000–800) for each barrel of oil. If the well flows at 600 BOPD, then the bottomhole flow rate of free gas is $600 \times 200 = 120{,}000$ scf/D. Note that this is expressed at standard conditions. If $1/B_g = 120$, the actual downhole flow rate is 1,000 scf/D or 178 BGPD.

A quick graphical method of solving these problems is to return to an adaptation of Fig. 3.18, which is reproduced here as Fig. 3.23. From the pivot-point **b** defined by γ_o and γ_g, two lines may be drawn, one through p_b and another through p_{wf}. These will define Points **a** and **a′**. Joining **a** to T_{wf} defines R_{sb}. Joining **a′** to T_{wf} defines R_s. The difference between R_{sb} and R_s then quantifies the amount of free gas flowing downhole:

$$q_{gwf} = q_{osc}\left(R_{sb} - R_s\right)$$

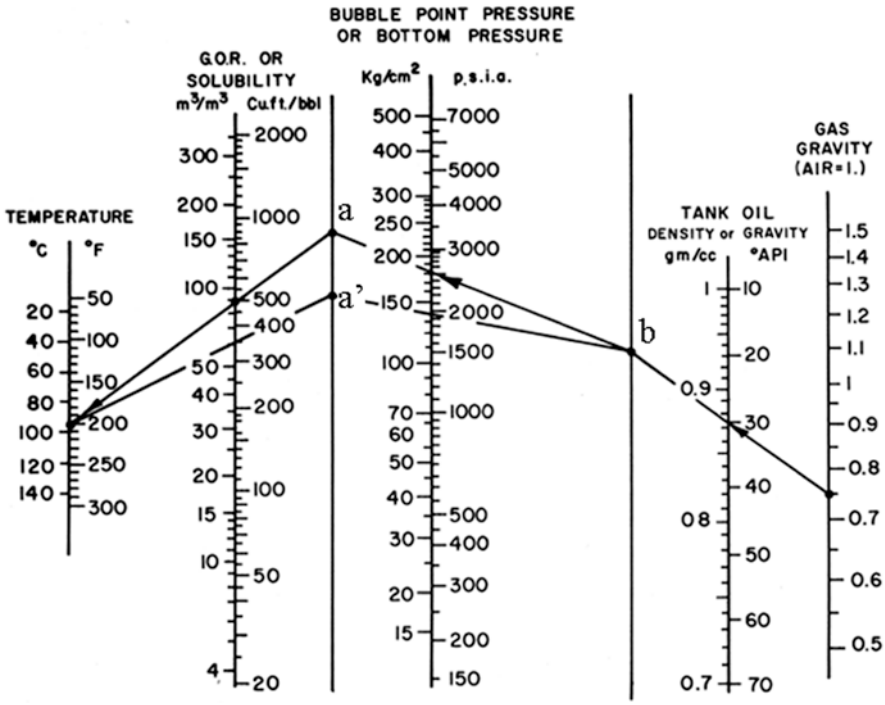

Fig. 3.23 Finding gas rate. Courtesy Schlumberger

Question #3.16 q_{owf},. q_{wwf}, and q_{qwf}

Given: q_{osc} = 50 B/D, q_{gsc} = 80 Mcf/D, q_{wsc} = 300 B/D, γ_o = 45° API, γ_g = 0.65, NaCl = 80,000 ppm, p_{wf} = 3,200 psi, T_{wf} = 170 °F

Find:

a. q_{owf} = ___BOPD
b. q_{wwf} = ___BWPD
c. q_{qwf} (free) = ___cf/D

Answers to Text Questions

Question #3.1
a. $\rho_{wsc} = 1.115$
b. $\rho_{wwf} = 1.08$
c. $B_w = 1.032$
d. $q_{wwf} = 310$ BWPD

Question #3.2
a. $R'_{sw} = 12$ cf/B
b. $F_{bc} = 0.9$
c. $R_{sw} = 10.8$ cf/B

Question #3.3
$\mu_{wwf} = 0.4$ cp

Question #3.4
$1/B_g = 190$

Question #3.5
a. $T_{pc} = 420$ °R
b. $P_{pc} = 662$ psi

Question #3.6
a. $P_{pr} = 4.4$
b. $T_{pr} = 1.45$
c. $Z = 0.76$

Question #3.7
a. $1/B_g = 222.6$
b. $q_{wwf} = 4491.6$ scfg/D

Question #3.8
$\rho_{qwf} = 0.086$ g/cm^3

Question #3.9
$\mu_g = 0.02$ cp

Question #3.10
$p_b = 3{,}900$ psi

Question #3.11
a. $B_{ob} = 1.9$
b. $q_{owf} = 1{,}900$ BOPD

Question #3.12
a. $C_o = 10 \times 10^{-6}$
b. $k = 0.5$

Question #3.13
a. $B_o = 1.43$
b. $B_o = 1.22$

Question #3.14
$P_{owf} = 0.68$ g/cm^3

Question #3.15
a. $\mu_{ob} = 0.2$ cp
b. $\mu_{owf} = 0.22$ cp

Question #3.16
a. $q_{owf} = 80$ BOPD
b. $q_{wwf} = 306$ BWPD
c. q_{gwf} (free) $= 98$ cf/D

Appendix: Standard pressures and temperatures

Place	Standard pressure (psi)	Standard temperature (°F)
Arkansas	14.65	60
California	14.73	60
Colorado	15.025	60
Illinois	14.65	60
Kansas	14.65	60
Louisiana	15.025	60
Michigan	14.73	60
Mississippi	15.025	60
New Mexico	15.025	60
Oklahoma	14.65	60
Texas	14.65	60
Utah	15.025	60
West Virginia	14.85	60
Wyoming	15.025	60
US Federal Leases	14.73	60
Canada	14.696	59 (15 °C)

Bibliography

Brown GG, Katz DL, Oberfell GG, Alden RC. Natural gasoline and the volatile hydrocarbons. Tulsa: Natural Gas Association of America; 1948.

Calhoun JC. Fundamentals of reservoir engineering. Norman, OK: University of Oklahoma Press; 1953.

Dodson CR, Standing MB. Pressure–volume–temperature and solubility relations for natural-gas–water mixture. In: Drilling and production practice, API. Washington, DC: American Petroleum Institute; 1944. p. 173–9.

Fluid Conversions in Production Log Interpretation, Schlumberger Limited, New York; 1974.

Fundamentals of Formation Testing, Schlumberger; 2006; 06-FE-014.

Production Log Interpretation, Schlumberger; 1970.

"Reservoir and Production Fundamentals, Schlumberger; 1980.

Standing MB. A pressure–volume–temperature correlation for mixtures of California oils and gases. In: Drilling and production practice, API. Washington, DC: American Petroleum Institute; 1947. p. 275.

Standing MB, Katz DL. Density of crude oils saturated with gas. In: Transactions of AIME; 1942. p. 146.

Flow Regimes

4

In this chapter, types of fluid flow will be discussed. In particular, three important concepts will be covered:

1. Laminar and turbulent flow
2. Superficial velocity
3. Holdup

A proper understanding of these concepts is essential before any quantitative interpretation of production logs is possible.

Laminar and Turbulent Flow

The flow of fluids in pipes can take place in a smooth, "streamlined" fashion or in a turbulent mode. The controlling factors are the fluid density, the superficial velocity, the pipe diameter, and the fluid density. The superficial velocity (V) is defined as the volumetric flow rate divided by the area of the pipe available for flow; that is,

$$V = 4q / \pi d^2.$$

The actual velocity of the fluid will be greater than V in the center of the pipe and less than V at the fluid/pipe interface, just as a river flows more rapidly at its middle than at its banks. A plot of fluid velocity across the pipe is shown in Fig. 4.1. Note that the velocity contrast between the center of the pipe and the superficial (or average) velocity is greater in the case of laminar flow than in the case of turbulent flow.

R.M. Bateman, *Cased-Hole Log Analysis and Reservoir Performance Monitoring*,
DOI 10.1007/978-1-4939-2068-6_4

If a logging tool, such as a spinner flowmeter, takes a measurement of fluid velocity in the center of the pipe, then it holds that some corrections must be made before converting that velocity to a volumetric flow rate. The normal practice is to take 85 % of the fluid velocity in the center of the pipe as being the superficial velocity. This is based on the assumption that flow is turbulent. The kind of flow that will occur is predicted by use of the Reynolds number, N, which is defined as:

$$N = \rho V d / \mu,$$

where:

ρ = fluid density in g/cc
V = superficial velocity in cm/s
d = inside pipe diameter in cm
μ = fluid viscosity in poise

Reynolds numbers in laminar flow are less than 2,000. In turbulent flow, they are greater than 4,000. Figure 4.2 shows a plot of flow rate vs. Reynolds number for a number of pipe IDs and viscosities.

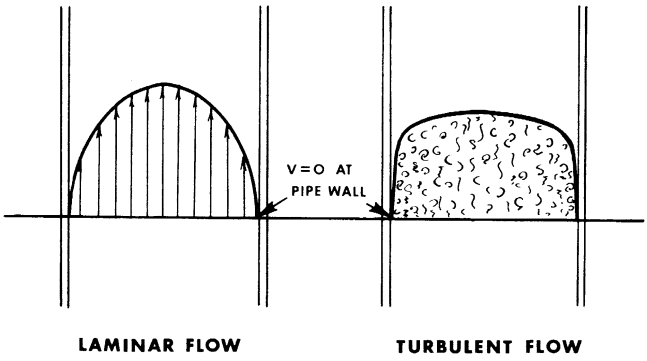

Fig. 4.1 Velocity profiles for laminar and turbulent flow—Courtesy Baker Hughes

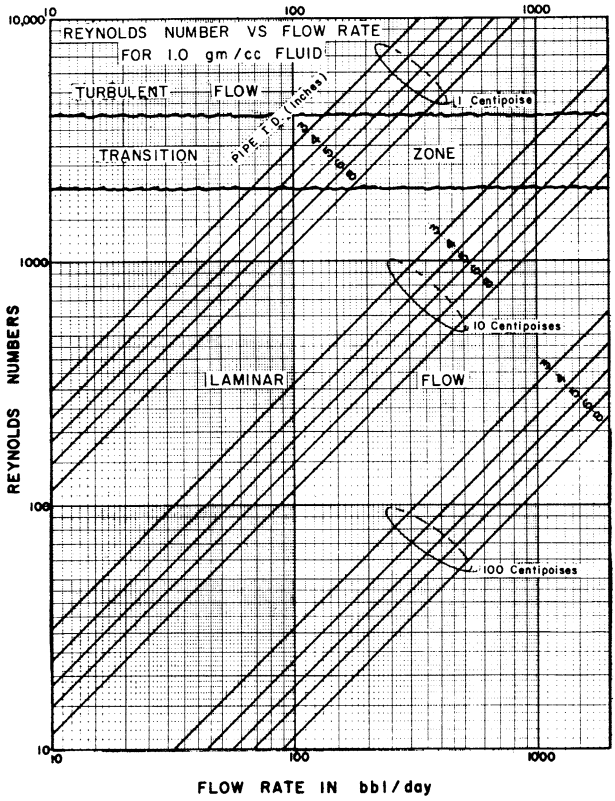

Fig. 4.2 Flow rate vs. Reynolds number—Courtesy Schlumberger

Question #4.1
Given:

$\rho = 1.0$ g/cc
$\mu = 1$ cp
$d = 5$ in.
$q = 100$ B/D

(a) Find N from Fig. 4.2.
(b) What kind of flow would you expect?

Returning to the problem of correcting flowmeter-measured velocities to superficial velocities we can now quantify the correction factor as a function of the Reynolds number. Figure 4.3 plots the correction factor directly as a function of N.

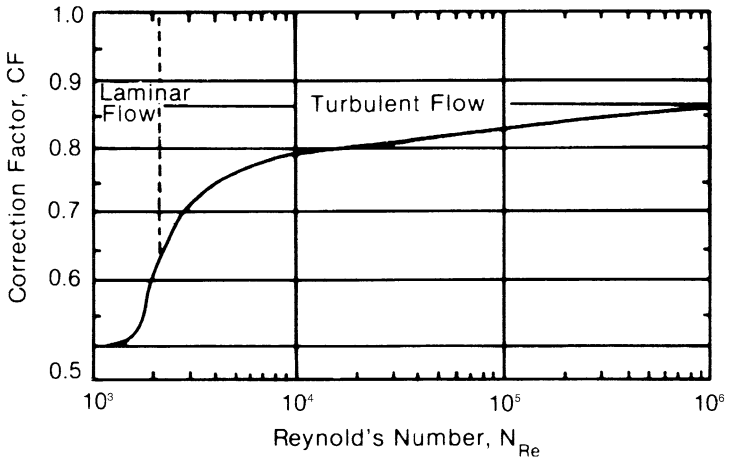

Fig. 4.3 Correction factor vs. *N*. Courtesy Baker Hughes

Unit Conversions

At this point, it is worthwhile to pause and face the problem of units. Until we are all comfortable with the SI system of units, there will be confusion when dealing with speeds, flow rates, etc., that are mixed. Flowmeters measure fluid velocities in ft/min. Flow rates are quoted in barrels/day. Pipe IDs are in inches, etc. Thus, some handy conversion formulae are in order.

Velocity

$$V = 0.363\left(q / d^2\right),$$

where:

V = superficial velocity in cm/s
q = flow rate in B/D
d = pipe ID in inches
and

$$V \text{ ft / min} = 1.969V \text{ cm / s}.$$

Flow Rate

$$q = 2.75Vd^2,$$

where:

q = flow rate in B/D
V = superficial velocity in cm/s
d = pipe ID in inches

A more complete set of conversion factors can be found in Appendix A.

Flow Regimes

If more than one fluid is flowing in the pipe, the flow regime becomes more complex. For example, liquid and gas mixtures can form a number of flow regimes depending on the relative amounts of each in the total flow pattern. These can be categorized as:

Bubble flow: bubbles of gas in liquid
Slug flow: gas bubbles reach pipe ID
Froth flow: gas carries liquid froth with it
Mist flow: liquid carried as a mist in the gas

Figure 4.4 plots dimensionless liquid velocity against dimensionless gas velocity and exhibits these various flow regimes. Note that, in general, the lighter phase in the mixture travels fastest. Bubbles of gas in a glass of beer can be seen to rise through the static liquid. Experiments show that the difference in velocity (slip velocity) of two phases is generally related to their density difference. Typical values for slip velocities are:

Oil-water mix: 20–30 ft/min
Oil-gas mix: 5–10 ft/min
Gas-water mix: 40–50 ft/min

Slip velocity as a function of density difference is shown in Fig. 4.5. The subscripts *hp* and *lp* refer to the heavy and light phases respectively.

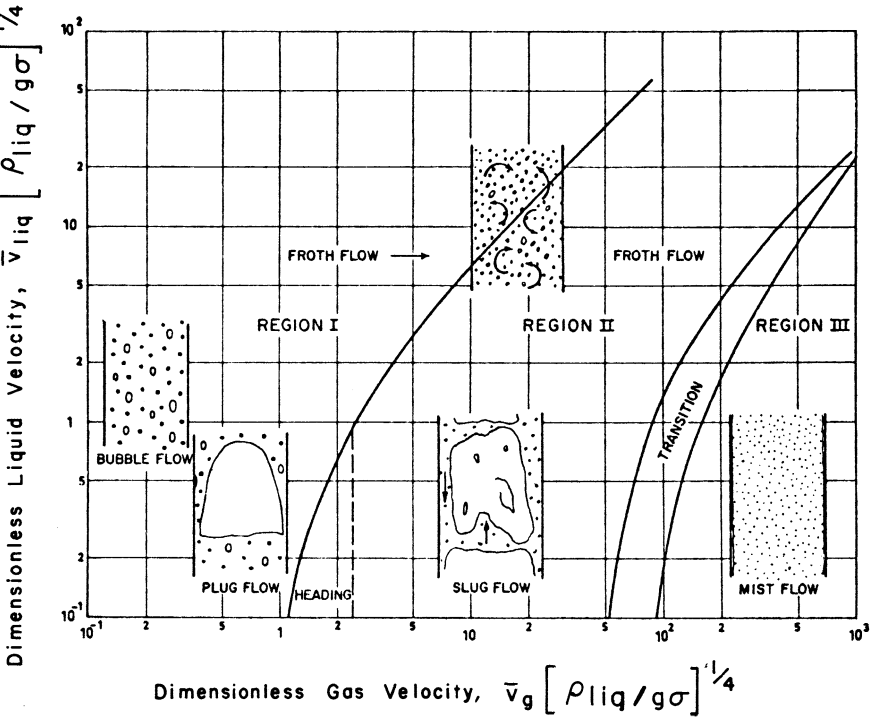

Fig. 4.4 Gas/liquid flow regimes. Courtesy Schlumberger. Reprinted by permission of the SPE-AIME from Ros (1961)

Holdup

The concept of two (or more) phases moving together up a pipe, but each with its own velocity, leads to the concept of *holdup*. To understand holdup, it is vital to bear in mind that in an oil-water mix, for example, the oil travels up the pipe faster than the water. This has a remarkable effect on production logging tools that measure fluid density.

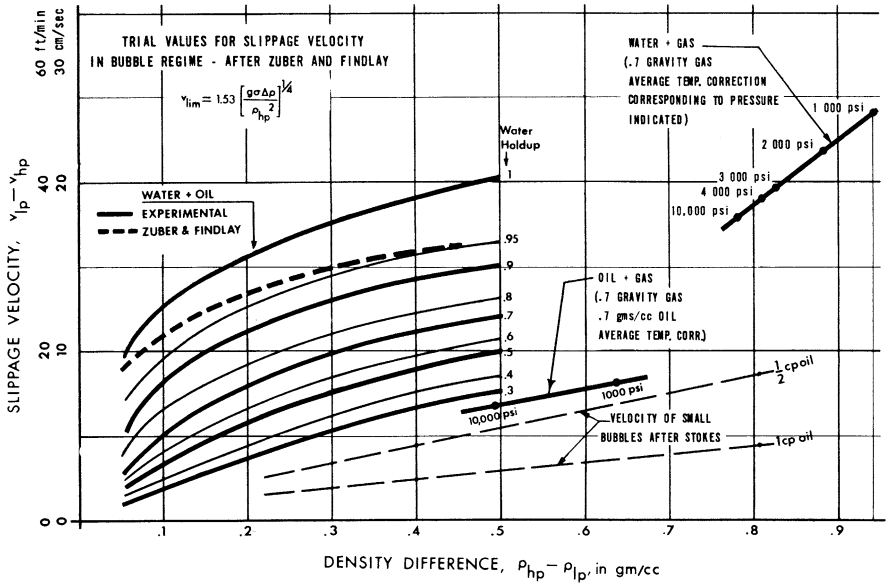

Fig. 4.5 Slip velocities. Courtesy Schlumberger (data from Zuber & Findlay 1965)

Figure 4.6 shows a section of pipe with internal cross-sectional area A, in which a mixture of oil and water is flowing. The velocity of the water is V_w. The velocity of the oil is V_o. Since the oil is traveling faster by an amount V_s, the slip velocity, we may write

$$V_o = V_w + V_s.$$

The flow rates are q_w and q_o. If we define y_w as the fraction of the cross-sectional area taken up by the water, we may write:

$$q_w = y_w A V_w,$$

$$q_o = (1 - y_w) A V_o,$$

$$q_t = q_o + q_w \,(\text{total flow}).$$

Combining all these equations it is possible to derive an expression for y_w:

$$y_w = \frac{(AV_s - q_t) \pm \sqrt{(q_t - AV_s)^2 + 4q_w AV_s}}{2AV_s}.$$

That is, we find that y_w, the fraction of the pipe area actually occupied by water, is a quadratic function of the actual water cut. Figure 4.7 shows a plot of y_w, the water holdup, against total flow as a function of water cut for flow in a 6-in. ID pipe. Note that, for example, with a 50 % water cut at a flow rate of 200 B/D some 90 % of the pipe area is in fact occupied with water.

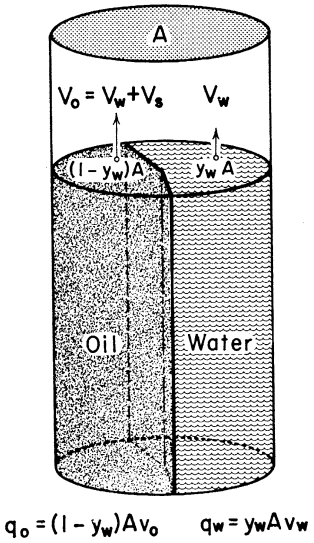

Fig. 4.6 Simplified model showing the relationship between flow rate (q), holdup (y), and velocity (V). Courtesy Schlumberger

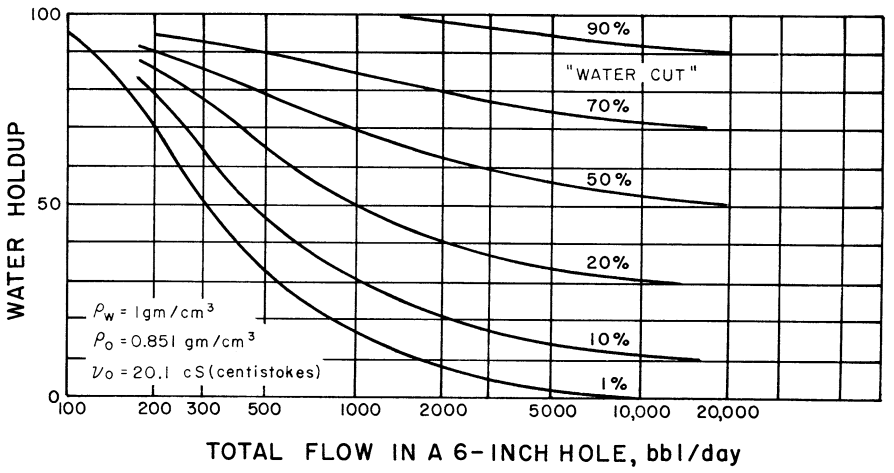

Fig. 4.7 Water holdup vs. flow rate. Courtesy Schlumberger

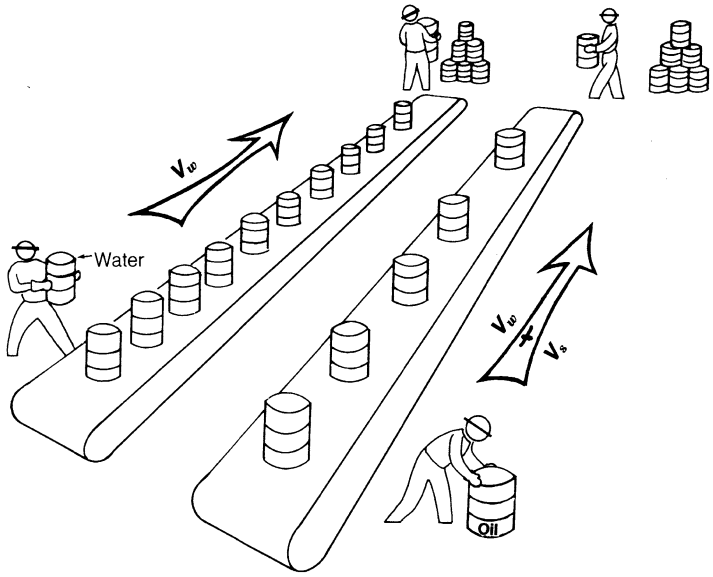

Fig. 4.8 Concept of holdup

This surprising result may be grasped more easily by reference to Fig. 4.8. Two conveyer belts are transporting barrels. One travels a constant speed of V_w transporting water and the other travels faster, at a speed of $V_w + V_s$, transporting oil. On both belts, one barrel is placed every minute. At the other end, one barrel of each is offloaded each minute. So the "production" of oil and water is equal on the two belts. However, someone unaware of the difference in speed of the two belts could conclude that the system was "producing" more water than oil since there are more barrels of water on the left belt than barrels of oil on the right belt. The gradiomanometer tool, for example, just measures liquid density and has no knowledge of flow rates or slip velocities. Proper interpretation of the average density requires computation of the holdup.

Question #4.2

y_w

Pipe area = 200 cm^2
Slip velocity = 10 cm/s
Total flow rate = 4,800 cc/s
Water cut = 50 %

(a) Find y_w.
(b) If $\rho_o = 0.6$ g/cc and $\rho_w = 1.0$ g/cc, what will be the density of the flowing mixture?

Bibliography

Interpretative methods of production well logs. 2nd ed. Dresser Atlas; 1982.
Schlumberger. Production log interpretation; 1973.
Ros NC. Simultaneous flow of gas and liquid as encountered in well tubing. J Pet Technol. 1961
Zuber N, Findlay JA. Average volumetric concentration in two-phase flow systems. J Heat Transfer. 1965;87:453.

Answers to Text Questions

Question #4.1
(a) $N = 1{,}847.6$
(b) Laminar

Question #4.2
(a) $y_w = 0.6$
(b) $\rho_{mix} = (0.6 \cdot 1.0) + (0.4 \cdot 0.6) = 0.84$ g/cc

Flowmeters

5

Applications

Tools that measure flow rate or trace where fluids have gone have applications in both producing and injecting wells. Specifically, these types of tools may be used for:

1. Production profiles
2. Injection profiles
3. Finding casing and tubing leaks
4. Gauging the effectiveness of well treatments

The tools available for making the appropriate measurements are:

Packer flowmeters (including basket type)
Continuous flowmeters (spinners)
Full-bore flowmeters
Oxygen activation (using a pulsed neutron tool)
Radioactive tracers (gamma ray)
Temperature gauging devices (both conventional thermometers and fiber optics)

Each tool has its particular merits for certain well conditions and ranges of flow rates. Table 5.1 summarizes each tool's applicability.

R.M. Bateman, *Cased-Hole Log Analysis and Reservoir Performance Monitoring*,
DOI 10.1007/978-1-4939-2068-6_5

Table 5.1 Flow-measuring devices

Tool	Flow rate
Packer/basket	Low flow (10–1,900 B/D)
Continuous flowmeters	High flow (3,000 B/D and up)
Full-bore flowmeters	Medium flow (50 B/D and up)
Radioactive tracers	Any rate
Oxygen activation	(Special limitation)
(Thermometers)	(Qualitative only)

Packer and Basket Flowmeters

Packer flowmeters and basket flowmeters both operate in a similar mode. The tool is lowered through the tubing and then held stationary in the casing. The total flow is then forced to pass through a central tube containing a spinner. This is achieved in the case of the packer flowmeters by means of an inflatable packer bag. The basket flowmeters open overlapping metal "petals." Figure 5.1 illustrates a packer flowmeter with its packer bag inflated. Stationary measurements are normally made in the casing between sets of perforations. The flow into or out of any set of perforations is deduced from the measured flow above and below that set of perforations. Raw tool readings are in terms of spinner revolutions per second. Depending on the diameter and pitch of the spinner used, the measured rate of rotation [revolutions per second (rps)] is converted into a flow rate in barrels per day. Presentation of the log may be in the form of a flow profile or by contribution to total flow by zone. Figure 5.2 illustrates a basket flowmeter survey for a producing well.

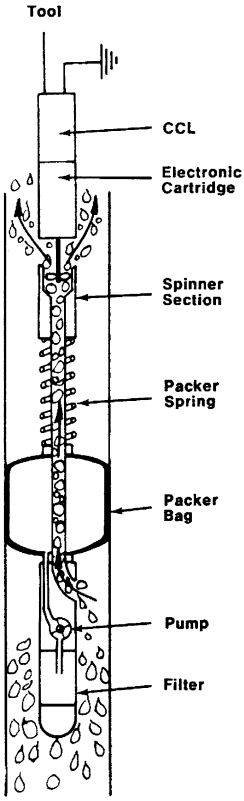

Fig. 5.1 Inflatable packer flowmeter. Courtesy Schlumberger

The advantages of packer and basket flowmeters are:

1. In biphasic flow, holdup becomes insignificant. Because flow is restricted to a small area, the actual flow rate in the tool is very high.
2. In inclined pipes, the problems of gravity segregation of fluids are minimized.

The disadvantages are:

1. A fairly large pressure drop develops across the tool, and this may eventually blow the tool up-hole like a piston in a cylinder.
2. The packer bags are quite prone to mechanical wear and once a leak develops it is impossible to get a seal and make a representative measurement.

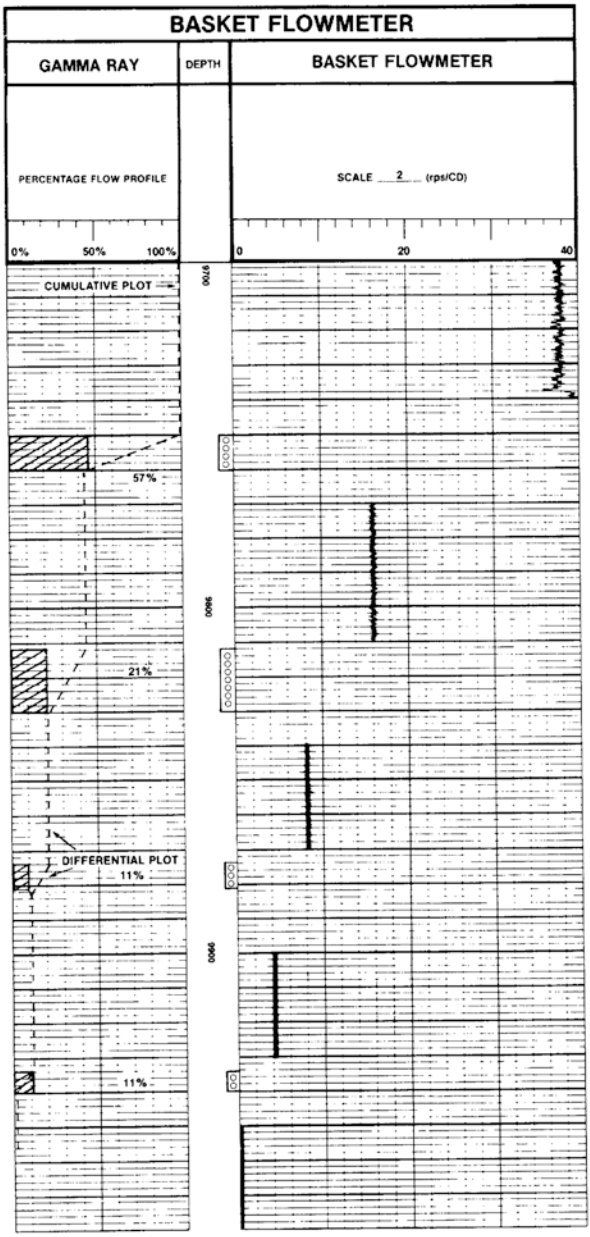

Fig. 5.2 Basket flowmeter survey. Courtesy Baker Atlas

Continuous Flowmeters

The continuous flowmeter is so named because, unlike the packer flowmeter which makes station measurements, it makes a continuous log of flow against depth. Figure 5.3 shows the general form of these tools. Figure 5.4 shows details of the spinner section. Note that the cross-sectional area "seen" by the spinner is very small compared to the total area available to wellbore fluids. For this reason, these tools are less sensitive than the packer flowmeter, but can record much higher flow rates without danger of being shot out of the hole.

Fig. 5.3 Continuous flowmeter. Courtesy Titan

Since the continuous flowmeter log is recorded with the tool in motion, the fluid velocity active on the spinner is the algebraic sum of the cable speed *and* the fluid speed. The normal mode of operation is to move the tool against the flow. An important part of the measurement is thus the cable speed itself and this is usually recorded in Track 1 of the log. Figure 5.5 shows a typical continuous flowmeter recording.

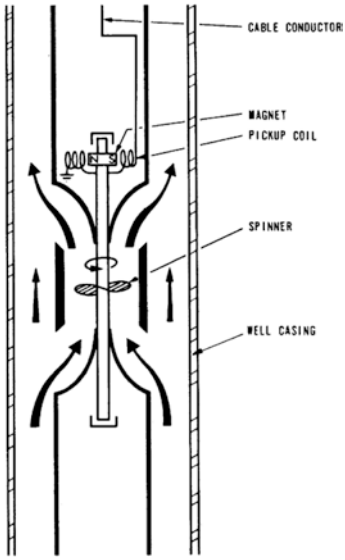

Fig. 5.4 Detail of spinner section of a continuous flowmeter. Courtesy Schlumberger

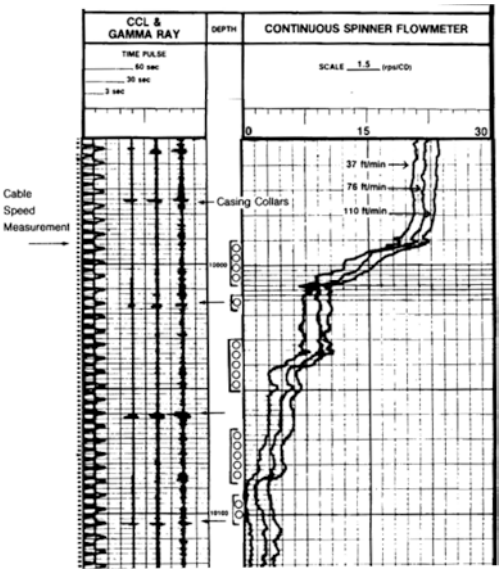

Fig. 5.5 Continuous flowmeter log. Courtesy Baker Atlas

Full-Bore Flowmeters

The full-bore flowmeter is a variation of the continuous flowmeter. In the collapsed mode, the tool will fit inside the tubing. Once past the end of the tubing and into the casing, the tool may be opened and spinner blades will be extended to cover a large portion of the area available for wellbore fluids. This mechanical marvel thus extends the usefulness of continuous flowmeters to cover low-flow rates and can record flows of as little as 200 B/D in 5½-in. pipe. Figure 5.6 shows the full-bore flowmeter in the closed and opened modes.

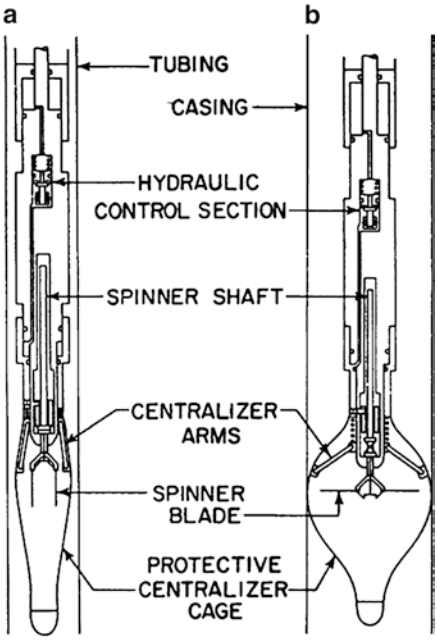

Fig. 5.6 Full-bore flowmeter. (**a**) Tool closed, (**b**) Tool open. Courtesy Schlumberger

Combination Tools

It should be noted that flowmetering tools are frequently run in combination with other sensors such as temperature, fluid density, fluid pressure, etc. Examples of these combined tools include the PCT (production combination tool) illustrated in Fig. 5.7.

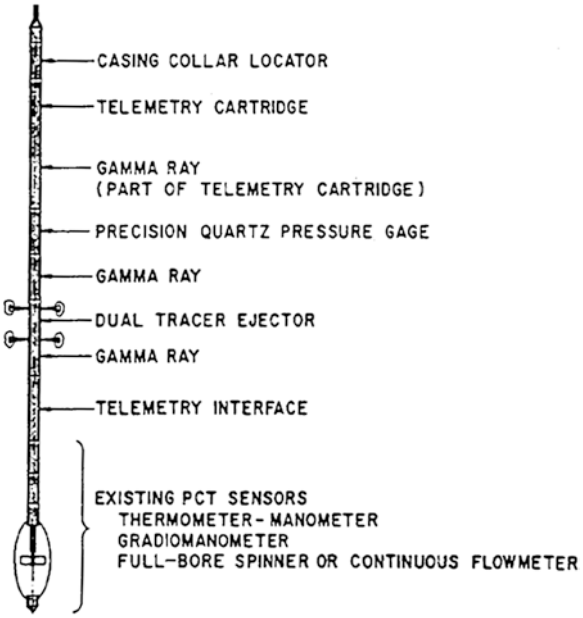

Fig. 5.7 Production combination tool. Courtesy Schlumberger

Interpretation of Flowmeter Surveys

Interpretation of the packer flowmeter is straightforward, since flow rate is a direct function of spinner rps. Interpretation of the continuous flowmeters, however, is more intricate. If the spinner was frictionless, the response of the tool would be linear and depend only on the geometry of the spinner. Figure 5.8 plots rps against fluid velocity for the ideal frictionless-spinner case.

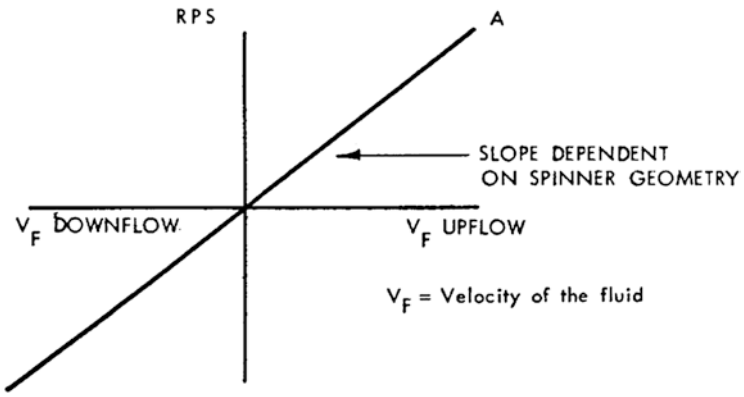

Fig. 5.8 Ideal spinner response. Courtesy Schlumberger

The fact that spinner mountings are not frictionless causes the real response to differ from the ideal. Additionally, the effects of the viscosity of the fluid cause further deviations from the ideal. Figure 5.9 shows the same plot of rps against fluid velocity but adds the effects of fluid viscosity. The viscous-fluid response lines are shown as being continuous; however, the friction of the spinner in its mounting results in a threshold below which the spinner will not turn. The true response therefore is as shown in Fig. 5.10. Note that where fluid velocities are small, regardless of direction, the spinner will not turn at all.

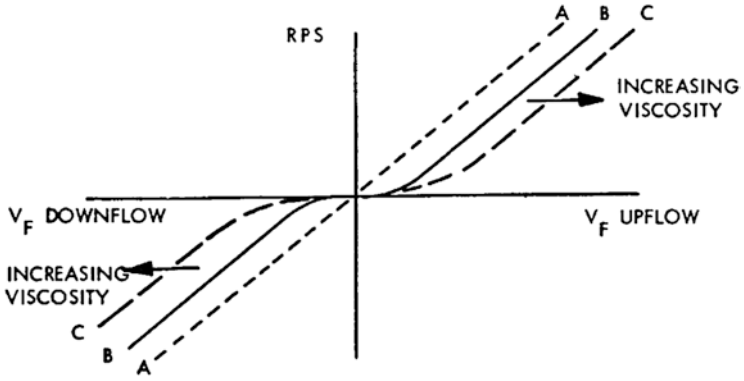

Fig. 5.9 Spinner response in viscous fluids. Courtesy Schlumberger

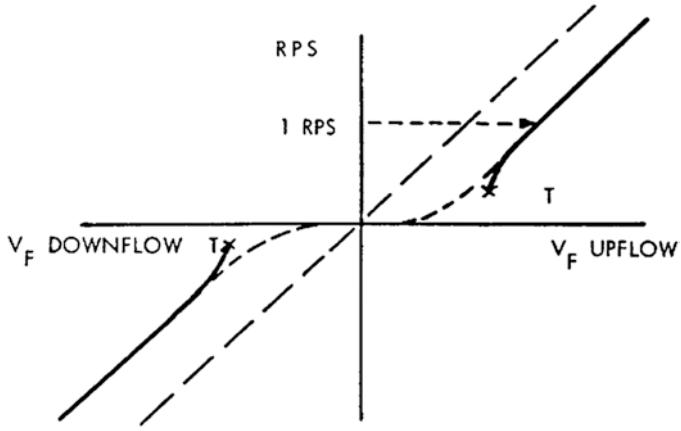

Fig. 5.10 True response of spinner. Courtesy Schlumberger

The generally accepted practice is to calibrate the continuous flowmeter in the well itself rather than trying to estimate the effects of viscosity and friction. The technique calls for several passes to be made in the well at different cable speeds both against and with the flow direction. A plot may then be prepared from which the analyst can deduce the fluid speed at each point in the well. Figure 5.11 illustrates the technique.

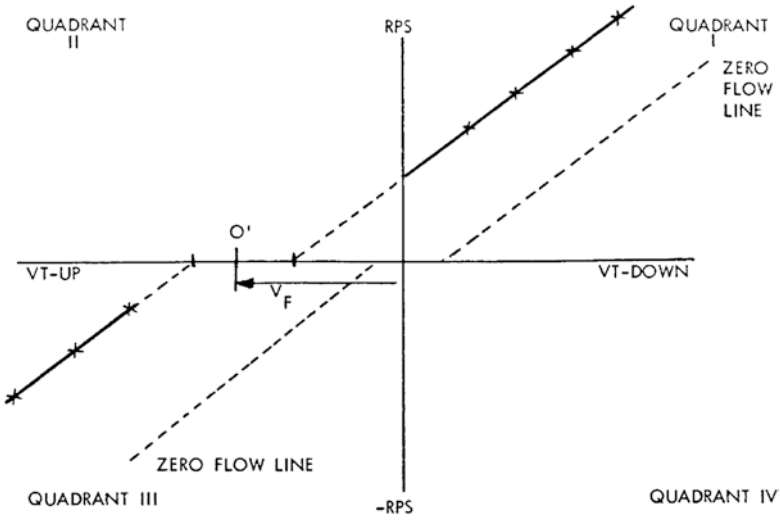

Fig. 5.11 Calibration of continuous flowmeter. Courtesy Schlumberger

The tool velocity (from the cable speed and direction recording in Track 1) is plotted against rps for a single depth in the well for several passes of the tool. In this example, four passes were made going down (see Quadrant I) and three coming up (Quadrant III). The procedure is to extend a line through the "down" points to intersect the zero rps line *and* extend another line through the "up" points to intersect the same line. Midway between these two intersections is marked the point O'. The true fluid velocity is then read off from zero tool velocity line to the point O'.

A graph of this sort is prepared for each point in the well for which a flow rate is required. (Normally the service company engineer will make these calibration plots. However, the reader should know how to do it.)

Note that flow rate is still unknown. The tool has measured the fluid speed and direction. It remains to convert the fluid speed to a volumetric flow rate by multiplying by the cross-sectional area of the pipe. Conventionally, flowmeter results are quoted as fluid speeds in feet per minute. A useful conversion is:

$$\mathrm{B/D} = 1.4 \times \mathrm{ft/min} \times \left(\text{casing ID in inches}\right)^2 .$$

Before making the conversion, remember that flowmeters are run centralized in the pipe and therefore record the speed of the fluid in the center of the pipe.

Figure 5.12a shows the position of the tool in the flow stream together with the flow profile. The flow profile across the pipe is a function of the Reynolds number (see Chap. 4). Use of the fluid speed measured by a flowmeter without correction would overestimate true flow rate. The correction factor as a function of the Reynolds number is shown in Fig. 5.12b. In most cases, this factor is between 0.84 and 0.85. It is applied as follows:

$$V_{\text{superficial}} = V_{\text{measured}} \times \text{Correction factor.}$$

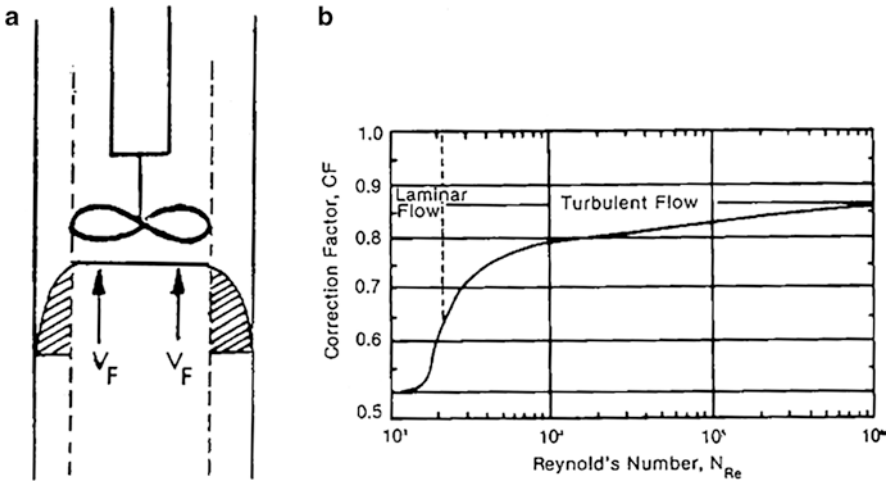

Fig. 5.12 Flowmeter correction factor. (**a**) Courtesy Schlumberger and (**b**) Courtesy Baker Atlas

Question #5.1

A flowmeter survey completed 6 passes. The cable speed, direction, and corresponding spinner rps were as follows:

	Tool speed (ft/min) rps	rps
Logging down	10	5
	60	10
	110	15
Logging up	−110	−5
	−160	−10
	−210	−15

(a) Plot these points on linear graph and determine the fluid speed.
(b) Use a correction factor of 0.85 and determine the flow rate in B/D for 7-in. 20-lb pipe.

Where Continuous flowmeter surveys are run in barefoot completions, a measure of the hole size is vital to the correct computation of flow rates. Such hole-size gauging can be obtained from a through-tubing caliper of the sort illustrated in Fig. 5.13.

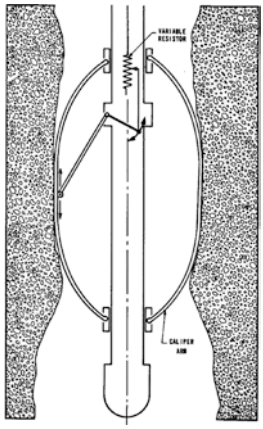

Fig. 5.13 Through-tubing caliper. Courtesy Schlumberger

Measurements in Deviated Holes

There are grave dangers in running flowmeters in deviated holes. Controlled experiments in flow loops, where the deviated angle of the hole can be changed at will, have shown that, if the flowmeter tool lies on the low side of the pipe, it may record a downflow even in places where the flow is upward. Figure 5.14 illustrates the mechanics of these erroneous measurements.

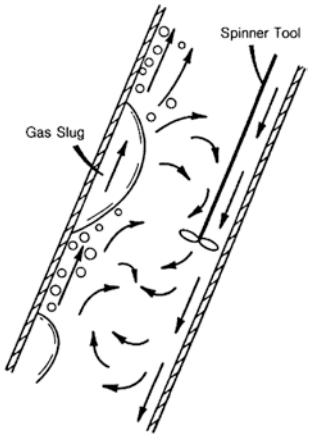

Fig. 5.14 Erroneous flow measurement in a deviated pipe. Reprinted with permission of the SPE from Hill and Dolman 1982, fig. 2, p. 2433.©1981

Measurements in Horizontal Holes

The challenge in horizontal holes is even greater since gravity segregation of gas, oil, and water can produce uneven flow regimes and flow directions. To combat these effects production logging tool designers have made a number of flow measurement approaches. In one, multiple small spinners are arrayed across the diameter of the pipe, as illustrated in Fig. 5.15.

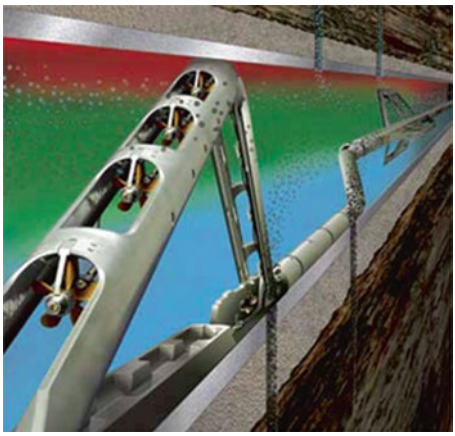

Fig. 5.15 Vertically arrayed spinners in horizontal pipe. Image copyright Schlumberger. Used with permission

An alternative approach uses a circumferential array of spinners to better map the flow regimes in different sectors of the near horizontal flow pattern as illustrated in Fig. 5.16.

Fig. 5.16 Spinner array tool (SAT) in horizontal pipe. Courtesy GE Oil & Gas, 2014

Flow measurement alone is not sufficient to completely describe both the flow rate of each phase and whether its position within the cross section is of the quasi-horizontal or highly deviated pipe string. Of assistance in this task is a sister tool that uses a circumferential array of capacitance sensors that can distinguish between water and hydrocarbons that have different dielectric properties. Figure 5.17 illustrates such a capacitance array tool.

Fig. 5.17 Capacitance array tool (CAT) sensors. Courtesy GE Oil & Gas, 2014

Other sensors are also available to help distinguish which fluid phase is traveling in which direction in what sector of the pipe being studied and by combining such multiple measurements, 3-D "maps" of fluid type and flow can be constructed and the results visualized as shown in Fig. 5.18. More will be discussed on this topic in Chap. 10.

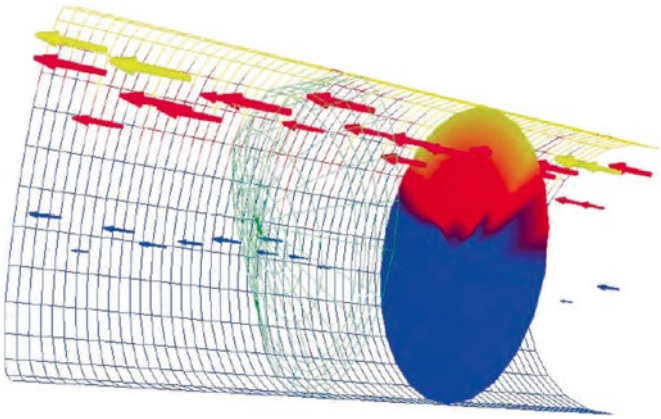

Fig. 5.18 Visualization of fluid phase and flow rate using MAP view software. Courtesy GE Oil & Gas, 2014

Oxygen Activation Logging

Pulsed neutron logging is covered in Chap. 11 in detail. The normal use of tools that rely on pulsed neutron capture (PNC) is for the determination of the captured cross section, sigma (Σ), of the materials surrounding the logging tool. In a cased-hole environment these materials include both the borehole fluids inside the casing and the formation outside the casing. A correctly compensated PNC measurement can then indicate the water saturation in the formation surrounding the casing.

A secondary use for PNC tools is as an indicator of the flow of water. Although it was never intended as a flowmeter some quirks of nuclear physics allow a tool that was designed for formation evaluation can also be used for flow metering. The mechanism that makes this possible is called nuclear activation. It takes place when fast neutrons emitted from the PNC's neutron generator collide with atoms of oxygen and "activate" them. Oxygen atoms have nuclei that include eight neutrons and eight protons. In the activation process an extra neutron is temporally added to an oxygen nucleus producing an unstable isotope (Oxygen 17). This in turn decays with the emission of a beta particle and gamma rays leaving behind an atom of nitrogen. The process has a short half life of just over 7 s. The gamma rays that are emitted in this activation process can be detected with the PNC tool itself.

Any oxygen atom is fair game for this process whether it be in the form of water (H_2O) or part of another compound (e.g. $CaCO_3$). The application in flow metering is by "tagging" water in a flow stream and detecting gamma ray increases over background as the activated water flows past the tool.

Figure 5.19 gives a schematic of a typical PNC tool. Note that there are three gamma ray detectors. The "upper" detector is a conventional gamma ray detector run in continuous mode to serve as a measure of natural formation radioactivity (as used for depth correlation, etc.). Two additional gamma ray detectors (referred to as the "near" and the "far" detectors) are used when PNC tools are measuring Σ. These are sampled at specific short time intervals to gauge the rate at which gamma rays of capture, emanating from the formation, die away as a function of time. In the flow metering mode, the gamma ray detectors are used to time, when the activated oxygen atoms pass in front of the detectors. For this purpose the "far" and the "upper" detectors are used.

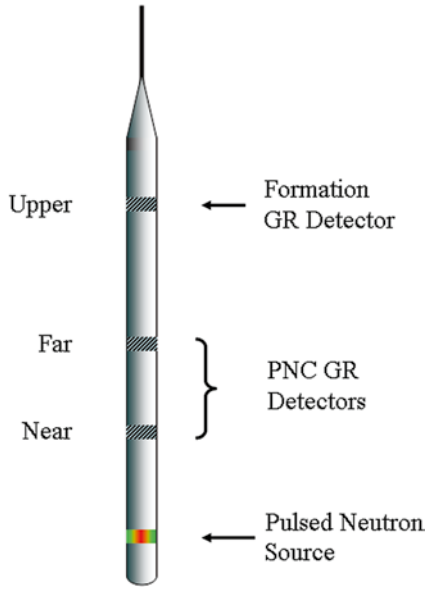

Fig. 5.19 Typical pulsed neutron tool

In the flowmeter mode the PNC tool is used to record a background gamma ray log with the neutron generator switched off. The gamma rays detected come only from the natural decay of radioactive materials in the formation surrounding the borehole (potassium, thorium, and uranium).

The tool is then lowered to the bottom of the hole and the neutron generator switched on. Provided that the flow speed of the activated oxygen in the tool-casing annulus is greater the speed of the tool as it is raised in the well then the gamma rays emitted from the activation decay will show up as the water stream catches up with and passes the gamma ray detector on the tool. The speed at which the activated oxygen flows, depend simply on the upward volumetric flow rate of the wellbore fluids and the available cross-sectional area between the tool and the ID of the casing (or tubing, as the case may be). This is beyond the control of the operator conducting the survey. However the logging speed can be controlled and indeed must be in order to assure that usable data be recoded. If the tool is reeled in too fast and the flow rate of water is low the activated oxygen may never catch up with the upper gamma ray detector and be seen.

In practice any attempt at quantification of flow rates and water flow entry points must rely on the knowledge of the distance L between the neutron source and the gamma ray detector. L for the "upper" detector might typically be close to 20 ft. To the "far" may be 2 ft. The tool speed also needs to be accurately known. The displacement D between the point on the log where a difference is seen between the original background log and the flowing log needs to be referenced to the point where the neutron source was when the oxygen (water) sample became activated. The speed of the flow stream V is then related to the measured quantities by the equation:

$$V = \frac{L \times \text{Tool Speed}}{D - L}$$

The main uses today for activation logging are:

- Determination of water entry into tubing
- Identification of watered-out perforations
- Detecting the upward flow of water behind casing (channeling) in some cases

Radioactive Tracers and Thermometers

Both radioactive tracer-tool surveys and temperature logs can indicate flow rates and flow directions. However, since they each form a subject in itself they are treated separately. Chapter 6 covers the radioactive tracer logs in detail and Chap. 7 covers temperature logs.

Bibliography

Arnold DM, Papp HJ. Quantitative monitoring of water flow behind and in wellbore casing. J Pet Technol. 1979;31:121–30.

Anderson RA, Smolen JJ, Laverdiere L, Davis JA. A production logging tool with simultaneous measurements. J Pet Technol. 1980;32:191–8.

de Rosset WHM. Examples of detection of water flow by oxygen activation on pulsed neutron logs. SPWLA Twenty-seventh annual logging symposium, June 9–13, 1986, Paper CCC.

Hill AD, Dolman T. Production logging tool behavior in two-phase inclined flow. J Pet Technol. 1982;34:2432–40.

Lamb G, Webber G. Measurement of water flow in deviated production wells by oxygen activation logging. SPWLA transactions, June 1983, Paper Z.

Leach BC, Jameson JB, Smolen JJ, Nicolas Y. The full bore flowmeter. Paper SPE 5089 presented at the SPE 49th annual meeting, Houston, Oct 6–9, 1974.

Peebler B. Multipass interpretation of the full bore spinner. Schlumberger publication C-11993.

Answers to Text Question

Question #5.1

(a) Fluid speed = 50 ft/min
Corrected speed = 42.5 ft/min

(b) Flow rate = 2,471 B/D

Radioactive Tracer Logs

6

Applications

Radioactive tracers have three main applications:

1. Determining flow rates and flow profiles
2. Diagnosing completion problems
3. Evaluating treatment effectiveness

The essential components of radioactive tracer logs are a radioactive material and a gamma ray detector. And the methods of using radioactive materials together with gamma ray detectors include:

Treating the well with a radioactive injectant
Using a tracer ejector tool
Monitoring the deposit of radioactive salts on the casing from water production

Well Treatment

A common practice is to frac a well using specially "doped" radioactive sand. Before the frac a base gamma ray log is run. After the frac a second gamma ray log is run. Where differences in the two gamma ray logs appear, it is assumed that the formation took the frac material. Sometimes formations will be tested for injectivity before attempting a frac. In that case, after the base gamma ray log is run, injection water, containing a soluble radioactive material, will be injected. A post inject log

R.M. Bateman, *Cased-Hole Log Analysis and Reservoir Performance Monitoring*,
DOI 10.1007/978-1-4939-2068-6_6

may indicate which zones are most likely to take frac material. If a particular zone takes a disproportionate share of the injectant, there is time to place a bridge plug or perform a cement squeeze before proceeding with a frac job. Figure 6.1 illustrates a gamma ray log used to monitor well treatment.

Tracer Ejector Tool

The tracer ejector tool (also known as the nuclear flolog) is illustrated in Fig. 6.2. A casing-collar locator helps to place the tool in depth. A reservoir of radioactive material is housed inside the tool and small quantities of it may be ejected on command by the operator at the surface. Beneath the ejector port lie one or two gamma ray detectors. There are two methods of using this tool, one known as the *velocity shot* and the other as the *timed-run*.

Velocity Shot

With the velocity shot, the tool is held stationary in the well bore and a "shot" of radioactive fluid is ejected. The two gamma ray detectors record gamma ray intensity as a function of time. Figure 6.3 shows such a log in an injection well. Note that the passage of the radioactive slug past each detector causes a gamma ray peak. By measuring the time difference between the two peaks and knowing the spacing of the two detectors it is a simple matter to calculate the flow rate.

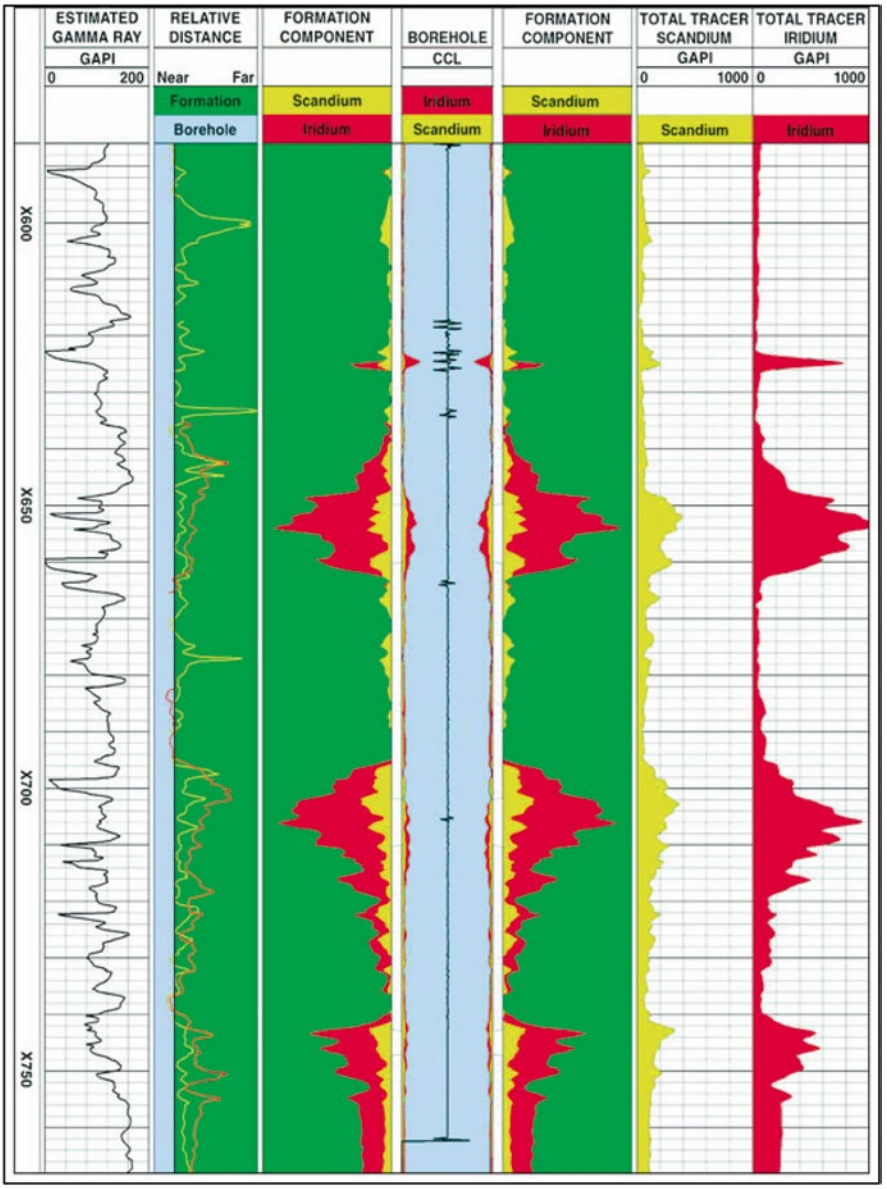

Fig. 6.1 Radioactive tracer log after frac. Courtesy SPE, after Gadeken, 1992

The factors entering into calculation of flow rate are:

Casing ID
Tool OD
Time between peaks
Distance between the detectors

It is essential to remember that the speed of the fluid in the tool casing annulus is greater than the speed of the fluid in the undisturbed wellbore. Thus,

$$q = \frac{\text{detector spacing}}{\text{time}} \times \text{area available for flow},$$

and

$$\text{area} = \frac{\pi}{4}\left[\left(\text{Casing ID}\right)^2 - \left(\text{Tool OD}\right)^2\right]$$

In order to express flow rates in barrels per day, some constant is required, if detector spacing, casing size, and tool OD are measured in inches and time is in seconds,

$$\text{B / D} = \left(\text{cubic inches / second}\right) \times 8.905.$$

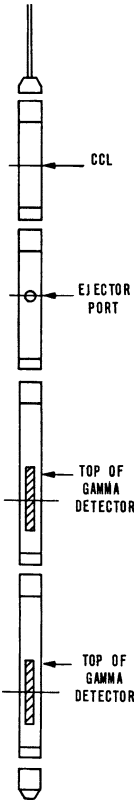

Fig. 6.2 The tracer ejector tool. Courtesy Schlumberger

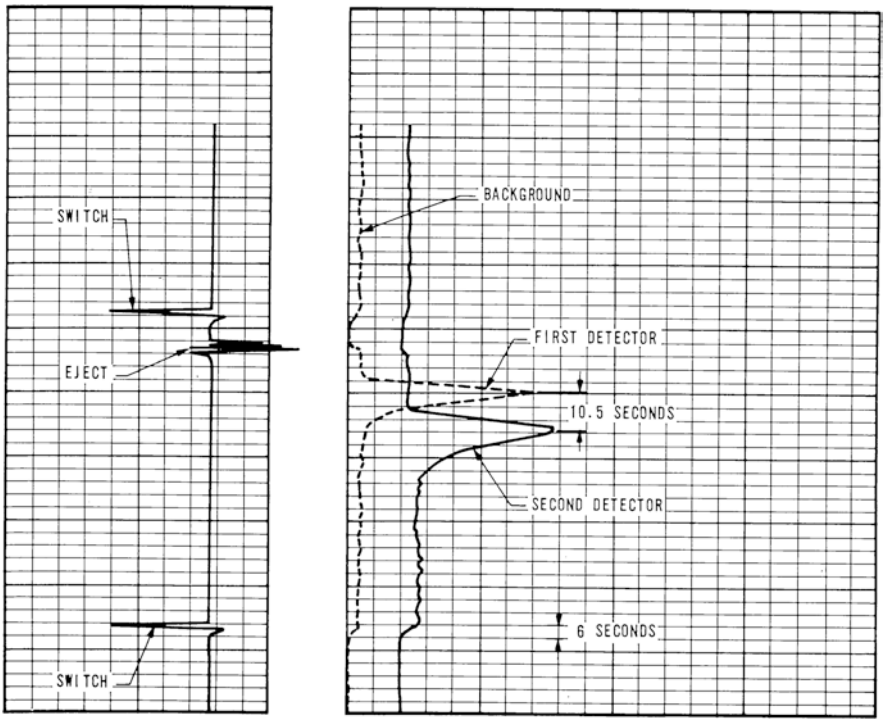

Fig. 6.3 Velocity shot log. Courtesy Schlumberger

Question # 6.1
Casing is 7-in. 26 lb.
Tool OD is 1–11/16 in.
Time between peaks = 18 s.
Detector spacing = 59 in.
Find flow rate in B/D.

Timed-Run Analysis

In the timed-run analysis, a slug of radioactive material is ejected and then a gamma ray log (vs. depth) is made repeatedly at various time intervals to trace where the radioactive slug eventually ends up. Figure 6.4 illustrates such a log.

Question # 6.2

Inspect the log of Fig. 6.4 and write down which sands. Actually take injection water. Explain why.

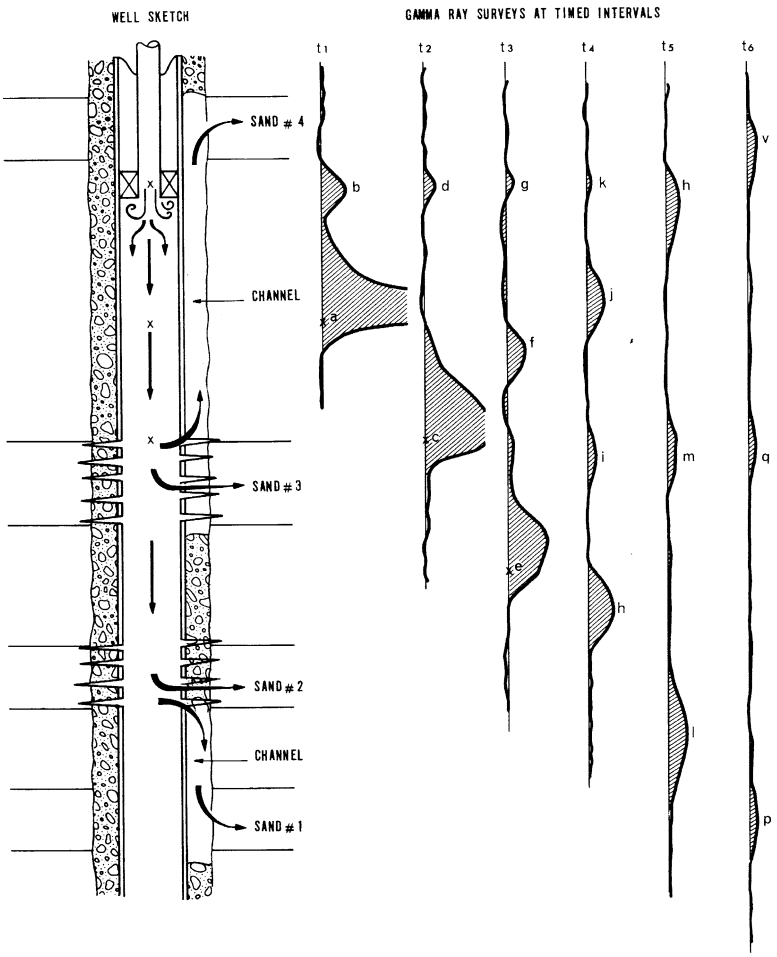

Fig. 6.4 Timed-run analysis. Courtesy Schlumberger

Choice of Radioactive Tracer Materials

In general, a radioactive tracer material should be chosen that is soluble or miscible with the fluid to be profiled or traced. Since surveys may be run in oil, water, or gas flows, several different substances are required. Table 6.1 lists oil, water-, and gas-soluble tracers. Note that the half-life is listed for each material. The half-life for most radioactive tracers is in the order of days or weeks. For safety reasons, radioactive tracers are used only in injection wells. Their use in producing wells raises problems with disposal of radioactive fluids at the surface and contamination of separator and other surface equipment.

Table 6.1 Tracer materials

Isotope	Carrier	Half-life	Predominant Gamma	Uses
Water-soluble tracers				
Iodine-131	NaI in water	8.05 days	0.364 MeV (80 %)	Waterflood profiles, channeling, cement location
Iridium-192	Na_2TrCl in hydrochloric acid	74 days	0.46 MeV (94 %)	Same as above
Oil-soluble tracers				
Iodine-131	C_6H_5I in organic solvent benzene, gasoline	8.05 days	0.364 MeV (80 %)	Oil-injectivity profiles, oil–cement slurry location, erratic results if water present
Iridium-192	Na_2IrCl in organic solvent benzene, xylene	74 days	0.46 MeV (94 %)	Same as above
Universal—Oil- or water-soluble tracers				
Iodine-131	Special solvent	8.05 days	0.364 MeV (80 %)	Profiles in oil or water or oil–water mixtures
Iridium-192	Special solvent	74 days	0.46 MeV (94 %)	
Gas tracers				
Iodine-131	Methyl iodide (CH_3I)	8.1 days	0.364 MeV	Gas-injectivity profiles. Methyl iodine furnished in glass ampules, boils at 72.2 °C or 162.2 °F
Iodine-131	Ethyl iodide (C_2H_5I)	8.1 days	0.364 MeV	Gas-injectivity profiles. Ethyl iodine furnished in glass ampules, boils at 42.5 °C or 106 °F

Source: General Nuclear, Inc., Houston, Texas
Note: Aside from normal radioactivity hazard, methyl and ethyl iodides are very toxic gases with low boiling points and must be handled accordingly. Neoprene O-rings also deteriorate rapidly in the presence of these gases

Monitoring Natural Radioactive Deposits

In some reservoirs, the rise of the water table can be monitored very simply by running a gamma ray log at time intervals throughout the life of a well. The rising water table will make itself visible on the repeated gamma ray logs as an increase in radioactivity. It is thought that the formation water carries with it dissolved radioactive salts that deposit on the casing as precipitates, which build up over a period of time.

Studies suggest that a considerable volume of water production or that flow past the well bore is required before any detectable change can be seen on a GR log. Figure 6.5 shows a time lapse gamma ray log run in a well before and after production. The oil/water contact (OWC) is shown by the radioactive scale (Uranium salts) that have been deposited where water has been flowing. The contact appears to have risen to XX667 ft between the first gamma ray log and the second—a period of 11 years. This technique is by no means universal but should be taken advantage of when it works.

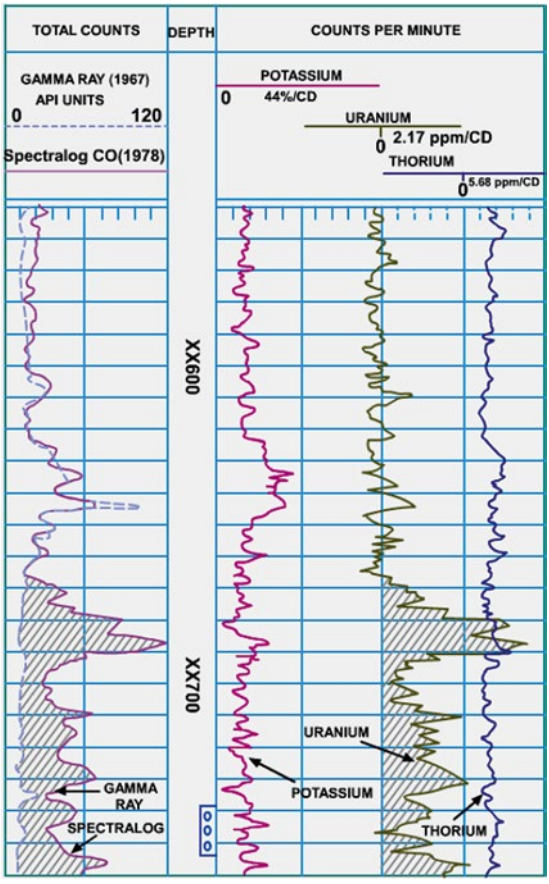

Fig. 6.5 Monitoring OWC changes with a GR log

Carbon Dioxide Injection

The injection of carbon dioxide (CO_2) into porous formations is now a common practice. The primary reason is for enhanced oil recovery (EOR) projects. These include secondary and/or tertiary recovery programs to recover residual hydrocarbons left in a reservoir after primary production and/or water flooding has run its course. The source for the CO_2 in these cases is normally a naturally occurring deposit generated by volcanic activity over geologic time. The gas percolates along fractures up into a porous rock that traps sizeable accumulations. In such deposits some of the gas may be free and some dissolved in an aquifer, if present. An example of such a deposit is the Bravo Dome in New Mexico.

A secondary reason is for the purposeful sequestration of CO_2 released by, for example, electricity generating plants that burn fossil fuels. In either case the injection well operators need to know if the CO_2 injectant is going where it is supposed to go. Two principle logging methods are used to monitor where the CO_2 ends up after it has left the cased borehole and entered the target formation.

The first method involves running compensated thermal neutron logs at regular time intervals and comparing the surveys run after injection has taken place with a base log run before the injection was started. Since thermal neutron logs respond mainly to the hydrogen content of a formation the displacement of water and hydrocarbons (both have hydrogen atoms in their molecular makeup) by CO_2 causes a marked change in the logging tool response in the zones where the CO_2 injection has taken place successfully.

A second method involves adding a radioactive isotope to the CO_2 injectant and then logging the injection well with a gamma ray logging tool. Short-lived iodine isotopes are frequently used for this purpose. Depths in the wellbore where gamma radiation levels are higher than the naturally occurring background radiation levels indicate the zones where the CO_2 injection has been successful.

Bibliography

Interpretative methods for production well logs. second edition, Dresser Atlas (1982), section 4. Production log interpretation. Schlumberger (1973) 20–23.

Answers to Text Questions

Question # 6.1
Casing ID = 6.276
Tool OD = 1.6875
Area for flow = 28.7 sq in.
Speed = 59/18 = 3.28 in/s
Flow rate = 94.07 cu in./s = 837.7 B/D

Question # 6.2
Sands taking water:
#4 (via channel behind packer)
#3
#1 (via channel)

Fluid Identification

7

Production logging tools that can differentiate between oil, gas, and water in a producing well allow diagnosis of completion and production problems. They offer the operator assistance in planning remedial work and in monitoring reservoir performance. In particular, these tools help:

(a) To pinpoint gas, oil, and water entries into, and exits from, the production string
(b) To determine, in combination with flow measurements, how much of which fluid is produced from which zone

Tools Available

Devices used for fluid identification can be broadly categorized into two groups:

1. Those that respond directly to the physical properties of wellbore fluids (such as density, dielectric constant, resistivity, etc.)
2. Those that respond to the physical effects caused by the actual flow of fluids (such as temperature changes, noise, etc.)

The devices in the second group require that the well be flowing in order to function, but the devices from the first group work even if the wellbore fluids are static.

R.M. Bateman, *Cased-Hole Log Analysis and Reservoir Performance Monitoring*,
DOI 10.1007/978-1-4939-2068-6_7

Table 7.1 summarizes the fluid-typing tools available. The following devices are discussed in this chapter:

Table 7.1 Fluid identification tools

Tool type	Parameter measured	Service company name
Density	Pressure differential	Gradiomanometer
	Gamma ray absorption	Fluid density tool
	Vibration	Densimeter
Dielectric	Electrical capacitance	Watercutmeter
		Hydrolog
Manometer	Pressure	Manometer
HP quartz gauge	Pressure	Quartz pressure
Noise	Noise frequency spectrum	BATS
Thermometer	Temperature	
	Differential temperature	
	Radial temperatures	
Fluid sampler	PVT sample recovery	Borehole fluid sampler

Gradiomanometer
Gamma ray absorption
Gamma ray back scattering
Resonators (vibrators)
Capacitance (dielectric)
Optical fluid density
Fluid resistivity
Fluid samplers
Manometers and other measurements

Gradiomanometer

The gradiomanometer tool (see Fig. 7.1) effectively measures the pressure difference between two points by measuring the expansion or contraction of a metal bellows system filled with oil. In a vertical wellbore, the pressure difference measured may be directly converted into a pressure gradient, and hence to a fluid density in grams per cubic centimeter.

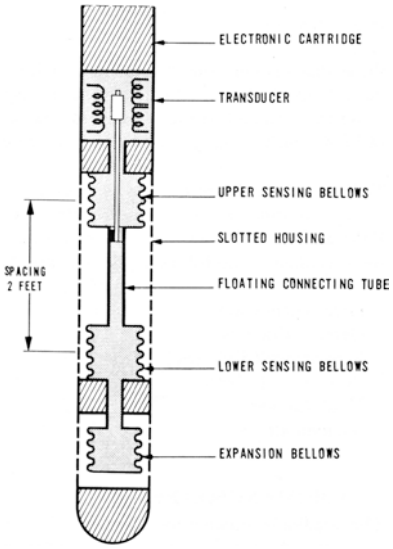

Fig. 7.1 Gradiomanometer tool. Courtesy Schlumberger

In deviated wellbores, the pressure difference measured requires a correction equal to the cosine of the deviation angle in order to convert the measurement to a fluid density (see Fig. 7.2). Since the measurement made is that of a pressure difference, it is assumed that the only cause of the pressure difference is the hydrostatic head of the well bore fluid. But this assumption is not valid if fluid flow is restricted to a small cross-sectional area. In that case, the measured pressure difference will be the sum of both the hydrostatic component and a friction gradient.

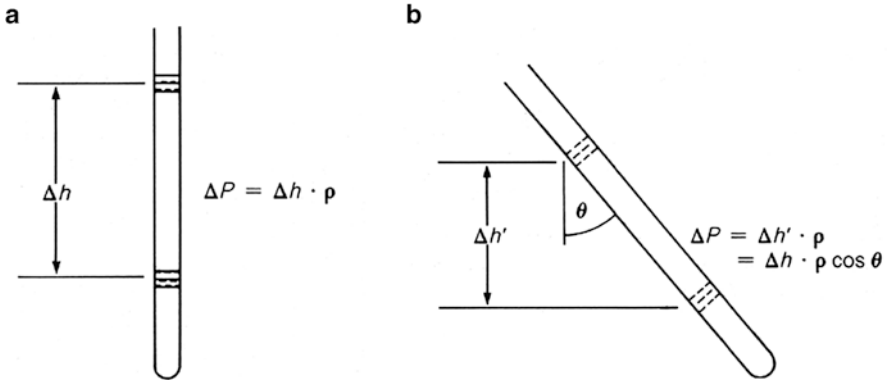

Fig. 7.2 Gradiomanometer measurements in deviated wellbores: (**a**) Vertical wellbore, (**b**) Deviated wellbore

Figure 7.3 shows the expected friction gradient as a function of pipe ID and flow rate. In normal circumstances (5½- or 7-in. casing), the friction term is negligible.

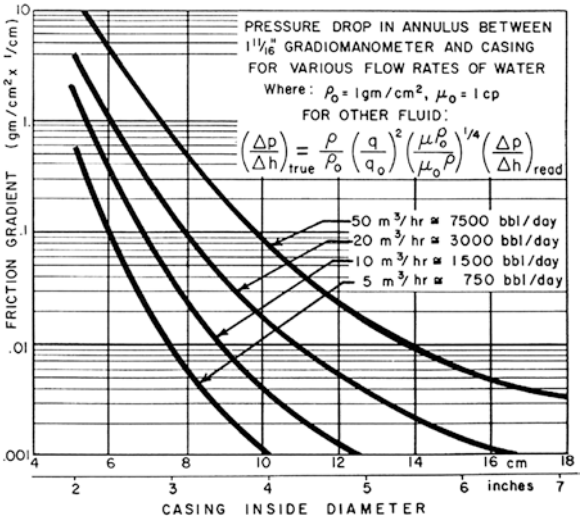

Fig. 7.3 Friction gradients caused by fluid flow in small pipe. Courtesy Schlumberger

Figure 7.4 shows a gradiomanometer recording. The tool is logged continuously up (or down) the hole and records fluid density vs. depth. The log is normally recorded with a sensitivity of 1 g/cm^3 per log track. An amplified curve with 5–10 times the sensitivity is commonly recorded as well.

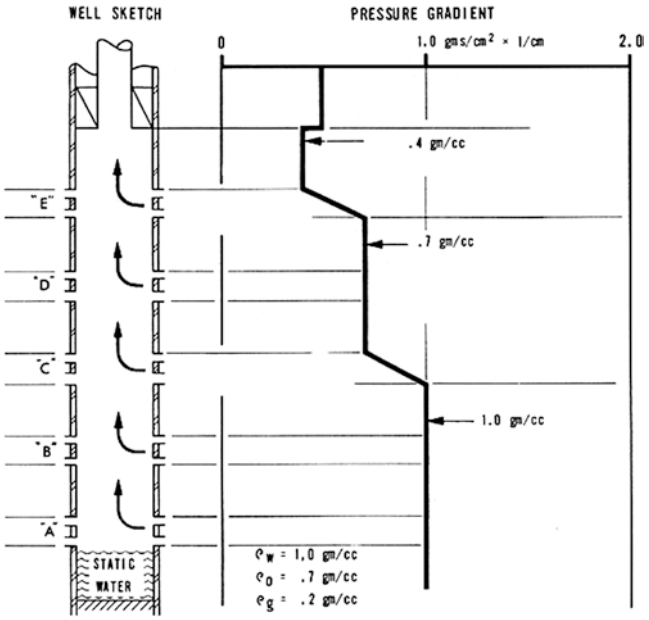

Fig. 7.4 Gradiomanometer log. Courtesy Schlumberger

Question # 7.1
Inspect the log shown in Fig. 7.4 and deduce the fluid(s) produced from each set of perforations.

If a bubble-flow regime exists in the wellbore, the interpretation of measured fluid density must take into account the holdup of the flowing mixture. In general, we may always write:

$$\rho_{\text{mix}} = \rho_h y_h + \rho_l \left(1 - y_h\right),$$

where ***h*** denotes the heavier phase and ***l*** the lighter one, and ***y*** is the holdup. It follows, therefore, that if the densities of the light and heavy phases are known, the holdup may be deduced by:

$$y_h = \frac{\rho_{\text{mix}} - \rho_l}{\rho_h - \rho_l}$$

The holdup, once determined in this manner, may be used in conjunction with the holdup equation (derived in Chap. 4) to deduce the flow rates of both the light and heavy phases.

Fluid Density Tool (Gamma Ray Absorption)

The fluid density tool operates on much the same principle as the formation density tools (i.e., a source of gamma rays is positioned with respect to a detector of gamma rays so that the wellbore fluid acts as an absorber). Figure 7.5 illustrates the operating principle. A high count rate indicates a fluid of low density and a low count rate indicates a fluid of high density. Figure 7.6 shows a fluid density log.

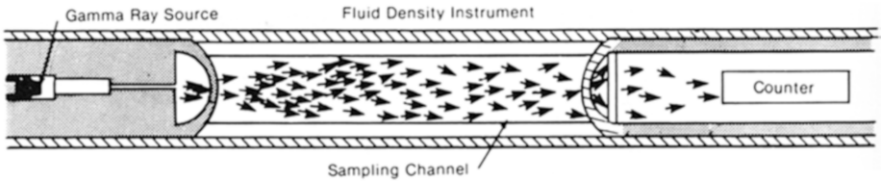

Fig. 7.5 The fluid density tool. Courtesy Baker Atlas

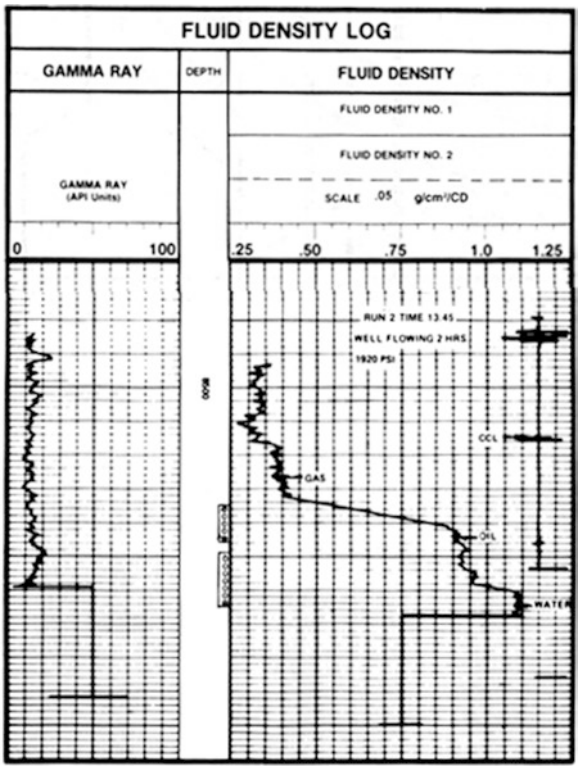

Fig. 7.6 A fluid density log. Courtesy Baker Atlas

The advantages of this type of tool over the gradiomanometer are that (a) its measurement is not affected by the wellbore deviation angle, or by friction effects. However, since it is a tool relying on a statistical radioactive decay, the readings are subject to statistical variations. It should also be noted that the measured quantity is the average density of the flowing mixture and thus subject to the same holdup effects as the gradiomanometer.

A variation employs the detection of back scattered gamma rays rather than their adsorption by the wellbore fluids. Figure 7.7 illustrates one embodiment of this principle.

Fig. 7.7 Gas holdup tool

The tool employs a Cobalt-57 source which emits γ-rays. The detector is shielded from any γ-rays coming directly from the source by means of a tungsten disk, as shown in Fig. 7.8. The detector is therefore responding to back scattered γ-rays. The intensity of the back scattered radiation is a function of the fluids surrounding the tool. If gas is present the number of γ-rays detected is small. If liquid oil or water is present the number of back scattered γ-rays is large.

Fig. 7.8 Gas holdup tool schematic

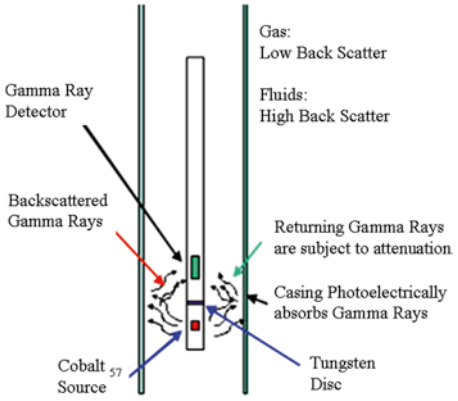

Resonator (Vibrator)

Tools that measure fluid density by means of mechanical vibration have been in use for some time. They are designed so that the flow stream is directed to pass through a hollow metal cylinder containing radial blades in line with the fluid stream. The cylinder is set into circular vibration by an electromagnetic driving system and oscillates at a natural frequency that depends on the density of the fluids passing through the cylinder. The raw reading of the tool is a frequency. Each tool has a calibration chart to convert from frequency to a density index. The main problem with tools of this sort is their tendency to plug up with sand or other grains carried in the flow stream. Figure 7.9 illustrates a fluid density inertial tool which employs this principle of operation.

Fig. 7.9 Fluid density inertial tool

Capacitance (Dielectric) Tools

Another group of tools widely used to distinguish water from hydrocarbons depend for their operation on the difference between the dielectric constant of water (~80) and that of oil or gas (~6). A simple way to find the dielectric constant of a fluid is to use the fluid itself as the dielectric between the plates of a capacitor. The capacitance of the resulting capacitor may be found by classical methods such as including it in an RC network and finding the resonant frequency.

A conventional design is shown in Fig. 7.10. Two cylindrical metal tubes are arranged so that well bore fluids flow through the annular space between them. The raw readings of such a device are in terms of a frequency. Each tool will have a calibration graph to convert a measured frequency to a watercut value. These tools behave well provided that the continuous phase is oil. In practice, the measurement may become unreliable if the watercut in the flowing mixture exceeds 30 %.

Array Capacitance Tools

In circumstances where the flow stream is not homogenized the simple cylindrical instrument will not truly reflect the distribution of different phases across the actual flow stream. Water, oil, and gas may become segregated when flow is in an inclined pipe or a horizontally completed well. In such cases an array of capacitance measuring sensors may be advantageously employed. Such an embodiment is illustrated in Fig. 7.11.

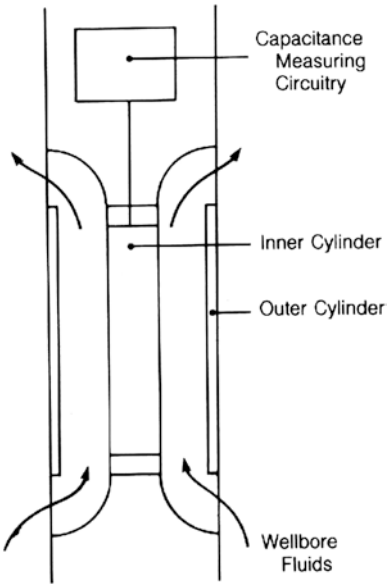

Fig. 7.10 Capacitance watercut meter

Fig. 7.11 Capacitance array tool. Courtesy GE Oil & Gas, 2014

An array of 12 capacitance sensors mounted inside a set of collapsible bow springs. The 12 measurements can be transmitted simultaneously to the surface or recorded on a memory package. The measurements are taken in a single plane across the diameter of the wellbore and allow for cross-sectional plot of fluid phases, as shown in Fig. 7.12.

Fluid Resistivity Measurements

Cross-sectional water holdup profiling and 3D imaging of water holdup is possible by use of the resistivity array tool as illustrated in Fig. 7.13. The tool relies on the resistivity contrast between water and hydrocarbons but is unable to distinguish between oil and gas.

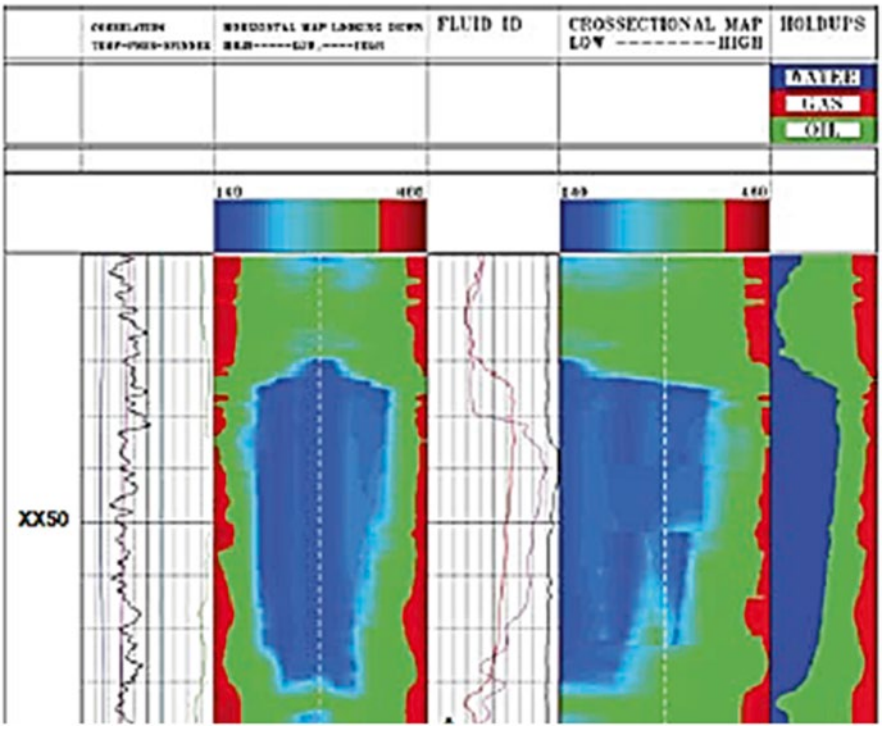

Fig. 7.12 Fluid distribution cross-sectional map from capacitance array tool

Fig. 7.13 Resistivity array tool. Courtesy GE Oil & Gas, 2014

Optical Fluid Density

Yet another way to distinguish between water, oil, and gas is by use of the measurement of the optical fluid density. A light source provides beams of light at different frequencies or colors, some in the visible spectrum and others in the near infrared. The percentage of the incident light that passes through a known thickness of the fluid being sampled is characteristic of the fluid involved. This technology is used in open-hole wireline formation testers to determine what fluid is being pumped out of the formation under test and is useful in that application to indicate to the operator when the initial flow of mud filtrate has been exhausted and the virgin formation fluids are then flowing into the sample chamber. In production logging, the same technology can be applied to distinguish the components of a flow stream in a well. Figure 7.14 shows a schematic of the optical fluid analysis device and Fig. 7.15 the optical fluid density of a number of fluids as a function of the wavelength of the light employed.

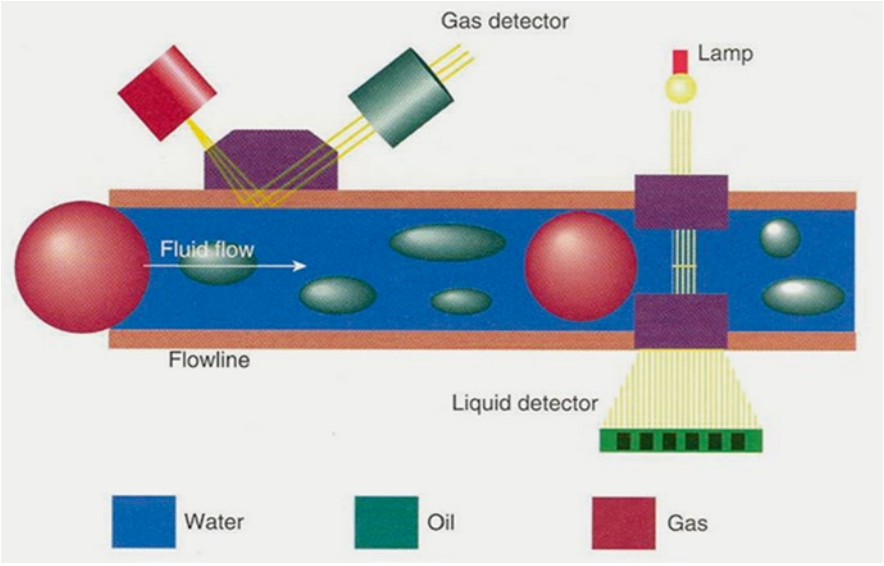

Fig. 7.14 Optical fluid analysis device. Image copyright Schlumberger. Used with permission

Fluid Sampler

The fluid sampler is analogous to a formation tester, the difference being that the latter takes samples of the formation fluids but the former takes samples of the well bore fluids. Figure 7.16 shows the tool. It is run into the well to the required depth and then actuated by the operator on the surface. A valve opens and a sample chamber fills with the fluids in the wellbore. The valve is then closed and the sample is recovered and analyzed at the surface. For this purpose a mini-separator is used to gauge the relative amounts of oil, water, and gas recovered.

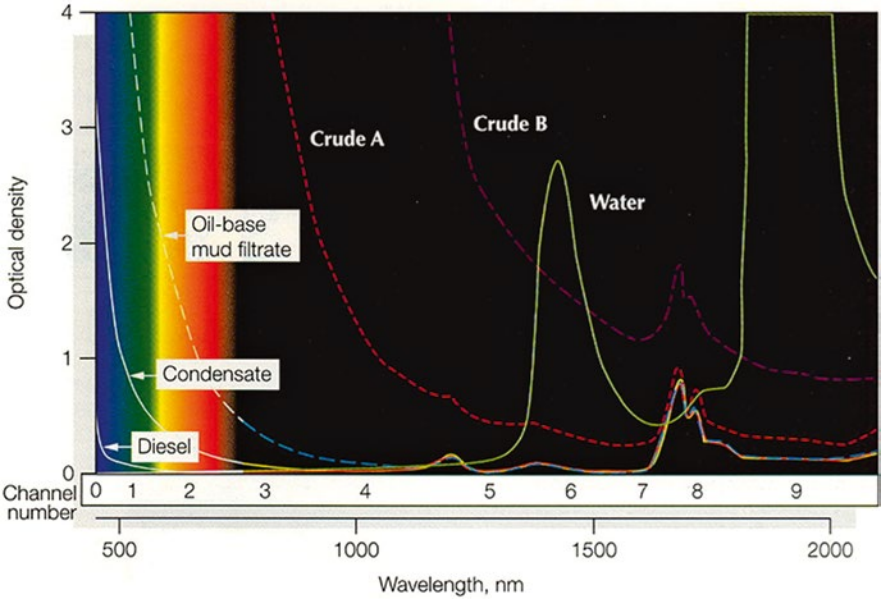

Fig. 7.15 Optical fluid density as a function of wavelength. Image copyright Schlumberger. Used with permission

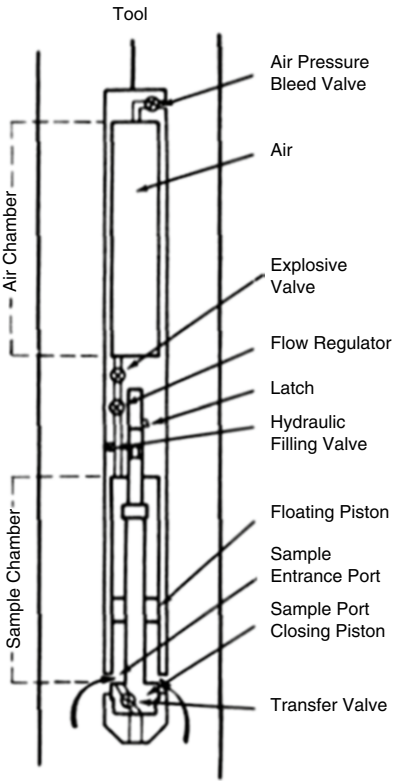

Fig. 7.16 The fluid sampler tool. Courtesy Schlumberger

Manometer

The manometer is a pressure gauge. It may be used in two ways, either to provide a continuous recording of pressure against depth or to provide a recording of pressure versus time at some fixed point in the well. When used in the continuous logging mode, the manometer will show a pressure gradient reflecting the density of the fluid in the well. Changes in this gradient indicate density changes in the well fluids and thus serve to pick up fluid entries. When used in the stationary mode, the manometer can be used in the familiar mode of a pressure bomb. Either the well can be shut in for a pressure buildup test, or the well can be flowed on different chokes for a step-rate test. Figure 7.17 shows a pressure buildup test recorded with a manometer, and Fig. 7.18 a pressure buildup plot used to interpret the data.

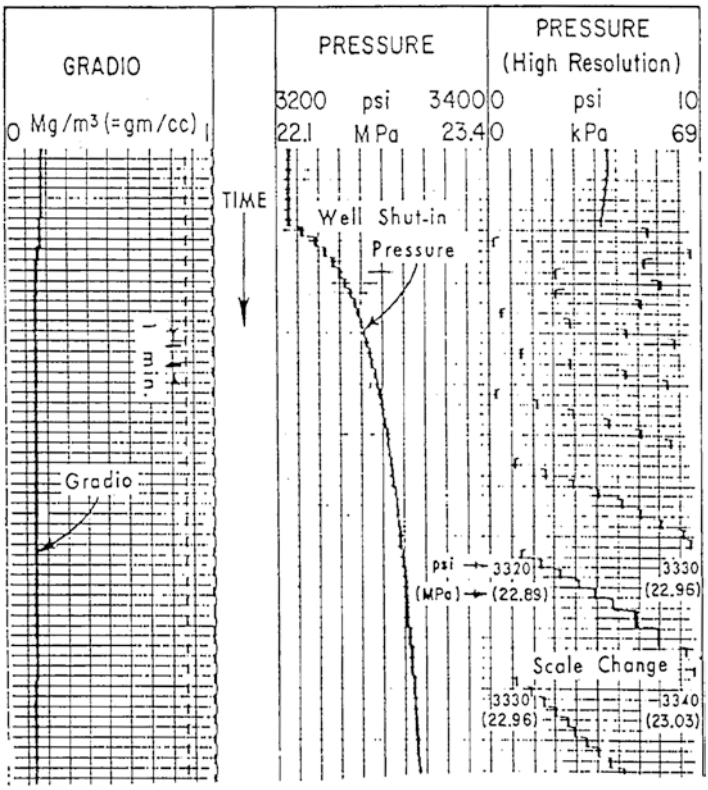

Fig. 7.17 Pressure buildup recording with a manometer. Reprinted with permission of the SPE from Anderson et al. 1980, fig. 5A, p. 195

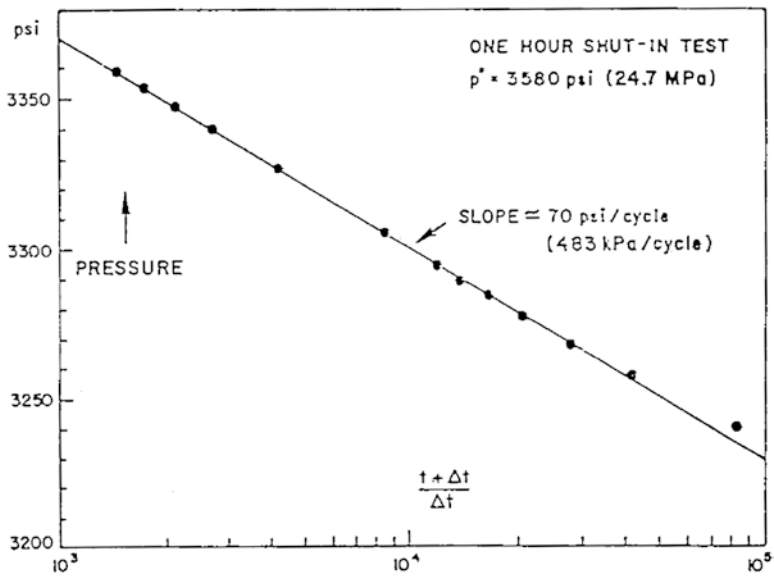

Fig. 7.18 "Horner" plot from log shown in Fig. 7.17. Reprinted with permission of the SPE from Anderson et al. 1980, fig. 58, p. 195

Other Measurements

The use of temperature logs to detect which type of fluid is flowing is covered in Chap. 8. The use of sibilation or noise logs is covered in Chap. 9. These logs are mentioned here to assure that they are remembered in the correct perspective as fluid-identifying devices.

Many service companies offer tools that combine numerous sensors in one tool string. This simplifies the practical problem of obtaining logs when working against wellhead pressure with a riser and pressure-control equipment, since all the required measurements can be made on one trip in the hole without time delays caused by frequent tool changes. A schematic of such a combination tool is given in Fig. 7.19 and an example log is shown in Fig. 7.20.

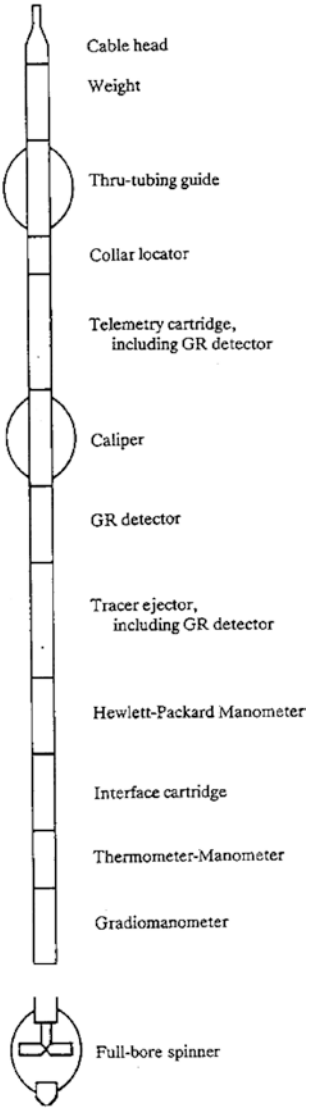

Fig. 7.19 The production logging tool (PLT). Courtesy Schlumberger

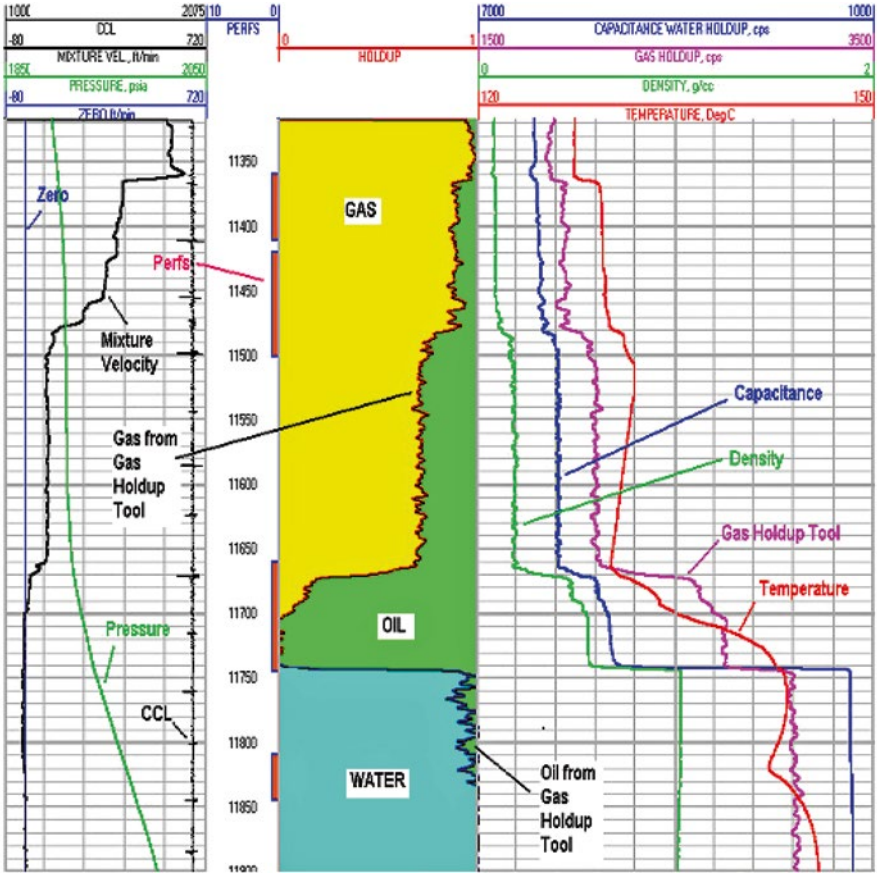

Fig. 7.20 Production logs run with combination tool

Bibliography

Anderson RA, Smolen JJ, Laverdiere L, Davis A. A production-logging tool with simultaneous measurements. Paper SPE 7447 presented at the SPE 53rd annual technical conference and exhibition, Houston, Oct. 1–4, 1978; J Pet Tech (Feb. 1980).

Answers to Text Question

Question # 7.1

Intervals:	*Fluid type & movement*
A and B:	water column, either static or moving
C:	hydrocarbon entry, possibly with some water
D:	no entry or mixed entry
E:	gas or gas and liquid entry

Temperature Logging

8

Among the reasons for using temperature logs are:

1. To find the cement top after a recent cementing operation
2. To find a lost-circulation zone in a currently drilling well
3. To find fluid entry and exit points in production and injection wells

Temperature logging tools employ a variety of sensors including temperature-sensitive resistors, thermistors and diodes. In order to react quickly to temperature changes, temperature logging tools are designed with the sensing element exposed directly to the wellbore fluids. For this reason, they are delicate instruments easily damaged by physical abuse or by the junk normally found at the bottom of a well.

Resistance Temperature Detector (RTD)

Most premium tools contain a platinum resistance temperature detector (RTD) which exploits the tendency of a metallic conductor to exhibit a change in resistance with temperature. An RTD is essentially a temperature-sensitive resistor with a positive temperature coefficient, which means that the resistance of the metal increases with temperature. RTDs are made from a number of different metals, but the platinum RTD has captured most of the industrial market, and is now used in most modern temperature logging tools. The major drawback is a rather small change in resistance per degree of temperature change, mandating special signal processing for signal amplification.

R.M. Bateman, *Cased-Hole Log Analysis and Reservoir Performance Monitoring*,
DOI 10.1007/978-1-4939-2068-6_8

Thermistors

Some tools contain thermistor sensors which are metal oxide semiconductor devices. Thermistors provide a large change in resistance per degree change in temperature, but they are highly nonlinear devices. There are a number of linearizing schemes used, but in logging tools, where a dynamic range of 300 °F or more may be needed, thermistors are problematic.

Diodes

Diodes have been used as temperature sensors in a few tools. Diodes produce a relatively high change in voltage per degree, but they are limited with respect to high wellbore temperatures.

Figure 8.1 illustrates a temperature logging tool and Fig. 8.2 a typical temperature log.

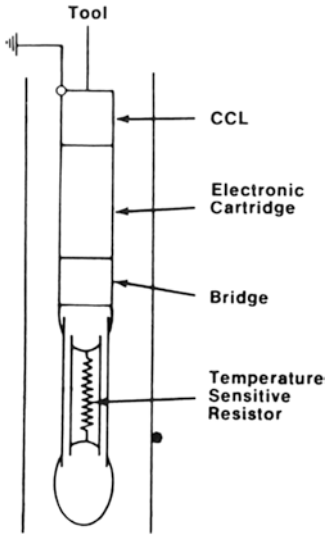

Fig. 8.1 High-resolution thermometer. Courtesy Schlumberger

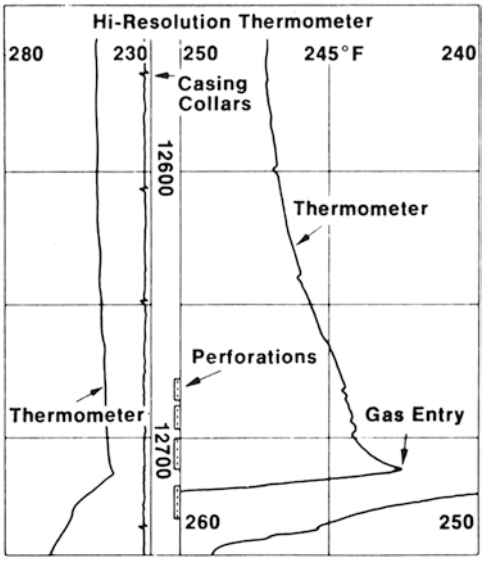

Fig. 8.2 Typical temperature log. Courtesy Schlumberger

Fundamentals

Undisturbed formation temperature increases predictably with depth. This increase in temperature with depth is known as the *geothermal gradient* (G) and is usually in the range of 1–2 °F per 100 ft. Figure 8.3 is a useful guide to geothermal gradients—the temperature at any depth may be extrapolated using the relationship.

$$T_{\text{form}} = T_{\text{surf}} + \text{depth} \bullet G.$$

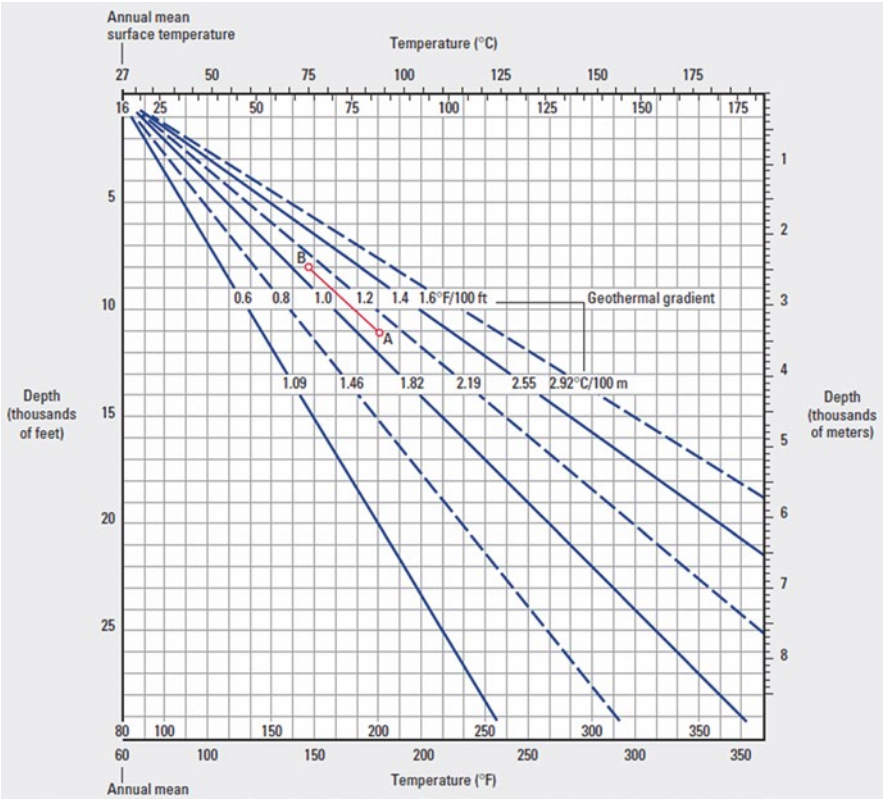

Fig. 8.3 Geothermal gradients. Courtesy Schlumberger

Obviously, the actual temperature on the surface fluctuates seasonally so the value used for the *surface temperature* is actually the mean annual surface temperature and will be in the range of 60–70 °F in temperate climates. Seasonal near-surface temperature changes do not penetrate very deeply into the ground and well logging purposes can be ignored. One exception is the permafrost zone that can exist near polar regions.

Estimation of formation temperature from open-hole logs can be made provided it is borne in mind that at the time a logging run is made the wellbore is cooler than the surrounding formation, due to mud circulation. If several logging runs are made in the same hole, undisturbed formation temperature can be estimated from a plot of temperature against time. The method of Dowdle and Cobb is recommended.

Bottomhole Temperature Extrapolation

If t_k is the circulation time and Δt is the time since circulation stopped, then a plot of the observed temperature at time Δt against $(t_k + \Delta t)/\Delta t$ on a log scale should give a straight line with an intercept at $(t_k + \Delta t)/\Delta t = 1$ which will indicate the undisturbed formation temperature, T_i. Figure 8.4 illustrates the method. A worked example is shown below. Table 8.1 lists time and temperature data recoded on sequential logging runs in the same hole. The well was drilled to a depth of 7,646 ft and drilling stopped at 22:00 on the 2nd. Circulation stopped at 02:30 on the 3rd giving a circulation time of 4½ h. Analysis of this data is shown on the plot in Fig. 8.4 that indicates an undisturbed formation temperature close to 116 °F.

Table 8.1 Time and temperature data

Logging run	Thermometer depth (ft)	Time off bottom	Time since circulation stopped (h)	Temperature °F
1	7,608	07:36/3rd	5:06	99
2	7,608	12:48/3rd	10:18	106
3	7,620	14:29/3rd	14:29	107
4	7,620	20:37/3rd	18:07	110

Question # 8.1
Depth: 16,200 ft.
Drilling stopped: 00:30 h.
Circulation stopped: 04:00 h.
Circulation time: 3.5 h.

Three log runs were made, the corresponding times and temperatures were:

Tool	Time off bottom	Time since circulation stopped	Temp. (°F)
Induction	12:15	8:15	241
Density	15:00	11:00	257
Dipmeter	17:30	13:30	262

Plot temperature vs. $(t_k + \Delta t)/\Delta t$ and deduced static formation temperature.

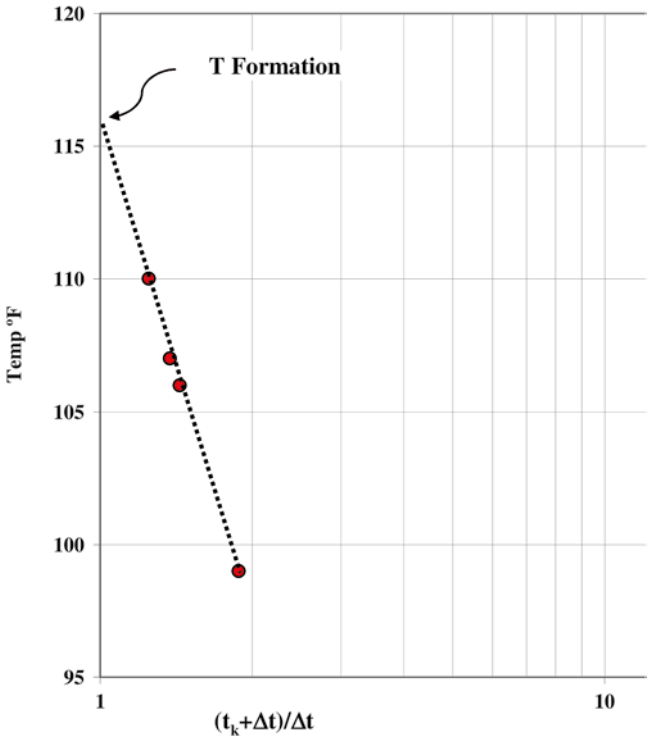

Fig. 8.4 Determination of static formation temperature. Reprinted with permission of the SPE-AIME from Dowdle and Cobb (1975)

Cement-Top Evaluation

Although no longer widely used for finding cement tops in recently cemented wells, the temperature log may be used for this purpose—its advantage being that it is cheap and demands less rig time. Its disadvantage is that it gives no indication of the cement quality or the ability of the cement job to make a hydraulic seal. The principle involved is the exothermic chemical reaction that takes place while cement is curing. The heat given off raises the temperature in and around the borehole at those places where cement is placed. Thus, a marked drop in temperature may be expected at the cement top. Figure 8.5 shows a temperature log run in a recently cemented well and the corresponding pick for the cement top.

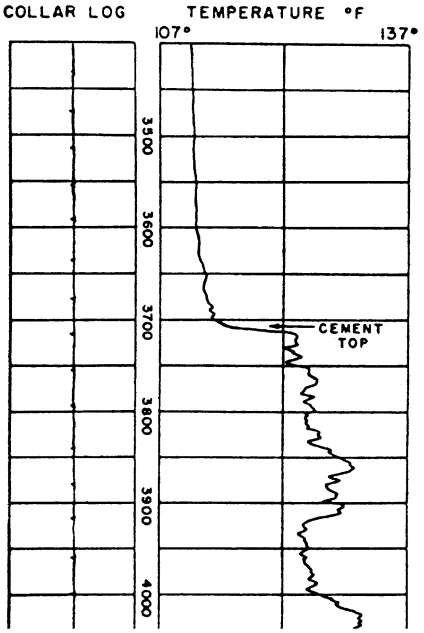

Fig. 8.5 Cement-top pick from temperature log

Lost-Circulation Zones

In the event that circulation is lost in a currently drilling well, a temperature log can be a useful indicator of the thief zone in question. Just below the point of lost circulation, the mud in the hole is likely to have been stagnant for some time and therefore to have assumed a higher temperature than the mud in the column, which is still free to circulate. Thus, a temperature discontinuity will exist across the lost-circulation zone. Figure 8.6 illustrates the effect.

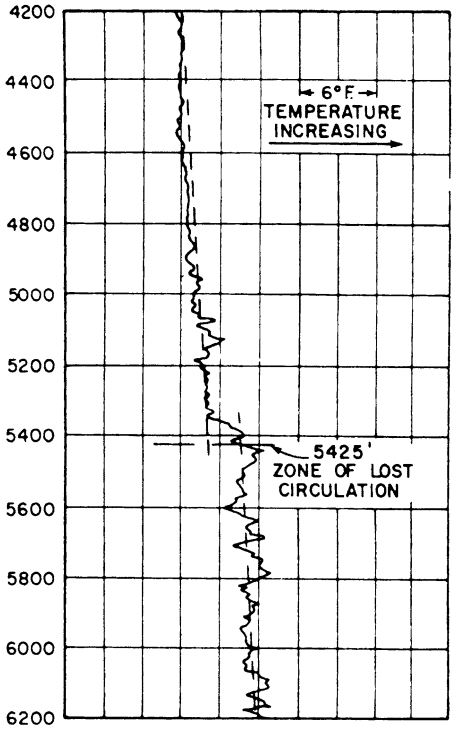

Fig. 8.6 Lost-circulation zone detection with a temperature log

Temperature Profiles in Production and Injection Wells

General

If left undisturbed, the temperature in a well bore will assume the ambient temperature of the surrounding formations; and a log of temperature against depth will indicate the geothermal gradient. However, if the well is flowing, either due to production or injection of fluids, then the observed temperature profile will depart from the geothermal gradient. This surprisingly simple rule should always be borne in mind when analyzing temperature logs. Look for departures from the geothermal gradient as the prime indicator of fluid movement. Once a particular flow regime has reached thermal equilibrium, the difference between the observed temperature in the borehole and the geothermal gradient is related to the mass flow by the equation:

$$\Delta T = bM / G$$

where: ΔT = the temperature difference, b = a constant that depends on the physical characteristics of the fluid produced and on the thermal conductivity of the formation, M = the mass flow rate, and G = the geothermal gradient.

Thus, other things being equal, the ΔT is proportional to the weight of fluid produced or injected per unit time.

Liquid Production

Figure 8.7 shows a temperature profile for a single-point entry of liquid production. Things to note include:

(a) Below the production point, the temperature profile follows the geothermal profile.
(b) At the production point, the temperature profile is vertical.
(c) Above the production point, the temperature profile asymptotically approaches a new gradient offset from the geothermal by an amount ΔT.

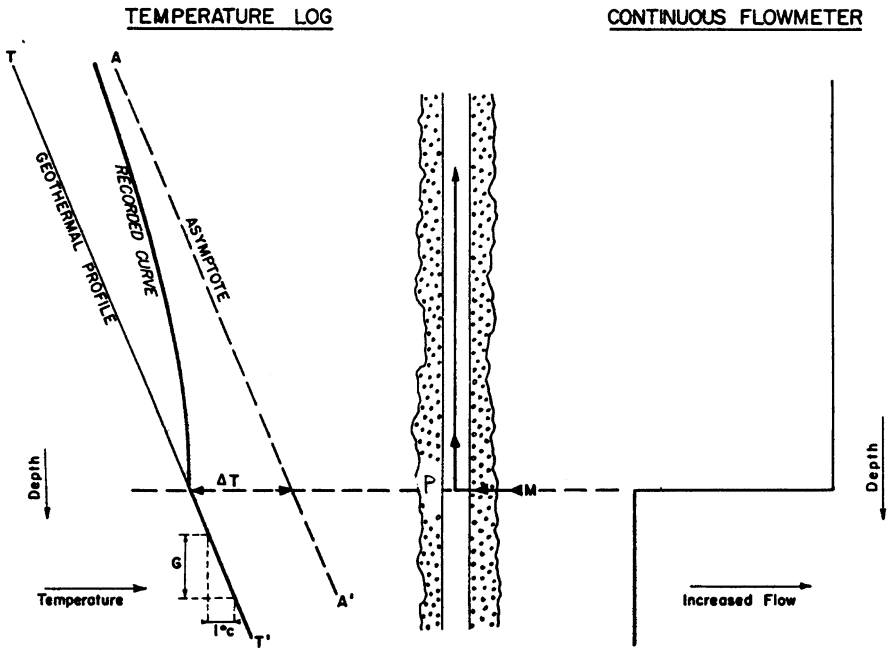

Fig. 8.7 Liquid-production temperature profile. Courtesy Schlumberger

Gas Production

Figure 8.8 shows temperature profiles for a single-point entry of gas. Things to note include:

(a) Below the production point, the temperature profile follows the geothermal profile.
(b) At the production point, the temperature profile is *horizontal* and shows a marked cooling effect due to gas expansion from reservoir pressure to well flowing pressure.

(c) Above the production point, the temperature rises, crosses the geothermal, and approaches an asymptote offset ΔT above the geothermal.

Two traces are shown on Fig. 8.8—one for a high-permeability formation and one for a low-permeability formation. Note that the initial cooling effect at the point of production is less for the high-permeability formation than for the low.

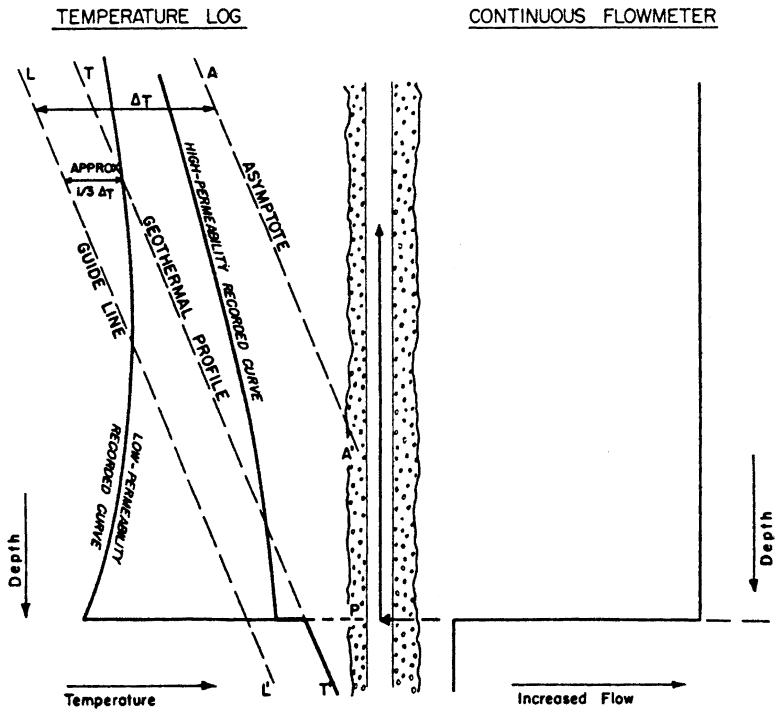

Fig. 8.8 Gas-production temperature profiles. Courtesy Schlumberger

Water Injection

Figure 8.9 illustrates the temperature profiles to be expected in a water-injection well. Things to note are:

(a) Depending on the temperature of the injected water relative to the undisturbed formation temperature, the temperature profile above the injection point may show an increase or a decrease with depth.
(b) At the injection point, the temperature profile is horizontal.
(c) Below the injection point, the temperature profile returns to geothermal.

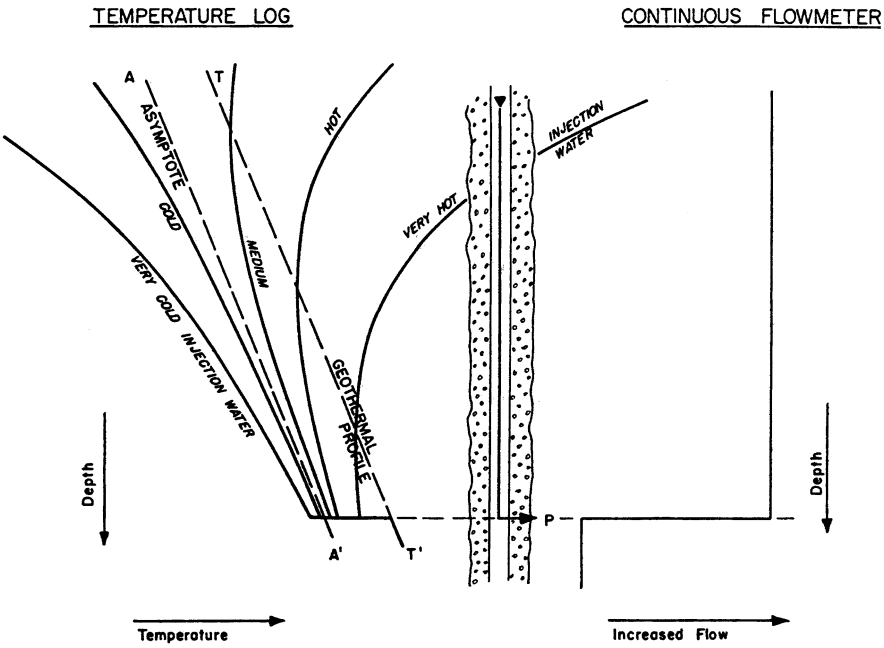

Fig. 8.9 Water-injection temperature profiles. Courtesy Schlumberger

Gas Injection

The temperature profiles for a gas-injection well (Fig. 8.10) are entirely similar to those of a water-injection well, and the same observations apply.

Further examples of liquid and gas production and injection profiles—together with the effects of casing leaks, casing-formation annulus flow, etc. are given in a paper entitled "Temperature Logs in Production and Injection Wells," by A. Poupon and J. Loeb. The reader is encouraged to read this paper in its entirety.

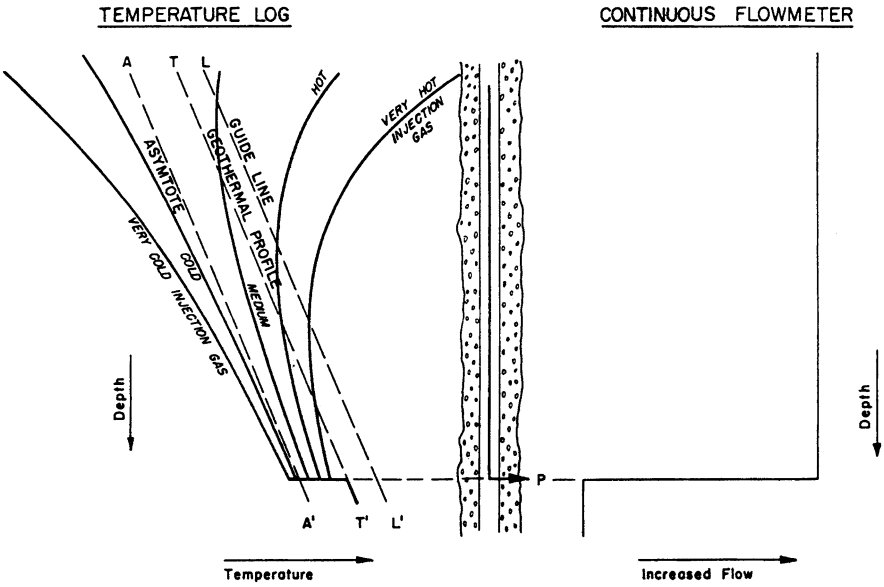

Fig. 8.10 Gas-injection temperature profiles. Courtesy Schlumberger

Logging Techniques

Several special logging techniques can improve interpretation of temperature profiles. These include:

1. Shut-in temperature surveys
2. Differential-temperature logs
3. Radial differential-temperature logs

Shut-In Temperature Surveys

If more than one zone is taking water in an injection well, it is sometimes difficult to judge from the flowing temperature profile which zone is taking what percentage of the injected total. Two techniques are offered here. The first simply relates the ΔT value to the volumetric flow. Figure 8.11 illustrates the concept. In the figure, T_G is the undisturbed formation temperature and T_h is the temperature observed in the borehole.

A second useful technique is to stop injection altogether and repeat the temperature profile several times at various time intervals, such as at 3, 6, 12, and 24 h. Or, depending on the local conditions, at 12, 24, and 48 h. Zones that were taking relatively cool injection water will remain cooler than surrounding formations for a relatively long time and will be visible on the repeat profiles. Figure 8.12 shows such an example.

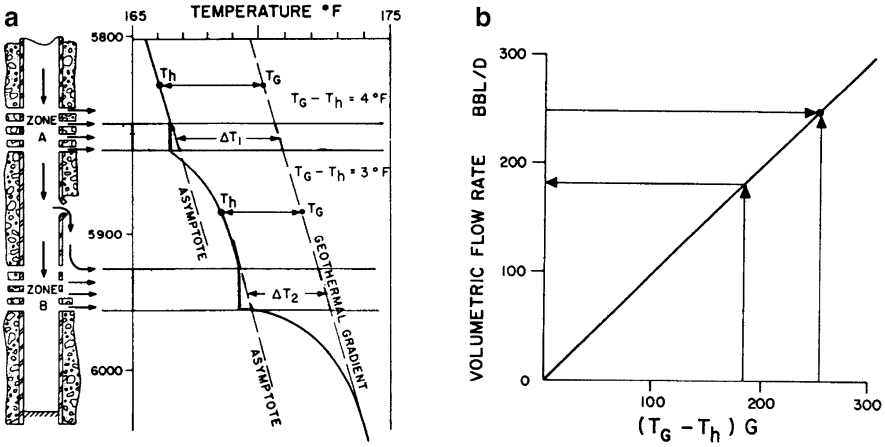

Fig. 8.11 Water injection: (**a**) Temperature Profile, (**b**) Flow rate vs. ΔT. Reprinted with permission of the SPE-AIME from Witterholt and Tixier (1972)

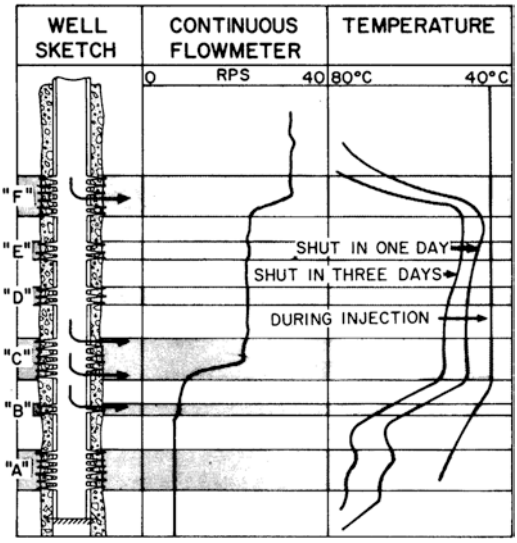

Fig. 8.12 Shut-in temperature survey. Reprinted with permission of the SPE-AIME from Witterholt and Tixier (1972)

Differential-Temperature Surveys

A differential-temperature log is a recording made, versus depth, of the difference in temperature between two points in the well. Effectively, the trace is a differentiation of the temperature curve itself. In practice this is accomplished either by having matched sensors on the logging probe some short distance apart or by memorizing

the temperature taken at one point and comparing it to the temperature taken at some other point, such as 1 ft deeper, or shallower, depending on the direction of logging. Differentiation can be on a depth or on a time basis. Provided that the logging speed remains constant, both methods produce the same answer. Figure 8.13 shows a conventional temperature survey together with a differential-temperature curve. Note that where even slight changes in temperature occur the differential curve accentuates the occurrence. Where the temperature does not change with depth, the differential curve is likewise unchanged.

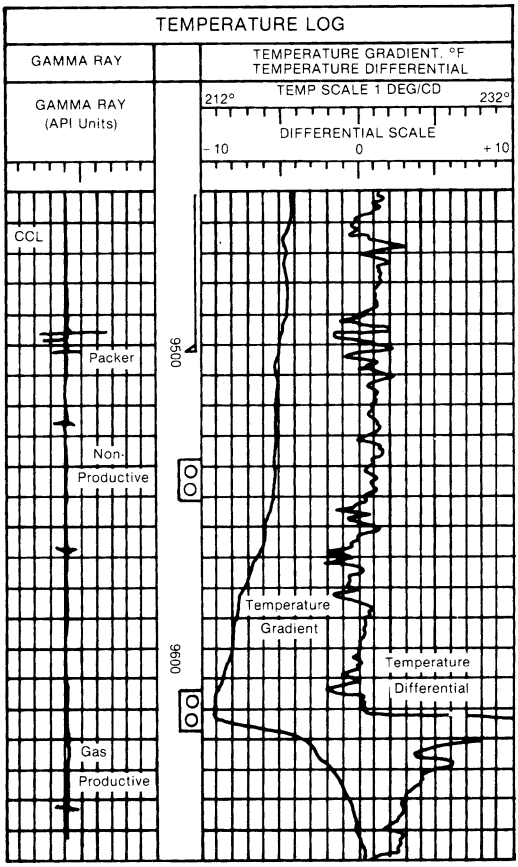

Fig. 8.13 Differential-temperature log. Courtesy Baker Hughes

Radial Differential-Temperature Tool

The radial differential-temperature tool (RDT) was designed to detect channels behind pipe. The operating principle relies on the probability that the temperature in the channel is different from the temperature in the surrounding formation. If fluid is channeling from above or below it is probable that such a temperature difference will be present. Figure 8.14 shows a plan view of a channel. The temperature on the side of the casing near the channel, T_{w1}, is likely to be different from the temperature of the casing opposite the channel, T_{w2}. Thus, a temperature sensor held stationary at a given depth, but free to rotate through 360°, should observe a temperature fluctuation if a channel with fluid flowing in it is present.

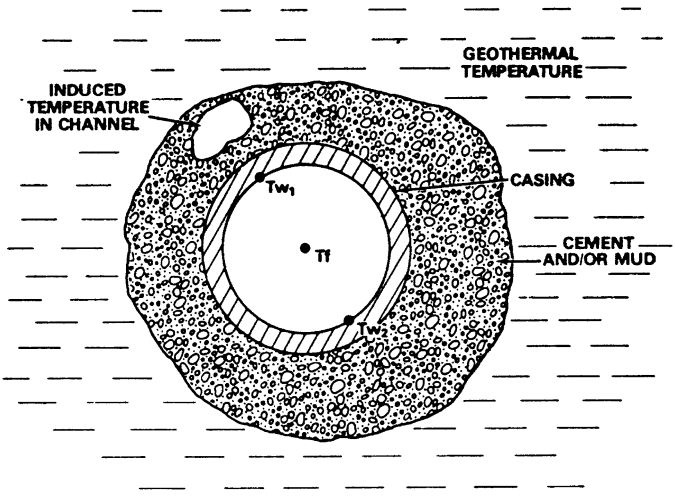

Fig. 8.14 Temperatures in and around a cased well. Reprinted with permission of the SPE-AIME from Cooke (1979)

The method used to make the horizontal scan is shown in Fig. 8.15. Anchor springs hold the tool in the casing and a rotation motor is actuated to cause the RDT sensor to scan round the casing. The resulting log is shown in Fig. 8.16. Note that the log is a record of temperature versus degrees of rotation round the casing. This particular survey with measurements made at 6,400, 6,440, 6,500, and 6,560 ft shows that gas is channeling from the lower sand (marked "L" on the figure) to the upper sand (marked "U"). For remedial action, the tool carries a perforating gun that can shoot squeeze perforations directly into the channel once it is detected.

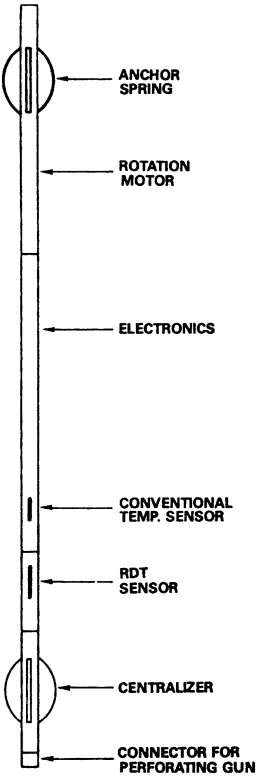

Fig. 8.15 RDT tool. Reprinted with permission of the SPE-AIME from Cooke (1979)

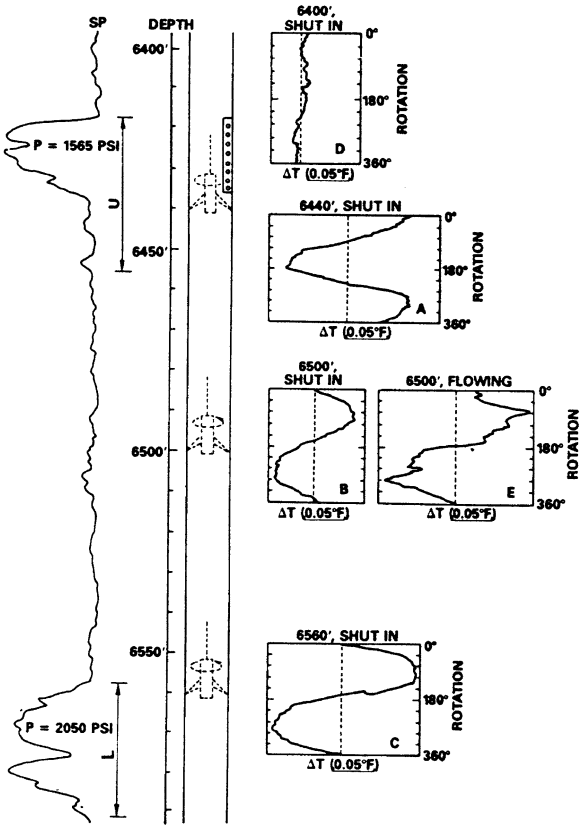

Fig. 8.16 RDT scan showing gas channel. Reprinted with permission of the SPE-AIME from Cooke (1979)

Bibliography

Aslanyan A, Wilson M, Al-Shammakhy A, Sristov S. Evaluating injection performance with high-precision temperature logging and numerical temperature modeling. SPE reservoir characterization and simulation conference and exhibition held in Abu Dhabi, UAE, 16–18 September 2013.

Cooke CE. Radial differential temperature (RDT) logging—a new tool for detecting and treating flow behind casing. Paper SPE 7558 presented at the SPE-AIME 53rd annual technical conference and exhibition, Houston, Oct. 1–3, 1978.

Dowdle WL, Cobb WM. Static formation temperature from well logs—an empirical method. J Pet Technol. 1975;27:1326–30.

Ghalem S, Draoui E, Mohamed A, Keshta O, Serry AM, Al-Felasi A, Berrim A, Chaker HA. Innovative noise and high-precision temperature logging tool for diagnosing complex well problems. Abu Dhabi international petroleum exhibition and conference held in Abu Dhabi, UAE, 11–14 November, 2012, SPE 161712.

Hill AD. Temperature logging in "Production logging–theoretical and interpretive elements", SPE monograph series, Volume 14, Henry Doherty memorial fund of AIME society of petroleum engineers, Richardson, TX USA, 1990; pp. 19–36.

Poupon A, Loeb J. Temperature logs in production and injection wells. Presented at the 27th meeting of European assn. of expl. geophysicists, Madrid, 1965.

Witterholt E, Tixier MP. Temperature logging in injection wells. SPE 4022, 1972.

Answer to Text Question

Question # 8.1
297 °F

Noise Logging

9

Noise logging is applicable whenever fluid flow, either in the borehole or in the casing formation annulus, produces a detectable noise. Detection is by means of a microphone suspended in the well. Experience teaches that analysis of noise is a refined technique for deducing the source of the noise. Student life in the low-rent district is enough to turn even the untrained ear into a veritable Sherlock Holmes, distinguishing the characteristic sounds of flushing toilets from draining bath tubs. The human ear and brain perform this function well by making an amplitude-frequency analysis of the total audible spectrum. Tools for well-flow analysis have to perform a similar function in order to earn their keep. Only by this kind of frequency analysis can the hiss of gas be distinguished from the gurgle of liquids.

Tools Available

Many service companies offer noise logging service, under a number of trade names such as:

- Sonan Log
- Audio Log
- Borehole Audio Tracer Survey (BATS)
- Noise Log
- Borehole Sound Survey

In general, measurements are made at preselected stations in the well. At each station, the amplitude of the noise in a number of frequency bands is determined and plotted on the log. Subsequently, these individual station readings may be joined together by straight lines to give the appearance of a continuous log. Figure 9.1 illustrates such a log. The total noise amplitude is generated by flow from formation A via the casing/formation annulus to formation C. Note the increase in noise at restriction B.

R.M. Bateman, *Cased-Hole Log Analysis and Reservoir Performance Monitoring*,
DOI 10.1007/978-1-4939-2068-6_9

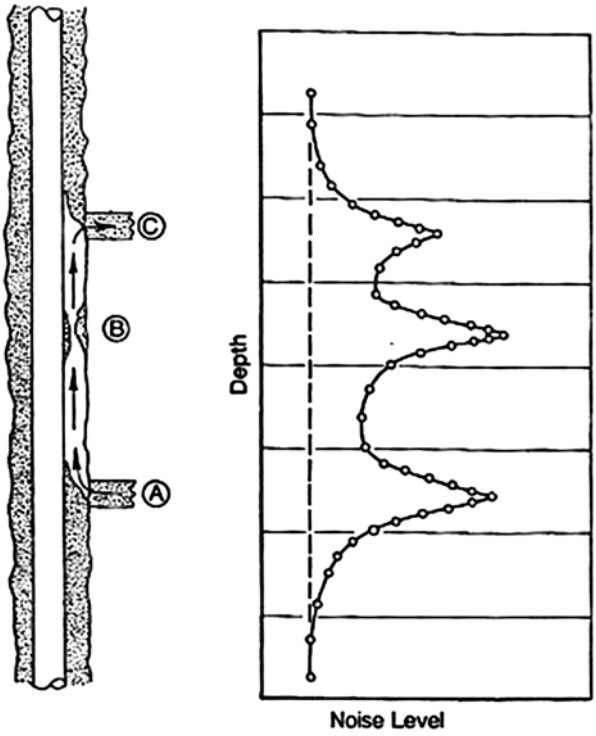

Fig. 9.1 Noise log

Operating Principle

Through controlled experiments it is possible to derive noise amplitude-frequency spectra that are characteristic of fluid flow regimes. For example, Fig. 9.2 shows the spectrum for 70 BWPD expanding across a 90 psi differential into a channel behind the pipe. Note that the majority of the noise energy is concentrated in the frequency range from 800 to 2,000 Hz.

By contrast, Fig. 9.3 shows the spectrum for sound emanating from 3.8 Mcf/D of gas expanding across a pressure differential of 10 psi into a gas-filled channel behind the pipe. Note the two peaks at 800 and 1,800 Hz.

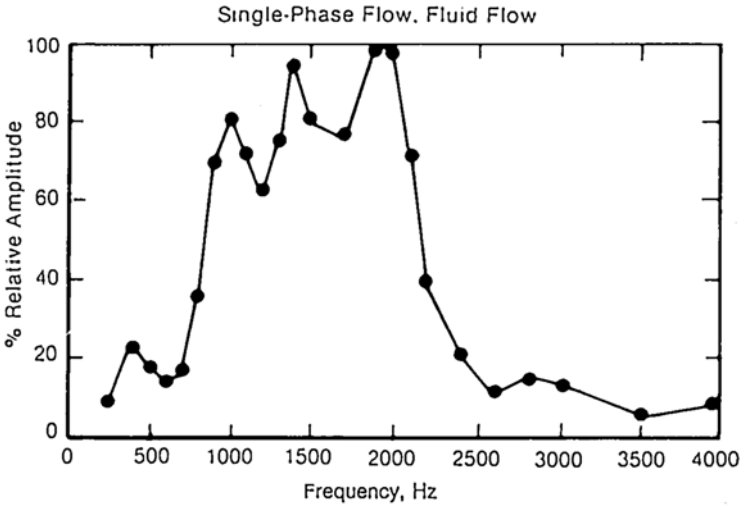

Fig. 9.2 Noise generated from a 70 BWPD flow into a channel behind pipe. Courtesy Baker Hughes

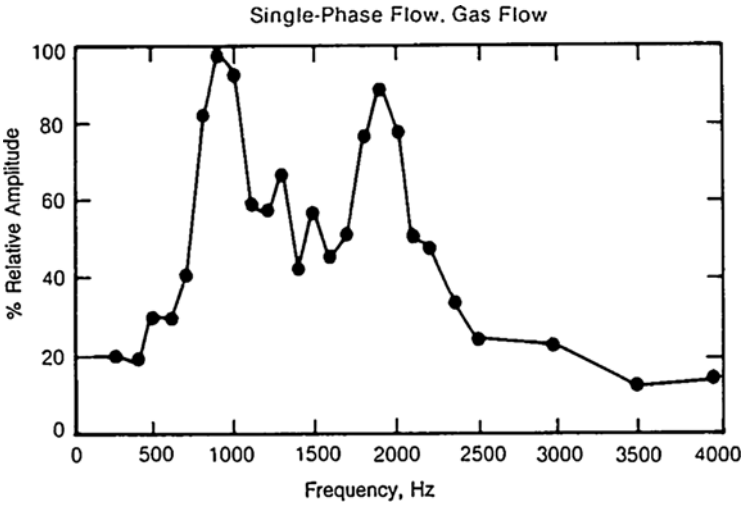

Fig. 9.3 Noise spectrum for single-phase gas flow. Courtesy Baker Hughes

Figure 9.4 shows a very different spectrum, obtained when 0.3 Mcf/D of gas expands into a water-filled channel. Here the peak noise is at less than 500 Hz.

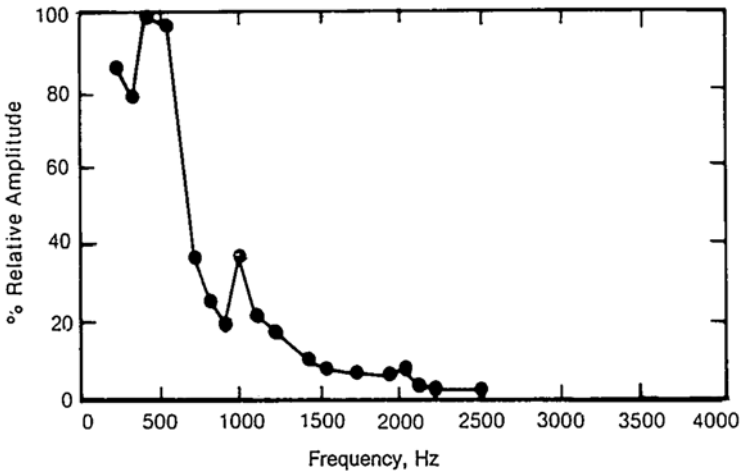

Fig. 9.4 Noise spectrum for two-phase flow (gas/water). Courtesy Baker Hughes

In order to distinguish these spectra from one another, the total signal is filtered through band-pass filters that allow the frequencies ≥200+, ≥600+, ≥1,000+, and ≥2,000+ Hz to pass. The choice of limits on these bands varies somewhat between different service companies. Since the 200-Hz filter allows all frequencies above 200 Hz to pass, this filter normally gives the highest amplitude. The 2,000-Hz filter, which only allows frequencies above 2,000 Hz to pass, normally gives the lowest amplitude. Figure 9.5 illustrates the band-pass filter response.

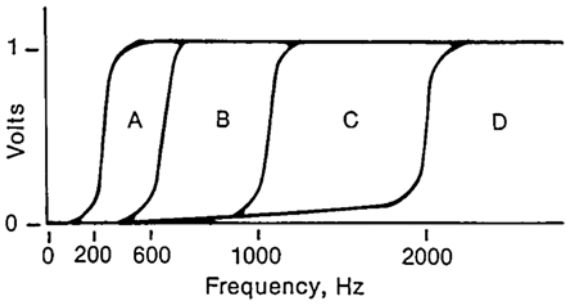

Fig. 9.5 Filter response in noise logging. Courtesy Baker Atlas

Interpretation

The interpretation of noise logs is an empirical art governed by common sense and a body of experimental data. In general, the noise level in the low-frequency bands correlates fairly well with a normalized gas flow rate, the normalization factor depending on the pressure drop. Figure 9.6 shows such a correlation.

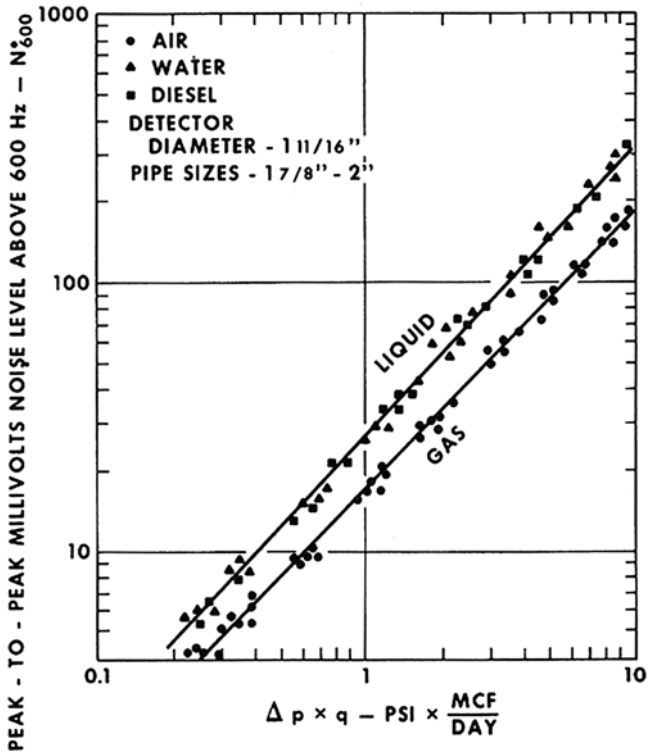

Fig. 9.6 Noise (N_{600}) vs. normalized flow rate for liquid and gas flow

In general experimental calibration of noise levels to flow rate shows that the related variables are:

- Fluid density
- Flow rate
- Pressure gradient
- Tool OD and Casing (or tubing) ID

For example the log shown in Fig. 9.7 records the noise level above the 600 Hz filter. The cube of the flow rate may be related to the recorded noise and inversely proportional to the density of the fluid flowing.

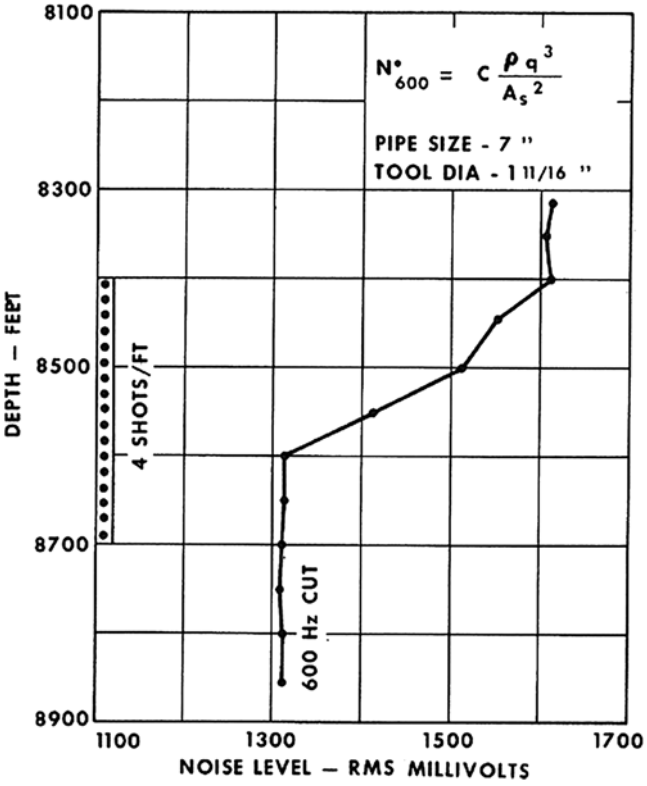

Fig. 9.7 Noise log over a gas producing interval

Sounds carry great distances in cased wells. Any surface noise should be eliminated before attempting a noise survey. Pump jacks, motors, etc., can generate noise unrelated to fluid flow in the well and confuse interpretation of noise logs. Two general rules apply:

1. Changes in noise level indicate a change in volumetric flow rate.
2. Changes in the relative noise levels in different frequency bands indicate changes in the phase make-up of the fluid mixture.

Noise and Temperature Combinations

Often a judicious combination of a noise log with a temperature survey can provide a superior analysis than could be obtained from either one singly. It is now possible to make accurate heat transfer models of the formations traversed by a well based on thermal conductivity and specific heat data and/or assumptions. When coupled with spectral noise analysis and/or flowmeter profiles obtained in the borehole a much more accurate and precise picture can be drawn of the flow of fluids into, out of, and around the cased well. Figure 9.8 illustrates a combination of noise and temperature logging where the challenge was to quantify the relative production from two perforated zones. Temperature logs were run both during production and after shut-in and warm-back was permitted. During the dynamic flow period a noise spectrum was also recorded as shown in the right-hand track. The color coded images show the noise amplitude (dB) by the colored band (red is loud, blue is quieter) across the track and the noise frequency distribution via position from the left edge of the track (100 Hz on the left, 30 kHz on the right).

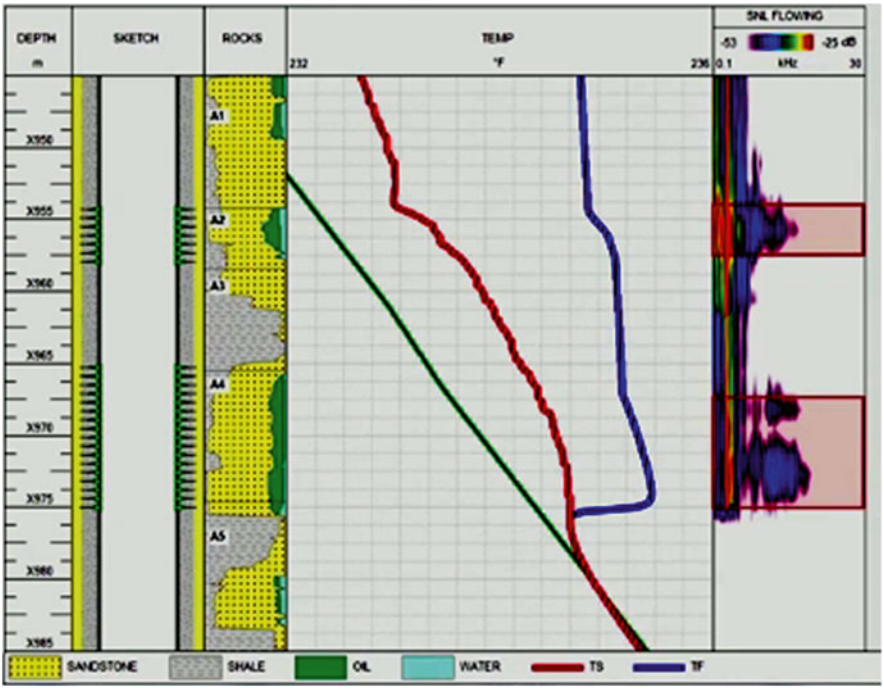

Fig. 9.8 Combination noise and temperature logs. Courtesy TGT

The green temperature line shows the geothermal gradient. The blue trace shows the flowing condition temperature distribution and the red trace the distribution after extended shut-in. Multiple computer modeling iterations can match expected profiles to the observed ones by varying the relative flow rates from the two producing intervals.

Noise and Flowmeter Combinations

Noise spectral analysis can also provide useful complementary data when analyzing flowmeter logs. An example is given in Fig. 9.9 where a fluid entry point in the well, as seen by the flowmeter alone, fails to detect that in fact flow from the formation is more extensive and that there is cross-flow behind pipe before it reaches the entry point in to the wellbore. The wellbore-noise, reservoir-matrix-noise, and the flow-through-perforation-noise can be nicely discriminated by the color coded frequency/amplitude track on the right-hand side of the figure. A possible explanation for such flow behavior could be plugged perforations. In such a case re-perforating the interval could well result in increased flow rate.

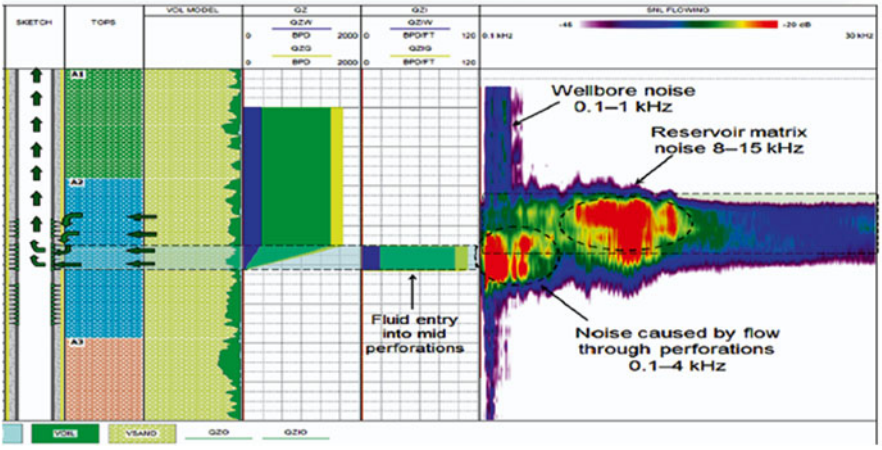

Fig. 9.9 Cross-flow detected by spinner and noise log. Courtesy TGT

Fiber Optic Sensors

The use of fiber optics to continuously measure temperature and sound energy along the entire completion string is covered in Chap. 14. Commonly referred to as *Distributed Audio System* (DAS) and *Distributed Temperature System* (DTS) these high tech permanent gauges open up an entirely new way of production monitoring.

Bibliography

An introduction to Sonan logging. Technical Memorandum 9385. Dresser Atlas.

Britt EL. Theory and application of the borehole audio tracer survey. In: SPWLA 17th annual logging symposium transactions, Denver; 9–12 June 1976.

General Catalog. The DIA-LOG Company.

Mohamed IN, El-Hamawi M, Al Hassan RA, Aslanyan A, Filenev M, Aslanyan I, Bargouthi J, Salim B. Leak detection by temperature and noise logging. In: Abu Dhabi international petroleum exhibition and conference, Abu Dhabi, UAE, 11–14 Nov 2012, SPE 161983.

Maslennikova YS, Bochkarev VV, Savinkov AV, Davydov DA. Spectral noise logging data processing technology. In: SPE Russian oil and gas exploration and production technical conferences and exhibition, Moscow, Russia; 16–18 Oct 2012, SPE 162081.

McKinley RM, Bower FM, Rumble RC. The structure and interpretation of noise from flow behind cemented casing. J Pet Technol. 1973;25(3):329–38. SPE-3999-PA.

McKinley RM, Bower FM. Specialized applications of noise logging. J Pet Technol. 1979;31(11):1387–95. SPE-6784-PA.

Noise logging service. Brochure no. 75M/5-76/C & A, N. 1. McCullough, Houston.

Robinson WS. Field results from the noise-logging technique. J Pet Technol (1976). Presented at the SPE 49th annual meeting, Houston, 6–7 Oct 1974.

Interpretation 10

Holdup Equations

The basics of biphasic flow have been covered in Chap. 4. In this chapter, the practical applications of the holdup equation will be covered. The purpose is to equip the analyst with a practical tool with which to analyze a combination of a flowmeter log and a holdup log (whether this be from a gradiomanometer or other tool). The methods described will allow the analyst to calculate the flow rate for each phase of a biphasic mixture at each point in the well and hence to deduce the production of each phase from each perforated interval. This is an essential step in quantitative analysis without which remedial action cannot be planned properly.

Figure 10.1 depicts the simultaneous flow of two phases in a vertical pipe. One phase is referred to as the *heavy* phase and the other as the *light* phase. Depending on the mixture these may be:

Mixture	Light phase	Heavy phase
Oil and water	Oil	Water
Oil and gas	Gas	Oil
Gas and water	Gas	Water

The holdup equation states that the density of a flowing biphasic mixture is given by:

$$\rho_m = y_h \times \rho_h + (1 - y_h)\rho_l$$

where:

ρ_m is the density of the mixture
ρ_h is the density of the heavy phase
ρ_l is the density of the light phase

R.M. Bateman, *Cased-Hole Log Analysis and Reservoir Performance Monitoring*,
DOI 10.1007/978-1-4939-2068-6_10

The holdup of the heavy phase is therefore given by:

$$y_h = \frac{\rho_m - \rho_l}{\rho_h - \rho_l}$$

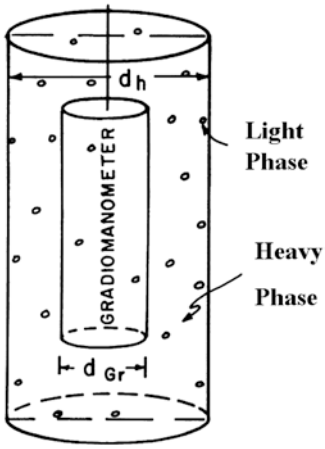

Fig. 10.1 Biphasic flow—Courtesy Schlumberger

Question #10.1
Oil and water flow together and have a density of 0.8 g/cc.

If the oil has a density of 0.6 g/cc and the water a density of 1.0 g/cc, what is the water holdup in this flow mixture?

The holdup only tells us what fraction of the cross-sectional area available for fluid flow is occupied by a particular phase. In order to tell the actual flow rates of each phase we need additional data, namely, total flow rate, the pipe cross-sectional area, the tool diameter, and the inter-phase slip velocity. In general, the equations will be:

$$Q_t = Q_h + Q_l$$
$$Q_h = y_h A V_h$$
$$Q_l = y_l A V_l$$
$$V_l = V_h + V_s$$
$$1 = y_h + y_l$$

where:

Q_t = total flow rate
Q_h = heavy-phase flow rate

Q_l = light-phase flow rate
A = cross-sectional area
V_h = heavy-phase velocity
V_l = light-phase velocity
V_s = slip velocity

The known quantities are normally Q_t, A, V_s, and y_h. The unknown quantities are Q_h and Q_l. With some minor algebraic manipulation an expression can be derived for Q_h or Q_l as follows:

$$Q_h = Q_t - Q_l = Q_t - (1 - y_h) \cdot A \cdot (V_h + V_s)$$

But,

$$V_h = Q_h / y_h A$$

Thus,

$$Q_h = Q_t - (1 - y_h) \cdot A \cdot (Q_h / y_h A + V_s)$$

hence

$$Q_h = y_h \left[Q_t - (1 - y_h) \cdot A \cdot V_s \right]$$

Once Q_h is determined, Q_l can be found from

$$Q_l = Q_t - Q_h$$

Practical Applications

In order to apply this equation to find the volumetric flow rates of the two phases, consistency of units of measurement must be maintained. If flow rates are to be expressed in barrels per day then the product A. V_s must also be in barrels per day. However A, the cross-sectional area of the pipe available for flow, will normally be quoted either in square inches or square centimeters, and V_s, the slip velocity, will normally be quoted in feet per minute or centimeters per second. Therefore, a conversion constant is required to convert the area x speed product into a flow rate in B/D. Thus, in practical terms, the flow rate equation reduces to:

$$Q_h = y_h \left[Q_t - (1 - y_h) \cdot A \cdot V_s \cdot 1.781 \right]$$

where A is in sq in. and V_s is in ft/ min, or to

$$Q_h = y_h \left[Q_t - (1 - y_h) \cdot A \cdot V_s \cdot 0.5433 \right]$$

where A is in cm^2 and V_s is in cm/s.

Note that the cross-sectional area referred to is the net area available for flow in the casing/tool annulus. Thus, both the ID of the casing and the OD of the tool must be known in order to solve the flow equation accurately. This net area may be calculated from:

$$A = \pi \left[\left(\frac{\text{Casing ID}}{2} \right)^2 - \left(\frac{\text{Tool OD}}{2} \right)^2 \right]$$

This type of calculation may be performed either using a calculator or, graphically, using a chart of the type shown in Fig. 10.2. On the graph, the *Y*-axis plots the heavy-phase flow rate and the *X*-axis the light-phase flow rate. In Fig. 10.2, there are two series lines. One set (running diagonally from NW to SE) corresponds to constant total flow rate. Another set (running diagonally from NE to SW) corresponds to constant values of heavy-phase holdup, y_h. To solve for the light and heavy-phase flow rates the analyst should enter the chart and locate the intersection of the total flow rate (Q_t) and the heavy-phase holdup (y_h). From that point the corresponding flow rates can be read by moving leftward, parallel to the *x*-axis for the heavy-phase flow rate and down the page, parallel to the *y*-axis to obtain the light-phase flow rate.

Question #10.2
Oil and water flow in 5-in. 15.5-lb casing which has an ID of 4.95 in. The slip velocity, V_s, is 20 ft/min. The water holdup has been found from a gradiomanometer survey to be 0.7. Assume that a one 11/16-in. OD tool was used to make the measurements, and that the total flow rate is 1,000 B/D.

(a) What is the water flow rate?
(b) What is the oil flow rate?

Note also that the chart shown in Fig. 10.2 is specifically built for a given set of values for casing size and weight (and therefore casing ID), tool OD, and slip velocity, V_s. If the analyst chooses to use the graphical method, an appropriate chart should be obtained from the relevant service-company publication to suit the particular circumstances.

Flowmeter and Gradiomanometer Combinations

As an example of the practical method to be employed, the log shown in Fig. 10.3 will be considered. This well produces oil and water from two perforated intervals. Total flow rate is 850 B/D (at down-hole conditions) with 485 BOPD and 365 BWPD. Down-hole fluid densities are 1.05 g/ cc for the water and 0.8 g/cc for the oil. The objective of the analysis is to deduce the oil and water flow rates at each station where a total flow rate has been determined and thereby to determine the oil and water production rates from each perforated interval.

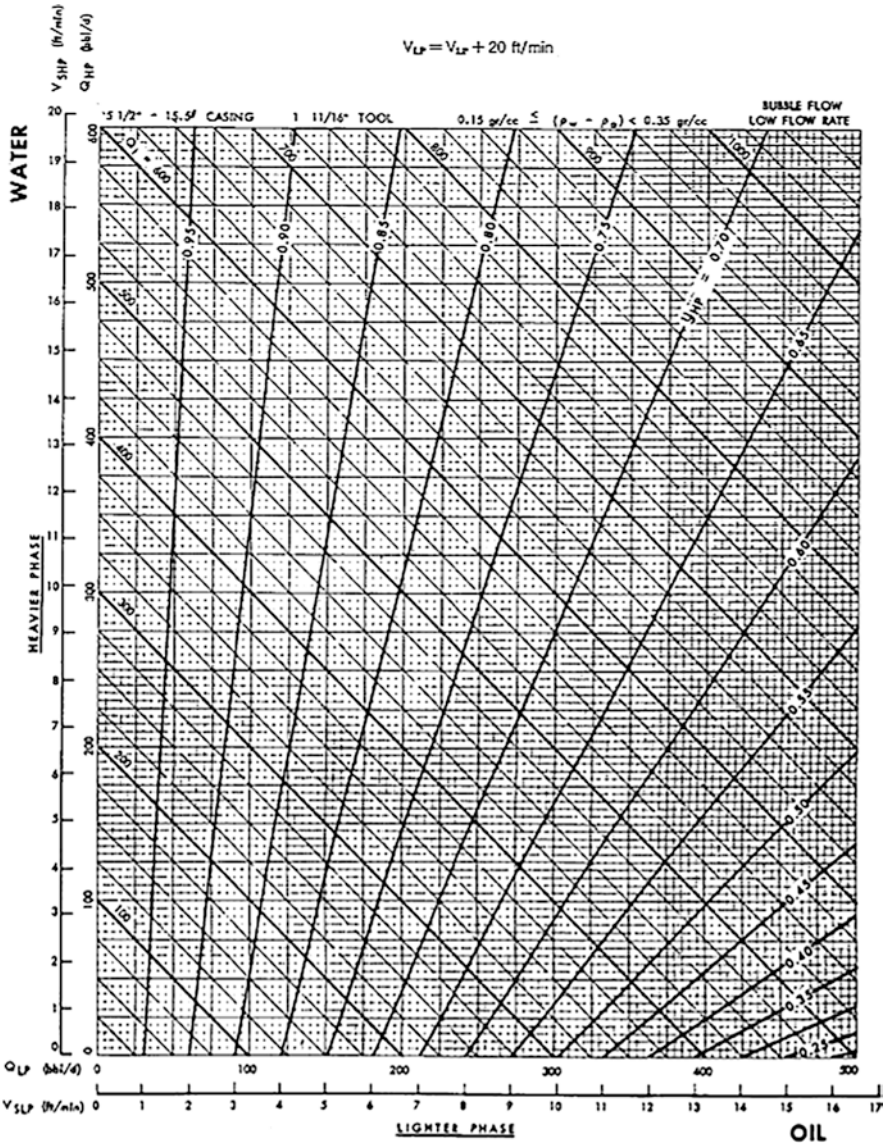

Fig. 10.2 Flow rate and holdup chart—Courtesy Schlumberger

Notice that the gradiomanometer log (Fig. 10.3) has both a direct recording (the solid trace) and an amplified trace (dotted). It is customary to use the amplified trace since it allows better resolution. However, since use of the amplified trace requires a rescaling in terms of heavy-phase holdup, the amplified gradiomanometer trace is usually read in terms of chart divisions.

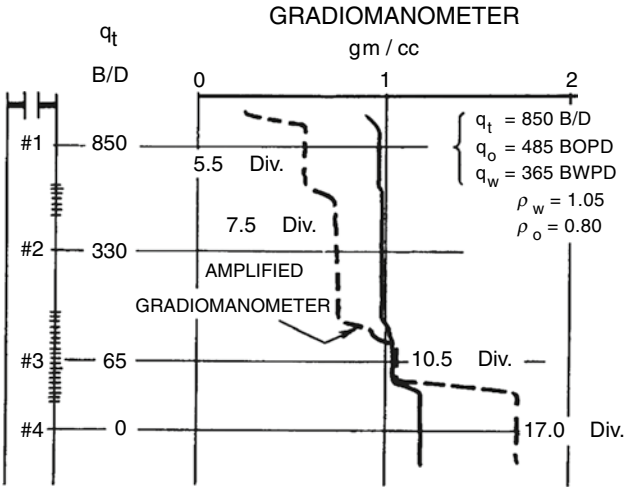

Fig. 10.3 Gradiomanometer log in a well producing oil and water. Reprinted by permission of the SPE from Curtis (1967)

In order to rescale the gradiomanometer, two points on the log need to be considered. At Station #4, an assumption is made that the reading of 17.0 divisions corresponds to 100 % water, for which, obviously, $y_h = 1.0$. At Station #1, the reading of 5.5 divisions corresponds to some value of y_h that can be back-calculated from the known flow rates, casing and tool sizes, and slip velocity. Mathematically,

$$y_h = \frac{-(Q_t - AV_s) \pm \sqrt{(Q_t - AV_s)^2 + 4Q_h AV_s}}{2AV_s}$$

In this case, the product AV_s in B/D is computed as:

$$AV_s = \frac{\pi\left(4.95^2 - 1.6875^2\right)}{4} \times 20 \times 1.781$$
$$= 605.81 \text{ B/D}$$

The heavy-phase holdup at Station #1 is then calculated as:

$$y_h = \frac{-244.19 \pm 971.65}{2 \times 605.81} = 0.6$$

An alternative method of finding y_h above all the perforated intervals is to use the holdup and flow rate chart, as shown in Fig. 10.4. By plotting the point corresponding to 485 BOPD and 365 BWPD the holdup of 0.6 is directly determined.

The gradiomanometer may now be recalibrated in terms of y_h using the two calibration points determined, that is:

$y_h = 1.0$ when gradio reads 17.0 divisions
$y_h = 0.6$ when gradio reads 5.5 divisions

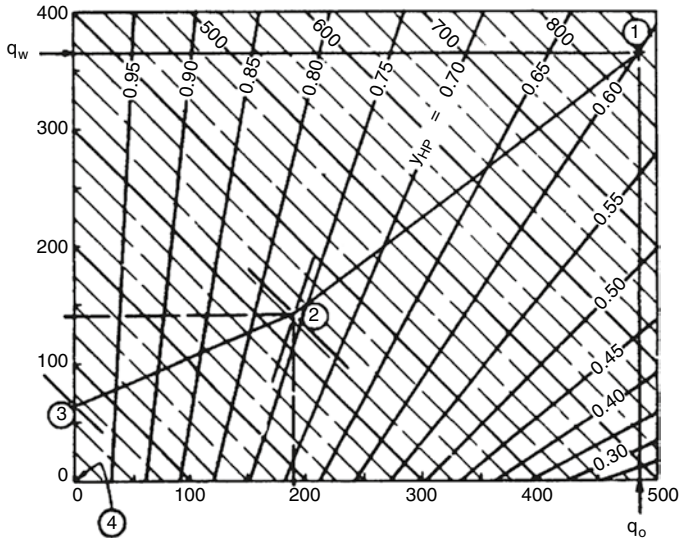

Fig. 10.4 Use of holdup and flow rate chart. Reprinted by permission of the SPE—from Curtis (1967)

Thus, for any gradio reading, y_h may be calculated for this particular log by:

$$y_h = 0.41 + \frac{\text{gradio divisions}}{28.75}$$

A more straightforward method is to simply plot a recalibration graph on a sheet of linear graph paper as shown in Fig. 10.5.

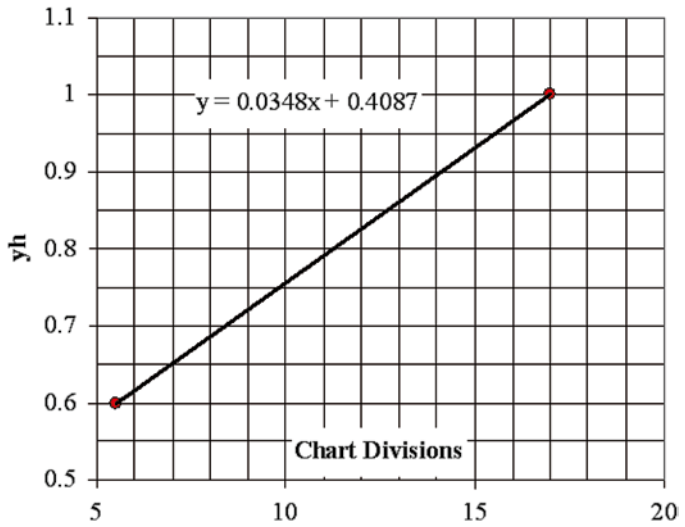

Fig. 10.5 Recalibration of gradiomanometer log in terms of y_h

Everything is now in place to proceed with station-by-station analysis. The procedure will be as follows for each station:

1. Read gradiomanometer log.
2. Convert reading to y_h (holdup value).
3. Plot total flow rate and y_h on the holdup-flowrate graph.
4. Read the water and oil flow rates on the *X*- and *Y*-axes.
5. Repeat process for next station.

Table 10.1 Tabulation of log data and calculations

Station #	Total flow rate B/D	Amplified gradio divisions	y_h	Q_w	Q_o	Production	
						BWPD	BOPD
1	850	5.5	0.6	365	485		
						278	242
2	330	7.5	0.67	87	243		
						87	243
4	0	17	1	0	0		

In order to keep track of the log readings and the calculated answers it is useful to work with a table of the sort shown in Table 10.1. Note that the production rate from any set of perforations can be deduced from the oil and flow rate found above and below those perforations. A useful way of presenting the results is shown in Fig. 10.6. Flow rate is plotted against depth for both oil and water and one phase or the other is shaded or color coded. Coded bar-graphs may also be used to show the production from each set of perforations.

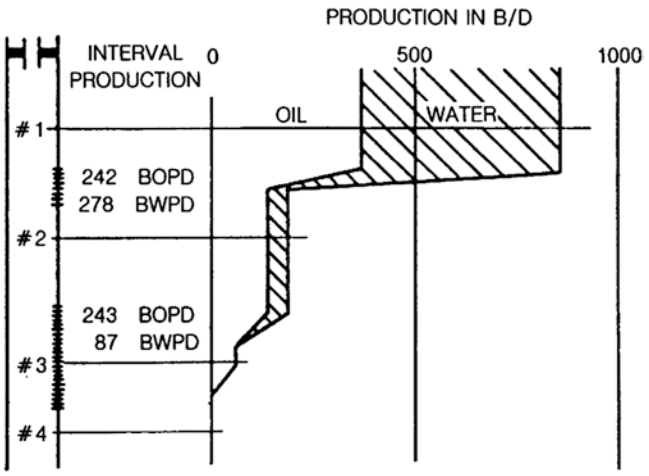

Fig. 10.6 Presentation of results of gradiomanometer analysis. Reprinted by permission of the SPE, adapted from Curtis (1967)

Bibliography

Curtis MR. Flow analysis in producing wells. In: Paper SPE 1908 presented at the SPE 42nd annual meeting, Houston; October 1967.
Nicolas Y, Witterholt E. Measurements of multiphase fluid flow. In: Paper SPE 4023 presented at the SPE 47th annual meeting, San Antonio; 8–11 Oct 1972.

Answers to Text Questions

Question #10.1
$y_h = 0.5$

Question #10.2
(a) 572.8 BWPD
(b) 427.2 BOPD

Formation Evaluation Through Casing 11

Tools and Techniques Available

A number of tools are available for formation evaluation through tubing and casing. They include:

1. Measurements of formation resistivity through casing
2. Passive detection of natural gamma radiation from the formation
3. Neutron logging to detect the thermal-neutron flux returning from the formation after neutron bombardment from a chemical source
4. Pulsed neutron logging
5. Elemental concentration logging

Resistivity Through Casing

Tools to measure formation resistivity through casing are now available. These tools require that any tubing in the well be pulled prior to running the resistivity logging tool into the hole. They are equipped with a number of electrode pads that are forced against the inside of the casing once the tool reaches the bottom of the hole or the depth from which the log is to be attempted. If good physical and electric contact can be maintained between the pads and the casing then a reasonable measurement of the formation resistivity behind the casing may be obtained.

The operating principal relies on the fact that while the majority of any current flowing will be "short circuited" by the conductive casing itself a minute portion will in fact "leak off" and be detectable by measurement of the minute voltage difference between the tool and "ground" electrode located at surface. The principal is illustrated in Fig. 11.1.

The logical application of resistivity through casing measurements is in old wells where either no resistivity log is available or where a comparison can be made between original and the current formation resistivities. Potential benefits include detection of bypassed pay zones and/or mapping of fluid contact changes with time.

R.M. Bateman, *Cased-Hole Log Analysis and Reservoir Performance Monitoring*,
DOI 10.1007/978-1-4939-2068-6_11

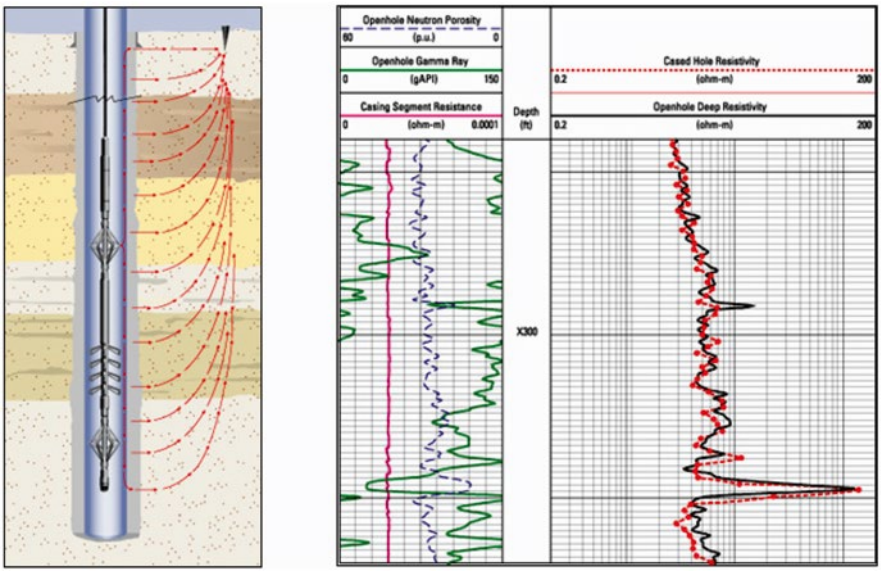

Fig. 11.1 Measurement of formation resistivity through casing

The Gamma Ray Log

Gamma ray logs are used for four main purposes:

1. Correlation and depth positioning
2. Evaluation of the shale content of a formation
3. Mineral analysis
4. Monitoring of radioactive salts deposited on tubulars

The gamma ray log measures the natural gamma ray emissions from subsurface formations. Since gamma rays can pass through steel casing, measurements can be made in both open and cased holes. In other applications, induced gamma rays are measured. These may be γ-rays of capture as used in pulsed neutron logging, or γ-rays produced by inelastic neutron interaction with nuclei in the formation. These latter are used to identify the formation elemental concentrations. These will be discussed later in this chapter.

Figure 11.2 shows a typical gamma ray log. It is normally presented in Track 1 on a linear grid and is scaled in API units, which will be defined later. On this grid, gamma ray activity increases from left to right. Modern gamma ray tools are in the form of double-ended subs that can be sandwiched into practically any logging tool string; thus, the gamma ray can be run with practically any tool available.

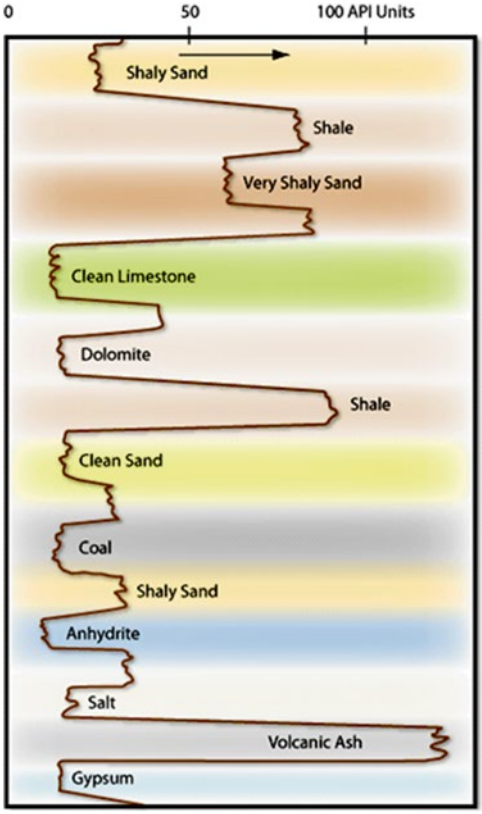

Fig. 11.2 Gamma ray log presentation

Origin of Natural Gamma Rays

Gamma rays originate from three sources in nature: the radioactive elements in the Uranium and Thorium groups, and Potassium. Uranium^{235}, Uranium^{238}, and Thorium^{232} all decay, via a long chain of daughter products, to stable lead isotopes. An isotope of Potassium, K^{40}, decays to Argon, giving off a gamma ray as shown in Fig. 11.3.

Note that each type of decay is characterized by a gamma ray of a specific energy (wave length) and that the frequency of occurrence for each specific energy level is different. Figure 11.4 shows this relationship between gamma ray energy and frequency of occurrence. This is an important concept, since it is used as the basis for measurement in the natural gamma spectroscopy tools.

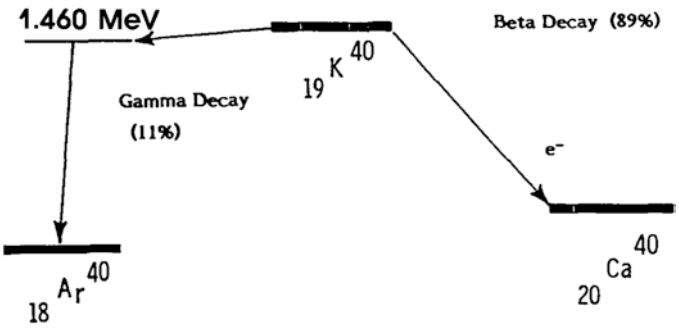

Fig. 11.3 Decay scheme of $_{19}K^{40}$

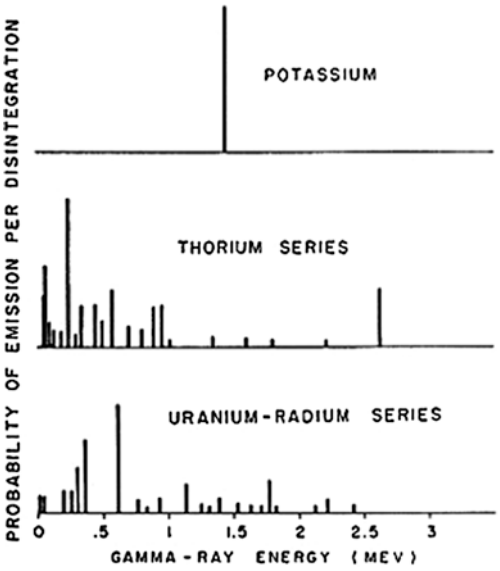

Fig. 11.4 Gamma ray emission spectra of radioactive minerals

Abundance of Naturally Occurring Radioactive Minerals

An average shale contains 6 ppm Uranium, 12 ppm Thorium, and 2 % Potassium. Since the various gamma ray sources are not all equally effective, it is more informative to consider this mix of radioactive materials on a common basis, for example, by reference to Potassium equivalents (i.e., the amount of Potassium that would produce the same number of gamma rays per unit of time). Reduced to a common denominator, the average shale contains Uranium equivalent to 4.3 % Potassium, Thorium equivalent to 3.5 % Potassium, and 2 % Potassium. An *average* shale is hard to find.

Shale is a mixture of clay minerals, sand, silts, and other extraneous materials; thus, there can be no "standard" gamma ray activity for shale. Indeed, the main clay minerals vary enormously in their natural radioactivity. Kaolinite has no Potassium, whereas Illite contains between 4 and 8 % Potassium. Montmorillonite contains less than 1 % Potassium. Occasionally, natural radioactivity may be due to the presence of dissolved Potassium or other salts in the water contained in the pores of the shale.

Operating Principle of Gamma ray Tools

Gamma ray tools consist of a gamma ray detector and the associated electronics for passing the gamma ray count rate to the surface. Traditionally, two types of gamma ray detectors have been used in the logging industry: Geiger-Müeller and scintillation detectors. Today, practically all gamma ray tools use scintillation detectors containing a sodium iodide crystal[1] (Fig. 11.5). When a gamma ray strikes the crystal, a single photon of light is emitted. This tiny flash of light then strikes a photo cathode made from cesium antimony or silver magnesium. Each photon, when hitting the photo cathode, releases a bundle of electrons. These in turn are accelerated in an electric field to strike another electrode producing an even bigger bundle (a shower) of electrons. This process is repeated through a number of stages until a final electrode conducts a small current through a measure resistor to give a voltage pulse that signals that a gamma ray struck the sodium iodide crystal. The system has a very short dead time and can register many counts per second without becoming swamped by numerous simultaneous signals.

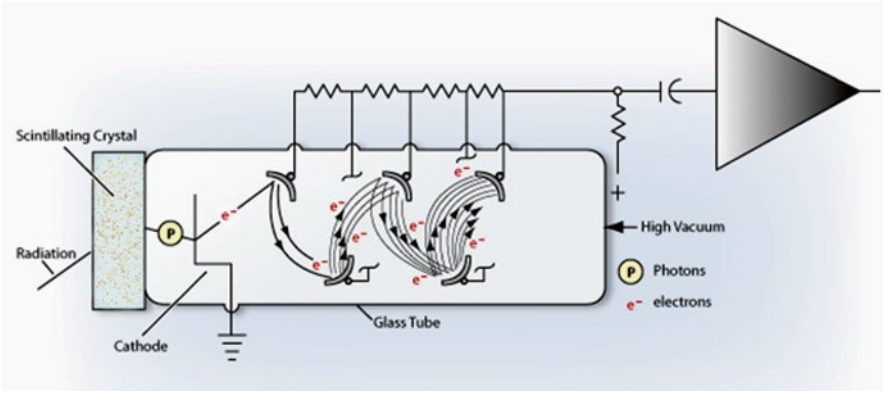

Fig. 11.5 Scintillation counter. Courtesy Halliburton

[1] Sodium Iodide (NaI) and Cesium Iodide (CsI) crystal detectors have relatively poor resolution. Modern "High Resolution" GR logging tools now use Barium Germanite (BGO) detectors, which have better resolution. The better resolution yet can be obtained, using intrinsic Germanium (GSO) or Germanium-Iodide (GeI) or Lanthium Halide (LaBr3 - BrilLanCe™) which must be cryogenetically cooled.

Calibration of Gamma Ray Detectors and Logs

One of the problems of gamma ray logging is the choice of a standard calibration system, since all logging companies use counters of different sizes and shapes encased in steel housings with varying characteristics. On very old logs, the scale might be quoted in micrograms of radium per ton of formation. For many reasons this was found to be an unsatisfactory method of calibration for gamma ray logs, so an API standard was devised. A test pit (installed at the University of Houston) contains an "artificial shale," as illustrated in Fig. 11.6. A cylindrical artificial well, 4 ft in diameter and 24 ft deep contains a central 8-ft section consisting of cement mixed with 13-ppm Uranium, 24 ppm Thorium, and 4 % Potassium. On either side of this central section are 8-ft sections of neat Portland cement. This sandwich is cased with 5½″, J55 casing. The API standard defines the difference in gamma ray count rate between the neat cement and the radioactively doped cement as 200 API units. Any logging service company may place its gamma ray tool in this pit to make a calibration. Field calibration is performed using a portable jig that contains a radioactive pill. The pill typically might be a low activity radium 226 source (e.g., 0.1 milli-curie). When placed at a known radial distance from the center of the gamma ray detector, it produces a known increase over the background count rate. This increase is equivalent to a known number of API units, depending on the tool type and size and the counter it encloses.

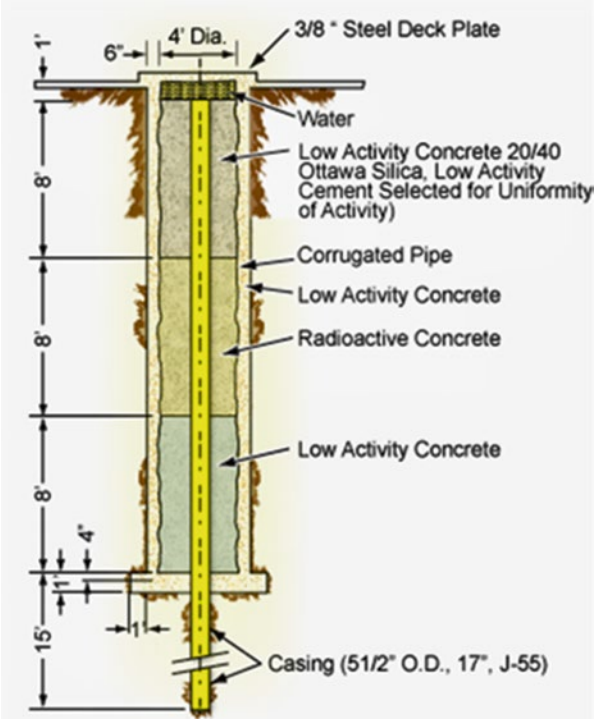

Fig. 11.6 API Gamma Ray Test Pit at the University of Houston

Time Constants

All radioactive processes are subject to statistical variations. For example, if a source of gamma rays emits an average of 100 gamma rays each second over a period of hours, the source will emit 360,000 gamma rays per hour (100/s × 60 s × 60 min). However, if the count is measured for 1 s, the actual count might be less than 100 or more than 100. Thus, a choice must be made. Gamma rays can be counted for a very short interval of time, resulting in a poor estimate of the real count rate; or the gamma rays can be counted for a long time, resulting in a more accurate estimate of the count rate at the expense of an inordinately long time period. In order to average out the statistical variations, various *time constants* may be selected according to the radioactivity level measured. The lower the count rate, the longer the time constant required for adequate averaging of the variations.

In the logging environment, gamma rays can be counted for a short period of time (e.g., 1 s) with the recognition that during that time period, the detector will have moved past the formation whose activity is being measured. Thus, the logging speed and the time interval used to average count rates are interrelated. The following rules of thumb are generally recognized:

Logging speed (ft/h)	Time constant (s)
3,600	1
1,800	2
1,200	3
900	4

At very slow logging speeds (900 ft/h = 1.5 ft/s) and long time constants, a more accurate measurement of absolute activity is obtained at the expense of good bed resolution. At high logging speeds and short time constants, somewhat better bed resolution is obtained at the expense of absolute accuracy. At some future time, when the efficiency of gamma ray detectors and their associated electronics improve by one or two orders of magnitude, the use of a time constant will be obsolete except in the cases of very very inactive formations with intrinsically low gamma ray count rates.

To illustrate this interdependence of logging speed and time constant, Fig. 11.7 shows the same formation logged at two different speeds. On the first run, the logging speed was 80 ft/min and the time constant 1 s. On the second run, the speed was 30 ft/min and the time constant was 2 s. Note the differences in both statistics and bed resolution between the two runs.

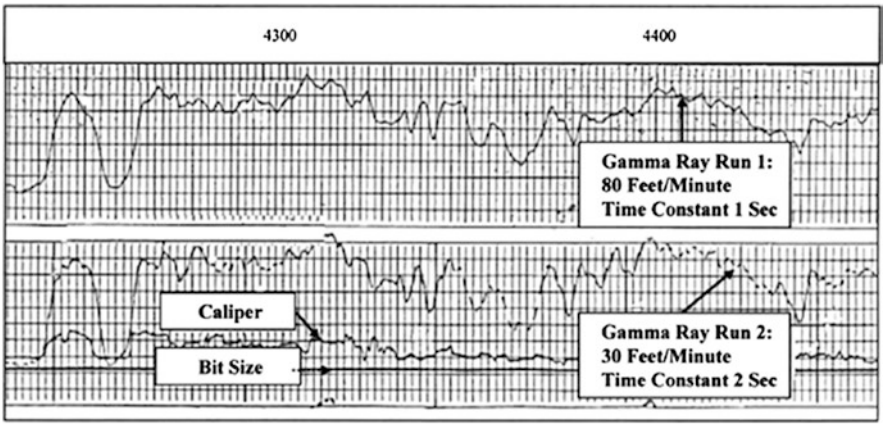

Fig. 11.7 Effects of logging speed and time constant on gamma ray log

Perturbing Effects on Gamma Ray Logs

Gamma ray logs are subject to a number of perturbing effects including:

Sonde position in the hole (centering/eccentering)
Hole size
Mud weight
Casing size and weight
Cement thickness

Since there are innumerable combinations of hole size, mud weights, and tool positions, an arbitrary standard set of conditions is defined as a 3 5/8″ OD tool eccentered in an 8″ hole filled with 10-lb mud. Service company chart books provide analog systems for manually applying corrections but modern logs are almost universally subjected to environmental corrections in real time as the logs are being run that take into account the disturbing effects of temperature, hydrostatic pressure, mud weight, hole and casing size, etc.

Estimating Shale Content from Gamma Ray Logs

Since it is common to find radioactive materials associated with the clay minerals that constitute shales, it is a commonly accepted practice to use the relative gamma ray deflection as a shale-volume indicator. The simplest procedure is to rescale the gamma ray log between its minimum and maximum values from 0 to 100 % shale. A number of studies have shown that this is not necessarily the best method, and alternative relationships have been proposed. To further explain these methods, the

Gamma Ray Index is defined as a linear rescaling of the *GR* log between GR_{min} and GR_{max} such that:

$$\text{Gamma Ray Index} = \frac{GR - GR_{min}}{GR_{max} - GR_{min}}$$

If this index is called *X*, then the alternative relationships can be stated in terms of *X* as follows:

Relationship	Equation
Linear	$V_{sh} = X$
Clavier	$V_{sh} = 1.7 - \sqrt{\left[3.38 - \left(X + 0.7\right)^2\right]}$
Steiber	$V_{sh} = \frac{0.5X}{\left(1.5 - X\right)}$
Bateman	$V_{sh} = X^{(X + \text{GR Factor})}$

where the *GR Factor* is a number chosen to force the result to imitate the behavior of either the Clavier or the Steiber relationship. Figure 11.8 illustrates comparatively the difference between these alternative relationships.

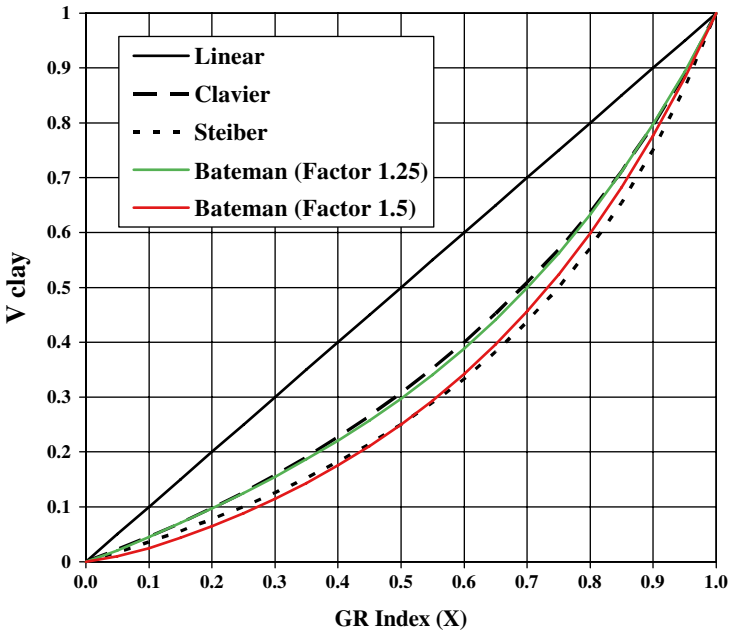

Fig. 11.8 V_{clay} as a function of Gamma Ray Index

Gamma Ray Spectroscopy

Each radioactive decay produces a gamma ray that is unique. These various gamma rays have characteristic energy levels and occur in characteristic abundance, as expressed in counts per time period. The simple method of just counting how many gamma rays a formation produces can be carried a step further to count how many gamma rays from each energy group it produces. The spectrum produced when the number of occurrences is plotted against the energy group is characteristic of the formation logged. Figure 11.9 shows such a spectrum, where energies from 0 to approximately 3 MeV have been split into 256 specific energy bins. The number of gamma rays in each bin is plotted on the *Y*-axis. This spectrum can be thought of as a mixture of the three individual spectra belonging to uranium, thorium, and potassium. Some unique mixture of these three radioactive families would have the same spectrum as the observed one. The trick is to find a quick and easy method of discovering that unique mixture. Fortunately, on-board computers in logging trucks are capable of quickly finding a "best fit" and producing continuous curves showing the concentrations of U, Th, and K.

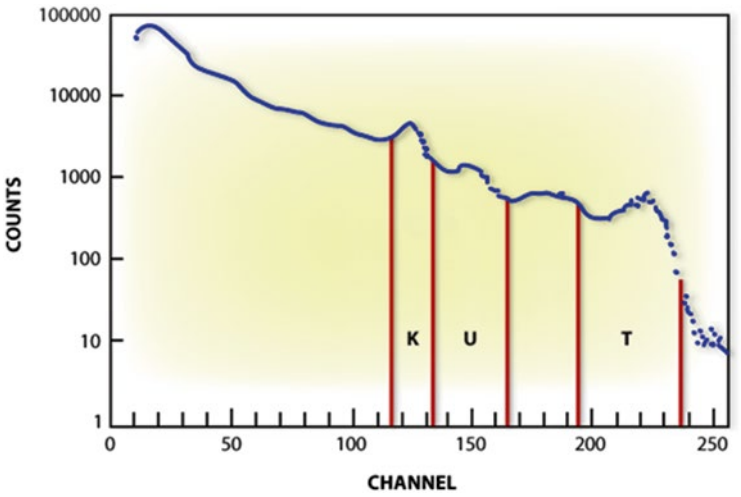

Fig. 11.9 Gamma ray energy spectrum and elemental "windows"

Figure 11.10 illustrates a gamma ray spectral log. Both total gamma ray activity (SGR) and a uranium-free version of the total activity are displayed in Track 1. Units are API. In Tracks 2 and 3, the concentration of U, Th, and K are displayed. Depending on the logging service company, the units may be in counts/s, ppm, or percent.

Question #11.1
In the example shown in Fig. 11.10, determine which element is responsible for the high activity seen on the total gamma ray intensity curve at the point marked A.

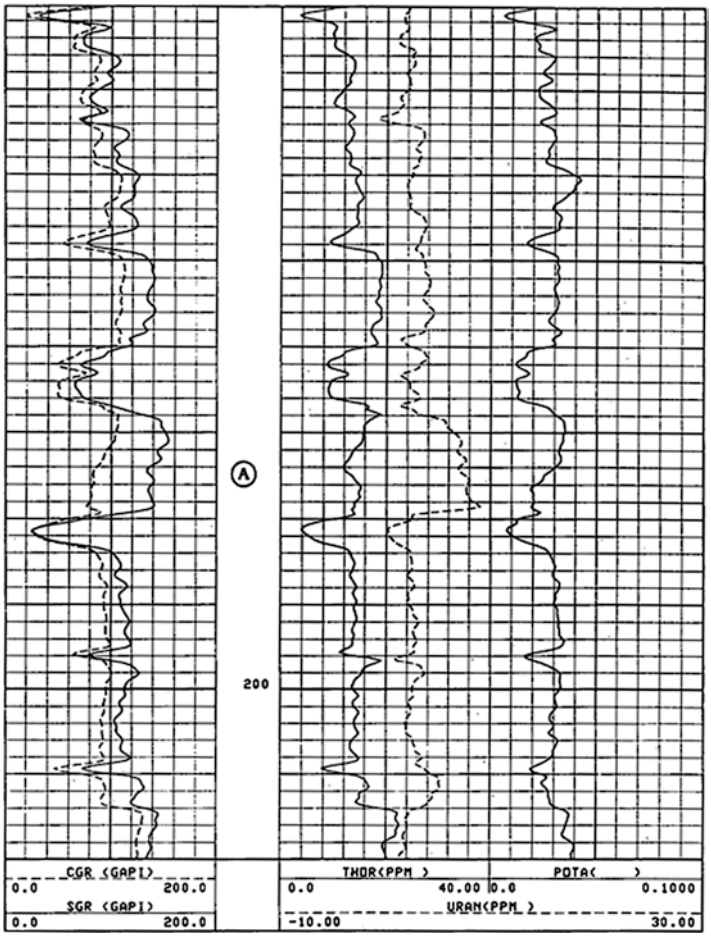

Fig. 11.10 Spectral gamma ray log. Courtesy Schlumberger

Interpretation of Natural Gamma Ray Spectra Logs

Several techniques are in use for the interpretation of natural gamma ray spectra logs. One is the use of the uranium curve as an indicator of fractures. This is more fully described by Fertl et al. More recently the development of unconventional reservoirs has benefited for the presence of uranium in organic shales that may be hydraulically fractured (fracked) and produced. In these formations the uranium content is often related to the total organic carbon (TOC) content of the formation.

Another technique is to apply the U, Th, and K concentrations in combination with other log data to determine lithology and clay type, as described by Marett et al. Still another approach could be called the geochemical method as described by Hassan et al. (1976). Figure 11.11 illustrates the variation of the thorium/potassium ratio in a number of minerals ranging from potassium-feldspar to bauxite.

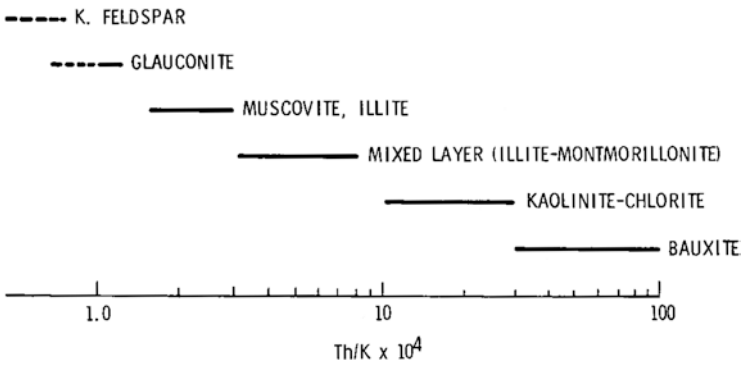

Fig. 11.11 Thorium/Potassium ratios for various minerals. Reprinted by permission of the SPWLA from Hassan et al. 1976. Courtesy Schlumberger

Figure 11.12 maps a number of radioactive minerals as a function of their thorium and potassium content. Other elemental ratios are also useful indicators. For example, a low U/Th ratio indicates reduced black shales. Uranium by itself may indicate a high organic carbon content, which in turn may indicate the presence of gas.

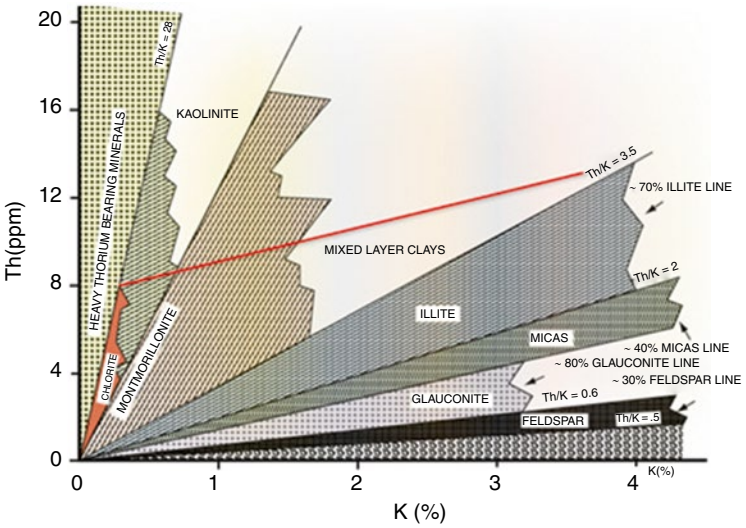

Fig. 11.12 Thorium/Potassium crossplot for minerals identification. Courtesy Schlumberger

Field presentations of gamma ray spectra can assist the analyst in the task of mineral identification by offering curve plots with ratios of the three components (U, Th, and K) already computed. Figure 11.13 gives an example of one such presentation. Track 1 shows total gamma ray together with a uranium-free curve. Track 2 gives three ratios, uranium/potassium, thorium/uranium, and thorium/potassium. Track 3 gives a coded display on which the coded area represents the formations with both the highest potassium and the highest thorium content.

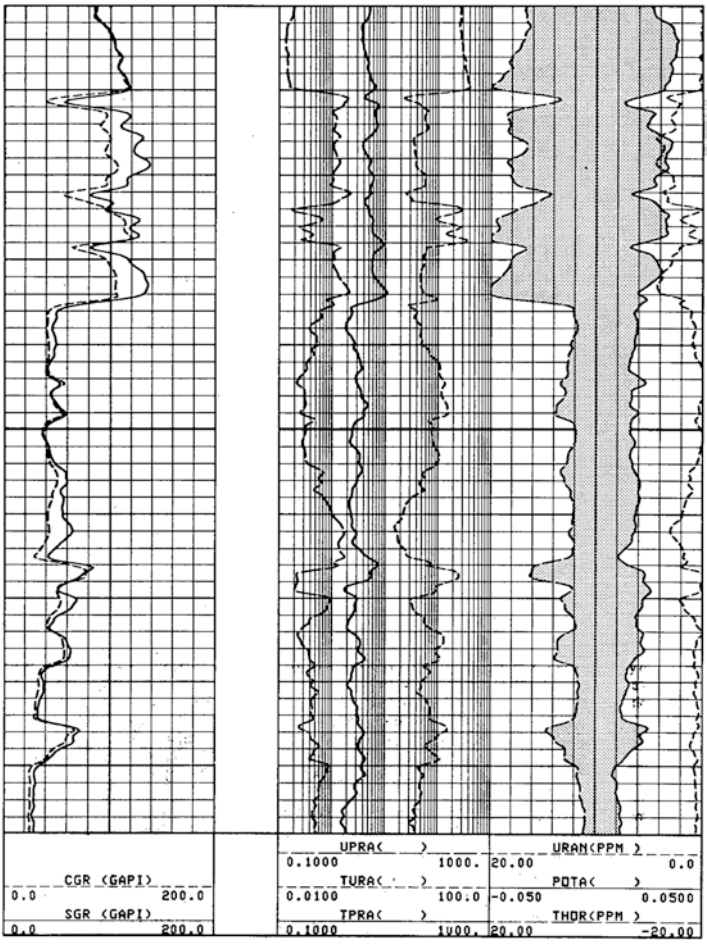

Fig. 11.13 Th, K, and U ratios display. Courtesy Schlumberger

Pulsed Neutron Logging

Pulsed neutron logs provide a means of evaluating a formation after the well has been cased. It is of particular value for:

1. Evaluating old wells, where the original open-hole logs are inadequate or nonexistent.
2. Monitoring reservoir performance over an extended period of time.
3. Monitoring the progress of secondary and tertiary recovery projects.
4. Formation evaluation, as a last resort should the drill-pipe become stuck.

It is one of the most widely used logging methods in cased holes at the present time. Other nuclear measurements that have been developed as extensions of the basic pulsed neutron technology include logs based on the detection of gamma rays resulting from inelastic neutron collisions with nuclei in the formation. These include carbon/oxygen logs and the so-called elemental concentration logs. The same basic tool with some modification can also be used for oxygen activation logging as a flow measuring system. Such applications are covered in Chap. 5.

Principle of Measurement

Many different service company tools are available for use in cased wells. A typical through tubing version will have an OD of 1–11/16″. For use in cased holes without tubing full diameter tools (3–5/8″ OD) are also commonly used. Regardless of the tool used, the principle of measurement remains the same although their operating systems are all slightly different.[2]

A neutron generator is turned on for a very short period of time. As a result, a burst of fast neutrons leaves the tool; and, since neutrons can easily pass through both the steel housing of the tool and the tubing/casing, a cloud of neutrons is formed in the formation. Fast neutrons soon became “thermalized” by collisions with atoms in the formation. The most effective thermalizing agent is the hydrogen present in the pore space in the form of water or hydrocarbon. Once in the thermal state, a neutron is liable to be captured. The capture process depends on the capture cross section of the formation. In general, chlorine dominates the capture process. Since chlorine is present in formation water in the form of salt (NaCl), the ability of the formation to capture thermal neutrons reflects the salt content and hence the water saturation. The capturing of a thermal neutron by a chlorine atom gives rise to a capture gamma ray. Pulsed neutron tools therefore monitor these capture gamma rays. Thus, the common elements of all commercial pulsed neutron tools are (1) a

[2] Historically the first pulsed neutron tool was the Dresser Atlas Nuclear Lifetime Log (NLL) later to become the PDK-100. Schlumberger’s tool was known as the TDT and Halliburton’s as the TMD Descendents of these pioneering tools now go by such trade names as TDT-P, RPM & CRE.

pulsed neutron generator, and (2) gamma ray detectors at different distances from the neutron generator. A generalized neutron tool is shown in Fig. 11.14.

The cloud of neutrons produced by the initial neutron burst from the generator results in a cloud of thermal neutrons in the vicinity of the tool. This cloud dies away due to capture by chlorine atoms or other neutron absorbers in the formation. If there is plenty of chlorine present (i.e., high water saturation), then the cloud of thermal neutrons disappears quite quickly. If, however, hydrocarbons are present (i.e., low water saturation), then the cloud of thermal neutrons decays much more slowly. The rate of decay is measured by monitoring how many capture gamma rays enter the gamma ray counter(s) as a function of time.

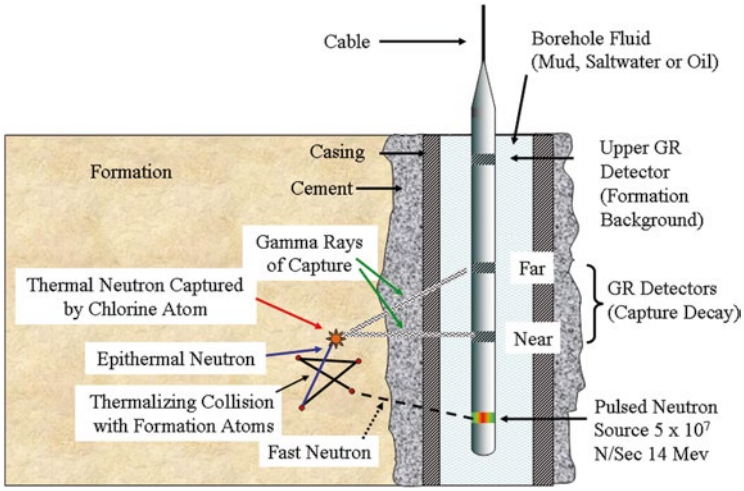

Fig. 11.14 Generalized pulsed neutron tool

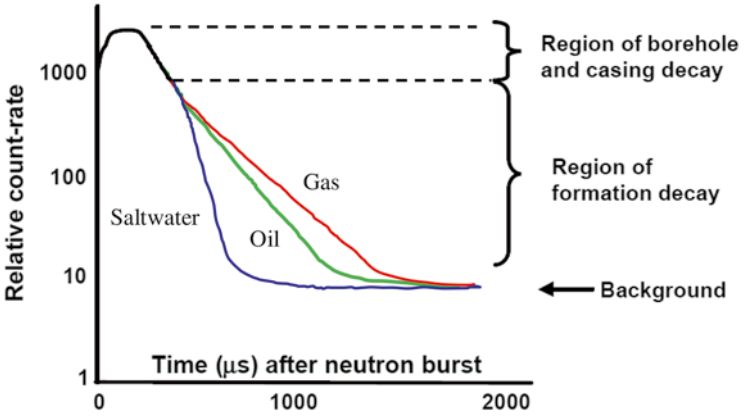

Fig. 11.15 Thermal-neutron decay curves for oil, gas, and water-bearing formations

Figure 11.15 plots the relative counting rate on the *Y*-axis and the time (microseconds) since the initial burst of fast neutrons on the *X*-axis. Note that after a few hundred microseconds a straight-line portion of the decay curve develops. Note also how the water line has a steeper slope than the oil line. Note, too, that at late times the background gamma ray count rate remains substantially constant. The *Y*-axis on Fig. 11.15 is logarithmic, but the time scale (*X*-axis) is linear. Thus, the straight-line portions of the curve represent exponential decays. If N is the number of gamma rays observed at time t and N_o is the number observed at $t=0$, then

$$N = N_o e^{-t/\tau},$$

where τ (Greek letter tau) is the time constant of the decay process. Tau is measured in units of time. It is convenient to quote values of tau in microseconds (1 μs = 10^{-6} s). The capture cross section of the formation, the property of interest, is directly related to tau by the equation

$$\Sigma = 4{,}550 / \tau,$$

where Σ (Greek letter sigma) is the capture cross section measured in capture units (cu). Thus, the essence of measuring Σ is to first find the straight-line portion of the capture gamma ray decay, and then to measure its slope. This is accomplished in different ways by the various commercially available tools.

Log Presentations

On a typical pulsed neutron log, there may be up to nine curves displayed. The curves are illustrated in the Thermal Decay Time (TDT) log presentation of Fig. 11.16

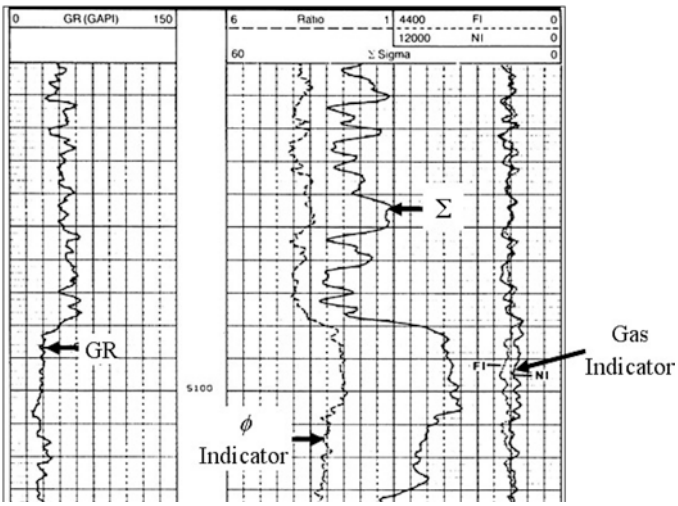

Fig. 11.16 TDT log presentation. Courtesy Schlumberger

Sigma Curve

The Σ curve is the principal pulsed neutron measurement and behaves rather like an open-hole resistivity curve, that is, it deflects to the left (high values of Σ) in wet zones and to the right (low values of Σ) in hydrocarbon-bearing zones or low-porosity formations. Σ values in shales are quite high, tending to mask the effect of hydrocarbons. Thus shaly pay zones can appear to be water-bearing on the first inspection. Figure 11.17 shows a schematic comparison of Σ with resistivity.

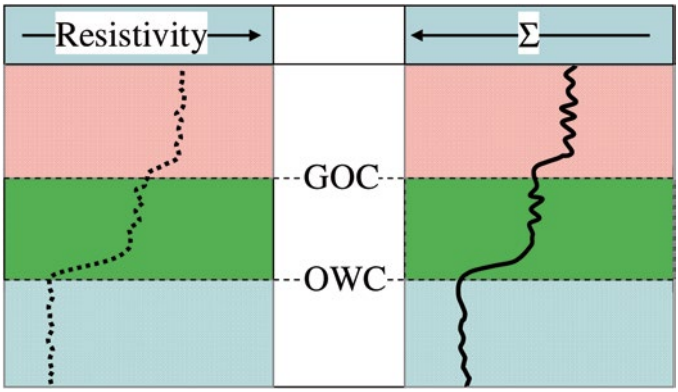

Fig. 11.17 Σ-resistivity comparison

Tau Curve

Tau is just another way of looking at Σ. In fact, τ (the decay-time constant for the thermal-neutron population) is the basic measurement of a pulsed neutron tool. However, all interpretation equations for pulsed neutron logs are linear functions of Σ; and it is much easier to work with Σ rather than with τ. It is recommended that τ be recorded, but left off the log presentation, since its scaled reciprocal, Σ, gives exactly the same information in a form that is easier to work with.

Ratio Curve

The ratio curve is a porosity indicator. It is derived by taking the ratio of the gamma ray counts seen at the near and far detectors respectively. The ratio curve behaves very much like a compensated thermal-neutron (CNL) porosity curve, i.e., it deflects to the right (low ratio) in low porosity, or in the presence of gas. Figure 11.18 shows the ratio curve response to a pocket of gas trapped below a packer behind a tubing nipple. In the absence of any open-hole porosity logs, the ratio can be used in combination with Σ to find formation porosity.

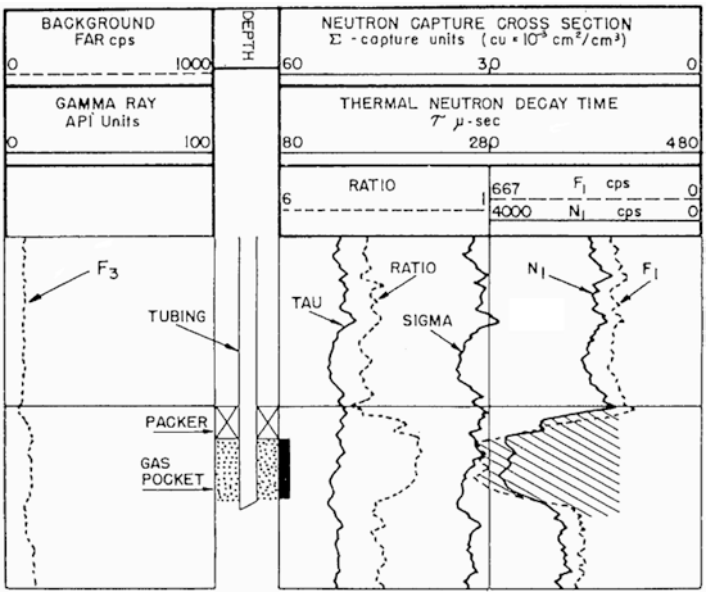

Fig. 11.18 Ratio curve response to gas. Courtesy Schlumberger

Near and Far Count-Rate Display

In Track 3, the near and far count rates are displayed as an overlay. Figure 11.19 illustrates this presentation. When the correct scales are chosen for the near (N_1) and far (F_1) count-rate displays, a useful quick-look log results, with the following properties:

- In 100 % water (section A), $F_1 = N_1$
- In gas (section C), $F_1 > N_1$ (dotted line is left of solid)
- In shales (at the top of the log), $F_1 < N_1$ (dotted line right of solid)

Question # 11.2

Refer to Fig. 11.19

(a) Color code the gas-bearing intervals on the near/far count-rate display using red or pink.
(b) Color code the shale zone at the top of the log green.
(c) Why do you think the oil–water contact is marked where it is (i.e., at 4,535 ft)?
(d) Read the average value of Σ in the water-bearing zone.

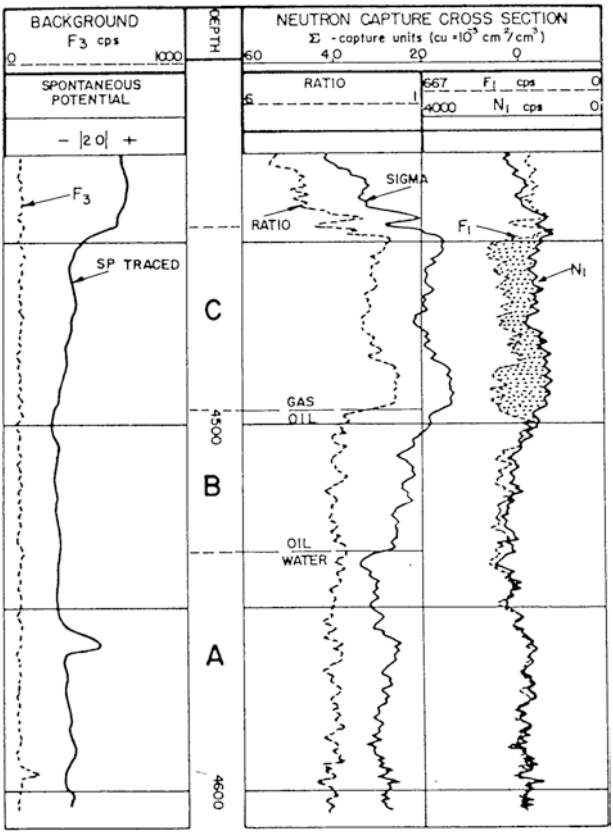

Fig. 11.19 Near/far count-rate display. Courtesy Schlumberger

Background and Quality Curves

The background curve is a very insensitive natural gamma ray curve. There should be little movement on this curve except in "hot" zones which are very radioactive. This curve is sometimes omitted without any great loss.

Summary

The most important curves of the pulsed neutron log are:

Σ	for water saturation
Ratio	for porosity
GR	for shale content
Near/Far display	for gas indications

Capture Cross Sections

The capture cross section of a formation depends on the elements that make up the formation and their relative abundance. Σ values vary over a wide range. The capture cross sections for thermal neutrons are listed in Table 11.1 for a number of elements and in Table 11.2 for various compounds found in rocks.

Table 11.1 Capture cross sections of elements

Element	Σ (cu)
Common elements	
Chlorine	570
Hydrogen	200
Nitrogen	83
Potassium	32
Iron	28
Sodium	14
Sulfur	9.8
Calcium	6.6
Aluminum	5.4
Phosphorus	3.9
Silicon	3.4
Magnesium	1.7
Carbon	0.16
Oxygen	0.01
Rare elements	
Boron	45,000
Cadmium	18,000
Lithium	6,200
Mercury	1,100
Manganese	150

Table 11.2 Capture cross sections of compounds

Compound	Element	Σ (cu)
Basic minerals		
Quartz	SiO_2	4.2
Calcite	$CaCo_3$	7.3
Dolomite	$CaCo_3\ MgCo_3$	4.8
Feldspars		
Albite	$NaAlSi_3o_8$	7.6
Anorthite	$CaAlSi_2O_8$	7.4
Orthoclase	$KAlSi_3o_8$	15
Evaporites		
Anhydrite	$CaSO_4$	13
Gypsum	$CaSO_4 \cdot H_2O$	19
Halite	NaCl	770
Sylvite	KCl	580
Carnallite	$KCl \cdot MgCl_2 \cdot 6H_2O$	370
Borax	$Na_2B_4O_7 \cdot 10H_2O$	9,000
Kernite	$Na_2B_4O_7 \cdot 4H_2O$	10,500
Iron-bearing minerals		
Goethite	FeO(OH)	89
Hematite	Fe_2O_3	104
Magnetite	Fe_3O_4	107
Limonite	$FeO(OH) \cdot 3H_2O$	80
Pyrite	FeS_2	90
Siderite	$FeCO_3$	52
Miscellaneous clays and micas		
Glauconite		22 + 5
Chlorite		25 + 5
Mica/biotite		35 + 10
Pyrolusite	MnO_2	440
Manganite	MnO(OH)	400
Cinnabar	HgS	7,800
Shales		35–55

Basic Interpretation

Clean Formations

Practical interpretation of pulsed neutron logs is conceptually very simple. The total formation capture cross section, Σ, recorded on the log, is just the sum of the products of the volume fractions found in the formation and their respective capture cross sections. Thus, in its simplest form,

$$\Sigma_{\text{Log}} = \Sigma_{\text{matrix}} \cdot (1-\phi) + \Sigma_{\text{fluid}} \cdot \phi$$

Figure 11.20 should clarify the mathematical relationship.

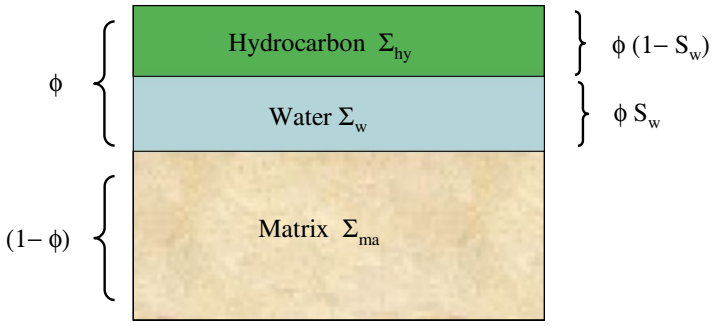

Fig. 11.20 Components of $\boldsymbol{\Sigma}_{Log}$

Of course, the "fluid" may, in fact, be a mixture of oil and water, in which case, the log response is described by:

$$\Sigma_{Log} = \Sigma_{ma}\left(1-\phi\right)+\Sigma_{w}\phi S_{w}+\Sigma_{hy}\phi\left(1-S_{w}\right).$$

By rearrangement of the equation, we have:

$$S_{w}=\frac{\left(\Sigma_{Log}-\Sigma_{ma}\right)-\phi\left(\Sigma_{hy}-\Sigma_{ma}\right)}{\phi\left(\Sigma_{w}-\Sigma_{hy}\right)}$$

Question #11.3
Given: $\Sigma_{Log} = 25.3$ cu.
$\Sigma_{ma} = 10.0$ cu.
$\Sigma_{hy} = 22$ cu.
$\Sigma_{w} = 100$ cu.
$\phi = 30$ %.
Find $S_w =$ _____ .

In the previous example, the values for Σ_{ma}, Σ_{log}, and Σ_w were given. However, in practice, these values may not be known. As a guide, Table 11.3 gives values of Σ for commonly found materials. More exact methods for finding Σ_{ma}, Σ_w, and Σ_{hy} will be covered later in the text.

Log interpretation in clean formations is straightforward. The linear equations can also be thought of graphically. If, for example, a crossplot is made of Σ (on the *Y*-axis) and ϕ, (on the *X*-axis), straight lines represent mixtures of pairs of components.

Table 11.3 Σ values for log interpretation

Σ	Material	Sigma (Cu)
Matrix	Sand	8–10
	Limestone	12
	Dolomite	8
Hydrocarbon	Oil (function of R_s)	22
	Gas (function of γ_g, P, T)	8
Water	Fresh	23
	Seawater	34
	Brine	122

Figure 11.21 shows this method. Note that all water-bearing points fall on the line joining the matrix (porosity = 0, Σ = 10) to the water (porosity = 100, Σ = 100). Likewise, all 100 % oil-bearing points lie on the line joining the matrix to the oil (porosity = 100, Σ = 22). Thus, all points lie inside a solution triangle covered by the matrix, water, and oil points. By simple constructions, lines of constant S_w can be drawn. The dashed lines on Fig. 11.21 join at the point given in Question #11.3, ($\phi = 30$ %, $\Sigma_{Log} = 25.3$).

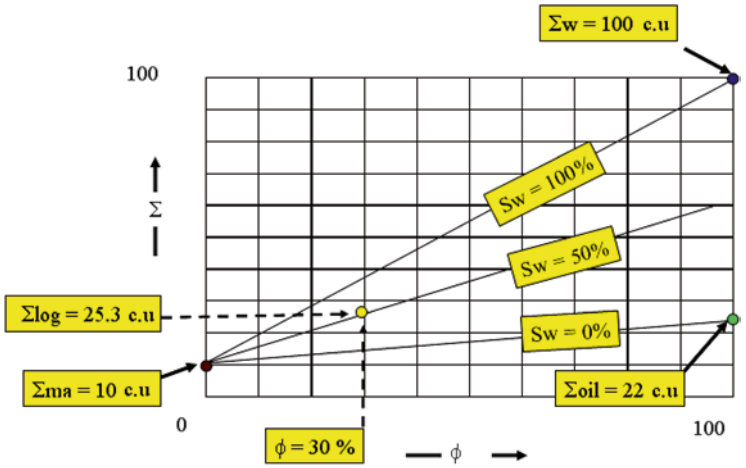

Fig. 11.21 Interpretation in clean formations

How much confidence can be placed in the value of S_w derived as in Fig. 11.21? To a large extent, the accuracy depends on the difference between Σ_{hy} and Σ_w. In fresh formation waters (low Σ_w), the interpretation will be very questionable; but in very salty formation waters (high S_w), it will be reliable. Figure 11.22 illustrates this concept.

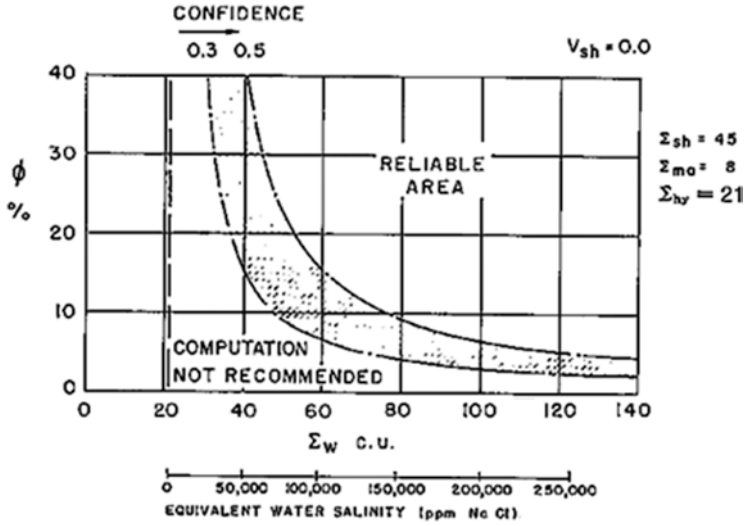

Fig. 11.22 Reliability of S_w Calculation in clean formations. Courtesy Schlumberger

Question #11.4
Color the "reliable" area of Fig. 11.22 with a yellow highlighter
Do the conditions in your district fall in the "reliable" area?

Shaly Formations

The addition of shale to the formation can be handled in the same linear fashion as before. That is:

$$\Sigma_{\text{Log}} = \Sigma_{\text{ma}} \cdot \left(1 - V_{\text{sh}} - \phi\right) + \Sigma_{\text{sh}} V_{\text{sh}} + \Sigma_{\text{w}} \phi S_{\text{w}} + \Sigma_{\text{hy}} \phi \left(1 - S_{\text{w}}\right)$$

which gives:

$$S_{\text{w}} = \frac{\left(\Sigma_{\text{log}} - \Sigma_{\text{ma}}\right) - \phi\left(\Sigma_{\text{hy}} - \Sigma_{\text{ma}}\right) - V_{\text{sh}}\left(\Sigma_{\text{sh}} - \Sigma_{\text{ma}}\right)}{\phi\left(\Sigma_{\text{w}} - \Sigma_{\text{hy}}\right)}$$

Figure 11.23 illustrates the shaly formation. Note that the solution for S_w requires a value for ϕ. In most practical cases, the porosity device used will also be affected by the presence of shale. For example, if a CNL is used as the porosity device, its reading will have to be corrected using:

$$\phi = \phi N - V_{\text{sh}} \cdot \phi N_{\text{sh}},$$

where ϕN is the log reading, V_{sh} is the shale volume % (from GR, etc.), and ϕN_{sh} is the response of the CNL in 100 % shale.

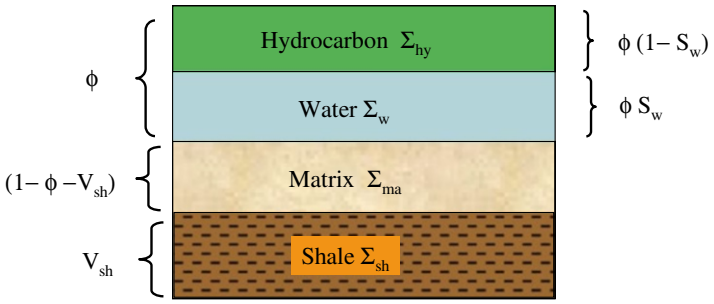

Fig. 11.23 Shaly formation schematic

Question #11.5. Shaly Formation
Given: $\Sigma_{Log} = 30.0$ cu.
$\Sigma_{ma} = 10$ cu.
$\Sigma_{hy} = 22$ cu.
$\Sigma_{w} = 100$ cu.
$\phi N = 37$ %.
$\phi N_{sh} = 35$ %.
$V_{sh} = 20$ %.
$\Sigma_{sh} = 35$ cu.

Find:
(a) $\phi =$ _____ .
(b) $S_w =$ _____ .
(c) $S_w =$ _____ , if you had assumed this was clean instead of a shaly formation.

Note that the equation for Σ_{Log} in shaly formations could be rearranged to read:

$$\Sigma_{Log} = \underbrace{\Sigma_{ma}(1-\phi) + \Sigma_{w}\phi S_{w} + \Sigma_{hy}\phi(1-S_{w}) + V_{sh}(\Sigma_{sh} - \Sigma_{ma})}_{\text{Clean component}} + \underbrace{V_{sh}(\Sigma_{sh} - \Sigma_{ma})}_{\text{Shale component}}$$

Thus, an equally valid method of computing S_w would be to correct Σ_{Log} for shale using the relationship:

$$\Sigma_{cor} = \Sigma_{Log} - V_{sh}(\Sigma_{sh} - \Sigma_{ma}).$$

The value Σ_{cor} can then be used in the normal equation for estimation of water saturation in clean formations. Needless to say, the accuracy of S_w results in shaly formations will be reduced due to uncertainties about the exact values of ϕ, V_{sh}, and Σ_{sh}.

Finding Interpretation Parameters

In order to perform a quantitative interpretation of a pulsed neutron log, certain parameters need to be known. These are:

Σ matrix
Σ water
Σ hydrocarbon (oil and/or gas)
Σ shale

We will now explore various methods of finding these parameters.

Sigma Water

Σ_w is a simple function of the water salinity (ppm NaCl) and temperature (see Fig. 11.24). If the salinity is not known, then a 100 % water-bearing section can give us the required data. Note that if $S_w = 100$, the basic equation reduces to:

$$\Sigma_{Log} = \Sigma_{ma}(1-\phi) + \Sigma_w \phi,$$

which can be rewritten to give:

$$\Sigma_w = \frac{\Sigma_{log} - \Sigma_{ma}(1-\phi)}{\phi}$$

Thus, provided Σ_{ma} and ϕ are known, Σ_w can be back calculated directly. Note that this method is similar to the R_{wa} technique used with open-hole logs. For that reason, the derived value of Σ_w is referred to as Σ_{wa} or *sigma water apparent*. If an extensive water-bearing interval has been logged, a graphical method can provide a "double whammy," both Σ_{ma} and Σ_w from one plot. If pairs of values of Σ and ϕ are plotted on a graph such as the one given in Fig. 11.25, all points at $S_w = 100\,\%$ will fall on a straight line connecting Σ_{ma} (at $\phi = 0\,\%$) and Σ_w (at $\phi = 100\,\%$).

Question #11.6. Σ_w
Given: Formation water salinity = 230,000 ppm NaCl.
Temperature = 200 °F.
Find Σ_w = _____ cu.

Question #11.7. Σ_w
Plot Σ vs. ϕ for the following log readings:

Level	Σ (cu)	ϕ (%)
1	17	28
2	21	32
3	23	26
4	27	28
5	21	13

Level	Σ (cu)	ϕ (%)
6	24	20
7	34	34
8	28	26
9	26	23
10	29	27

Now draw in the $S_w = 100$ % line and find:

(a) $\Sigma_{ma} =$ _____ cu

(b) $\Sigma_w =$ _____ cu

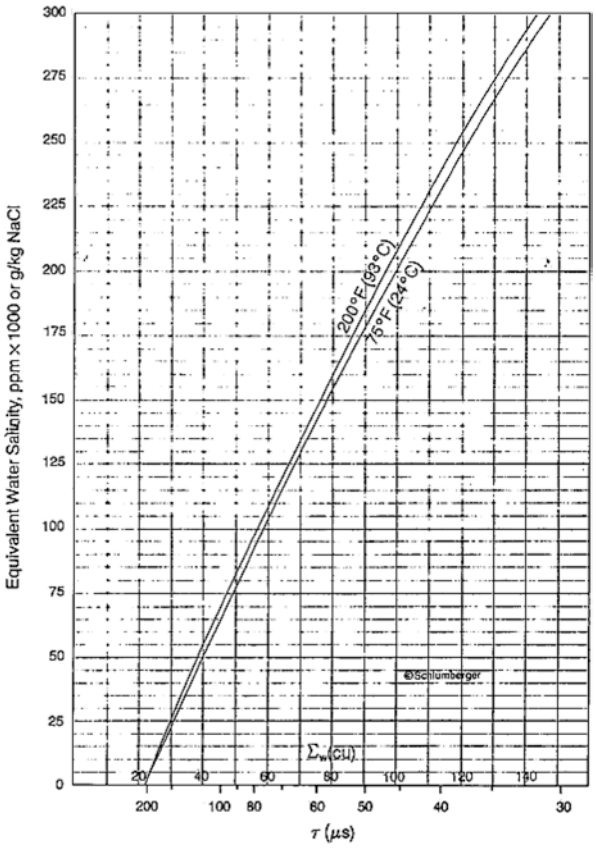

Fig. 11.24 Σ_w as a function of salinity and temperature. Courtesy Schlumberger

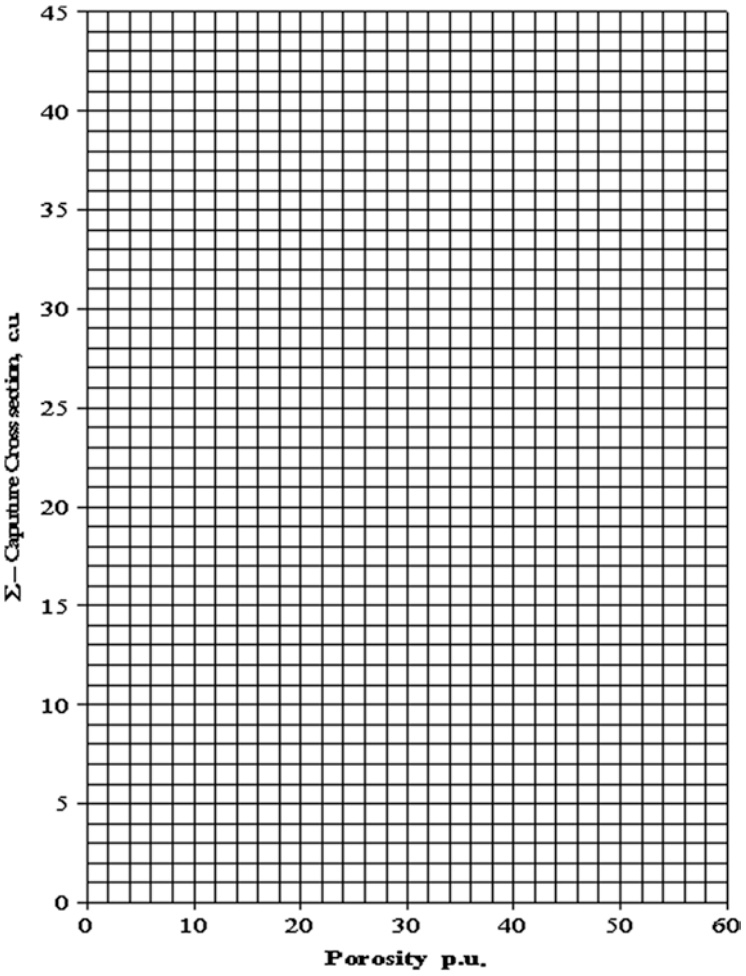

Fig. 11.25 Σ vs. ϕ Crossplot for determination of Σ_{ma} and Σ_{w}.

Sigma Oil

Σ_o is a function of the solution GOR (R_s) of the liquid hydrocarbon in question. Light, gassy oils tend to have lower values of Σ_o. Dead, heavy oils have a minimum Σ_o of about 22 cu. Figure 11.26 shows Σ_o as a function of R_s.

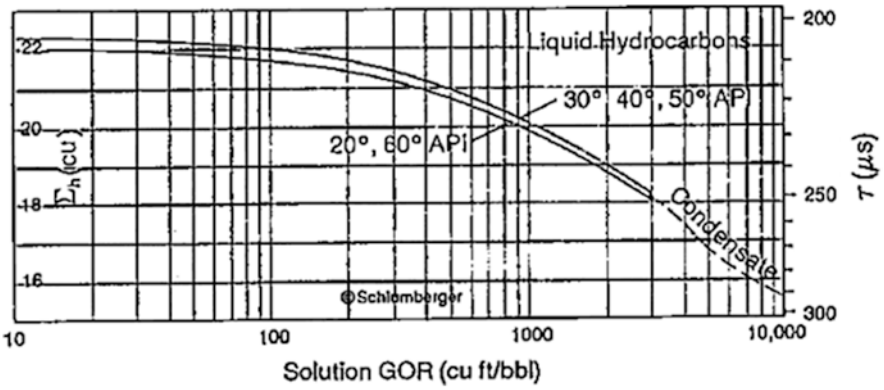

Fig. 11.26 Finding Σ_o. Courtesy Schlumberger

Question #11.8. Σ_o

An oil has a specific gravity of 40° API and an R_s of 400 cu ft/bbl.

Find Σ_o = cu

Sigma Gas

Σ_g is a function of pressure, temperature, and gas gravity. Figures 11.27 and 11.28 allow calculation of Σ_g for a variety of formation conditions. Figure 11.27 finds Σ methane. If the gas in question is methane, then no further work is required. However, if the gas in question is heavier than methane, Fig. 11.28 will convert Σ-CH4 into the appropriate value for Σ gas.

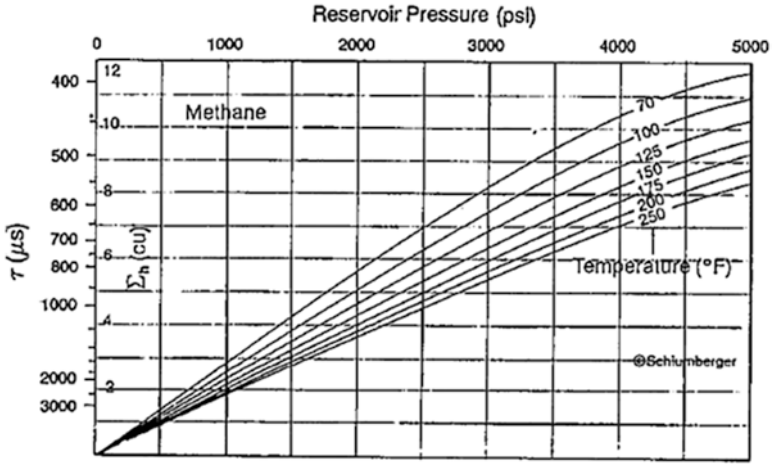

Fig. 11.27 Finding Σ methane. Courtesy Schlumberger

Question #11.9. Σ_g
Given: $p = 3{,}000$ psi.
$T = 150$ °F.
$\gamma_g = 0.65$.
Find $\Sigma_g =$ _____ cu

Sigma Shale

Σ_{sh} may be found by simple inspection of the log. Look for places where:

Gamma reads high
Near/far display indicates shale
Σ_{Log} is relatively high

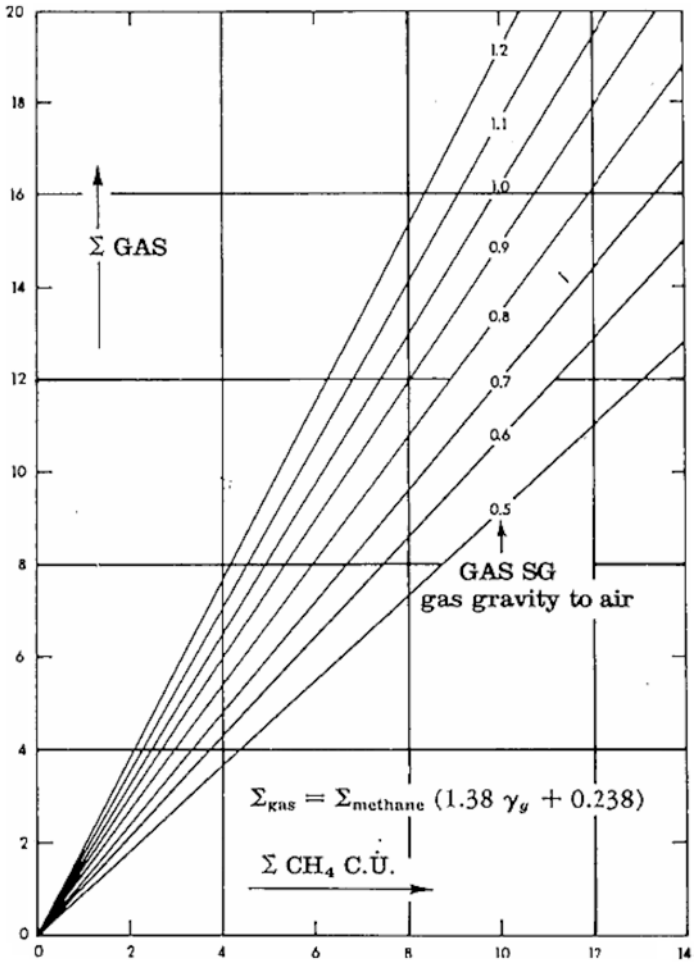

Fig. 11.28 Conversion of Σ methane to Σ gas

Sigma-Ratio Crossplot

If no open-hole logs are available one essential piece of information will be missing, namely, the porosity. Fortunately there is a method for finding porosity from pulsed neutron logs. It requires only the value of sigma and ratio, read directly from the log. These two readings are then cross-plotted to give porosity. A side benefit is that the plot also gives values of Σ_{wa}, the apparent capture cross section of the water. Figure 11.29 gives an example of this type of chart.

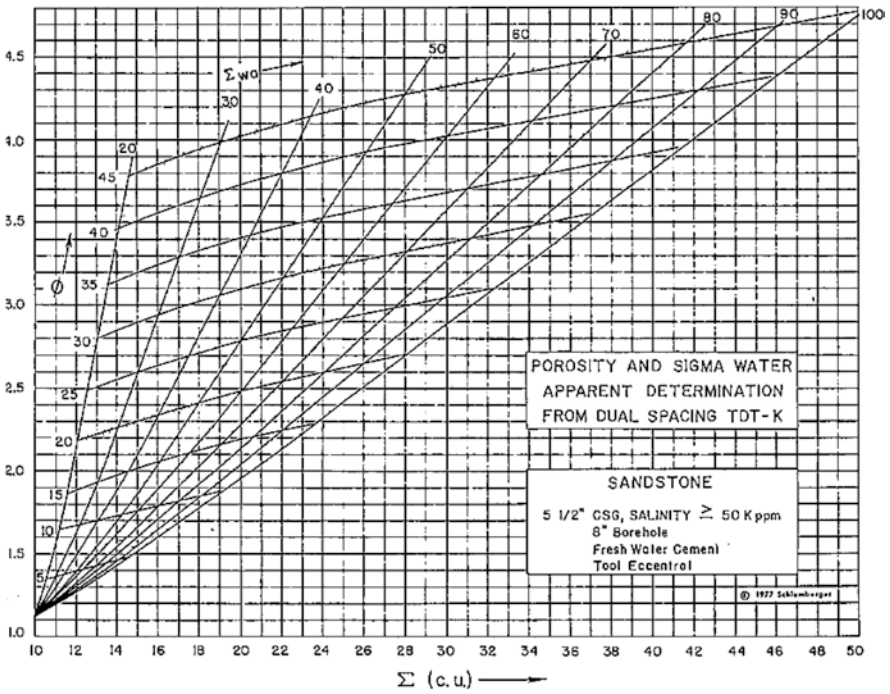

Fig. 11.29 Determination of ϕ and Σ_{wa} from Σ and ratio

It should be noted that many different charts are available form service companies that cover a multitude of different casing sizes and formation water salinities. The particular chart used here for illustrative purposes was built for 5½″ casing and water salinity >50 Kppm NaCl.

Question #11.10. Σ–Ratio Crossplot

A log is run in 5½″ casing with an 8–5/8″ open-hole. The borehole fluid salinity is 80,000 ppm NaCl; $\Sigma_{Log} = 20$ cu and the ratio = 2.8.

(a) Find $\phi =$ _____ %
(b) Find $\Sigma_{wa} =$ _____ cu

Reservoir Monitoring Time-Lapse Technique

Pulsed neutron logs are useful for monitoring the depletion of a reservoir. The *time-lapse* method is used. A base log is run in the well shortly after initial completion but before substantial depletion of the producing horizons. A few days, weeks, or even months of production are required to clean up near well bore effects of the drilling operation, such as mud-filtrate invasion, etc. Once a base log is obtained, the well may be re-logged at time intervals over the life of the field. Typically, a log will be run every six months or once a year, depending on production rate. Successive logs may be overlaid so that changes in saturation can be easily spotted by changes in sigma. A good example of this is given by Fig. 11.30, which shows a base log and three additional logs at roughly 6-month intervals.

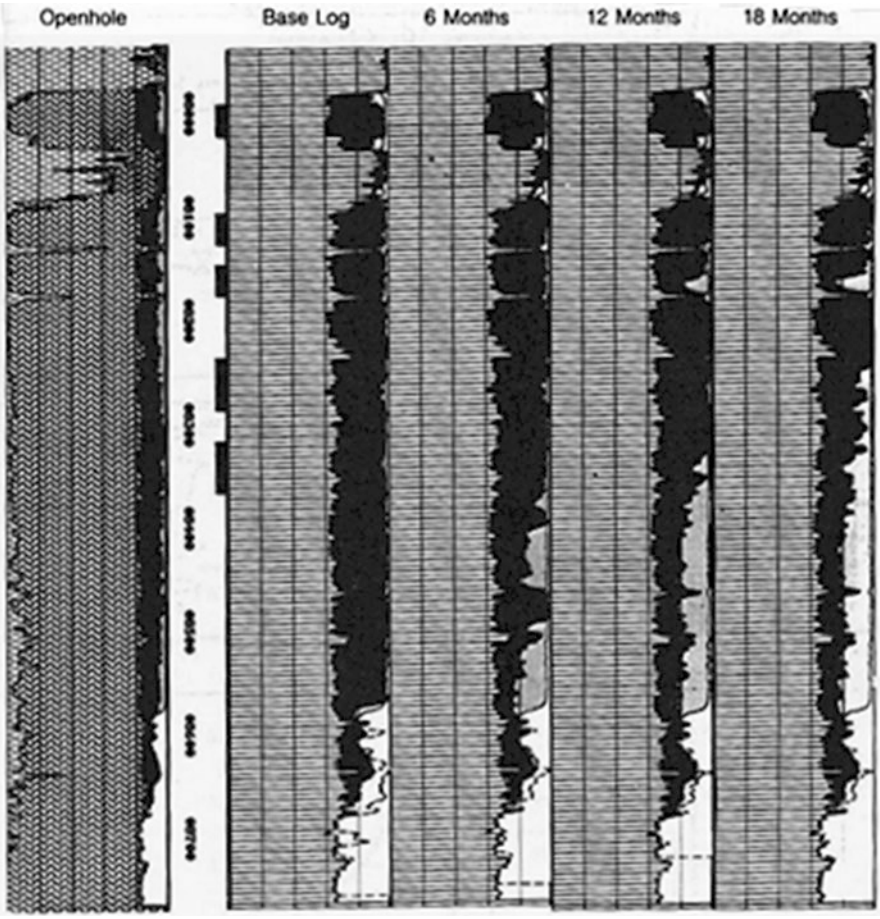

Fig. 11.30 Time-lapse logging

Note the rapid rise of the oil–water contact(s) with passage of time. It is simple to calculate changes in S_w. Consider the state of affairs at time t_1:

$$S_{w1} = \frac{\left(\Sigma_1 - \Sigma_{ma}\right) - \phi\left(\Sigma_{hy} - \Sigma_{ma}\right)}{\phi\left(\Sigma_w - \Sigma_{hy}\right)}$$

and some time later at time t_2:

$$S_{w2} = \frac{\left(\Sigma_2 - \Sigma_{ma}\right) - \phi\left(\Sigma_{hy} - \Sigma_{ma}\right)}{\phi\left(\Sigma_w - \Sigma_{hy}\right)}$$

The change is S_w is, therefore,

$$\Delta S_w = S_{w1} - S_{w2} = \frac{\left(\Sigma_1 - \Sigma_2\right)}{\phi\left(\Sigma_w - \Sigma_{hy}\right)} = \frac{\Delta\Sigma}{\phi\Delta\Sigma_{fluids}}$$

Log-Inject-Log

The log-inject-log technique is used to find residual oil saturations. A base log is run and then the formation is injected with brine and logged again. Finally, the formation is injected with fresh water and logged a third time (see Fig. 11.31).

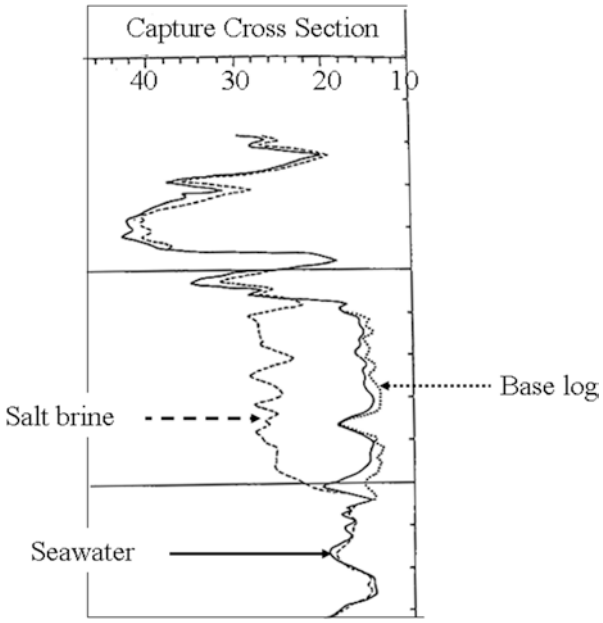

Fig. 11.31 Log-inject-log

Provided the capture cross section of the fresh and brine flushes are known, all the unknown quantities may be normalized out and the residual oil saturation found using:

$$S_o = 1 - \frac{\Sigma_{\text{log brine}} - \Sigma_{\text{log fresh}}}{\phi\left(\Sigma_{\text{brine}} - \Sigma_{\text{fresh}}\right)}$$

Note that it is not necessary to know either Σ_{ma} or Σ_o. The technique has many variations, some of which use specially chlorinated oil that has a high capture cross section.

Departure Curves

Ideally, pulsed neutron logs should be usable for quantitative interpretation without having to make any corrections to the values read from the log. However, in some cases (e.g., when a base log is run with a fresh completion fluid and a subsequent log is run with a salty completion fluid in the borehole, or if the base log is run *without* a liner and a subsequent log *with* a liner), corrections will be required to the raw log measurement of sigma before quantitative interpretation can be made. The required corrections are a function of three variables: casing size, hole size, and salinity of the borehole fluid.

Many sets of departure curves are published by the service companies for their specific tools as functions of open-hole size and casing size. Considerable controversy exists in the literature regarding the need for departure curves. One school of thought holds that the diffusion of neutrons from the borehole to the formation necessitates the use of departure curves. Others maintain that proper tool design and the associated gating systems used to calculate Σ eliminate the need for corrections since they are supposedly free of diffusion effects and the need for departure curves. Some pulsed neutron tool design call for a "dual burst" of neutrons. The decay of the neutron population in the borehole is monitored by a first burst and a second burst is used to monitor the decay in the formation proper.

Essentially pulsed neutron tool design is a delicate balancing act. On the one hand technological advances need to be incorporated in succeeding generations of any given service company's tool. When better gamma ray detectors become available allowing for greater sensitivity, higher count rates, and lower "dead" times then they are incorporated. When additional detectors, above and beyond the basic two conventionally used, then the door is opened for more sophisticated data analysis and better estimates of the true formation Σ, free from the disturbing effect of the borehole Σ. Where the log user is monitoring changes in Σ over time periods longer than tool development cycles sometimes the tool design changes may complicate legitimate log comparisons between today's version of what formation Σ is and what it was 10, 15, or 20 years ago as logged by an older version of the tool which was less technically equipped to unravel the effects of neutron diffusion, etc. As a result multi-detector tools are now emerging on the market (Zett et al. 2012a, b; Bertoli et al. 2013) as well as tools equipped with neutron detectors rather than gamma ray detectors which aim to directly measure the rate of decay of a pulsed package of fast neutrons (Arbuzov et al. 2012).

Depth of Investigation

Another item of interest is the depth of investigation of the pulsed neutron tool. As with most radioactivity measurements, there is no fixed depth of investigation. Rather, a geometric factor describes what percentage of the total signal comes from what radial distance from the borehole wall. Figure 11.32 shows the response of the TDT-K in 5½″ casing with a 1-in. cement sheath. Note that "depth of investigation" is somewhat deeper if salt water has invaded the formation. At all events, the majority of the signal comes from within one foot of the borehole wall.

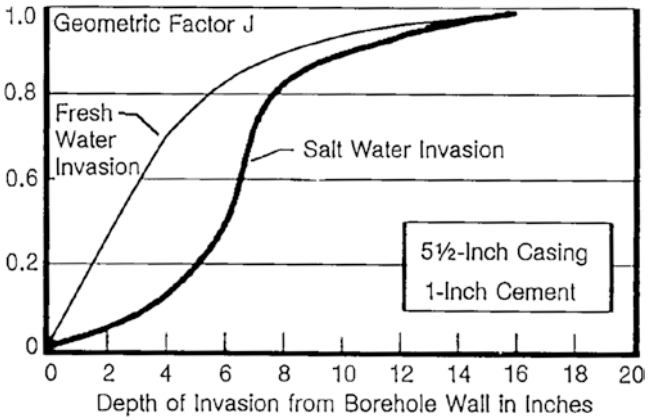

Fig. 11.32 Depth of investigation of typical pulsed neutron measurement

Inelastic Gamma Ray Logging

Neutron logging is continually evolving to reap evermore information about the formations surrounding the tools. Modern versions are used for what is termed elemental spectral analysis. This takes advantage of what are known as inelastic collisions between fast neutrons and the nuclei of the atoms that make up the chemical compounds found in the formation surrounding the cased borehole. When a fast neutron strikes a magnesium nucleus, for example, the nucleus is excited to a higher energy level and then returns to a lower energy level by emitting a gamma ray of characteristic energy. It turns out that the energy of the gamma ray emitted as a result of this inelastic collision can be classified as having come from a magnesium nucleus. Figure 11.33 gives a schematic of a generic neutron logging tool. Note that two annular volumes are depicted surrounding the tool. In the immediate vicinity of the tool is the region where the inelastic interactions take place. Further out radially note that there is a second annular volume of the formation from which gamma rays resulting from capture of thermalized neutrons emanate.

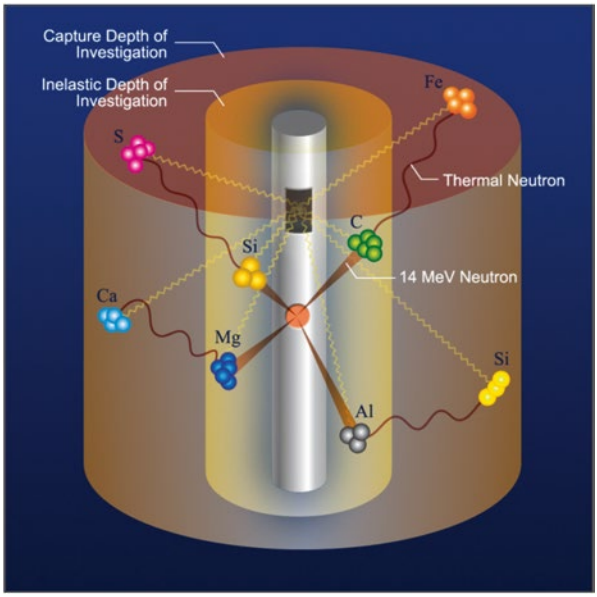

Fig. 11.33 Generic neutron logging tool. Courtesy Baker Hughes

In the figure note that fast neutrons are shown to be inelastically scattered by the nuclei of four elements, Mg, Al, C, and Si. The neutrons thus scattered then are seen to travel outwards to the second annular zone, further from the tool, where, once they are slowed down to thermal energies become captured respectively by atoms of Ca, Si, Fe, and S. The detectors in the tool gather the incoming gamma ray and perform spectroscopic analysis in order to "finger print" the elements present.

Carbon/Oxygen Logging

Initially inelastic neutron scattering was widely used to determine the ratio of carbon to oxygen in the formation surrounding a cased borehole. The underlying principle of the method was the assumption that carbon atoms were to be found in hydrocarbon molecules (e.g., gas and/or oil, C_nH_{2n+2}) and oxygen atoms found in water (H_2O). Thus, depending on the porosity, the C/O ratio would be an indicator of formation water saturation, S_w.

Figure 11.34 shows a typical "fan chart" relating the measured C/O ratio to $S_{w.}$ Note that there are two "fans" with one labeled "Sandstone" and the other "Limestone". The reason for this is the ambiguity of any given value for the C/O ratio. If the formation matrix is free of any carbon then, for example, a C/O ratio of 0.14 coupled with a formation porosity of 27.5 % would indicate a water saturation of zero. However the same log reading and porosity would indicate 100 % water if the matrix were limestone. This characteristic of C/O logs need not be fatal provided the logging is performed where the matrix elemental composition is known and/or the device is used to solely to monitor oil/water or gas/oil contact changes over time by performing repeat logs over the productive life of the reservoir.

C/O Logging for TOC

With the increased interest in characterizing the organic richness of shale gas reservoirs the C/O log has had a revival in that it affords and way to estimate the value of the all important TOC number. If the oxygen content of the formation is known then the carbon content can be calculated using:

$$C = C/O \times O$$

In turn the oxygen content of the formation can be calculated using:

$$O_{\text{formation}} = O_{\text{matrix}} + O_{\text{fluid}}$$

O_{matrix} will depend on the matrix material but surprisingly it does not vary very much as is shown in Table 11.4. For most commonly occurring organic rich shales the oxygen content lies in the range of 48–53 %.

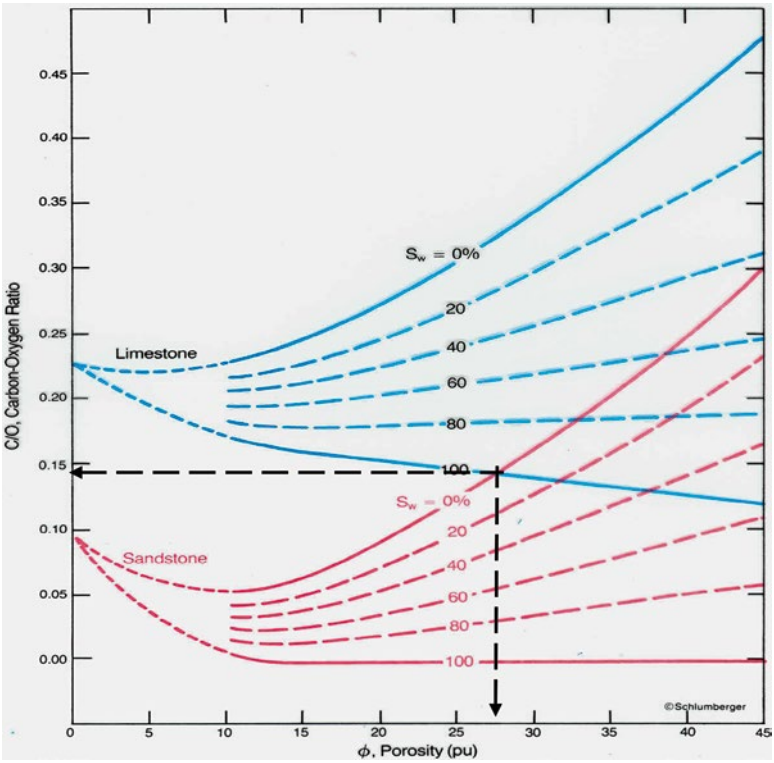

Fig. 11.34 Ambiguous C/O interpretation. Courtesy Schlumberger

O_{fluid} is based on an assumption that the fluid is water in which case it is equal to 89 %. Based on these assumptions, the formation oxygen content be calculated as follows:

$$O_{\text{formation}} = 0.89 \times \phi \times \rho_{\text{fluid}} + 0.53 \times (1 - \phi) \times \rho_{\text{matrix}}$$

For a C/O ratio of 0.1 even as ρ_{matrix} varies from 2.4 g/cc to 3 g/cc the calculated total carbon decreases by less than 0.1 wt% so the choice of ρ_{matrix} is very forgiving and one is justified in leaving it at 2.65 for a first approximation.

The oxygen content organic material (gas, oil, kerogen, etc.) is zero. Thus the formation oxygen content will also depend on the water saturation within the pore space available.

Table 11.4 Oxygen content of matrix materials (After Herron)

Mineral	Wt % O
Siderite	41
Orthoclase	46
Anorthite	47
Calcite	48
Albite	49
Illite	51
Dolomite	52
Quartz	53
Kaolinite	56
Gypsum	56
Montmorillonite	59

Total Carbon content of the formation is thus derived from the C/O ratio read from the log and an estimate of the formation oxygen content. However the carbon present in the formation may be in the form of organic carbon but could also be present in the form of carbonates such as calcite and dolomite. An independent measurement is thus required to "back out" the effect of any carbonate present. For this the same wireline inelastic gamma ray tool can be used to measure the calcium content of the formation and from there calculate the TOC as:

$$\text{TOC} = C_{\text{Total}} - C_{\text{Carbonates}}$$

An example calculation:

Porosity is 10 %, therefore,

$$O_{\text{formation}} = 0.89 \times 0.1 \times 1 + 0.53 \times 0.9 \times 2.65 = 1.35$$

And if the C/O ratio is 0.1 then,

$$C_{\text{total}} = 0.1 \times 1.35 = 0.135$$

If the carbon content of the formation due to carbonates is 10 % then the TOC would be given by:

$$\text{TOC} = 0.135 - 0.1 = 0.035 \text{ or } 3.5\%$$

Cased-Hole Wireline Formation Tester

Wireline formation testers are routinely used in open hole before casing is set in order to evaluate the formation pressure, permeability, and fluid content. The technology developed for such testing is also applicable to cased holes with some modifications. Essentially a standard tool is adapted to include the means to make a hole through the casing and cement and a way to seal such a hole when the test is complete. One embodiment of such a testing tool is shown in Fig. 11.35.

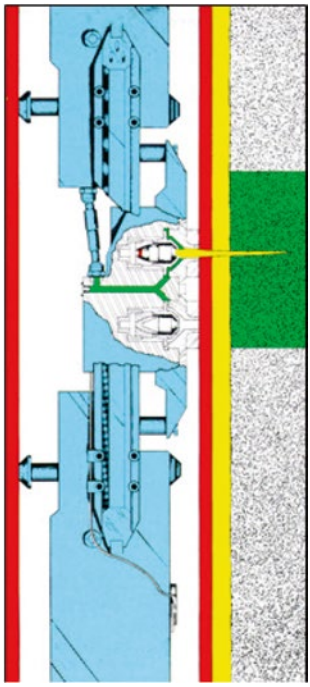

Fig. 11.35 Cased-hole wireline formation tester

The hole making part can be accomplished by either a motorized drill or by an explosive shaped charge. Once communication is established between the tool's plumbing and the formation beyond the casing and cement the actual testing is analogous to that performed in an open-hole test. Sealing of the hole is accomplished by injection of an appropriate epoxy sealer or similar substance. Application for these kinds of tools can be found in work-over situations where there is a lack of data in the well files and there is uncertainty regarding the current formation fluid content and pressure.

Appendix 1: Interpretation of Pulsed Neutron Logs Using the Dual-Water Method

The dual-water method of interpreting pulsed neutron logs is based on the assumption that shales are composed of dry clay, crystalline minerals to whose surface is bound a layer of water. This water is called *bound water*. A further assumption is that the properties of bound water (e.g., R_w, Σ_w) may be different from those of *free water* that exists in the effective, interconnected pore space. In particular, the theory of dual-water interpretation proposes that bound water is less saline than free water in most cases. Correct interpretation, therefore, calls for a means to find the amount of (1) dry clay and (2) bound water. The concept of *total porosity* ϕ_T, that is, the free fluids, ϕ_e, and the bound water, is an important part of the theory. Figure 11.36 illustrates the concepts by mapping bulk volume fractions of a shaly formation.

The following relationships pertain:

$$\phi_e = \phi_T - V_{wb}.$$

$$S_{wT} = \left(V_{wf} + V_{wb}\right) / \phi_T.$$

$$S_{we} = V_{wf} / \phi_e.$$

$$V_{sh} = V_{wb} + V_{dc}.$$

Essentially, there are five unknown quantities: $V_{ma}, V_{dc}, V_{wb}, V_{wf}$, and V_{hy}. The logs available are Σ, ratio, and GR. The identity:

$$V_{ma} + V_{dc} + V_{wb} + V_{wf} + V_{hy} = 1$$

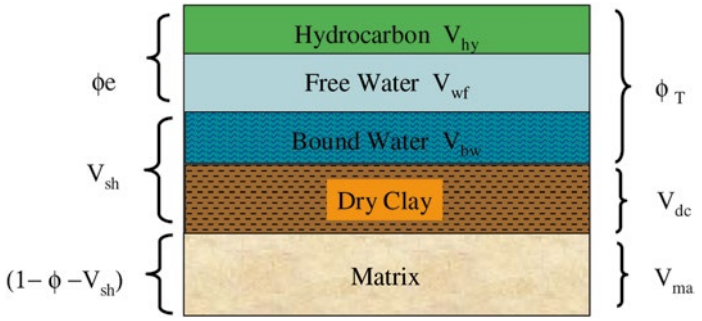

Fig. 11.36 Dual-water shaly formation

adds one more for a total of four measurements. Therefore, one unknown must be eliminated before a solution can be found. The normal way of doing this is to make an assumption about V_{wb} as a function of V_{dc}. That is, to assume that a unit volume of dry clay always has associated with it the same amount of bound water. In fact, in "pure shale," it would be quite common to find a "total porosity" of 30 or 40 % (as reflected by neutron log readings in shales). In this case, the amount of bound water associated with a dry clay can be back calculated.

For example, if a 100 % shale has a total porosity of 35 %, it follows that:

$$V_{wb} = 35\% \text{ and } V_{dc} = 65\%$$

and hence that:

$$V_{wb} = \alpha \cdot V_{dc},$$

where α is some constant which, in this example, is numerically equal to $35/65 = 0.538$. Having reduced the unknowns to four (V_{ma}, V_{dc}, V_{wf}, and V_{hy}), since V_{wb} can now be assumed equal to $\alpha \cdot V_{dc}$, the solution to the dual-water problem becomes straightforward.

The following steps are required:

1. Find all necessary parameters Σ_{ma}, Σ_{dc}, Σ_{wf}, Σ_{hy}, GR_{ma}, GR_{dc}.
2. Find ϕ_T and V_{dc}.
3. Solve for ϕ_e and S_{we}.

Finding Parameters

Crossplot techniques are particularly useful for finding the required parameters. The log data points should be divided into two groups: The 100 % shales and the clean-formation intervals. In clean formations, a plot of Σ vs. ϕ will define Σ_{ma} and Σ_{wf}, provided there is sufficient variation in porosity and enough points at 100 % water saturation. Figure 11.37 shows the procedure schematically.

A similar plot for finding Σ_{dc} and Σ_{wb} is shown in Fig. 11.38 (all points must come from the shale sections). Note that, on both plots, ϕ_T, derived from the Σ vs. ratio crossplot, is used. This entails an assumption that porosity measured in this way is, in fact, equal to total porosity.

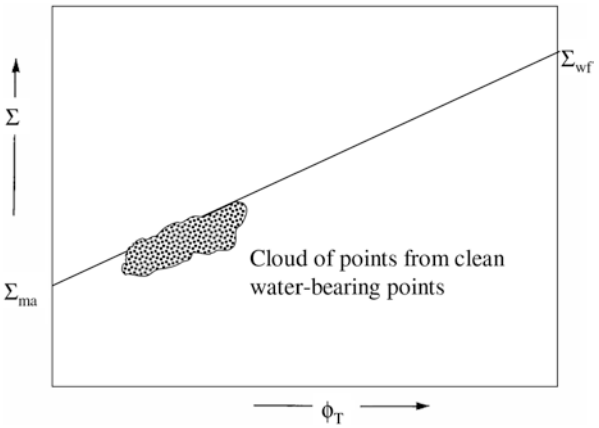

Fig. 11.37 Finding Σ_{ma} and Σ_{wf}.

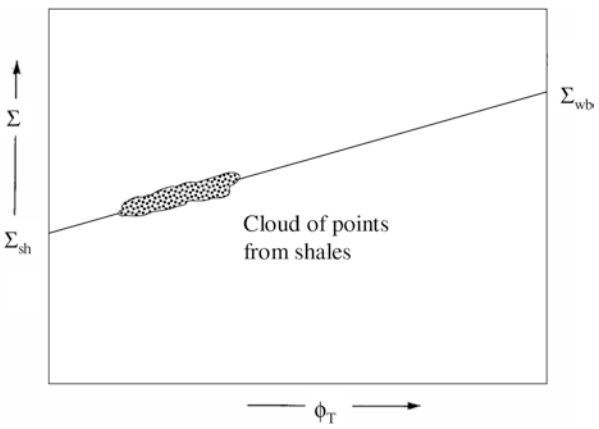

Fig. 11.38 Finding Σ_{dc} and Σ_{sb}

Σ_{hy} can be found by conventional means. Thus, only the gamma ray response to dry clay and response to the matrix remain to be found. It is assumed that neither formation water nor hydrocarbon contribute to the gamma ray response, so it can be written

$$\mathrm{GR} = \left(1-\phi_{\mathrm{T}}\right)\ \mathrm{GR}_{\mathrm{ma}} + V_{\mathrm{dc}}\,\mathrm{GR}_{\mathrm{dc}}.$$

From which it follows that, in shales,

$$\mathrm{GR}_{\mathrm{dc}} = \mathrm{GR}/\left(1-\phi_{\mathrm{T}}\right),$$

and, in clean intervals,

$$\mathrm{GR}_{\mathrm{ma}} = \mathrm{GR}/\left(1-\phi_{\mathrm{T}}\right).$$

For example, in a shale, GR = 110 and $\phi_T = 33$ %; but, in a clean section, GR = 25 and $\phi_T = 25$ %, so it follows that:

$GR_{dc} = 110/(1-0.33) = 149.25$, and

$GR_{ma} = 25/(1-0.25) = 33.3$.

Finding ϕ_T and V_{dc}

As already stated, ϕ_T is found from the Σ vs. ratio crossplot. V_{dc} can be found from the *GR* using:

$$V_{dc} = \frac{GR - GR_{ma}\left(1-\phi_T\right)}{GR_{dc} - GR_{ma}}$$

Solving for ϕ_e and S_{we}

Once V_{dc} and ϕ_T are established, the following relationships hold:

$\phi_e = \phi_T - V_{wb}$ (which also $= V_{hy} + V_{wf}$),

$V_{ma} = 1 - \phi_T - V_{dc}$, and $V_{wb} = \alpha V_{dc}$,

where α has been established in the shales as $\phi_{Tsh}/(1-\phi_{Tsh})$.

The response of the pulsed neutron log itself can be written as:

$$\Sigma = \Sigma_{ma} V_{ma} + \Sigma_{dc} V_{dc} + \Sigma_{wb} \alpha V_{dc} + \Sigma_{wf} V_{wf} + \Sigma_{hy} V_{hy},$$

hence:

$$\Sigma_{hy} V_{hy} + \Sigma_{wf} V_{wf} = \Sigma - \Sigma_{ma} V_{ma} - V_{dc}\left(\Sigma_{dc} + \alpha \Sigma_{wb}\right).$$

The right side of the equation can be evaluated since all the parameters and variables have now been defined. If this quantity is, in fact, Σ*, then

$$V_{wf} = \frac{\Sigma^* - \phi_e \Sigma_{hy}}{\Sigma_{wf} - \Sigma_{hy}}$$

By definition,

$$S_{we} = V_{wf} / \phi_e.$$

Appendix 2: Radioactive Elements, Minerals, and Rocks

Table 11.5 Natural gamma ray emitters

Nuclide		Mode of disintegration	Half-life
Uranium series			
UI	$_{92}U^{238}$	α	4.51×10^4 years
UX_1	$_{90}Th^{234}$	β	24.1 days
UX_2	$_{91}Pa^{234m}$	β, IT	1.18 min
UZ	$_{91}Pa^{234}$	β	6.66 h
UII	$_{92}U^{234}$	α	2.48×10^4 years
Io	$_{90}Th^{230}$	α	8.0×10^4 years
Ra	$_{88}Ra^{226}$	α	1620 years
Rn	$_{86}Em^{222}$	α	3.82 days
RaA	$_{84}Po^{218}$	α, β	3.05 min
RaA′	$_{85}At^{218}$	α, β	2 s
RaA″	$_{86}Em^{218}$	α	1.3 s
RaB	$_{82}Pb^{214}$	β	26.8 min
RaC	$_{83}Bi^{214}$	α, β	19.7 min
RaC′	$_{84}Po^{214}$	α	1.6×10^{-4} s
RaC″	$_{81}TI^{210}$	β	1.32 min
RaD	$_{82}Pb^{210}$	β	19.4 years
RaE	$_{83}Bi^{210}$	α, β	5.01 days
RaF	$_{84}Po^{210}$	α	138.4 days
RaE′	$_{81}TI^{206}$	β	4.2 min
RaG	$_{82}Pb^{206}$		Stable
Thorium series			
Th	$_{90}Th^{232}$	α	1.42×10^{10} yr
$MsTh_1$	$_{88}Ra^{228}$	β	6.7 years
$MsTh_2$	$_{89}Ac^{228}$	β	6.13 h
RdTh	$_{90}Th^{228}$	α	1.91 years
ThX	$_{88}Ra^{224}$	α	3.64 days
Tn	$_{86}Em^{220}$	α	51.5 s
ThA	$_{84}Po^{216}$	α	0.16 s
ThB	$_{82}Pb^{212}$	β	10.6 h
ThC	$_{83}Bi^{212}$	α, β	60.5 min
ThC′	$_{84}Po^{212}$	α	0.30 μs
ThC′	$_{81}T^{208}$	β	3.10 min
ThD	$_{82}Pb^{208}$		Stable

Table 11.6 Gamma ray lines[a] in the spectra of the important naturally occurring radionuclides

Nuclide	Gamma ray energy (MeV)	Number of photons per disintegration in equilibrium mixture
Bi^{214}(Rac)	0.609	0.47
	0.769	0.05
	1.120	0.17
	1.238	0.06
	1.379	0.05
	1.764	0.16
	2.204	0.05
$T4^{208}$(ThC′)	0.511	0.11
	0.533	0.28
	2.614	0.35
K^{40}	1.46	0.11

[a]With intensities greater than 0.05 photons per disintegration and energies greater than 100 kev

Table 11.7 Thorium-bearing minerals

Name	Composition	ThO_2 content %
Thorium minerals		
Cheralite	$(Th, Ca, Ce)(PO_4SiO_4)$	30, variable
Huttonite	$ThSiO_4$	81.5 (ideal)
Pilbarite	$ThO_2 \cdot UO_3 \cdot PbO \cdot 2SiO_2 \cdot 4H_2O$	31, variable
Thorianite	ThO_2	Isomorphous series to UO_2
Thorite[a]	$ThSiO_4$	25 to 63-81.5 (ideal)
Thorogummite[a]	$Th(SiO_4)_{1-x}(OH)_{4-x}$; $x < 0.25$	24–58 or more
Thorium-bearing minerals		
Allanite	$(Ca, Ce, Th)_2(Al, Fe, Mg)_3Si_3O_{12}(OH)$	0 to about 3
Bastnaesite	$(Ce, La)Co_3F$	Less than 1
Betafite	About $(U, Ca)(Nb, Ta, Ti)_30_9 \cdot nH_20$	0 to about 1
Brannerite	About $(U, Ca, Fe, Th, Y)_3Ti_5O_{16}$	0–12
Euxenite	$(Y, Ca, Ce, U, Th)(Nb, Ta, Ti)_2O_5$	0 to about 5
Eschynite	$(Ce, Ca, Fe, Th)(Ti, Nb)_2O_6$	0–17
Fergusonite	$(Y, Er, Ce, U, Th)(Nb, Ta, Ti)O_4$	0 to about 5
Monazite[b]	$(Ce, Y, La, Th)PO_4$	0 to about 30; usually 4–12
Samarskite	$(Y, Er, Ce, U, Fe, Th)(Nb, Ta)_2O_6$	0 to about 4
Thucholite	Hydrocarbon mixture containing U, Th, rare earth elements	
Uraninite	UO_2 (ideally) with Ce, Y, Pb, Th, etc.	0–14
Yttrocrasite	About $(Y, Th, U, Ca)_2(Ti, Fe, W)_4O_{11}$	7–9
Zircon	$ZrSiO_4$	Usually less than 1

Source: After Frondel, C., 1956, in Page, L. R., Stocking, H. E., and Smith, H. D., Jr., U.S. Geol. Survey Prof. Papers no. 300

[a]Potential thorium ore minerals

[b]Most important commercial ore of thorium. Deposits are found in Brazil, India, USSR, Scandinavia, South Africa, and the USA

Table 11.8 Uranium minerals

Autunite	$Ca(UO_2)_2(PO_4)_2$ 10-12H_2O
Tyuyamunite	$Ca(UO_2)_2(VO_4)_2$ 5-8H_2O
Carnotite	$K_2(UO_2)_2(UO_4)_2$ 1-3H_2O
Baltwoodite	U-silicate high in K
Weeksite	U-silicate high in Ca

Table 11.9 Potassium, Uranium, and Thorium distribution in rocks and minerals

	K (%)	U (ppm)	Th (ppm)
Accessory minerals			
Allanite		30–700	500–5,000
Apatite		5–150	20–150
Epidote		20–50	50–500
Monazite		500–3,000	2.5×10^4–20×10^4
Sphene		100–700	100–600
Xenotime		500-3, 4×10^4	Low
Zircon		300–3,000	100–2,500
Andesite (av.)	1.7	0.8	1.9
A., Oregon	2.9	2.0	2.0
Basalt			
Alkali basalt	0.61	0.99	4.6
Plateau basalt	0.61	0.53	1.96
Alkali olivine basalt	<1.4	<1.4	3.9
Tholeiites (orogene)	<0.6	<0.25	<0.05
(non orogene)	<1.3	<0.50	<2.0
Basalt in Oregon	1.7	1.7	6.8
Carbonates			
Range (average)	0.0–2.0 (0.3)	0.1–9.0 (2.2)	0.1–7.0(1.7)
Calcite, chalk, Limestone, olomite (all pure)	<0.1	<1.0	<0.5
Dolomite, West Texas (clean)	0.1-0.3	1.5-10	<2.0
Limestone (clean)			
Florida	<0.4	2.0	1.5
Cretaceous trend, Texas	<0.3	1.5-15	<2.0
Hunton lime, Okla.	<0.2	<1.0	<1.5
West Texas	<0.3	<1.5	<1.5
Clay minerals			
Bauxite		3–30	10–130
Glauconite	5.08–5.30		
Bentonite	<0.5	1–20	6–50
Montmorillonite	0.16	2–5	14–24
Kaolinite	0.42	1.5–3	6–19
Illite	4.5	1.5	
Mica			

(continued)

Table 11.9 (continued)

	K (%)	U (ppm)	Th (ppm)
Biotite	6.7–8.3		<0.01
Muscovite	7.9–9.8		<0.01
Diabase, Va.	<1.0	<1.0	2.4
Diorite, quartzodiorite	1.1	2.0	8.5
Dunite, Wa.	<0.02	<0.01	<0.01
Feldspars			
Plagioclase	0.54		<0.01
Orthoclase	11.8–14.0		<0.01
Microcline	10.9		<0.01
Gabbro (mafic igneous)	0.46–0.58	0.84–0.9	2.7–3.85
Granite (silic igneous)			
Rhode Island	2.7–4.26	3.6–4.7	19-20
New Hampshire	4.5–5	4.2	25–52
Precambrian (Okla.)	3.5–5	12–16	50–62
Minnesota, (Col. Tex.)	2–6	3.2–4.6	14–27
Grandodiorite	2–2.5	2.6	9.3–11
Colorado, Idaho	5.5	2–2.5	11.0–12.1
Oil shales, Colorado	<4.0	up to 500	1–30
Periodite	0.2	0.01	0.05
Phosphates		100–350	1–5
Rhyolite	4.2	5	
Sandstones, range (av.)	0.7–3.8 (1.1)	0.2–0.6 (0.5)	0.7–2.0 (1.7)
Silica, quartz, quartzite, (pure)	<0.15	<0.4	<0.2
Beach Sands, Gulf Coast	<1.2	0.84	2.8
Atlantic Coast (Fla., N.C.)	0.37	3.97	11.27
Atlantic Coast (N.J., Mass.)	0.3	0.8	2.07
Shales			
“Common” shales [range (av.)]	1.6–4.2 (2.7)	1.5–5.5 (3.7)	8–18 (12.0)
Shales (200 samples)	2.0	6.0	12.0
Schist (biotite)		2.4–4.7	13–25
Syenite	2.7	2,500	1,300
Tuff (feldspatic)	2.04	5.96	1.56

Table 11.10 Geological significance of natural gamma ratios

Ratios	Remarks
Thorium/ Uranium (Th/U)	In *sedimentary* rocks, Th/U varies with depositional environment Th/U
	>7: continental, oxidizing environment, weathered soils, etc.
	<7: marine deposits, gray and green shales, graywackes
	<2: marine black shales, phosphates
	In *igneous* rocks, high Th/U indicative of oxidizing conditions by magma
	Before crystallization and/or extensive leaching during
	Postcrystallization history
	Source rock potential estimates of argillaceous sediments (shales)
	Major geologic unconformities
	Distance to ancient shore lines or location of rapid uplift during time of deposition
	Stratigraphic correlations, transgression vs. regression, oxidation vs. reduction regimes, etc.
Uranium/ Potassium (U/K)	Source rock potential of argillaceous sediments
	Stratigraphic correlations
	Unconformities, diagenetic changes in argillaceous sediments, carbonates, etc.
	Frequent correlation with vugs and natural fracture systems in subsurface formations, including localized correlation with hydrocarbon shows on drilling mud logs and core samples both in clastic and carbonate reservoirs
Thorium/ Potassium (Th/K)	Recognition of rock types of different facies
	Paleographic and paleoclimatic interpretation of facies characteristics
	Depositional environments, distance from ancient shore lines, etc.
	Diagenetic changes of argillaceous sediments
	Clay typing: Th/K increases from glauconite ⇒ muscovite ⇒ illite ⇒ mixed-layer clays ⇒ kaolinite ⇒ chlorite ⇒ bauxite
	Correlation with crystallinity of illite, average reflectance power, paramagnetic electronic resonance

Bibliography

Al-Nasser MN, Ma M, Al-Mushrafi N, Al-Muthana AS, Riley S, Geevarghese AI. Quantifying gas saturation with pulsed neutron logging—an innovative approach. SPE 166025-MS. 2013.

Antkiw S. Depth of investigation of the dual-spacing thermal neutron decay time logging tool. In: SPWLA Trans. 17th Logging Symposium, Denver, Colo. 1976.

Arbuzov AA, Alekhin AP, Bochkarev VV, Minakhmetova RN, Chukhutin DV, Zakirov AN. Memory pulsed neutron-neutron logging. In: SPE Russian oil and gas exploration and production technical conferences and exhibition held in Moscow, Russia 16-18 October, SPE 162074. 2012.

Bertoli S, Borghi M, Galli G, Oprescu A, Riley S. Field trials of a new array pulsed neutron formation gas measurement in complex completions. Presented at the 11th Offshore Mediterranean Conference and Exhibition in Ravenna, Italy, March 20-22. 2013.

Blackburn JS, Brimage RC. Estimation of formation pressures in clean gas sands from the dual-spacing TDT log. In: SPWLA Trans. 19th Logging Symposium, EI Paso, Tex. 1978.

Clavier C, Hoyle W, Meunier D. Quantitative interpretation of thermal neutron decay time logs: part I. Fundamentals and techniques, part II. Interpretation examples, interpretation accuracy, and time-lapse technique. J Petrol Tech. 1971;23:743–63.

Departure curves for the thermal decay time log. Schlumberger, Publication C-11989; 1976.

Dewan JT, Johnstone CW, Jacobson LA, Wall WB, Alger RP. Thermal neutron decay time logging using dual detection. In: SPWLA Trans. 14th Logging Symposium, Lafayette, LA, May 1973.

Fertl WH, Frost Jr E. Experiences with natural gamma ray spectral logging in North America. Paper SPE 11145 presented at the SPE 57rd annual technical conference and exhibition, New Orleans, Sept. 25-29, 1982.

Fertl WH, Stapp WL, Vaello DB, Vercellino WC. Spectral gamma ray logging in the Texas Austin Chalk trend. J Petrol Tech. 1980; Presented at the SPE 53rd annual technical conference and exhibition, Houston, Oct. 1–4, 1978.

Frondel C. L. R. Page, H. E. Stocking, and H. B. Smith, U.S. Geol. Survey Prof. Papers No. 300; 1956.

Gadeken LL, Arnold DM, Smith Jr HD. Applications of the compensated spectral natural gamma tool. Paper presented at the 25th ANNUAL SPWLA symposium in New Orleans, June 1984.

Gamma ray spectral data assists in complex formation evaluation. Dresser Atlas, publication REP 06/80 5M 3335, Houston; February 1979.

Hall E, Johnstone CW, Baldwin L, Jacobson LA. A new thermal neutron decay logging system-TDT-M. Paper SPE 9462 presented at the SPE 55th annual technical conference and exhibition, Dallas, Sept. 21-24, 1980; J Petrol Tech. 1982.

Hassan M, Hossin A, Combaz A. Fundamentals of the differential gamma ray log-interpretation technique. Paper presented at the SPWLA 17th annual logging symposium, Denver, June 9-12, 1976.

Herron SL. A total organic carbon log for source rock evaluation. Paper HH, SPWLA symposium. 1986.

Jacobson LA, Ethridge R, Simpson G. A new small-diameter, high-performance reservoir monitoring tool. Halliburton Energy Services.

Kokesh FP. Gamma ray logging. Oil Gas J. 1951.

Marett G, Chevalier P, Souhaite P, Suau J. Shaly sand evaluation using gamma ray spectrometry applied to the North Sea Jurassic. In: SPWLA 17th annual symposium, Denver, June 1976.

McGhee BF, McGuire JA, Vacca HL. Examples of dual spacing thermal neutron decay time logs in Texas Coast oil & gas reservoirs. In: SPWLA Trans. 15th annual logging symposium, June 1974.

Mills Jr WR, Allen S, Caldwell RI, Salaita GN, Gray TJ. Pulsed-neutron experiments in a borehole model. Nucl Sci Eng. 1965;21:346–56.

Murphy RP, Owens WW. The use of special coring and logging procedures for defining reservoir residual oil saturations. J Petrol Tech. 1973:841–50.

Murphy RP, Foster GT, Owens WW. Evaluation of waterfiood residual oil saturations using log-inject-log procedures. J Petrol Tech. 1977:178–86.

Quirein JA, Gardner JS, Watson JT. Combined natural gamma ray spectral-litho-density measurements applied to complex lithologies. Paper SPE 11143 presented at the SPE 57th annual technical conference and exhibition, New Orleans, Sept. 25-29, 1982.

Reed S, Jacobson LA, Durbin D. Cased-hole KUTH logging using a PNS Tool. In: SPE annual technical conference and exhibition, Houston, Texas 26-29 September 2004.

Smith Jr HD, Robbins CA, Arnold DM, Deaton JG. A multi-function compensated spectral natural gamma ray logging system. Paper SPE 12050 presented at the SPE 58th annual technical conference and exhibition, San Francisco, Oct. 5-8, 1983.

Tittman J. “Radiation logging lecture I: physical principle” and “Lecture II: applications”. Petroleum engineering conference on the fundamental theory and quantitative analysis of electric and radioactivity logs, the University of Kansas; 1956.

Wahl JS, Nelligan WB, Frentrop AH, Johnstone, CW, Schwartz RJ. The thermal neutron decay time log. Soc Pet Eng J. 1970:365–37.

Weijun G, Jacobson L, Truax J, Dorffer D, Kwong S. A new three-detector 1-11/16-inch pulsed neutron tool for unconventional reservoirs. In: SPWLA 51st annual logging symposium, Perth, Australia, June 19-23, 2010.

Wiese HC. TDT log applications in California. J Petrol Tech. 1983:429–44.

Youmans AH, Hopkinson EC, Bergan RA, Oshry HI. Neutron lifetime, a new nuclear log. J Petrol Tech. 1964;16:319–28.

Zett A, Webster M, Spain D, Surles D, Colbert C. Application of new generation multi detector pulsed neutron technology in petrophysical surveillance. In: SPWLA 53rd annual logging symposium, June 16-20, 2012.

Zett A, Webster M, Rose H, Riley S, Trcka D, Kadam N. Surveillance of complex displacement mechanisms in mature reservoirs to maximize recovery. In: SPE annual technical conference and exhibition held in San Antonio, Texas, USA 8-10 October, 2012.

Answers to Text Questions

Question #11.1
Uranium

Question #11.2
(c) Σ increase
(d) 30 cu

Question #11.3
$S_w = 50\ \%$

Question #11.5
(a) $\phi = 30\ \%$
(b) $S_w = 50\ \%$
(c) $S_w = 55\ \%$

Question #11.6
$\Sigma_w = 110$ cu

Question #11.7
(a) $\Sigma_{ma} = 13$ cu
(b) $\Sigma_w = 75$ cu

Question #11.8
$\Sigma_o = 21.2$ cu

Question #11.9
Σ methane $= 6.5$ cu
$\Sigma_g = 8.0$ cu

Question #11.10
$\Sigma_{sh} = 33$ cu

Question #11.11
(a) $\phi = 25\ \%$
(b) $\Sigma_{wa} = 50$ cu

Cement Bond Logging

12

Cement bond logging (CBL) is an important part of a well-completion program and is also recommended for most workover programs. Most of the cementing-related problems encountered can be diagnosed by use of the CBL. However, successful interpretation of a CBL depends on certain minimum requirements:

- The tool must be run strictly centralized.
- A transit-time curve must be recorded.
- A wave train or VDL display must be available.

Before explaining these requirements in detail, however, it is worthwhile to review the principles of oil-well cementing, since many problems can be traced back to the primary cement job and the way it was conducted.

Principles of Oil-Well Cementing

Oil-well cementing is the process of mixing a slurry of cement, water, and additives and pumping it down through steel casing to the annular space between the well bore and the outside of the casing. Figure 12.1 illustrates the conventional cementing process. Sometimes it is advisable to cement a well in two or more stages in which case a more complex completion string is required, as shown in Fig. 12.2. This technique is employed when two or more zones have different cement requirements.

Cement has three principal functions in a well:

- To restrict fluid movement between formations
- To bond the casing to the formation
- To provide support for the casing

As long as an effective hydraulic seal is provided between porous and permeable zones in the well, a cement job may be considered as good. Important examples include

R.M. Bateman, *Cased-Hole Log Analysis and Reservoir Performance Monitoring*,
DOI 10.1007/978-1-4939-2068-6_12

isolation of gas-bearing formations and wet zones from primary oil-producing horizons and isolation of shallow drinking-water aquifers from deeper saltwater formations.

Cements themselves are classified by API classification letters A–J. Table 12.1 details the well depths, temperatures, and slurry weights for these cements. For further details, refer to service company handbooks.

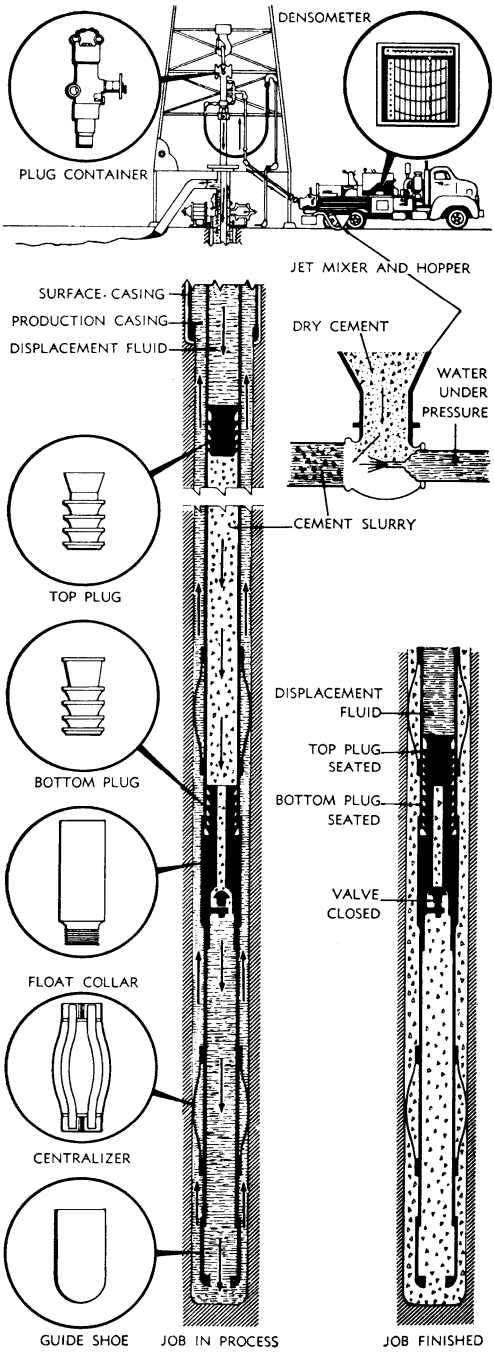

Fig. 12.1 Primary cementing procedures. Courtesy Halliburton Services

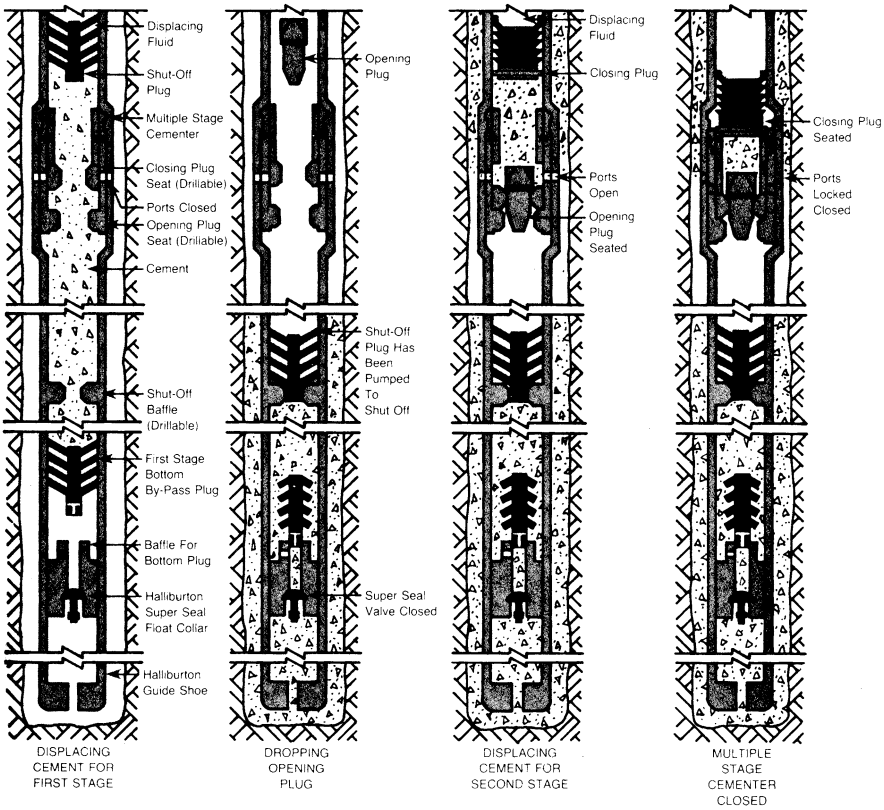

Fig. 12.2 Successive steps for stage cementing. Courtesy Halliburton Services

Table 12.1 API classification of cements

	Mixing	Slurry	Well	Static
API Classification	Water (gal/sack)	Weight (lb/gal)	Depth (ft)	Temperature (°F)
A (Portland)	5.2	15.6	0–6,000	80–170
B (Portland)	5.2	15.6	0–6,000	80–170
C (High Early)	6.3	14.8	0–6,000	80–170
D (Retarded)	4.3	16.4	6–12,000	170–260
E (Retarded)	4.3	16.4	6–14,000	170–290
F (Retarded)	4.5	16.2	10–16,000	230–320
G (Basic)[a]	5.0	15.8	0–8,000	80–200
H (Basic)[a]	4.3	16.4	0–8,000	80–200
J	4.9	15.4	12–16,000	260–320

Note: Reprinted with permission of Halliburton Services

[a]Can be accelerated or retarded for most well conditions

Various additives are commonly used with cements to control such variables as density, viscosity, setting time, and compressive strength. Table 12.2 details the effects of additives on cements.

Other practices commonly used during cementing operations include the use of casing centralizers, scratchers (to remove mudcake from the borehole wall), and turbolizers (to induce turbulent flow in the casing/formation annulus).

The use of cement additives and/or mechanical accoutrements can dramatically affect the quality of the final cement job. Anything, within reason, that assists in obtaining a good hydraulic seal should not be overlooked.

Table 12.2 Effects of some additives on the physical properties of cement

Additive \ Effect on	Density		Water required		Viscosity		Thickening time		Early strength		Final strength		Durability		Water loss	
	+	-	+	-	+	-	+	-	+	-	+	-	+	-	+	-
Bentonite		✹	✹		✧		✧			✧		✹		✧		✹
Diatomaceous Earth		✹	✹		✧		✧			✧		✹		✧	✧	
Pozzolan		✹	✧		✧					✧		✧	✹			
Sand	✹		✧		✧											
Heavy Weight	✹				✧							✧				
Accelerator						✧		✹	✹							
Sodium Chloride *	✧					✧	✧	✹	✹							
Retarder						✹	✹			✹	✹					✧
Friction Reducer			✧			✹	✧		✧		✹					✧
Low Waterloss Materials							✧			✧		✧				✹
Lost Circulation Materials			✧							✧		✧		✧		✧

Note: Reprinted with permission of Halliburton Services
✧ Denotes minor effect
✹ Denotes major effect and/or principal purpose for which used
* Small percentages of sodium chloride accelerate thickening
Large percentages may retard API class A cement

Principles of Cement Bond Logging

Conventional CBL tools rely for their operation on the fact that a compressional (acoustic) wave transmitted along the wall of a steel pipe becomes attenuated if the pipe has cement bonded to it. The relationship between the compressive strength of the cement and the attenuation rate (measured in db/ft) is shown in Fig. 12.3. Note that the type of cement is relatively unimportant and that, given the attenuation rate, a cement compressive strength can be deduced.

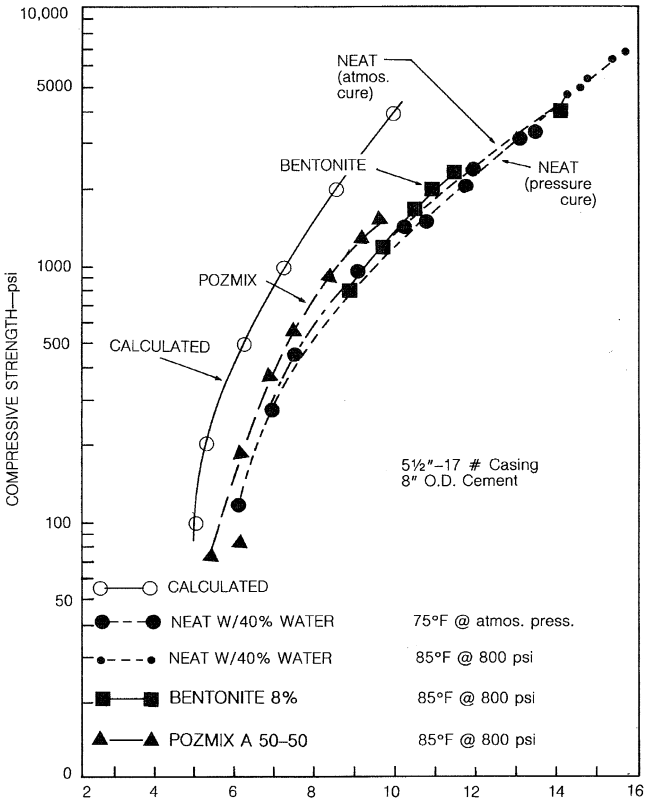

Fig. 12.3 Compressive strength vs. attenuation rate for various cements. Reprinted with permission of the SPE from Pardue et al. © 1963

The data for Fig. 12.3 refers to steel pipes completely surrounded by cement. In the case of partial cementation, it is of interest to note the data of Fig. 12.4 where the percentage of the pipe's circumference is plotted against the attenuation rate. This relationship is linear (i.e., the smaller the percentage of the circumference cemented, the less the attenuation rate). It is also worth noting that at least a ¾-in. thickness of cement is required in order for these relationships to hold. Figure 12.5 shows that after a thickness of ¾ in. is exceeded, attenuation rate is constant. Thus, measurement of the attenuation rate of a compressional wave propagated along the casing gives information regarding the bonding of the cement to the casing. Information regarding the bonding of the cement to the formation has to come from a separate source such as a wave-train recording which can be viewed as a variable-density display (VDL). In order to understand this more fully the tools used must be studied.

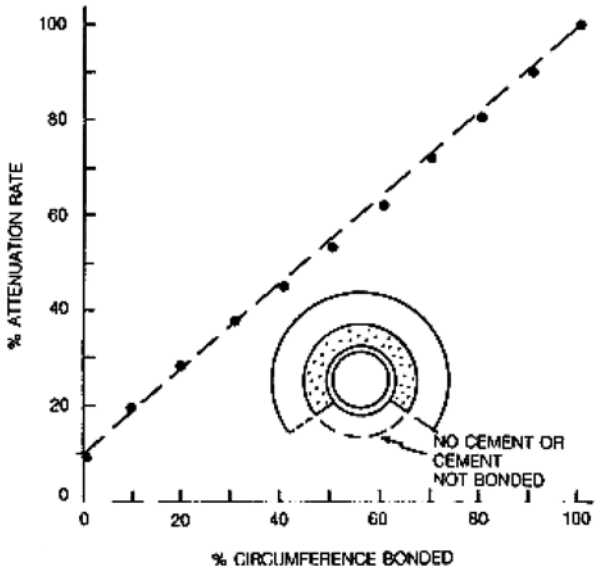

Fig. 12.4 Percent attenuation vs. percent circumference bonded. Reprinted with permission of the SPE from Pardue et al.© 1963

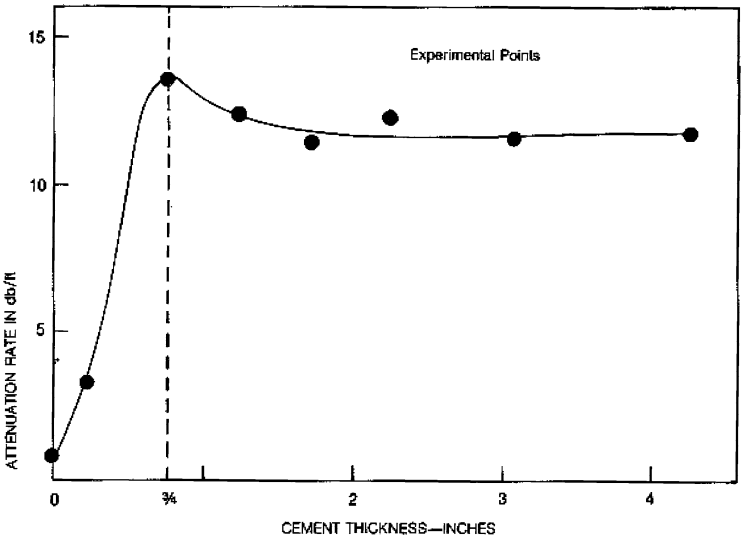

Fig. 12.5 Attenuation rate vs. cement thickness. Reprinted with permission of the SPE from Pardue et al. © 1963

Tools Available

In general conventional CBL, tools are available as either through-tubing versions (for workover jobs) which have a 1–11/16″ or 2–1/8″ diameter or as full-diameter tools for primary completions with a 3–5/8″ OD. Apart from these classifications, based on the physical dimensions, CBL tools are also available as the more modern ultrasonic scanning type. Both will be discussed.

Figure 12.6 illustrates a conventional CBL tool. It consists of an acoustic transmitter and two receivers. In actual practice, the tool may be identical with an open-hole sonic tool but with only one transmitter and two receivers being used. The near receiver is placed 3 ft from the transmitter and is used for amplitude measurements. The far receiver is placed 5 ft from the transmitter and is used for wave-train recordings.

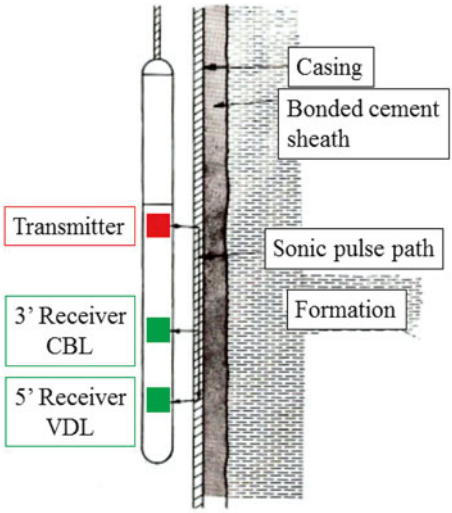

Fig. 12.6 Conventional CBL tool. After Schlumberger

Operating Principles

Three paths are available for a compressional wave emanating from the transmitter:

1. Through the casing
2. Through the formation
3. Through the borehole fluid

Typical travel times for these three media are 56 μs/ft for casing, 60–100 μs/ft for the formation, and 170–200 μs/ft for the borehole fluid. The shortest time path for the acoustic energy to travel is through the casing and the longest is through the

borehole fluid. Thus, at the receiver, the signal recorded will have three major components, the casing signal, the formation signal (if present), and the borehole signal. The initial transmitted pulse will be spread out into a wave train. Figure 12.7 illustrates a typical wave train seen at the receiver.

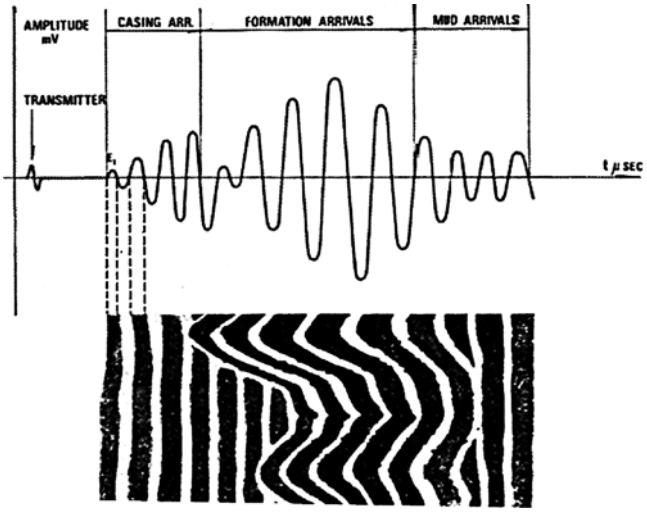

Fig. 12.7 CBL wave train. Courtesy Schlumberger

Amplitude Measurement

Since the amplitude of the casing wave is required for the attenuation measurement it is sufficient to measure the amplitude of the first arrival since this will be the one that has traveled through the casing. For convenience, the various arrival peaks are named E_1, E_2, E_3, etc.—E_1 being the first arrival. The form of the transmitted wave and the first arrivals at the 3-ft receiver are shown in Fig. 12.8.

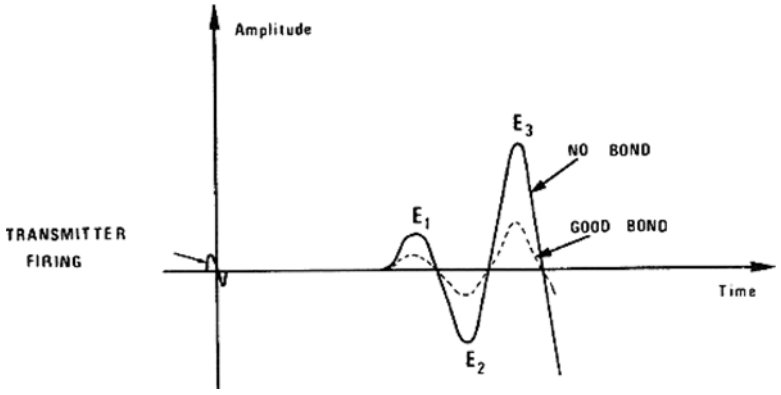

Fig. 12.8 Schematic receiver output signal with bonded and unbonded casing. Courtesy Schlumberger

Where there is no cement, the amplitude of E_1 is large and attenuation is small. Where cement is present, the amplitude of E_1 is small and attenuation is large. Due to the nature of the measuring system used, the amplitude of the first arrival, E_1, is displayed on the log in millivolts. A low value of millivolts means a high attenuation rate and good cement. A high value of millivolts means a low attenuation rate and poor cement. Typically, amplitudes are recorded on a scale of 0–50 mV across one track.

Travel-Time Measurement

At the same time the amplitude is measured, the one-way travel time from the transmitter to the receiver is also measured and displayed on the log. In casing of constant size, this travel time should be constant and a function solely of the tool and casing size. As we shall see later, this single-receiver Δt measurement is extremely valuable in diagnosing problems such as cycle skipping and tool eccentricity. Figure 12.9 shows the expected Δt values for 1–11/16 and 3–5/8-in. OD tools. This information is usually displayed in Track 1 of the log, with Δt increasing to the left.

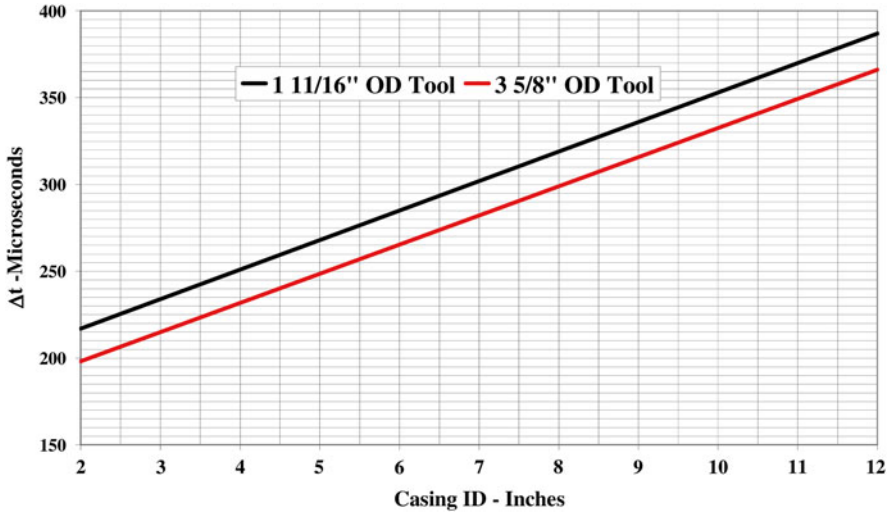

Fig. 12.9 Single-receiver (3-ft) Δt values for CBL tools

Wave-Train Display

The entire wave train can be conveniently displayed in a number of ways, the most common of which is the *variable-density display* (VDL), where bands of alternate dark and light shading reveal the peaks and valleys of the wave train. A common presentation is as shown in Fig. 12.10, where the VDL display is in Track 3 scaled from 200 to 1,200 μs. As examples of alternative ways to display the same information, Fig. 12.11 shows a full waveform display over the same section and Fig. 12.12 shows a half-wave display.

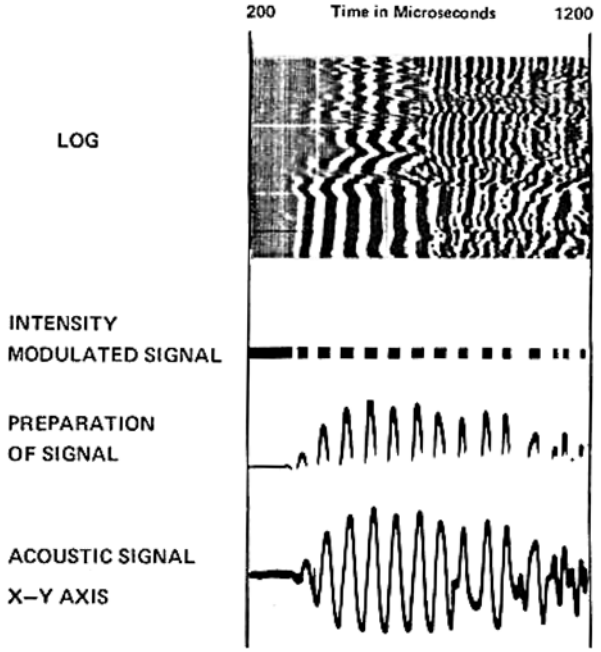

Fig. 12.10 CBL wave train and VDL

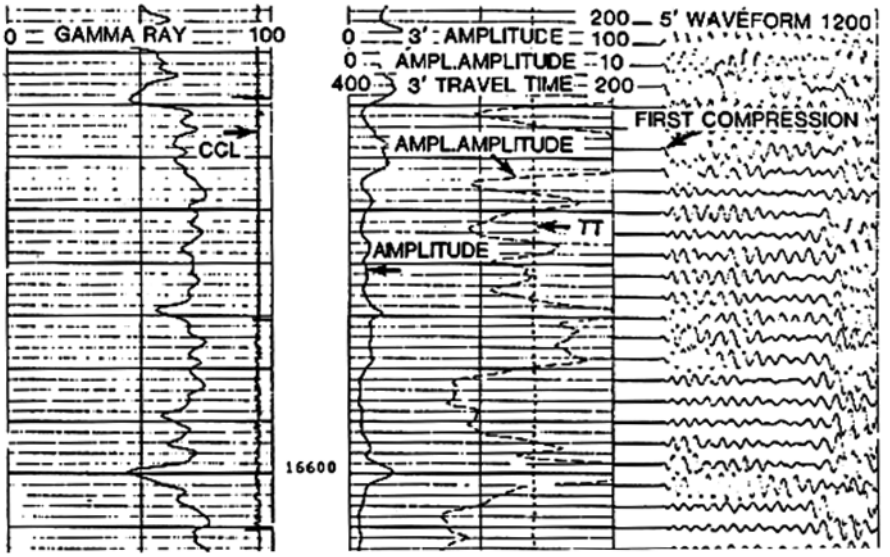

Fig. 12.11 CBL and full-wave display

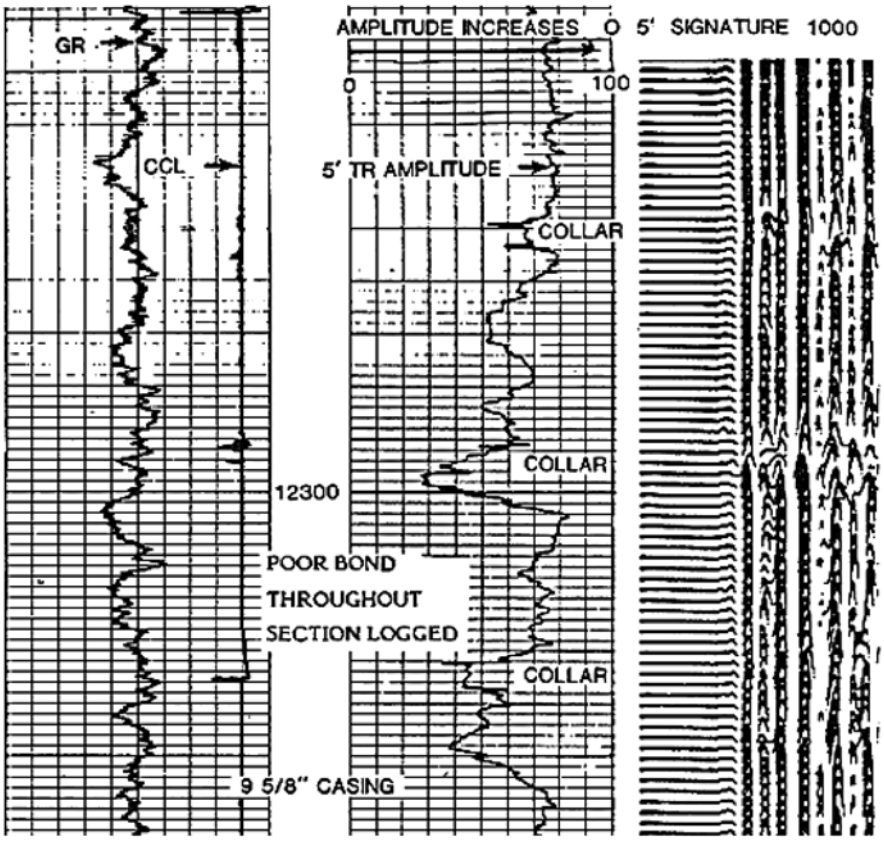

Fig. 12.12 Half-wave display

Δt Stretching

At the time the transmitter pulse is initiated, an electronic clock starts counting. A bias level is adjusted by the logging engineer to detect the first arrival at the 3-ft receiver, at which time the clock stops. Δt is the elapsed time recorded by the clock. The detection level must be set high enough so that the background noise does not trigger the system but not so high as to miss E_1 altogether and skip over to E_3, or even later arrivals. This method of measuring Δt exhibits two distinctive characteristics when the amplitude of E_1 is decreased due to good cement bonding. These are (1) Δt stretching and (2) cycle skipping. Δt stretching is shown in Fig. 12.13. Note that the amplitude of E_1 is decreased and, since the bias level remains in the same position, the measured transit time, Δt, is somewhat lengthened. This will be evident on the log and is a normal and acceptable phenomenon.

Cycle Skipping

If a further drop in amplitude causes the peak of E_1 to fall below the preselected bias level, detection will take place on E_3 and Δt will increase significantly. This is known as cycle skipping, as shown in Fig. 12.14. Cycle skipping may be unavoidable in very good bonding and although it gives a hashy appearance to the Δt curve, it is not all bad; at least there is a good bond! Figure 12.15 gives an example of cycle skipping in a very well-bonded section.

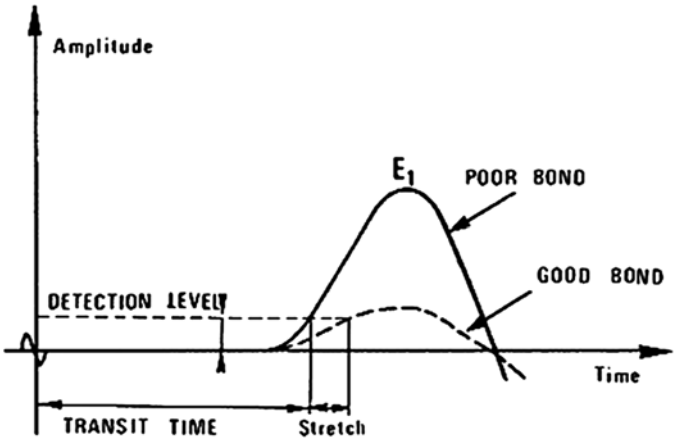

Fig. 12.13 Δt stretching due to good cement bond. Courtesy Schlumberger

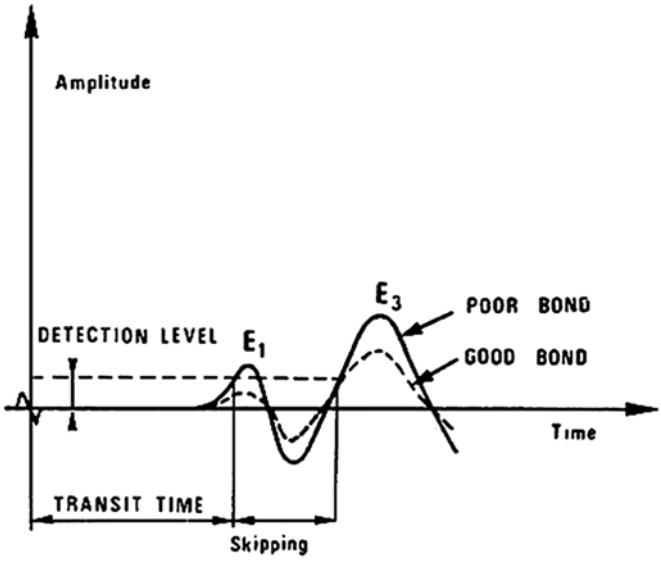

Fig. 12.14 Cycle skipping. Courtesy Schlumberger

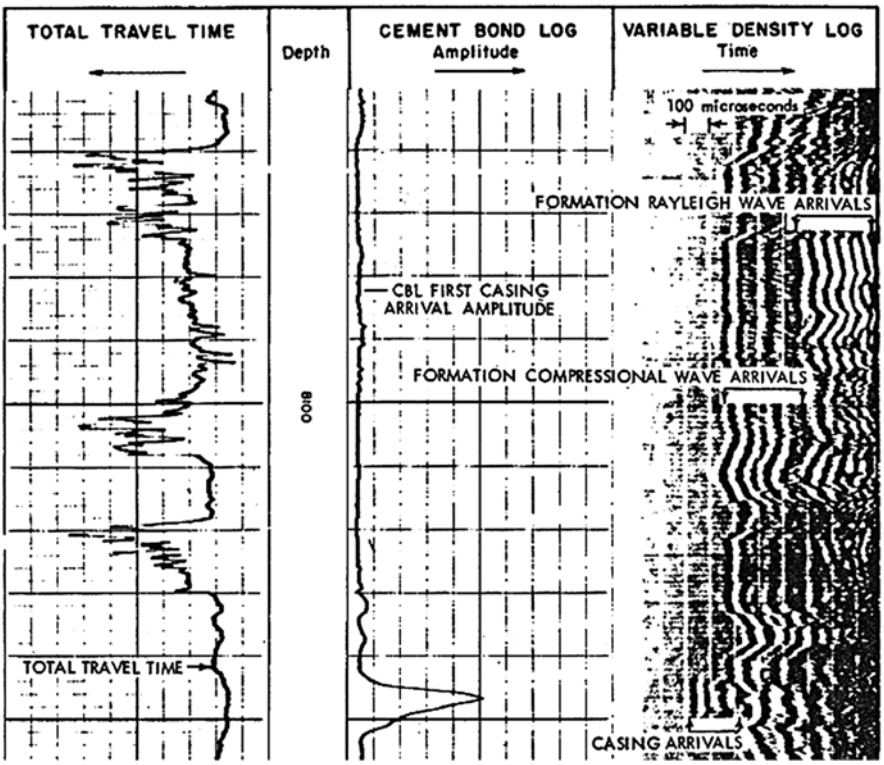

Fig. 12.15 Cycle skipping in well-bonded casing. Courtesy Schlumberger

Question #12.1
Inspect the Δt curve in Fig. 12.15. At the places where cycle skipping is most apparent, estimate which peak was actually detected (1.e., E_3, E_5, … etc.)

Gating Systems

The amplitude of the E_1 peak is detected by means of an electronic gate that opens for a predetermined time, takes the maximum value of the received wave during the time it is open, and records that amplitude on the log. There are two common methods of achieving the correct gate position in order to key on the E_1 peak: (1) a fixed gate that opens at a fixed time after the transmitter fires or, (2) a floating gate that only opens after E_1 has been detected by the Δt-measuring circuitry, which depends on the bias level set by the operator.

If the transit-time measurement is triggered by E_1, both systems give the same result. If there is cycle skipping, the two gating systems give different results since the fixed gate will read E_1, which will be small, and the floating gate will read E_3, which may be larger than E_1. The floating gate relieves the operator of the task of fine tuning the position of the fixed gate for changes in casing size and weight or borehole fluid, but at the same time it causes erroneously high values of amplitude in well-bonded pipe.

Deviated Holes and Eccentered Tools

The centering of the tool is very critical for the response of the CBL once the tool is off center, essentially two paths become available for the transmitted compressional wave (see Fig. 12.16a). As a result, the waveform at the receiver becomes "smeared" and this results in two effects on the log:

1. The measured Δt will be shortened
2. The measured amplitude will be too low, giving a false indication of good bonding (see Fig. 12.16b)

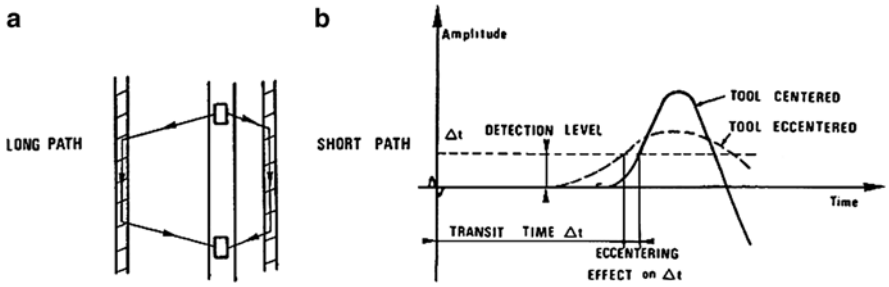

Fig. 12.16 (**a**) Eccentered tool and (**b**) waveforms both centered and eccentered. Courtesy Schlumberger

Figure 12.17 shows a section of log in a deviated hole where the tool was not properly centralized. Note that where Δt decreases so does the amplitude. The cure is to insist that the tool be centralized top, middle, and bottom with either rubber fins or spring centralizers.

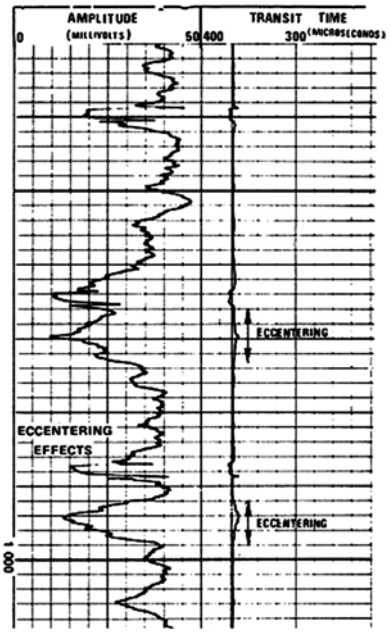

Fig. 12.17 CBL run in deviated hole. Courtesy Schlumberger

Interpretation

Cement Compressive Strength

For a given casing size and weight, the amplitude of the transmitted wave, measured in millivolts, may be converted to a cement compressive strength value in psi. This is conveniently achieved using the nomogram in Fig. 12.18. The required inputs are: (1) amplitude in mV from the log (2) casing size and (3) casing thickness (requires knowledge of casing weight).

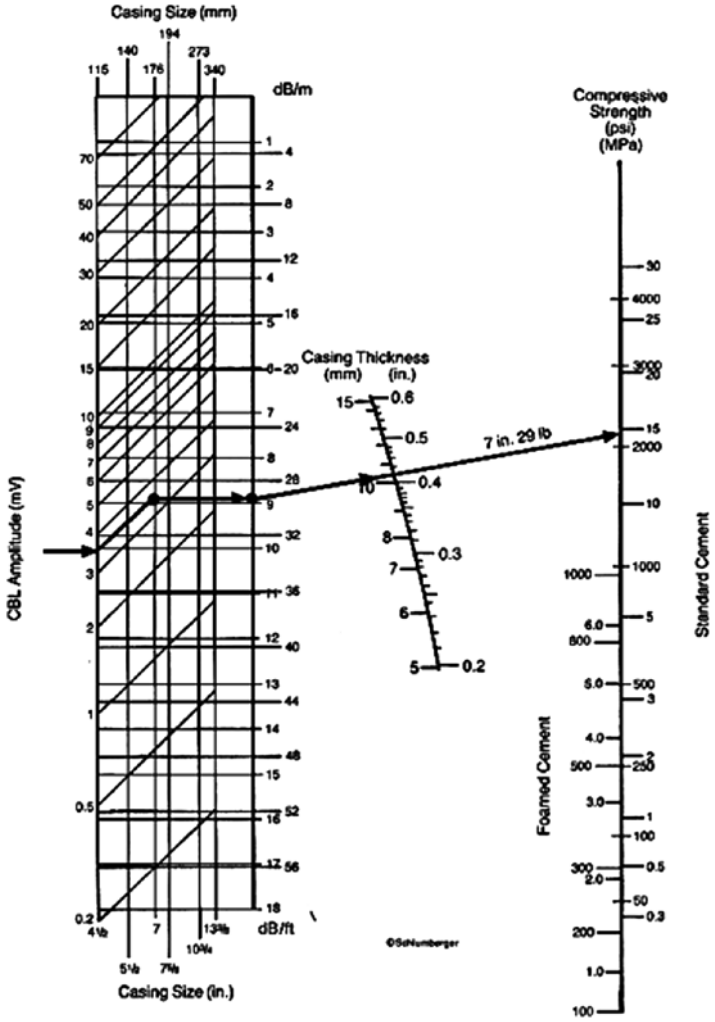

Fig. 12.18 CBL amplitude interpretation. Courtesy Schlumberger

Figure 12.19 allows quick calculation of casing thickness from casing OD and weight. Alternatively, the table given in the appendix to this chapter can be used to find the same values.

Question #12.2
If the amplitude reads 10 mV in 9–5/8-in. 40-lb casing, what is the compressive strength of the cement?

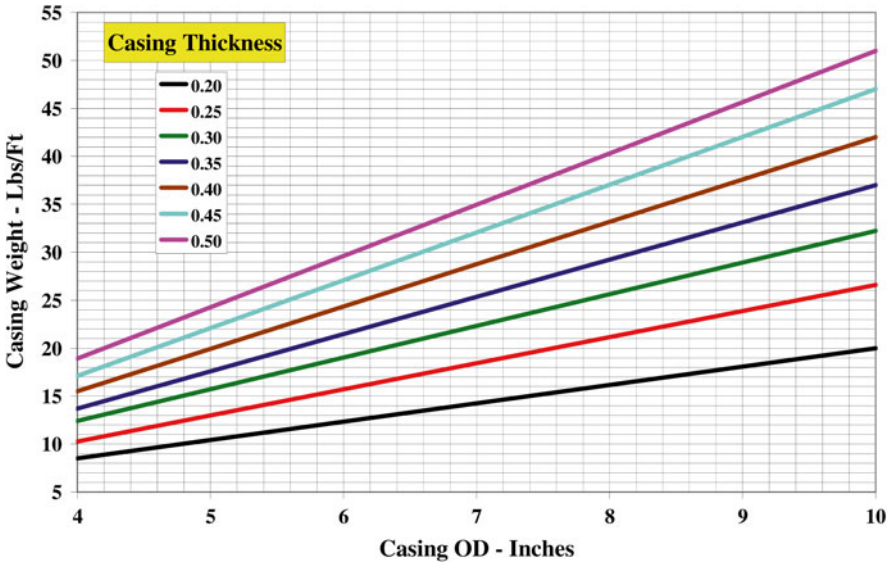

Fig. 12.19 Casing OD weight and thickness

Partial Cementation

The case where a section of pipe shows an amplitude higher than the minimum amplitude read in well-cemented pipe raises the possibility that a hydraulic seal does not exist. To quantify the analysis, a *bond index* is used:

$$\text{Bond index} = \frac{\text{Attenuation in suspectzone } (\text{dB/ft})}{\text{Attenuation in well cemented zone } (\text{dB/ft})}$$

Experience shows that if the bond index is at least 0.8 a seal can be expected, provided the poorly bonded section is sufficiently long. Figure 12.20 shows that the larger the casing size, the longer the interval needed at or above the bond index = 0.8 condition for a seal to be assured. A rough rule of thumb is to double the casing size in inches and subtract 5 to give the number of feet of section required.

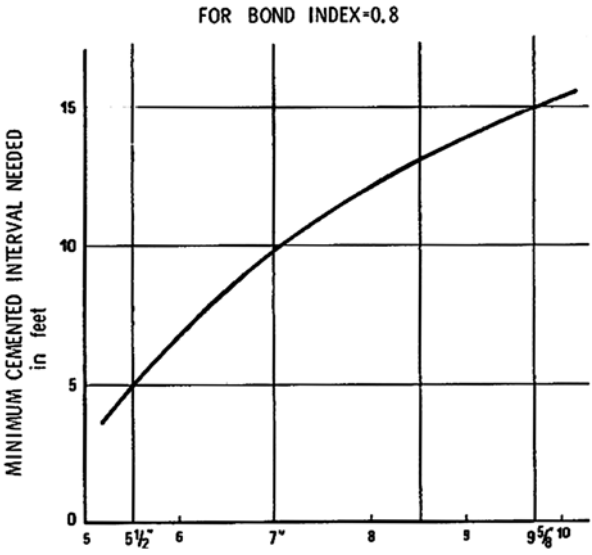

Fig. 12.20 Minimum requirements for hydraulic seal. Courtesy Schlumberger

Wave-Train Signatures

Figure 12.21 neatly summarizes the various patterns that may appear on a wave-train display such as the VDL. Typically, the VDL Track will be scaled 0–1,000 or 200–1,200 μs. The first 200 or 250 μs represent the time after the transmitter fires but before the first arrival at the 5-ft receiver. The next few hundred microseconds represent casing arrivals closely followed by formation arrivals, with mud arrivals coming last. The clue to reading VDL displays lies in observing the relative strength of the signals in these time intervals. For example, in free pipe, casing arrivals will be strong and formation arrivals weak. In well-bonded pipe, casing arrivals will be weak and formation arrivals strong, etc. By observing the amplitude, the transit time, and the VDL display, any condition of cementation can be diagnosed.

Free Pipe

Free pipe will exhibit: (1) steady travel time, with casing collars visible, (2) high amplitude (~50 mV), with casing collars giving a 10- to 15-mV reduction over a 3-ft depth interval and (3) a VDL display with parallel black and white bands showing chevron patterns at casing collars over a 5-ft depth interval. No formation arrivals will be visible. Figure 12.22 illustrates a free pipe log.

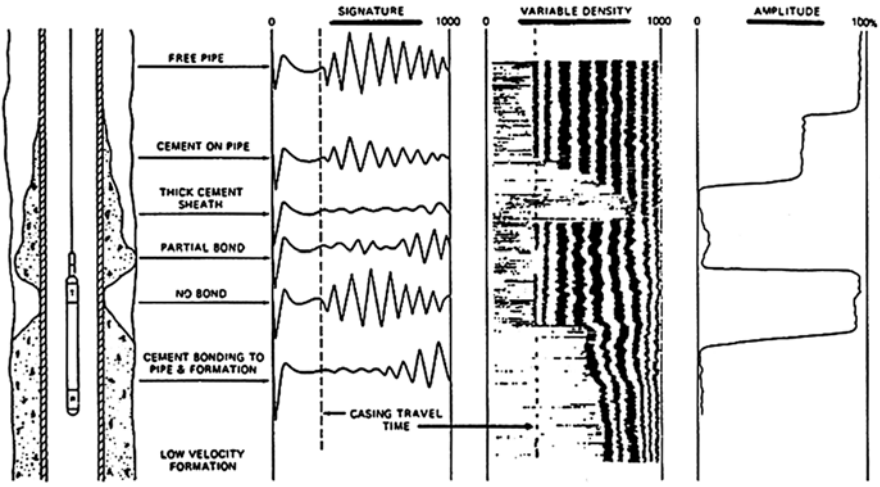

Fig. 12.21 CBL schematic showing VDL displays. Courtesy Baker Atlas

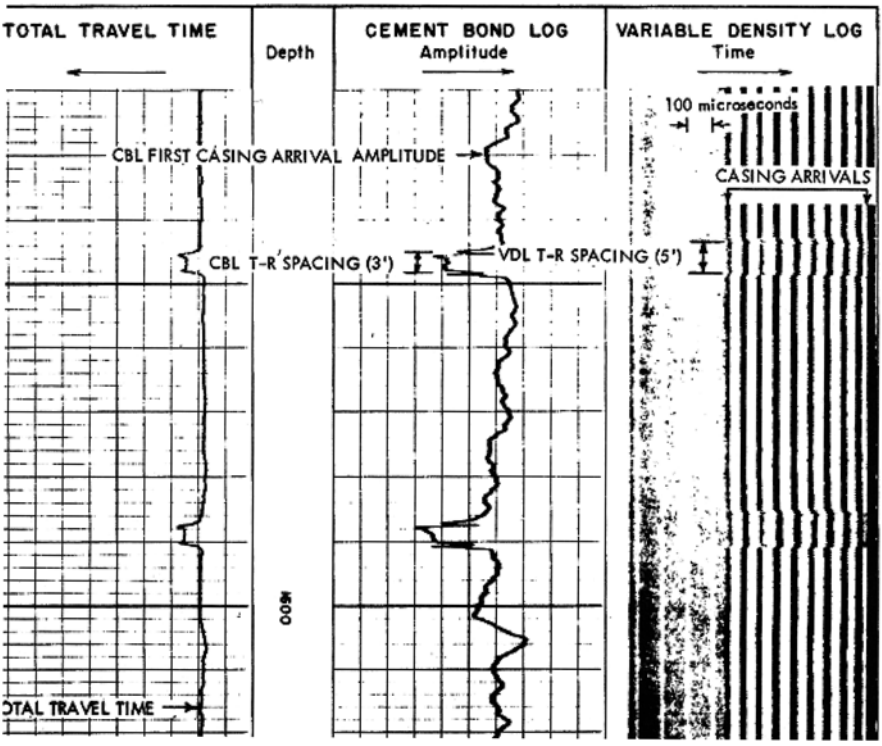

Fig. 12.22 Free-pipe CBL/VDL. Courtesy Schlumberger

Free Pipe in Deviated Hole

Where the pipe rests on the low side of a deviated hole, acoustic coupling can take place between the pipe and the formation. In that case, the VDL may show formation arrivals. Do not be fooled. Diagnostics are:

1. Transit time slightly reduced (tool eccentered)
2. Amplitude high
3. VDL shows weak casing arrivals and strong-to-moderate formation arrivals

Figure 12.23 illustrates this case

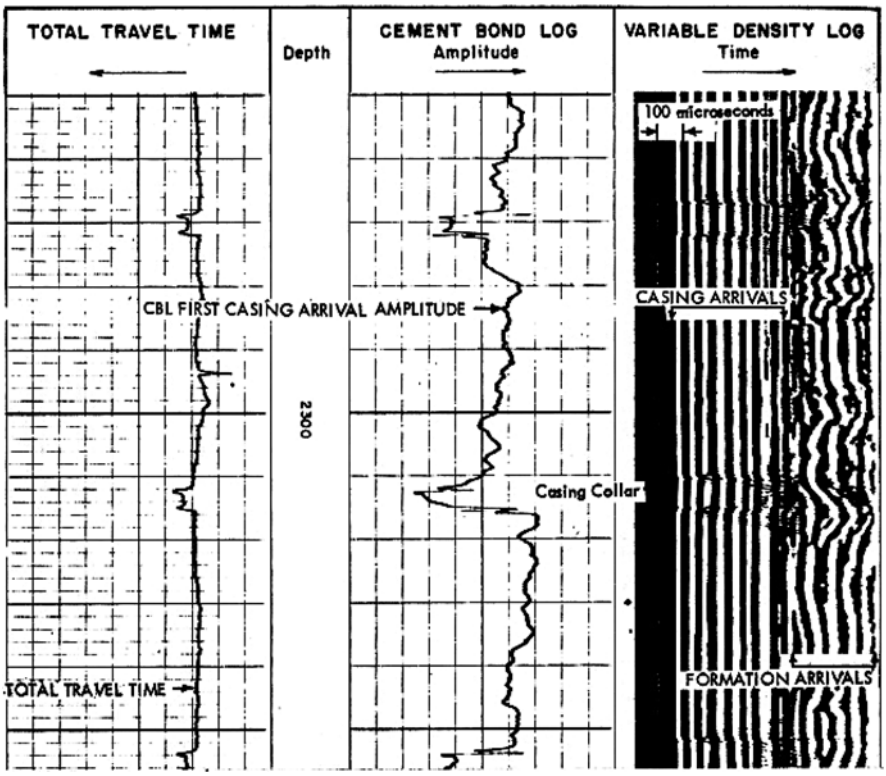

Fig. 12.23 CBL/VDL in deviated hole. Courtesy Schlumberger

Well-Cemented Pipe

In the ideal case of well-cemented pipe, the following diagnostics can be expected:

1. Low amplitude (a few millivolts only)
2. Transit time increasing due to stretch or cycle skips
3. Strong formation arrivals

Figure 12.24 illustrate logs for a well-cemented section.

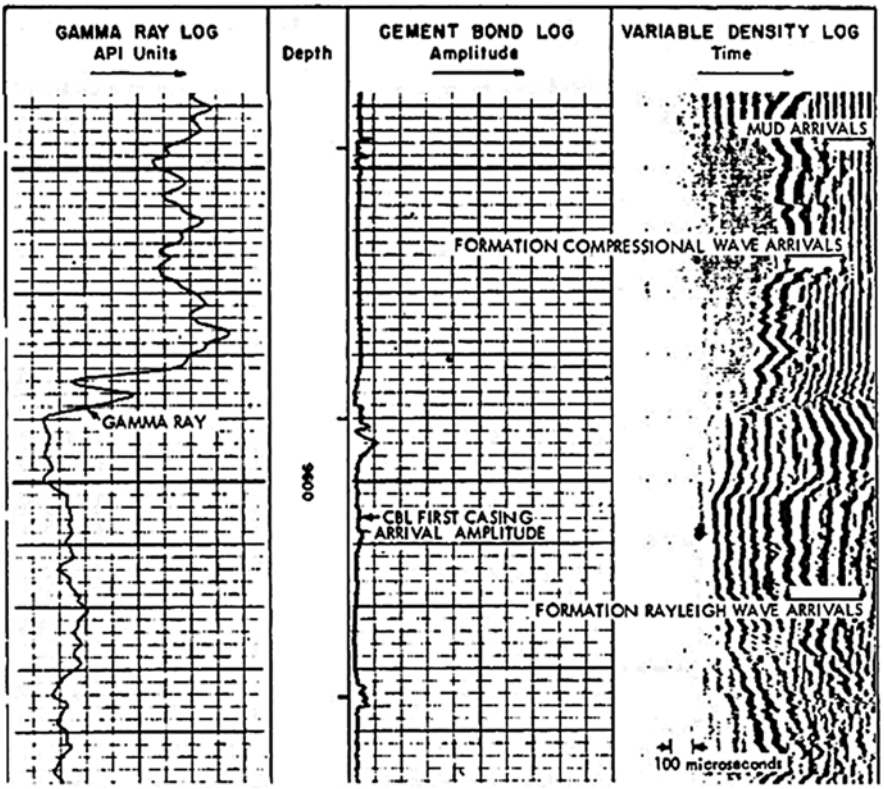

Fig. 12.24 CBL/VDL in a well-cemented pipe. Courtesy Schlumberger

Quick-Look for Conventional CBL Interpretation

Table 12.3 provides a quick-look summary of the diagnostics for the commonly found cement bond cases.

Table 12.3 Quick-look CBL diagnostics

Log		Cement Bonding		
Track	Parameter	None Free Pipe	Some Partial Bond	Complete 100% Bond Fm. & Csng
1	Δt (μsec/ft)	Steady	Steady	Ratty
2	Amplitude (mV)	High	Intermediate	Low
3	VDL Signature	Strong Csng Weak Fm.	Intermediate	Strong Fm. Weak Csng.

Microannulus/Channeling

It is not uncommon to find cases where it is difficult to assess whether partial bonding is due to channels or due to what is known as microannulus. Both cases may exhibit:

- Medium amplitude
- Moderate casing arrivals
- Moderate formation arrivals

One way to determine the cause of partial bonding is to rerun the log with pressure on the casing. The microannulus is a microscopic gap between the cement and the casing that forms very poor acoustic coupling. Thus, although cement is present, the log suggests otherwise. The root cause of the microannulus may be due to one or the other of the following:

(a) Pressure was held on the casing while the cement cured. Subsequent release of the casing pressure allowed the microannulus to form.
(b) The casing expanded due to the heat generated by the curing process and subsequently cooled and shrank back to normal size.
(c) Cold completion fluid was circulated just prior to running the CBL, causing thermal contraction of the casing.
(d) A completion fluid of lesser density was used to circulate out a heavy mud used to displace cement. The resulting reduction in pressure in the casing allowed the microannulus to form.

If a microannulus is suspected in the zone of interest, rerun the log with 500–1,000 psi at the casing head. The service company should come equipped with the appropriate pressure-control equipment to do the job safely. If the CBL amplitude is lower on the rerun under pressure, then there is no need to squeeze. No case has ever been documented where communication existed across a microannulus zone. If the CBL does not improve, channeling may be suspected and a squeeze should be attempted. Figure 12.25 documents a microannulus case.

Figure 12.26 is a useful reference for determining the pressure required to expand a given casing by a given amount. Normal microannuli are between 0.005 and 0.01 in..

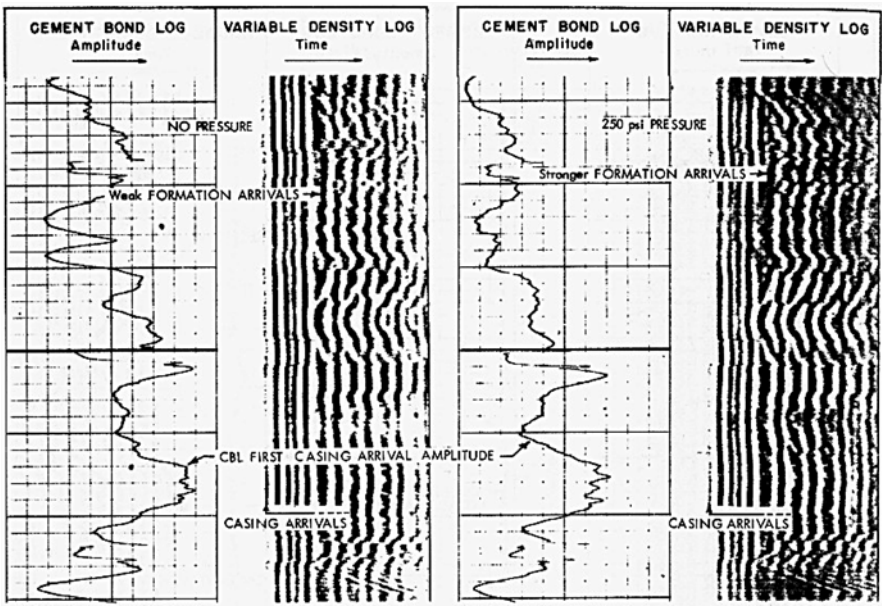

Fig. 12.25 Microannulus case. Courtesy Schlumberger

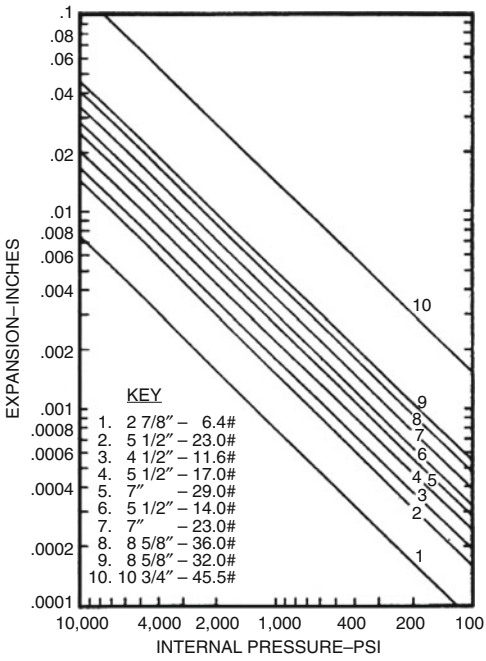

Fig. 12.26 Pressure vs. expansion for common casings. Reprinted with permission of the SPE from Carter and Evans. ©1964

Radial Differential Temperature Logging

In Chap. 8 the use of the Radial Differential Temperature survey for the detection of fluid flow behind pipe via channels in the cement was covered. Anchor springs hold the tool in the casing and a rotation motor is actuated to cause the sensor to scan round the casing through 360°. This directional temperature sensor detects temperature fluctuations if a channel with fluid flowing in it is present. For further details the reader is directed to the complete coverage in the cited chapter.

Ultrasonic Cement Bond Logging

Ultrasonic borehole imaging tools are widely used to produce images of the borehole wall in open-hole logging applications. These images are useful for providing the analyst with textural, structural, and sedimentary information about the column logged as well as offering geomechanical data regarding the presence and orientation of fractures and/or breakouts. The tools used to produce these images consist of a rotating emitter of ultrasonic waves that travel though the fluid in the borehole and are reflected back from the borehole wall. The time taken to travel from the emitter back to a receiver is an indication of the borehole diameter and the amplitude of the returning signal and indication of the material found at the reflecting interface.

This same technology can also be applied in cased-holes to evaluate cement behind casing. An ultrasonic transducer emits a beam of ultrasonic energy in a 300–600 kHz band. This energy pulse causes the casing to ring or resonate in its thickness dimensions. The vibrations die out quickly or slowly depending on the material behind the casing. Most of the energy is reflected back to the transducer where it is measured; the remainder passes into the casing wall and echoes back and forth until it is totally attenuated. Figure 12.27 gives a schematic of the transducer and the compressional wave paths through the completion fluid, reflection at the inner casing wall (first interface), reflection at the outer casing/cement boundary (second interface), and refection at the cement/formation boundary (third interface).

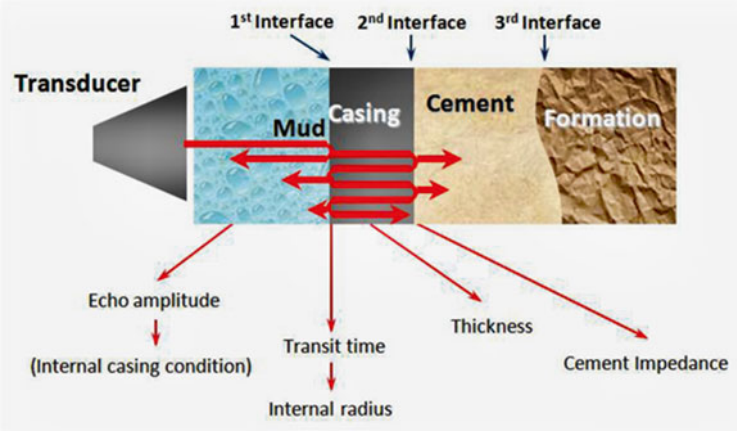

Fig. 12.27 Ultrasonic travel paths. Courtesy Schlumberger

By integrating both directional (rotational) and amplitude data of the complete wave train, 3D views of the state of the materials behind the casing can be constructed as shown in Fig. 12.28 which shows a portion of the cemented pipe with a channel.

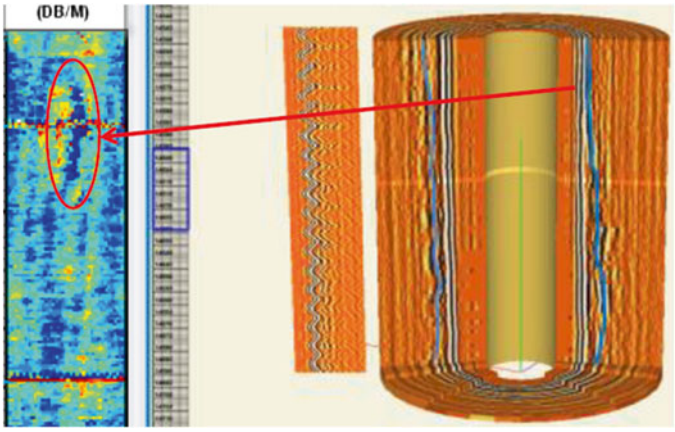

Fig. 12.28 Channel detection using the third echo interface. Courtesy Schlumberger

The data can also be presented as a series of color-coded tracks as illustrated in Fig. 12.29. The two principal diagnostics are presented in second and third tracks counted from the right-hand side of the log presentation.

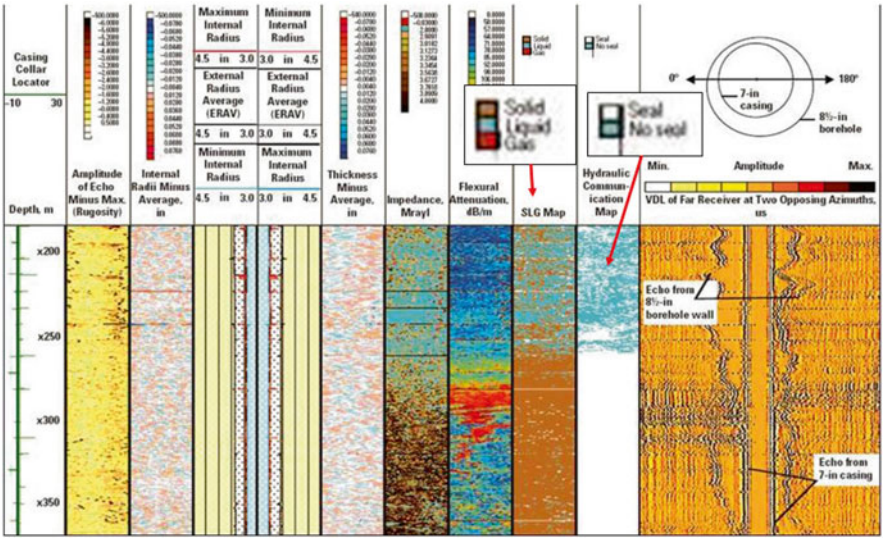

Fig. 12.29 Isolation scanner presentation. Courtesy Schlumberger

The "SLG Map" distinguishes between Solid, Liquid, and Gas in the annular space between the casing and the formation. Solid is colored an orange–brown shade, liquid blue and gas red. The "Seal-No Seal" track in similar fashion uses a simple color code to distinguish between a good seal (white) and no seal (blue). Figs. 12.30, 12.31, and 12.32 show, respectively, cases with well-cemented pipe, a cement top, and free pipe.

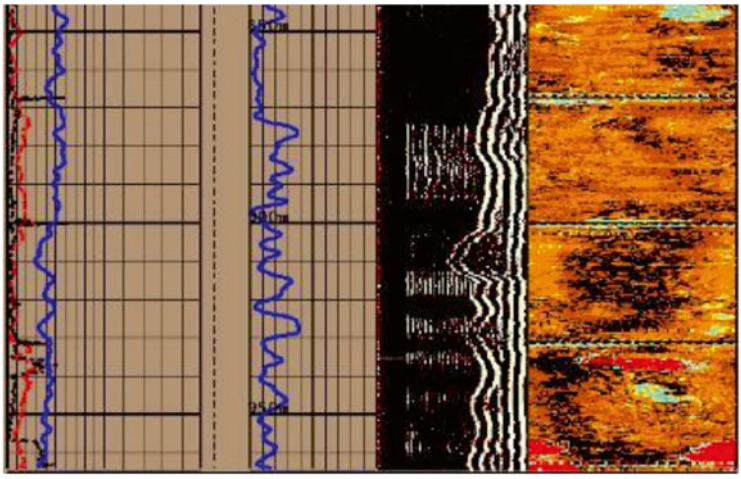

Fig. 12.30 Ultrasonic imager (USI) in well-cemented pipe. Courtesy Schlumberger

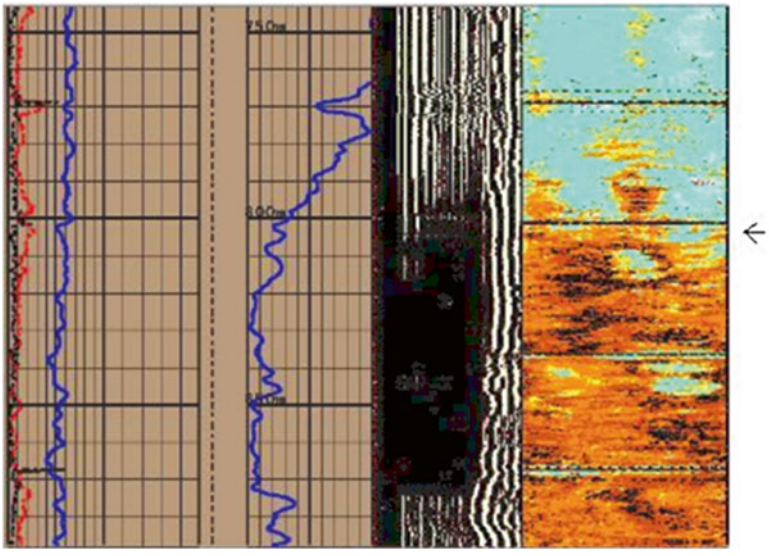

Fig. 12.31 Cement top (near 300 m). Courtesy Schlumberger

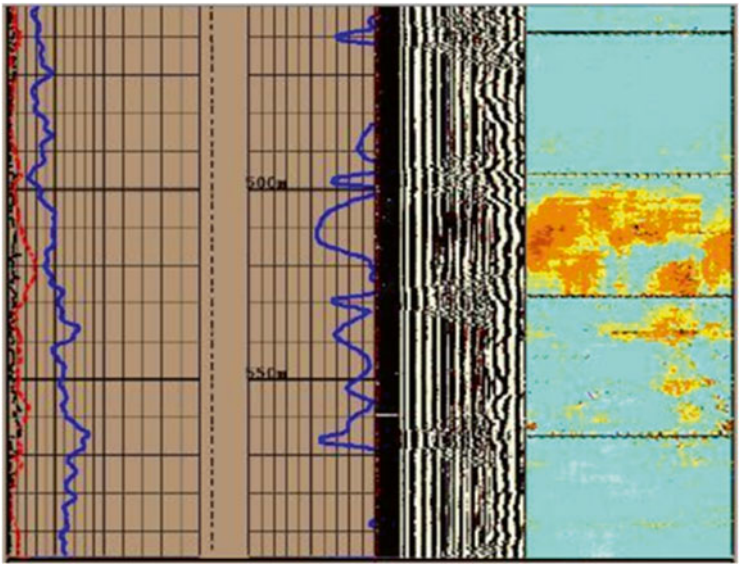

Fig. 12.32 Free pipe. Courtesy Schlumberger

An added refinement to the standard ultrasonic "pulse-echo" imaging technique is the generation and measurement of flexural waveforms using focused compressional waves and conventional amplitude detectors. Figure 12.30 shows the physical arrangement of the rotation transducers.

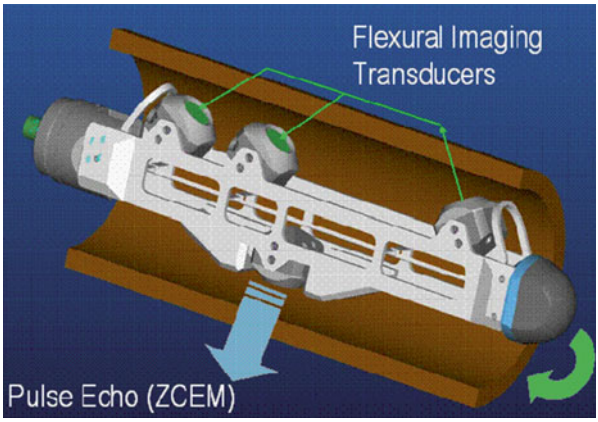

Fig. 12.33 Combined pulse-echo and flexural transducers. Courtesy Schlumberger

The addition of the flexural wave information allows for better cement evaluation when lightweight cements are used which have an acoustic impedance close to that of mud and in some cases can leave a conventional bond evaluation somewhat uncertain.

Log Quality Control

The two most important quality control aspects of CBL logging are:

1. Good centralization. Insist on at least three fin centralizers near the transmitter/receiver array and spring centralizers, top and bottom of the entire tool string.
2. Calibration tails should conform to the published service company specifications.

Appendix: Frequently Used Casing Dimensions

OD (inches)	Weight[a] (per foot)	Nominal (ID)	Drift diameter[b]
4	11.60	3.428	3.303
4½	9.50	4.090	3.965
	11.60	4.000	3.875
	13.50	3.920	3.795
4¾	16.00	4.082	3.957
5	11.50	4.560	4.435
	13.00	4.494	4.369
	15.00	4.408	4.283
	17.70	4.300	4.175
	18.00	4.276	4.151
	21.00	4.154	4.029
5½	13.00	5.044	4.919
	14.00	5.012	4.887
	15.00	4.974	4.849
	15.50	4.950	4.825
	17.00	4.892	4.767
	20.00	4.778	4.653
	23.00	4.670	4.545
5¾	14.00	5.290	5.165
	17.00	5.190	5.065
	19.50	5.090	4.965
	22.50	4.990	4.865

(continued)

(continued)

OD (inches)	Weight[a] (per foot)	Nominal (ID)	Drift diameter[b]
6	15.00	5.524	5.399
	16.00	5.500	5.375
	18.00	5.424	5.299
	20.00	5.352	5.227
	23.00	5.240	5.115
6–5/8	17.00	6.135	6.010
	20.00	6.049	5.924
	22.00	5.989	5.864
	24.00	5.921	5.796
	26.00	5.855	5.730
	26.80	5.837	5.712
	28.00	5.791	5.666
	29.00	5.761	5.636
	32.00	5.675	5.550
7	17.00	6.538	6.413
	20.00	6.456	6.331
	22.00	6.398	6.273
	23.00	6.366	6.241
	24.00	6.336	6.211
	26.00	6.276	6.151
	28.00	6.214	6.089
	29.00	6.184	6.059
	30.00	6.154	6.029
	32.00	6.094	5.969
	35.00	6.004	5.879
	38.00	5.920	5.795
	40.00	5.836	5.711
7–5/8	20.00	7.125	7.000
	24.00	7.025	6.900
	26.40	6.969	6.844
	29.70	6.875	6.750
	33.70	6.765	6.640
	39.00	6.625	6.500
8–5/8	24.00	8.097	7.972
	28.00	8.017	7.892
	32.00	7.921	7.796
	36.00	7.825	7.700
	38.00	7.775	7.650
	40.00	7.725	7.600
	43.00	7.651	7.526
	44.00	7.625	7.500
	49.00	7.511	7.386

(continued)

(continued)

9	34.00	8.290	8.165
	38.00	8.196	8.071
	40.00	8.150	8.025
	45.00	8.032	7.907
	55.00	7.812	7.687
9–5/8	29.30	9.063	8.907
	32.30	9.001	8.845
	36.00	8.921	8.765
	40.00	8.835	8.679
	43.50	8.755	8.599
	47.00	8.681	8.525
	53.50	8.535	8.379
10	33.00	9.384	9.228
10¾	32.75	10.192	10.036
	40.00	10.054	9.898
	40.50	10.050	9.894
	45.00	9.960	9.804
	45.50	9.950	9.794
	48.00	9.902	9.746
	51.00	9.850	9.694
	54.00	9.784	9.628
	55.50	9.760	9.604
11¾	38.00	11.150	10.994
	42.00	11.084	10.928
	47.00	11.000	10.844
	54.00	10.880	10.724
	60.00	10.772	10.616
12	40.00	11.384	11.228
13	40.00	12.438	12.282
13–3/8	48.00	12.715	12.559
16	55.00	15.375	15.187
18–5/8	78.00	17.855	17.667
20	90.00	19.190	19.002
21½	92.50	20.710	20.522
	103.00	20.610	20.422
	114.00	20.150	20.322
24½	100.50	23.750	23.562
	113.00	23.650	23.462

[a]Weight per foot (in pounds) is given for plain pipe (no threads or coupling)
[b]Drift diameter is the guaranteed minimum internal diameter of any part of the casing. Use drift diameter to determine the largest-diameter equipment that can be safely run inside the casing. Use internal diameter (ID) for calculations of volume capacity

Bibliography

Al-Suwaidi AS, Al-Marri FM, Sultan E, Ibrahim ME-S, Jammeli K. Increased certainty in determination of zonal isolation through the integration of annulus geometry imaging and improved solid-fluid discrimination. In: SPE-120061-PP, 16th SPE Middle East oil and gas show and conference, Bahrain, March 2009.

Brown HD, Grijalva VE, Raymer LL. New developments in sonic wave train display and analysis in cased holes. In: Log Analyst (Jan–Feb 1971), p. 27–40.

Chang SK, Everhart AH. A study of sonic logging in cased borehole, Paper SPE 11034. In: Presented at the 57th Annual Technical Conference and Exhibition, New Orleans, Sept 26–29, 1982.

Froelich B, Pittman D, Seeman B. Cement evaluation tool-a new approach 10 cement evaluation, Paper SPE 10207. In: Presented at the 56th Annual Technical Conference and Exhibition, San Antonio, Oct 5–7, 1981; J. Pet. Tech (August 1982).

Grosmangin M, Kokesh FP, Majani P. A sonic method for analyzing the quality of cementation of borehole casings. In: J. Pet. Tech. (Feb. 1961) p. 165–171; Trans., AIME.

Kuijk R van, Zeroug S, Froelich B, Allouche M, Bose S, Miller D, la Calvez J-L, Schoepf V, Pagnin A. A novel ultrasonic cased-hole imager for enhanced cement evaluation. In: IPTC paper 10546, Doha, Qatar, 21–23 November, 2005.

McGhee BF, Vacca HL. Guidelines for improved monitoring of cementing operations. In: SPWLA Trans. 21st Logging Symposium, July 1980.

Nelson E, Guillot D. Well cementing. 2nd ed. Houston: Schlumberger; 2006.

Pardue GH, Morris RL, Gollwitzer LH, Moran JH. Cement bond log-a study of cement and casing variables. In: J. Pet. Tech. (May 1963), p. 545–555; Trans., AIME.

Schlumberger's cement evaluation tool. Schlumberger, SMP/5040.

Tian J, Wang Q, Guo Q. Casing integrity evaluation in deep well with extreme heavy mud in tarim basin. In: SPE 140982 EUROPEC/EAGE Annual Conference and Exhibition, Vienne, Austria, May 2100.

Answers to Text Questions

Question #12.1
E_9 or E_{11}

Question #12.2
400 psi

Casing Inspection 13

Inspection of the mechanical state of the completion string is an important aspect of production logging. Many production (or injection) problems can be traced back to mechanical damage to, or corrosion of, the completion string. A number of inspection methods are available, including:

- Multi-fingered caliper logs
- Electrical-potential logs
- Electromagnetic inspection devices
- Borehole video cameras

Of these, the majority measure the extent to which corrosion has taken place. Only the electrical-potential log may indicate where corrosion is currently taking place. With the exception of the caliper logs, all the devices require that the tubing be pulled before running the survey, since (1) most are designed to inspect casing rather than tubing and (2) most are large-diameter tools.

Caliper Logs

Various arrangements of caliper mechanisms are available to gauge the internal shape of a casing or tubing string. Figure 13.1 illustrates three such tools. Table 13.1 lists the various sizes available (Dia-Log), their respective number of feelers, and the appropriate casing size.

Tubing Profiles

Tubing-profile calipers will determine the extent of wear and corrosion, and will detect holes in the tubing string—all in a single run into the well. The large number of feelers

R.M. Bateman, *Cased-Hole Log Analysis and Reservoir Performance Monitoring*,
DOI 10.1007/978-1-4939-2068-6_13

on each size of caliper insures detection of even very small irregularities in the tubing wall. In pumping wells, the tubing caliper log may be run by a single operator without the need for a pulling unit crew to be present. A "pullsheet" showing the maximum percentage of wall loss of every joint of tubing in the wall may be prepared. Before the well is pulled, a program for rearranging the tubing string can be provided. Moving partially worn joints nearer the surface and discarding thin-wall joints substantially prolong the effective life of tubing strings and reduce pulling costs in pumping wells. In flowing or gas-lift wells, the tubing-profile caliper provides an economical method to periodically check for corrosion damage, monitor the effectiveness of a corrosion inhibitor program, or detect damaged tubing joints when "working over" a well.

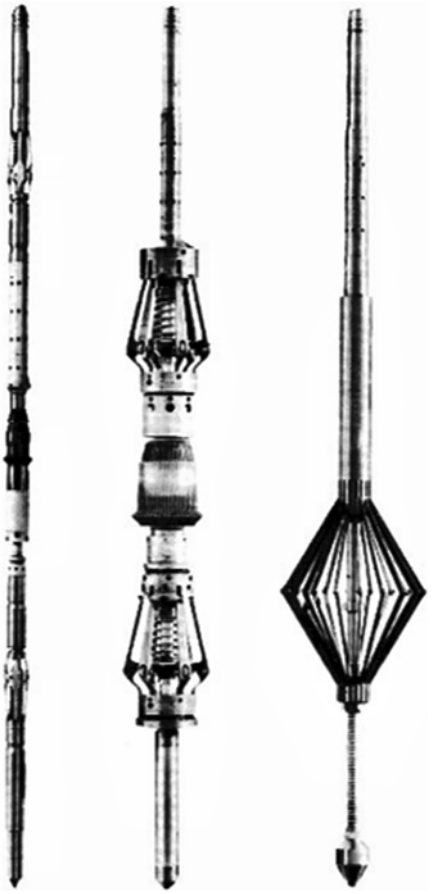

Fig. 13.1 Casing and tubing-profile caliper tools. Courtesy the DIA-LOG Company

An accessory tool, which may be run in combination with the tubing-profile caliper, is the Split Detector. This tool, functioning much like a magnetic collar locator, is designed to detect and log vertical splits or hairline cracks in the tubing that might be difficult to locate with the profile caliper. In practice, the split detector is used to log down the tubing, and the profile caliper to log up the tubing. This gives a

complete inspection for wall thickness and splits in one run of the cable in the well. Examples of a tubing profile and a split-detector log are shown in Fig. 13.2.

Table 13.1 Caliper sizes

Tool diameter (in.)	Number of feelers	Casing or tubing OD (in.)
Casing-profile calipers		
3 5/8	40	4 1/2 to 6
5 5/8	64	6 5/8 to 7 5/8
7 1/4	64	8 5/8 to 9
7 3/4	64	9 5/8
8 1/4	64	10 3/4
9 9/16	64	11 3/4
11 5/16	64	13 1/8
13 5/8	64	13 1/8
13 5/8	64	16
17 5/8	64	20
Tubing-profile calipers		
1 1/2	20	2
1 1/2	20	2 1/16
1 3/4	26	2 3/8
2 3/16	32	2 7/8
2 11/16	44	3 1/2
3 1/32	44	4

Casing Profiles

Casing-profile calipers are available to log 4½ through 20-in. OD casing. These tools are especially valuable where drilling operations have been carried on for an extended period of time through a string of casing. The determination of casing wear is of great importance when deciding if a liner can be safely hung, or if a full production string is required. In producing wells, the casing-profile caliper will locate holes or areas of corrosion that may require remedial work.

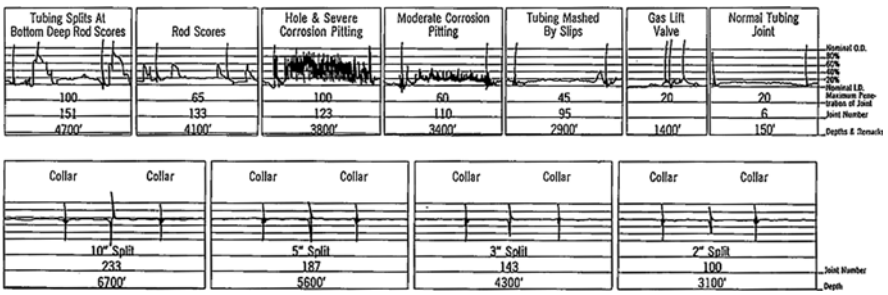

Fig. 13.2 Tubing-profile and split-detector logs. Courtesy DIA-LOG Company

These tools are also valuable when abandoning wells because they permit grading of casing to be salvaged before it is pulled. Figure 13.3 gives examples of casing-profile logs.

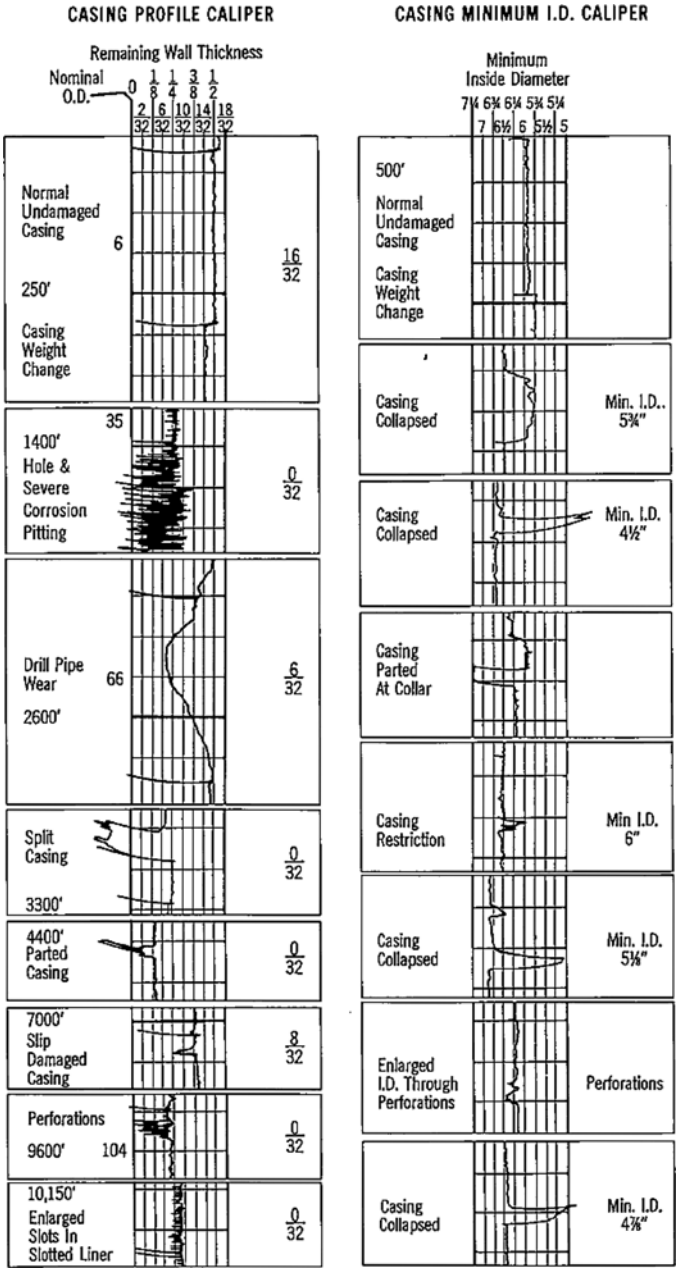

Fig. 13.3 Casing-profile logs. Courtesy DIA-LOG Company

Electrical-Potential Logs

An electrical-potential log determines the flow of galvanic current entering, or leaving, the casing. This will indicate not only where corrosion is taking place, and the amount of iron being lost, but also where cathodic protection will be effective. The magnitude and direction of the current within and external to the casing is derived mathematically from electrical-potential measurements made at fixed intervals throughout the casing string. In order to achieve reliable results from this kind of survey, the borehole fluid must be an electrical insulator; that is, the hole must be either empty or filled with oil or gas. Mud, or other aqueous solutions, will provide a "short" that invalidates the measurements. The log itself is a recording vs. depth of the small galvanic voltages detected. Figure 13.4 illustrates the tool used to make the measurements of potentials and current flow.

Fig. 13.4 Casing-corrosion tool. Courtesy Schlumberger

Figure 13.5 shows an interpretation of casing-potential profile logs run before (left panel) and after cathodic protection was installed. Note that the metal loss has been reduced to practically zero (right panel) by the application of appropriate cathodic protection.

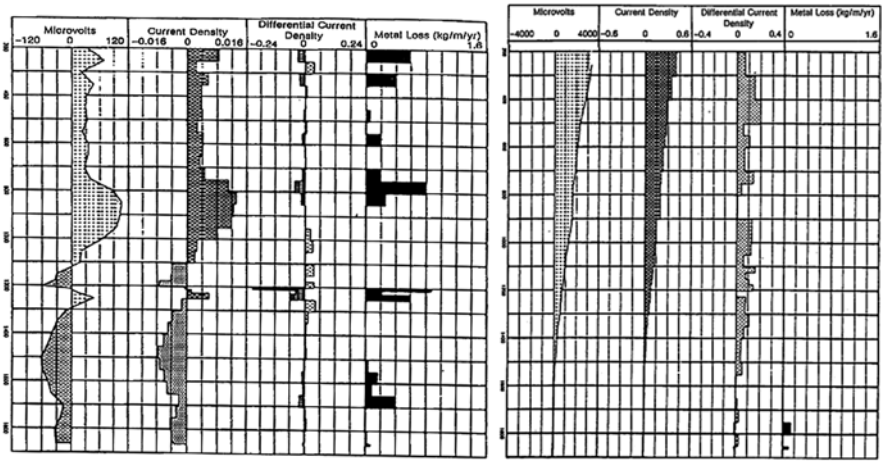

Fig. 13.5 Casing-potential profile before (*left*) and after (*right*) cathodic protection. Courtesy Baker Atlas

Electromagnetic Devices

The most common inspection tools used to assess casing corrosion are of the electromagnetic type. They come in two versions, those that attempt to measure the remaining metal thickness in a casing string and those that try to detect defects in the inner or outer wall of the casing. Although frequently run together, these tools will be discussed separately.

Electromagnetic Thickness Tool (ETT)

The electromagnetic thickness tools are available under a variety of trade names, such as ETT (Schlumberger), Magnelog (Baker Atlas), Electronic Casing Caliper Log (McCullough), and Defectoscope (TGT). They operate in a manner similar to open-hole induction tools. Each consists of a transmitter coil and a receiver coil. An alternating current is sent through the transmitter coil. This sets up an alternating magnetic field that interacts with both the casing and the receiver coil (see Fig. 13.6). The coils are spaced about three casing-diameters apart to ensure that the flux lines sensed by the receiver coil are those that have passed through the casing. The signal

induced in the receiver coil will be out of phase with the transmitted signal. In general, the phase difference is controlled by the thickness of the casing wall. The raw log measurement is one of phase lag in degrees and the log is scaled in degrees.

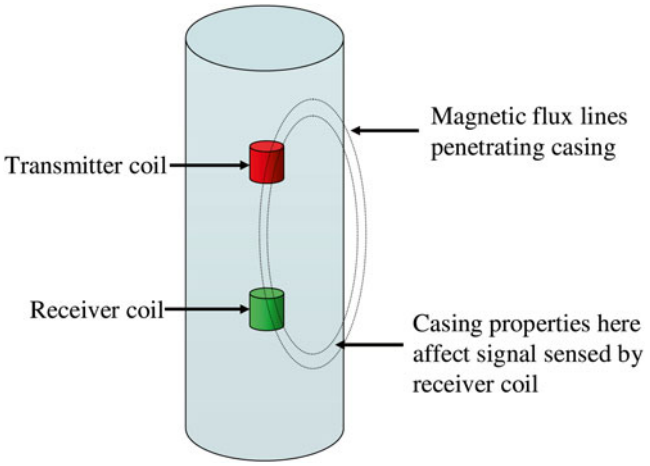

Fig. 13.6 Electromagnetic thickness tool

Figure 13.7 illustrates a modern tool that is tuned to allow measurement of the thickness of a casing string even while the tool itself is inside tubing.

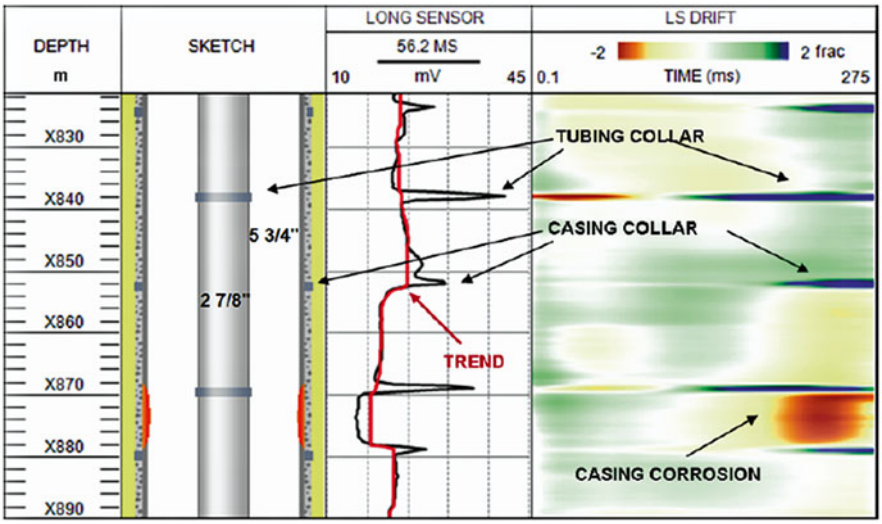

Fig. 13.7 Casing corrosion detected from tool inside tubing. Courtesy TGT®

Figure 13.8 illustrates the response of an electromagnetic thickness log when encountering a hole in the tubing string. Note the presentation is calibrated in actual tubing wall thickness. This rescaling requires that the operator make some calibration readings in a casing of the type present in the well. It is quite common to see quite large differences in thickness between adjacent stands due to a number of variables such as the drift diameter of the pipe, the weight/ft, the relative magnetic permeability of the steel used, etc.

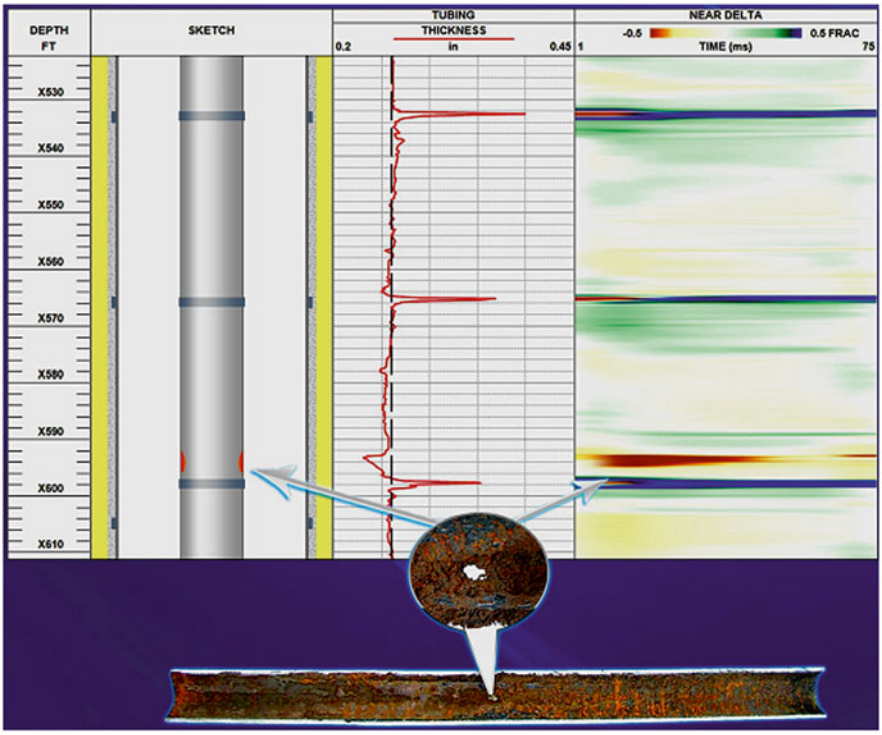

Fig. 13.8 Tubing thickness measurement. Courtesy TGT®

The electromagnetic-type tools are good at finding vertical splits in pipe since the magnetic-flux lines pass perpendicular to the casing wall. A horizontal circumferential anomaly is less well defined.

Pipe Analysis Log (PAL)

Another closely related measurement uses a slightly different technique and forms the basis of the Pipe Analysis Log (PAL), also known as the Vertilog. Two electromagnetic measurements are of interest in the context of the pipe analysis tool; magnetic-flux leakage and eddy-current distortion.

Flux Leakage

If the poles of a magnet are positioned near a sheet of steel, magnetic flux will flow through the sheet (Fig. 13.9). So long as the metal has no flaws, the flux lines will be parallel to the surface. However, at the location of a cavity, either on the surface of the sheet or inside it, the uniform flux pattern will be distorted.

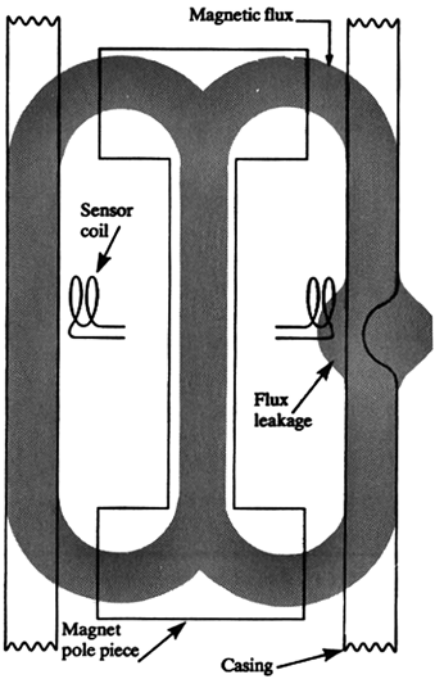

Fig. 13.9 Magnetic-flux-leakage principle. Courtesy Schlumberger

The flux lines will move away from the surface of the steel at the location of the anomaly, an effect known as flux leakage. The amount of flux distortion will depend upon the size of the defect. If a coil is moved at a constant speed along the direction of magnetic flux parallel to the metal sheet, a voltage will be induced in the coil as it passes through the area of flux leakage. The larger the anomaly, the greater the flux leakage, and therefore the greater the voltage induced. The magnetic flux is distorted on both faces of the sheet, regardless of the location of the defect, and therefore the coil only needs to be moved along one surface to survey the sheet completely. As the coil must be moved through a changing magnetic flux to produce a voltage, no signal is generated when it is moved parallel to the surface of an undamaged sheet of steel.

Eddy Currents

When an alternating current of relatively high frequency is applied to a coil close to a sheet of steel, the resulting magnetic field induces eddy currents in the steel (Fig. 13.10). These eddy currents in the turn produce a magnetic field that tends to cancel the original field; and the total magnetic field is the vector sum of the two fields. A measure voltage would be induced in a sensor coil situated in the magnetic field. The generation of eddy currents is, at relatively high frequencies, a near-surface effect; so, if the surface of the steel adjacent to the coil is damaged, the magnitude of the eddy currents will be reduced; and, consequently, the total magnetic field will be increased. This will result in a variation in the voltage in the sensor coil. A flaw in the sheet of metal, on the surface away from the coils, will not be detected; and, depending upon its distance from the surface, a cavity within the sheet will not influence the eddy currents either.

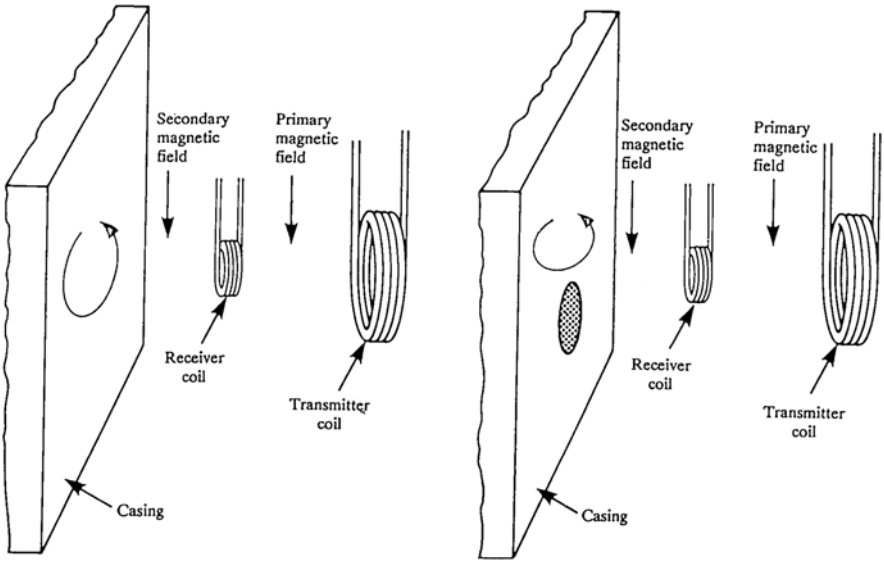

Fig. 13.10 Eddy-current principle. Courtesy Schlumberger

Tool Principle

The measuring sondes of pipe analysis type tools consist of an iron core with the pole pieces of an electromagnet at each end, and multiple sensor pads arrayed between the pole pieces (Fig. 13.11). The arrays are arranged to ensure complete coverage of the inner surface of the casing. Each of the pads contains a transmitting

coil for eddy-current measurement, and two sensor coils wound in opposite directions for both flux-leakage and eddy-current measurements. The sensor coils are wound in such a way that for both measurements there is zero voltage so long as no anomaly exists, but a signal will be produced when the quality of the casing changes. The same sensor coils can be used for both measurements, as two distinct frequencies are involved. Typically a frequency of 2 kHz is used for measurement of the eddy current, giving a depth of investigation of about 1 mm. The sensor pads are mounted on springs so that they are held in contact with the casing, facilitated through centralization of the sonde. Various sizes of magnet pole pieces are available and are selected according to the inside diameter of the casing, to optimize the signal strength for the flux-leakage measurement. The flux-leakage data correspond to anomalies located anywhere in the casing, while eddy-current distortion only occurs at the inside wall of the casing.

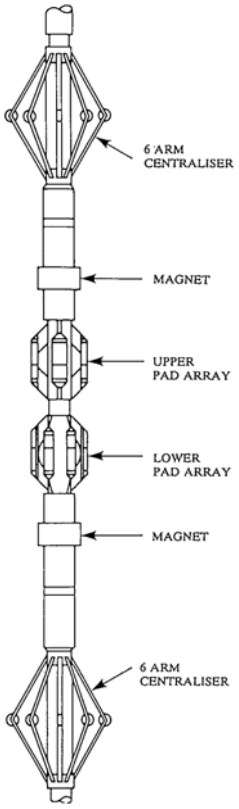

Fig. 13.11 One embodiment of a pipe analysis tool. Courtesy Schlumberger

Interpretation

Measurements made by the pipe analysis tools are generally only suitable for qualitative interpretation. This is because any voltages induced in the sensor coils are dependent not only upon the size of any flaws in the casing, but also upon the magnetic permeability of the casing, the logging speed, and the abruptness of a defect. The measurement is therefore primarily used to locate the presence of small defects in the casing, such as pits and holes; defects such as a gradual decrease of the wall thickness cannot be detected. These devices will give zero signal in the two extremes of no casing and perfect casing (except at the collars), so the electromagnetic thickness tool should also be used to measure the casing-wall thickness, in order to obtain a complete picture of the state of the casing.

Since two sets of data are recorded with one set influenced by defects occurring anywhere in the casing and the other by faults on the inner surface, it can be inferred by examination whether the casing is damaged on the inner or outer wall, assuming that there is no defect within the casing. Although the magnetic-flux bulges away from both sides of the casing at the location of a defect, the effect is greater on the side of the flaw, hence for the flux-leakage measurement, smaller defects can be detected on the inner surface than on the outer surface.

Eddy-current measurements are not able to detect flaws with a diameter smaller than about 0.39″, while the flux-leakage limit is somewhat lower (0.25″). This means that it cannot be determined whether an anomaly less than 0.39″ in size is on the inner or outer surface. If a deflection is noted on the eddy-current measurement but not on the flux measurement, it is assumed that the defect on the inner wall is less than 1 mm deep, and can usually be ignored. In addition, the flux-leakage readings show events that are not due to casing damage, but rather to the presence of localized magnetization in the casing. If a reference survey is run in new casing then a time-lapse technique can be used to determine casing damage at a later time. Typical logs for a variety of defects and anomalies are represented in Figs. 13.12, 13.13, 13.14, 13.15, 13.16.

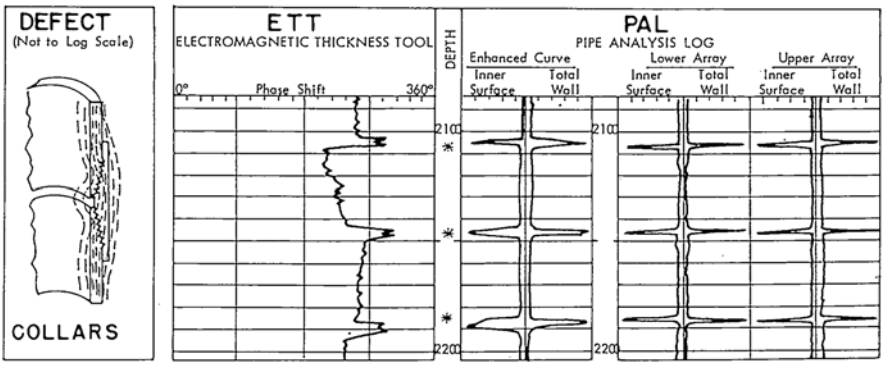

Fig. 13.12 Casing collars. Courtesy Schlumberger

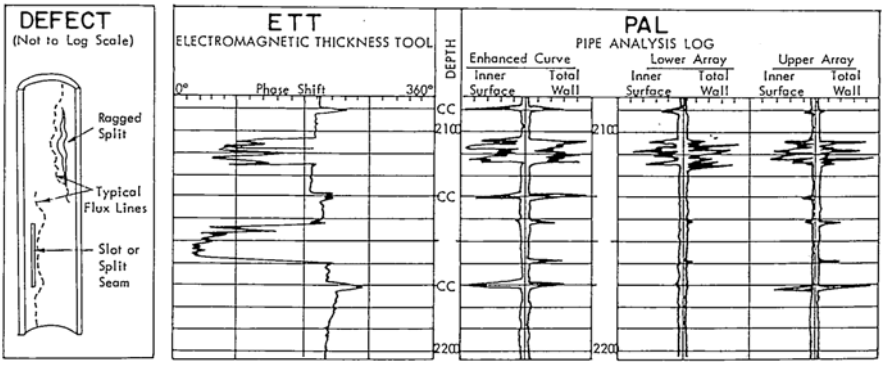

Fig. 13.13 Internal anomaly and OD pit. Courtesy Schlumberger

Comments

No inner-surface anomaly is indicated, therefore defect is neither measureable nor present on ID. Defect at 2127 ft is larger than defect at 2156 ft. Defect at 2127 ft may be severe OD defect since it has high PAT response and appears on ETT. Defect is probably OD pit or internal void due to ETT response at 2127 ft. OD pits are far more common than any other point defects not on ID. Magnetic anomalies have been observed in new N-80 casing. Stress points may occasionally be observed a few feet below collars as a result of clamping joint with tongs.

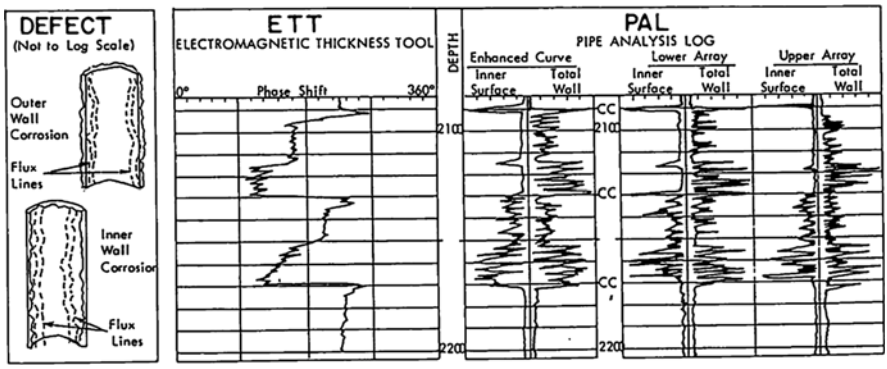

Fig. 13.14 Through hole and ID pit. Courtesy Schlumberger

Comments

If in new casing log indicates defects. If through holes they would correspond as follows:

2112 ft ¾″, through hole (drilled); 2119 ft ½″, through hole (drilled): 2132 ft 3/8″, through hole (drilled):2170 ft 1″ through hole (drilled). Inner-surface eddy-current measurement is not capable of less than ½″ diameter resolution. Flux-leakage response

larger for deep but small-diameter defects. Pad overlap effects apparent on both eddy-current and flux-leakage tests. Defect at 2158 ft does not show on flux-leakage (total wall) test and therefore is minor, <1 mm deep. Defect at 2164 ft shows larger on eddy-current than flux-leakage test, therefore shallow ID pit.

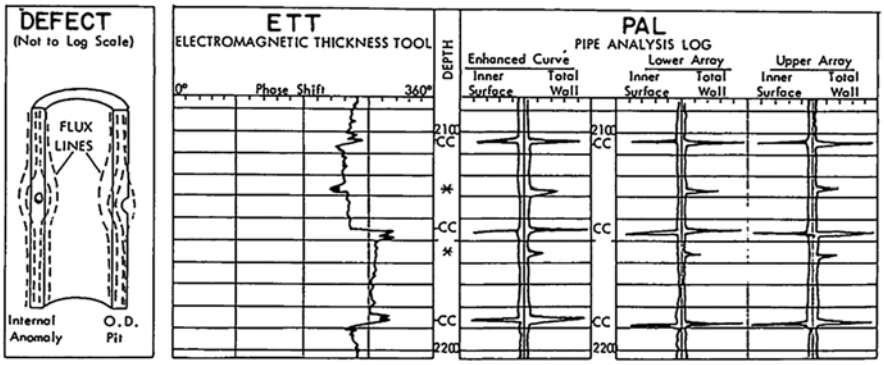

Fig. 13.15 Splits. Courtesy Schlumberger

Comments

Split from 2105 to 2115 ft is ragged. Note dramatic response to eddy-current (inner-surface) and flux-leakage (total wall) tests. ETT phase shift drops dramatically at split from 2105 to 2115 ft. Split from 2142 to 2159 ft cannot be determined with certainty using only the PAT. Since flux path leaks into wellbore only at ends of split, PAT indicates only point anomalies at 2142 and 2159 ft. Split from 2142 to 2159 ft shows up dramatically on ETT. With both ETT and PAT, this anomaly could easily be identified as a split seam in the casing.

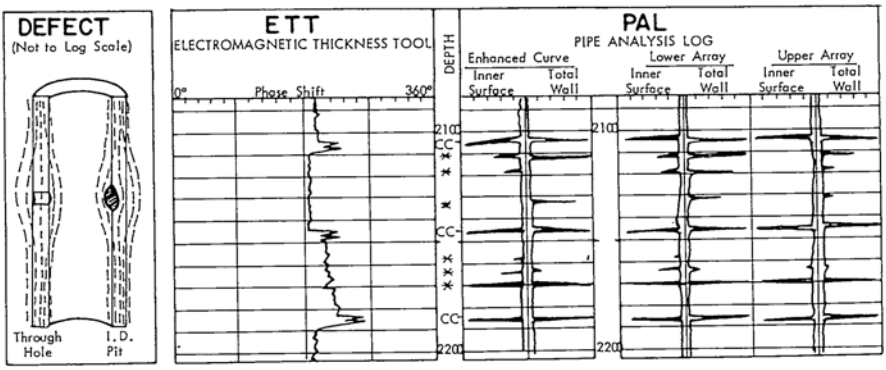

Fig. 13.16 Inner- and outer-wall corrosion. Courtesy Schlumberger

Comments
Joint from 2090 to 2130 ft has moderate outside-wall corrosion which becomes severe below about 2115 ft. A through hole appears to exist at 2116 ft. Note decrease in ETT phase shift from good casing above and along joint, verifying severe corrosion. Joint from 2130 to 2170 ft has moderate to severe interval-corrosion from 2130 to 2155 ft, and corrosion on inside is increasingly severe for remainder of joint. ETT verifies increasingly severe corrosion in lower part of joint from about 2130 to 2170 ft.

Borehole Televiewers

Three visualization tools are available for borehole scanning. The oldest is the Borehole Televiewer (BHTV) which uses a rotating ultrasonic transmitter and receiver to produce an image of the borehole or casing. An example of the BHTV log is given in Fig. 13.17.

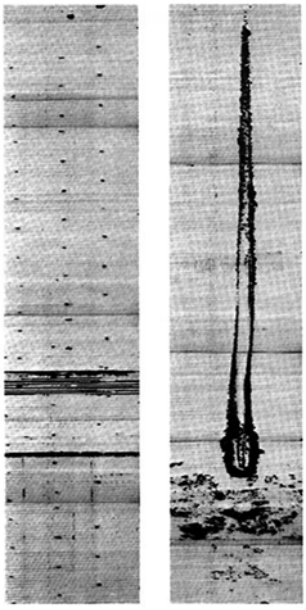

Fig. 13.17 BHTV log showing perforations (*left*) and split casing (*right*)

For practical results, this tool requires an unweighted fluid in the hole. With muds above 10 lb/gal, the signal is so attenuated as to give a useless log. Figure 13.18 illustrates the physical tool construction and modus operandi.

There are also wellbore inspection devices that use TV cameras and an intense light source to record and transmit visual images of the borehole wall to the surface. Figure 13.19 gives some examples of such images. Borehole television cameras provide digital records that can be viewed in real time when an immediate diagnosis is required as to the cause of obstructions in, or damage to, the casing.

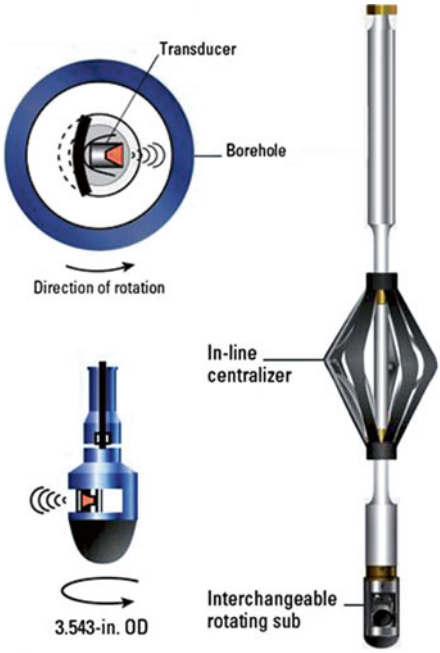

Fig. 13.18 Ultra sonic imager (USI). Courtesy Schlumberger

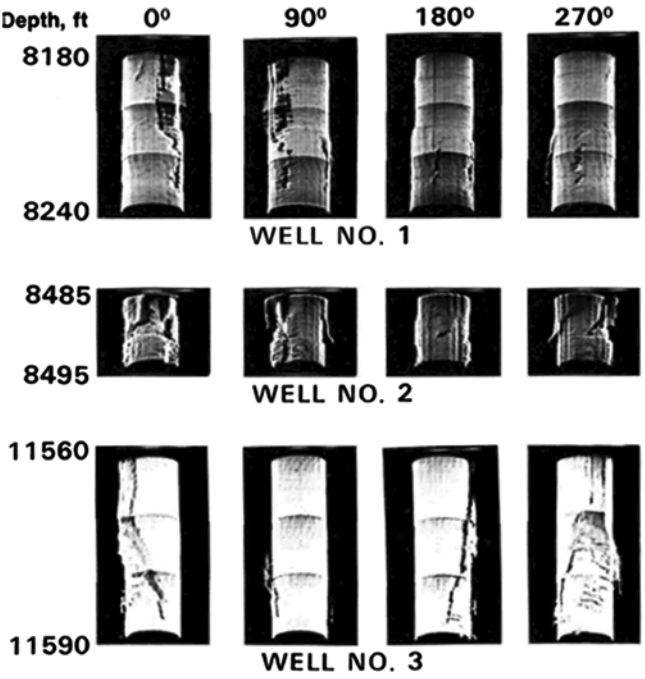

Fig. 13.19 Volumetric Scanning Log. Reprinted by permission of *World Oil*, Gulf Publishing Company from Broding 1982

Bibliography

Arbuzov AA, Bochkarev VV, Bragin AM, Maslennikova YS, Zagidullin BA, Achkeev AA, Kirillov RS. Memory magnetic imaging defectoscopy. In: SPE russian oil and gas exploration and production technical conferences and exhibition, Moscow, Russia; 16–18 Oct 2012, SPE 162054.

Broding RA. Volumetric scanning allows 3-D viewing of the borehole. World Oil. 1982;194(6):190–6.

Casing Evaluation Services, 1983. Dresser Atlas.

Cuthbert JF, Johnson Jr WM. New casing inspection log. Presented at the AGA operating section transmission conference, Bel Harbor, FL; 19–21 May 1975.

General Catalog. The DIA-LOG Company.

Illiyan IS, Colton Jr WJ, Brown GA. Test results of a corrosion logging technique using electromagnetic thickness and pipe analysis logging tools. J Pet Technol. 1983;35(4):801–8.

Well and Field Monitoring

14

It is now common to complete wells with permanent gauges that permit continuous or semi-continuous monitoring of the movement of fluids in the injection or production string. These gauges can come as wired or via the use of fiber optics, or both. Of these the fiber optics variety offers superior data gathering potential but at a higher cost.

Fiber Optic Sensing

Fiber optics are employed for two principal measurements:

***Distributed Temperature Sensing* (*DTS*)** which allows for a continuous monitoring of temperature along the entire length of a fiber optic cable. A pulse of light lasting 5 ns is sent down an optical fiber. This produces a 1 m band of light[1] that moves along the fiber and relays back temperature related information at each point along the way. Effectively the system measures the difference in temperature between the surface where the light pulse initiates and the point from which light is backscattered to the surface from any point downhole. If the surface temperature is known, then the actual downhole temperatures can be measured. The depth of the backscattering is determined by the time required for the pulse to return to the wellhead.

***Distributed Acoustic Sensing* (*DAS*)** which allows a continuous monitoring of sound noise, temperature, and strain related phenomenon along the entire length of a wellbore. DAS may also be referred as DSTS which stands for Distributed Strain and Temperature Sensing or DTSS short for Distributed Temperature and Strain Sensing. Only in the case where there is a pressure gauge at the end of the fiber will the pressures sensed along the well be absolute.

[1] Light travels at ≅300,000,000 m/s in vacuum. In a fiber optics cable light travels more slowly since the refractive index of the optical cable is ≅1.5. Thus in 5 ns a pulse travels $300{,}000{,}000 \times 5 \times 10^{-9}/1.5 = 1.0$ m.

R.M. Bateman, *Cased-Hole Log Analysis and Reservoir Performance Monitoring*,
DOI 10.1007/978-1-4939-2068-6_14

DTS Applications

DTS technology (in the United States) was first applied by NASA. They used fiber optics to monitor the fluid level inside fuel cells. As fluid levels within a cell vary local temperature changes help determine the new fluid level. This was used to obtain a good indication of fuel cell life. The same concept has since been adopted in both the upstream and downstream sectors of the oil industry. Some of the applications are:

Gas lift monitoring (whether a gas lift valve is open or to what extent).
Pressure vessels (measurement of interior wall temperature and/or temperature changes due to reactions).
Pipeline gas leak detection (fiber optic cable placed under the wrapper to monitor temperature change).
Cement job quality (real-time monitoring of fracturing and detection of inter-zonal communication).
Electric lines (overloading).
Packer seal (detection of fluid communication, i.e., under hydraulic fracturing process in open-hole well completion).
Static and dynamic fluid levels (determination in a wellbore, for Sucker Rod, Gas Lift & ESP applications).
Production in flow monitoring (real-time knowledge temperature distribution at perforations allows for inflow performance optimization).
Enhanced recovery—thermal and non-thermal (steam distribution at both injectors and producers can be monitored using DTS).
Electro submersible pumps (***ESP***) ***optimization*** (real-time monitoring of pump and electrical cable temperatures allows for pump performance optimization).
Real-time stimulation monitoring (most facets of hydraulic fracturing operations can be conveniently monitored including fracture height, well integrity, injection, packer seal efficiency as well as static and dynamic fluid levels).

Advantages of Fiber Optic Sensors

Fiber optic cables are essentially thin strands of glass and thus are made of electrically insulating material. Their use obviates the need for any electric cables. Thus they can be employed in high voltage environments since they are made from insulating material. They are also chemically passive and not subject to corrosion. Yet another added advantage is that a fiber optic cable is immune to electromagnetic interference. Glass fibers also have a very wide operating temperature range making them ideal for oilfield applications. Fiber optics are resistant to temperatures as high as 1100 °C. However, coating material resistance to such high temperatures may not

be as tolerant. Table 14.1 shows different coating materials and their suggested working temperature. Most fibers deployed for DTS and DAS applications are coated with polyimide for well monitoring purposes. Metal coatings are more thermally resistant than polymer coating; however, the coating process is more tedious and costly.

Table 14.1 Fiber optics coating material selection for high temperature

Coating material	Max. working temperature (°C)
UV—cured acrylate	100
UV—cured dual acrylate	150
Polyimide	400
Copper with polyimide	400
Aluminum	450
Copper alloy	600
Gold	>700

Disadvantages of Fiber Optic Sensors

Placement of fiber optic cables in the wellbore brings with it operational problems. Sometimes they may get washed out of hole. Existence of free hydrogen atoms (mainly in gaseous form such as hydrogen sulfide) can affect the performance of the fibers. This phenomenon is called "hydrogen darkening" which occurs with the physical process of hydrogen intrusion into the fiber. As a result the optical glass fiber degrades causing optical distortion. In this darkening process, the hydrogen atoms react with the silica glass (SiO_2) compound and form hydroxyl (OH) which interferes with the passage of light through the glass. One way to prevent such issue is carbon coating of the fiber together with other coating materials (see Table 14.1). Another approach is to use a purer silica as the fiber core. There are some other partial cures such as using gel to absorb hydrogen, etc.

Data storage is another issue that needs to be addressed. Generally speaking, DTS and DAS systems required huge electronic storage capacity if they are recording at a high resolution. For example to record 6 h of high resolution DTS (1,000 samples per second recording) requires a 1 TB hard drive capacity.

Types of Fiber Optics

Fiber optics may be categorized into two types, single mode and multi-mode. DTS fibers are multi-mode fibers and DAS fibers are single mode. Multi-mode fibers are thicker than single mode fibers (up to ten times greater core diameter) and are good

for shorter length applications. Single mode fibers allow signals to travel in one axis only. However, in multi-mode fiber, signals can travel in different modes such as spiral and zigzag albeit at a slower traveling speed than axial mode. Figure 14.1 demonstrates two different modes.

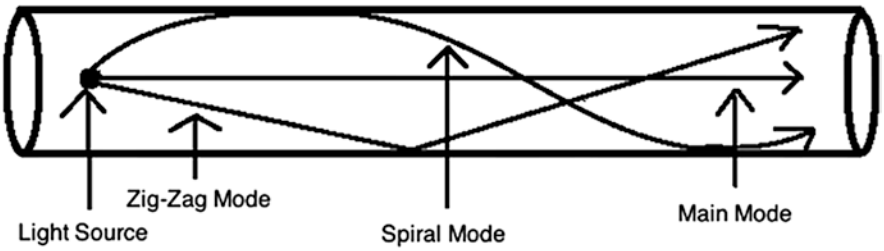

Fig. 14.1 Modes that light can travel along a glass fiber. Courtesy SPE 163688

Operating Principle

The physics behind the DTS and DAS (DSTS or DTSS) sensing rests on the way light is scattered. There are three principal mechanisms involved in the scattering of light. They are Raleigh, Raman, and Brillouin, named after the investigators who documented these observations.

In order for the system to discern between the backscattered signals, it has to wait to receive the sent signal back before sending another signal. Thus the repetition frequency is a function of fiber length. Equation (14.1) illustrates the relationship between the fiber length and the signal frequency.

$$f_{\max} = \frac{V_{fiber}}{l_{fiber(up+down)}} = \frac{V_{light} / n_{index}}{2 \times l_{fiber}} \tag{14.1}$$

Assuming that the refractive index (n) is 1.5 and the speed of light is 3×10^8 m/s then for a 10 km fiber, the maximum pulse frequency rate would be 10 kHz and the maximum frequency response would be 5 kHz. Thus if a pulse is generated at each 10 ns (10^{-8} s), the spatial resolution created by the laser pulse would be 1 m. Thus, there is a trade-off between the spatial resolution and the maximum length of fiber.

Rayleigh Scattering

Rayleigh scattering occurs when the wavelength of a light beam is close to the size of the objects through which it passes. For this reason white sun light is scattered when entering the Earth's atmosphere and encounters molecules of oxygen and nitrogen. The blue light is the one most easily scattered and the reason why we see a blue sky rather than a red one.

Rayleigh scattering can be considered to be due to fluctuation in the density, composition, and orientation of molecules. Hence it is dependent on the refractive index in small volumes of matter (particularly in gases or liquids). However Rayleigh scattering considers only random and incoherent thermal fluctuations, whereas Brillouin scattering responds to correlated, periodic fluctuations. Rayleigh scattering has no frequency shift associated with it. On the other hand, Brillouin and Raman scattering have frequency shifts associated with them. The components of these frequency shifts which are called ***Stokes*** and ***Anti-Stokes***.

Brillouin Scattering

Brillouin scattering, named after Léon Brillouin, occurs when light in a medium (such as air, water or a crystal) interacts with time-dependent optical density variations that change its energy (frequency) and path. The density variations may be due to acoustic modes or temperature gradients. As described in classical physics when the medium is compressed its index of refraction changes, and a fraction of the traveling light wave, interacting with refraction index variations, is deflected so its frequency changes.

Raman Scattering

Raman scattering[2] is another phenomenon involving inelastic scattering processes of light (photons) with vibrational properties of matter. However, a small fraction of the scattered photons (approximately one in ten million) is scattered by an excitation, with the scattered photons having a frequency different from, and usually lower than, that of the incident photons. In a gas, Raman scattering can occur with a change in energy of a molecule due to a transition. Chemists are concerned primarily with such transitional Raman Effect.

The detected frequency shift range and type of information extracted from a sample, however, are very different. Brillouin scattering denominates the scattering of photons from low-frequency phonons while for Raman scattering photons are scattered by interaction with vibrational and rotational transitions in single molecules. Therefore the two techniques provide very different information about a sample: Raman spectroscopy is used to determine the chemical composition and molecular structure, while Brillouin scattering measures properties on a larger scale—such as the elastic behavior. Experimentally, the frequency shifts in Brillouin scattering are detected with an interferometer (Brillouin sensor system), while the Raman setup can be based on either an interferometer or a dispersive grating spectrometer (fiber Bragg grating and spectrum analyzer).

[2] It was discovered by C.V. Raman and K.S. Krishnan in liquids, and by G. Landsberg and L.I. Mandelstam in crystals. The effect had been predicted theoretically by A. Smekal in 1923.

Practical Applications of Light Scattering in DTS

In order to place the above theoretical descriptions of scattering mechanisms in perspective we need to understand how these different possibilities of light scattering can be used to tell us something of practical use. In ***Rayleigh Scattering*** there is no exchange of energy and so incident and scattered photons have the same energy.

However there can also be scattering where there is an exchange of energy and this is referred to as ***Stokes Scattering*** where an atom or molecule absorbs energy. In this case the scattered photon has less energy than the incident photon. In other cases an atom or molecule can contribute energy and the scattered photon has more energy than the incident photon. This is referred to as ***Anti-Stokes Scattering***.

The Raman interaction thus leads to two possible outcomes: the material absorbs energy and the emitted photon has a lower energy than the absorbed photon. This outcome is labeled ***Stokes Raman Scattering***. Alternately the material loses energy and the emitted photon has a higher energy than the absorbed photon. This outcome is labeled ***Anti-Stokes Raman Scattering***.

Figure 14.2 illustrates the principle of DTS. A laser light source (see the "DTS Box") sends a very short pulse of light down the fiber optic cable installed in the well. A small fraction of the photons are backscattered from every point along the well and detected back at the analyzer.

There the detected change in frequency is interpreted as a temperature and the time taken for the light to travel from the laser back to the detector as a measure of distance from the light source and hence depth in the well. Since there are two effects that need to be detected the analyzer employs an interferometer for the frequency shifts in Brillouin scattering a dispersive grating spectrometer for the Raman scattering.

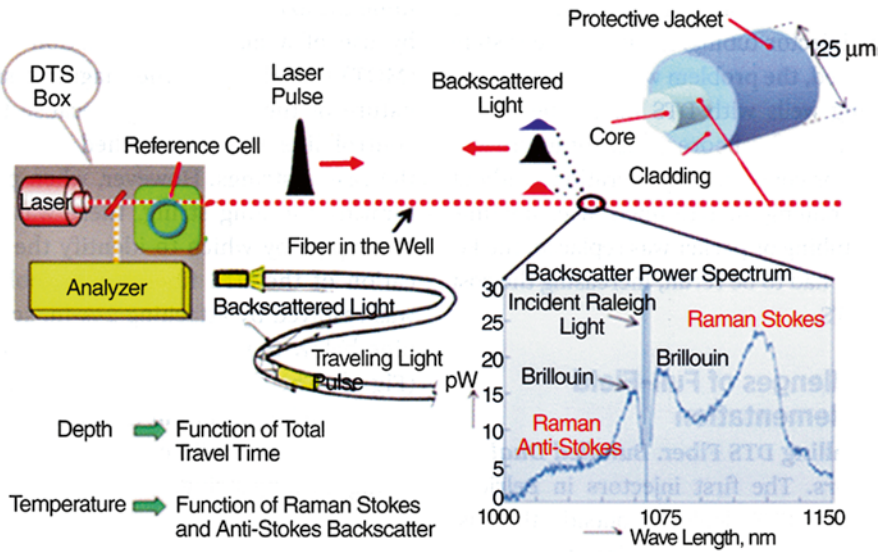

Fig. 14.2 Principle of distributed temperature sensing (DTS) with optical fiber. Courtesy SPE 144116

Since the change in frequency for the Brillouin photon is a function of both temperature and strain but that of the Raman photon is only dependant on temperature, both are needed to fully describe the DTS and DAS measurements as a function of depth. Figure 14.3 illustrates the principle of operation of the Brillouin sensor.

To place these measurements and their physical basis into perspective the reader is directed to Fig. 14.4 that summarizes the Raman and Brillouin backscattering along with their Stokes and Anti-Stokes components. Suffice that the technology now exists for a well (pipeline, stock tank or other surface facility) to be equipped with sensors that have the potential to indicate temperature and pressure practically every foot of the way from surface to TD and to do so many times each and every minute of the day.

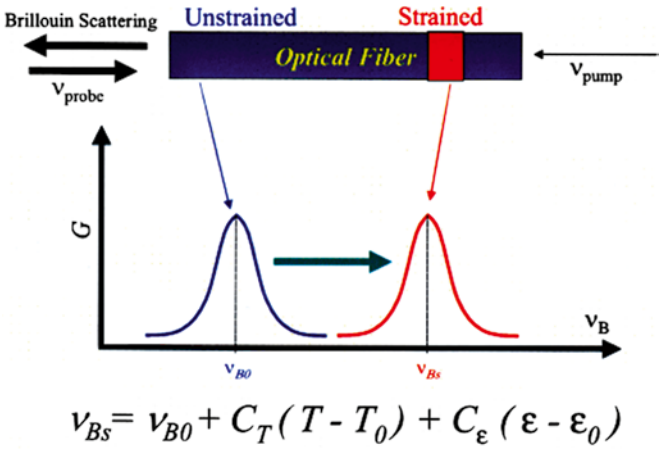

Fig. 14.3 Principle of operation of Brillouin sensor. Courtesy OZ Optics

DAS (DSTS or DTSS) Applications

Having DAS, an operator is capable of real-time continuous monitoring of sound noise, temperature, and strain. Briefly, DAS applications include the aforementioned DTS applications and the following:

Corrosion and leak detection (downhole and surface pipeline, pressure vessels, etc.).
Crack detection (cement bond and casing failure).
Fluid flow inside tubulars (during hydraulic fracturing process or acidizing, checking the ball actuated sleeves in multistage horizontal fracturing).

Water front encroachment (deploying DAS with special sensors at the producing well in waterflood process to detect water arrival at the producer).

Vertical Seismic Profiling (***VSP***) (this number of sweep signals to make DAS competitive with VSP is in the range of 20–40, which means more improvement is still required).

Thus the days of intervening in a completed well with production logging tools to make measurements at a single point in time have now potentially been replaced with the possibility of "running" a PL survey as often as the operator requires. Spatial resolution/accuracy is in the order of 10/5 cm. Strain/Temperature accuracy: ± 2με/0.1 °C.

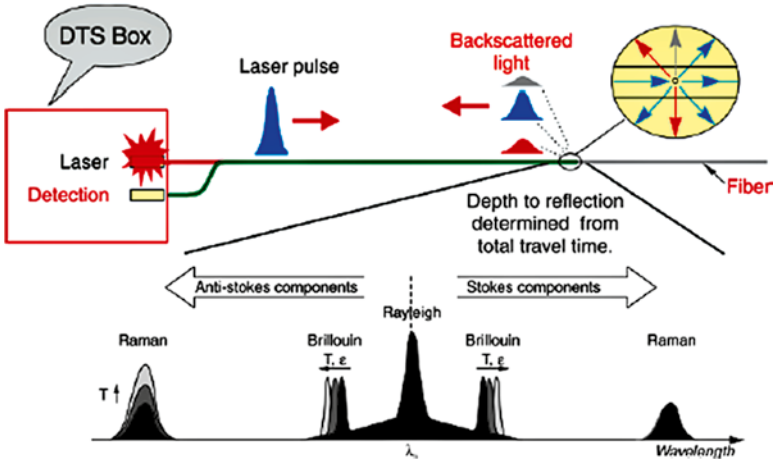

Fig. 14.4 Raman and Brillouin backscattering. Courtesy SPE 153131

Fiber Optic Placement

Figure 14.5 shows some of the methods of deployment of fiber optic cables. The left panel shows how the cable can be run into the well strapped between two strings of tubing. The center panel shows the cable placed on the outside of 5½″ casing which is cemented in place while the right hand panel shows the well-site running of a DTS cable on 5½″ casing.

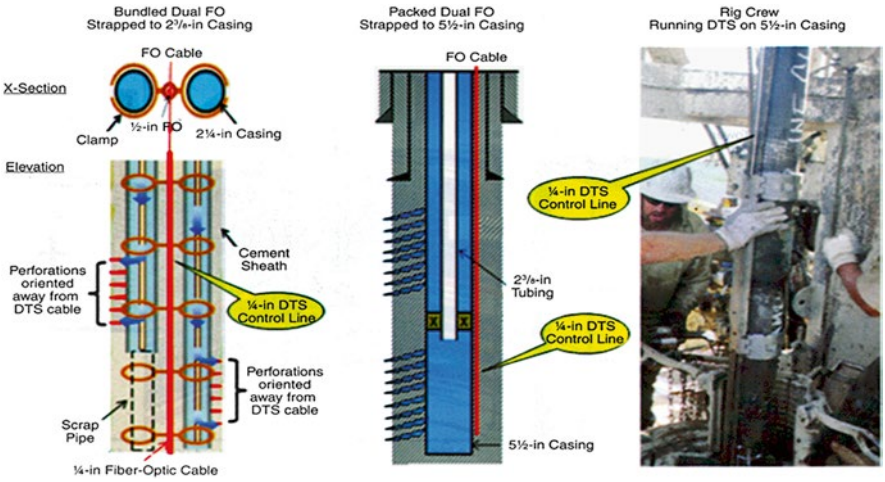

Fig. 14.5 DTS fiber deployment in different casing configurations. Courtesy SPE 163694

Types of DTS/DAS Installations

Essentially a fiber optic cable may be installed in a well either permanently, semi-permanently, or retrievably. In a permanent installation an armored cable is run outside the casing, strapped in place and cemented along with the casing. This method is only possible with new wells but it is applicable for vertical, deviated, and/or horizontal wells. Besides fiber optic lines, there will be a permanent magnet rod running inside the jacket of the armored cable. The magnetic rod is used to locate the optic fiber and allow a perforating gun to be oriented so as to avoid damaging the fiber optic cable.

In a semi-permanent installation, the fiber optic cable is pushed through the well and has the advantage that it can later be replaced if necessary. In a vertical well typically the cable is fed through the tubing. In deviated or horizontal wells a protected fiber optic cable is run built into coiled tubing.

Cables can be run in either single or double mode as illustrated in Fig. 14.6. Type A and B involve a single line, which cannot be calibrated to accurate temperature although very small temperature changes can be detected without knowing the absolute value. The resolution is as high as other types and can detect to within 0.1 °F. The pressure gauge in type B is a solar optic pressure gauge which works based on displacement of a diaphragm at different optical frequency. The displacement with time is then converted to pressure. DTS installation Type C allows for calibration via two temperature readings at the same depth.

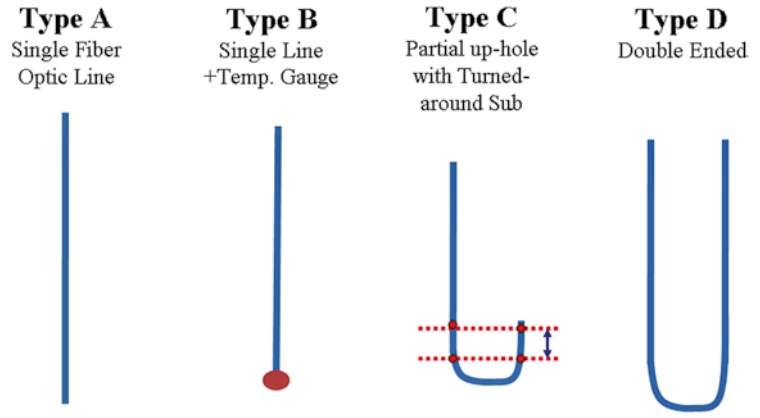

Fig. 14.6 Single and double installation modes. After Mehdi Shahri

DTS installation type D has the advantage that if the fiber breaks the system still works. It also allows for easy calibration even if the attenuation is not linear. However this kind of installation is more costly and the fiber may become damaged if it does not have sufficient protection.

Whatever the installation type there are some mechanical considerations that need to be taken into account. For example when "pushing" a fiber optic cable down tubing it may coil up producing an "over stuff". This may amount to as much as 3 % of the total cable length and may lead to inaccurate depth measurements. The "over-stuff" effect is lesser in smaller tubing sizes. A secondary effect is actual cable stretch under its own weight, much in the way that conventional wireline logging cables stretch when lowered into a well. However in the case of fiber optic cables this is less than 1 % in wells less than 15,000 ft deep.

DTS measurements which are based on the Raman scattering phenomenon are intensity based. In other words, they require calibrations where there is sensitivity to changes in wave attenuation. DAS measurements however are based on Brillouin scattering which is frequency based and is not sensitive to attenuation. So, once the DAS system is calibrated after setup, there is no extra calibration required.

DTS Applications

Real-time monitoring of completion operations is particularly useful in multistage fracking jobs. The presence of a DTS system in a new well allows continuous monitoring of the placement (or non-placement) of frac fluids and proppants via detailed sensing of temperature variations in both the time and depth domains. Figure 14.7 illustrates the first stage of a fracturing operation. The cooling is occurring at depth interval from 9,390 to 9,450 ft. The perforations are at 9,432–9,442 ft. This confirms that the colder injection fluid (compared to ambient reservoir temperature) is flowing into the desired perforations.

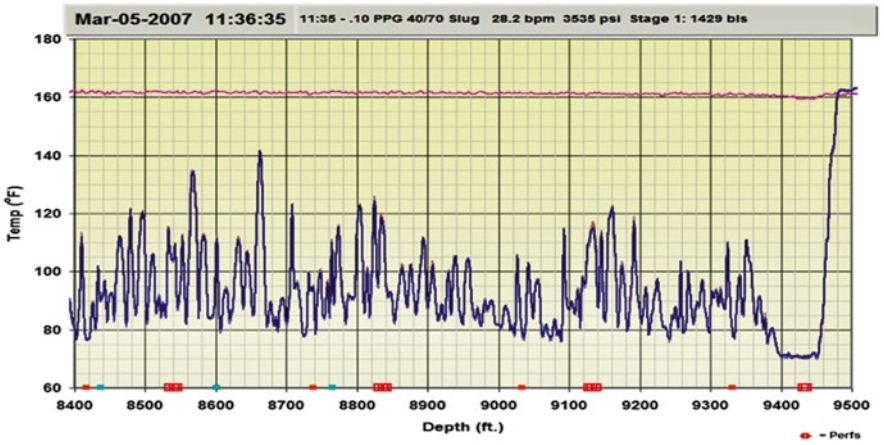

Fig. 14.7 DTS monitoring of a fracking operation. Courtesy SPE 118831

Post operational analysis is also made possible by the use of the DTS system to monitor changes in wellbore temperature with time after the treatment has been made. Figure 14.8 depicts the process of fracking stage 2 of the same well. The perforations are at depth of 9,129–9,139 ft. During the process of fracturing, a broad cooling response from 8,945 to 9,220 ft is recorded which demonstrates a very large annular communication resulting from a poor cement job in the annulus. The warm-back profile of stage 1 demonstrates a constrained transverse fracture extension from stage 1 perforations.

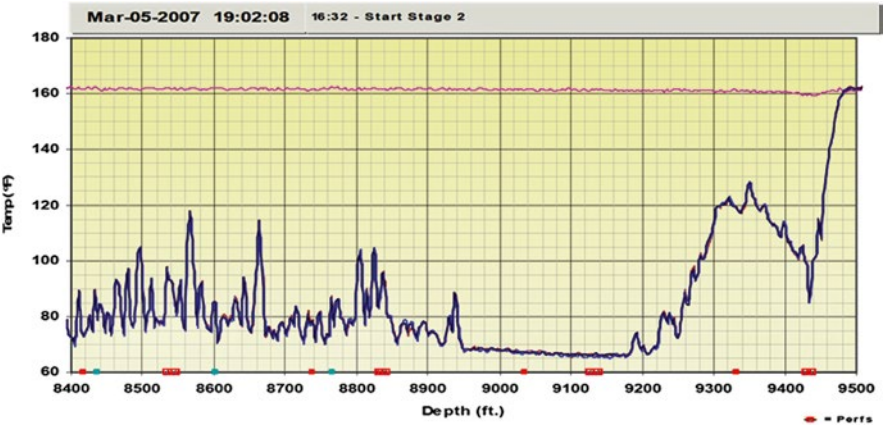

Fig. 14.8 DTS fracking and "Warm-back" monitoring. Courtesy SPE 118831

Figure 14.9 gives an example of a series of temperature measurements taken at spaced time intervals that show depth on the *x*-axis and temperature on the *y*-axis with the color coded traces keyed to increasing time after the treatment was completed.

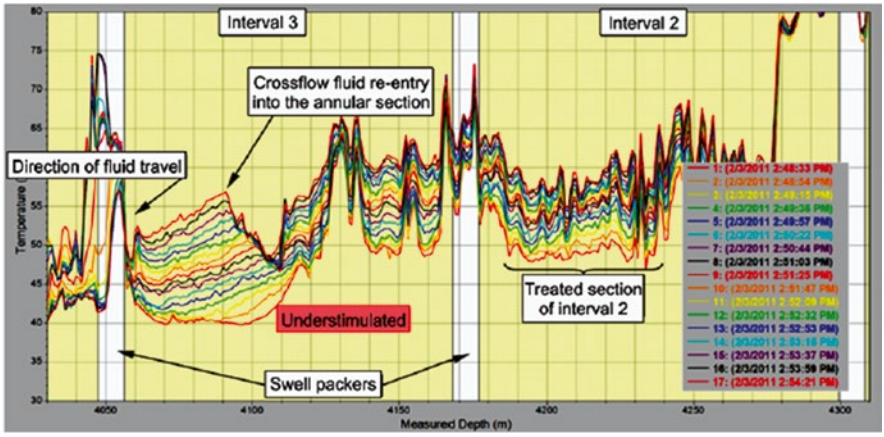

Fig. 14.9 DTS "Warm-back" and cross-flow monitoring. Courtesy SPE 153131

The analysis shows intervals that were under stimulated and intervals with cross-flow fluid re-entry. Note that the well has been completed open-hole and so the cross-flow occurs across the upper swell packer in interval 3.

Combining DTS with Microseismic (MSM)

Combining DTS with Microseismic (MSM) in hydraulic fracturing gives a good indication of both near wellbore fluid distribution and far field fracture network. Figure 14.10 demonstrates that all the perforations in that designated perforation cluster are taking fluid and MSM shows a good contained fracture network in that interval.

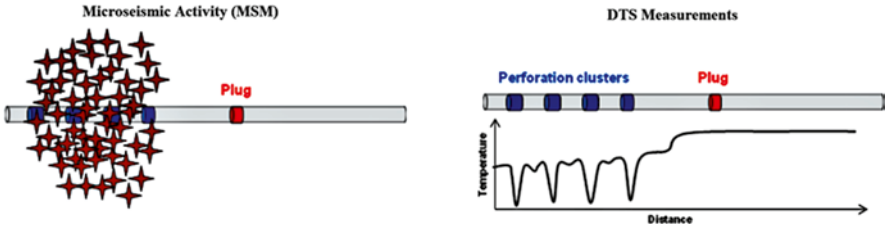

Fig. 14.10 Combining DTS with MSM. Courtesy SPE 136565

If the cement bond between the cement and formation is weak, the fracture may initiate where there is less resistance and thus not end up being placed in the planned location, as depicted in Fig. 14.11. The fluid flow did not go through all perforations indicating an isolation issue. As both the DTS and MSM show the fracture initiated and extended in the non-perforated interval, probably due to a poor cement job.

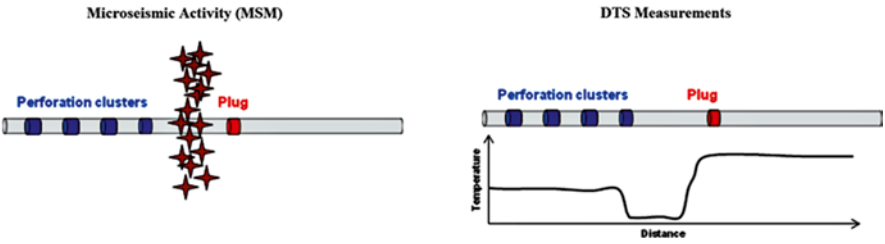

Fig. 14.11 Poor isolation detection using combination of DTS with MSM. Courtesy SPE 136565

Another application of DTS is for checking the plug isolation in a multistage hydraulic fracturing operation. Figure 14.12 shows a diagnostic response due to poor stage isolation which is caused by leaking plug or packer, poor cement, or a leak in the casing. It is hard to discern the exact reason for such occurrences just using MSM; however DTS can shed more light in such cases as they are near wellbore issues. By monitoring such problems in real-time, remedial solutions to divert the fluid to the interval of interest can be assessed and acted on in real time.

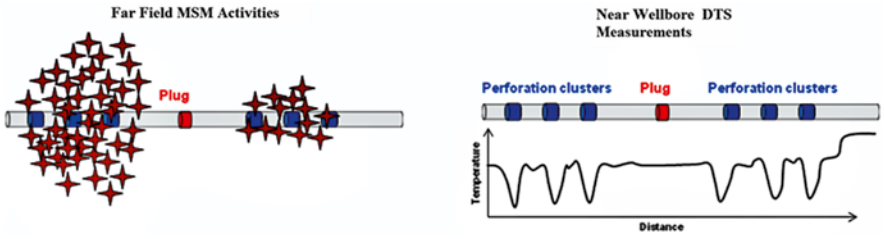

Fig. 14.12 Isolation issue revealed by combining MSM and DTS. Courtesy SPE 136565

DAS Applications

In order to discern between backscattered signals, the system must wait for the laser pulse to travel the full length of the fiber and come back. So the returned frequency response is a function of pulse frequency and length of fiber. In other words, the shorter the fiber length, the higher the spatial resolution. Monitoring of strain as well as temperature allows for additional information to be gathered, for example, the evaluation of the reliability of swell packer/ball actuated sleeves. Essentially any

near wellbore happenings that produce changes in pressure and hence deformation of the fiber optic cable may be monitored and displayed in a sound field display. Figure 14.13 gives an illustration.

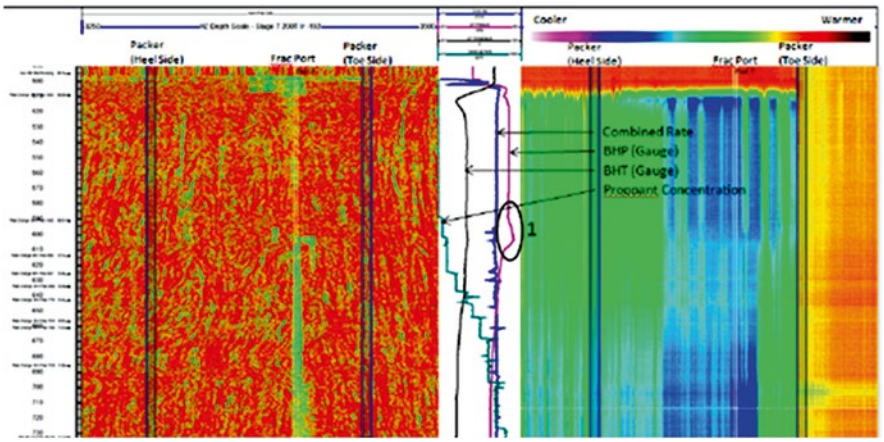

Fig. 14.13 DAS sound field display (*left*) and DTS display (*right*). Courtesy SPE 152422

DAS can be used to monitor the gas lift valve performance. In this approach, DAS fiber will collect the coherent light sources at the valve and along the tubing. With this, the operator can track the opening and closing of the valve as well as the slug flow and the exact velocity of the slug as it reaches the surface in real time.

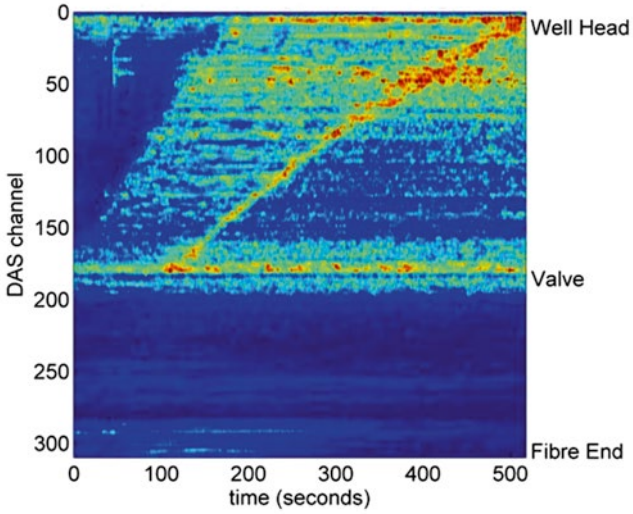

Fig. 14.14 DAS-recorded acoustic energy (*red*: high, *blue*: low) during startup of a gas lift operation. Courtesy SPE 150203

Figure 14.14 shows the flow pattern at and above the gas lift valve. Rising gas bubbles are shown as it takes 3 min from the valve to surface with a delay of 100 s.

Another application of DAS is for seismic surveys. Since DAS can pick up passive noises from a distance it has a bright future with applications in the fields of seismic and MSM. Figure 14.15a, b show the deployment of DAS fibers as well as seismic geophones for the purpose of vertical seismic profiling (VSP). This example is from a carbon capture and sequestration project in Canada. As shown in Fig. 14.15a, the DAS recordings are comparable to the geophone recordings. The noise level of DAS is higher than that of the geophones but doubtless will be lowered in future versions.

Figure 14.15b shows a comparison between a sonic log recording of sound velocity (made with a sonic log run on the borehole) and both the geophone and DAS recordings.

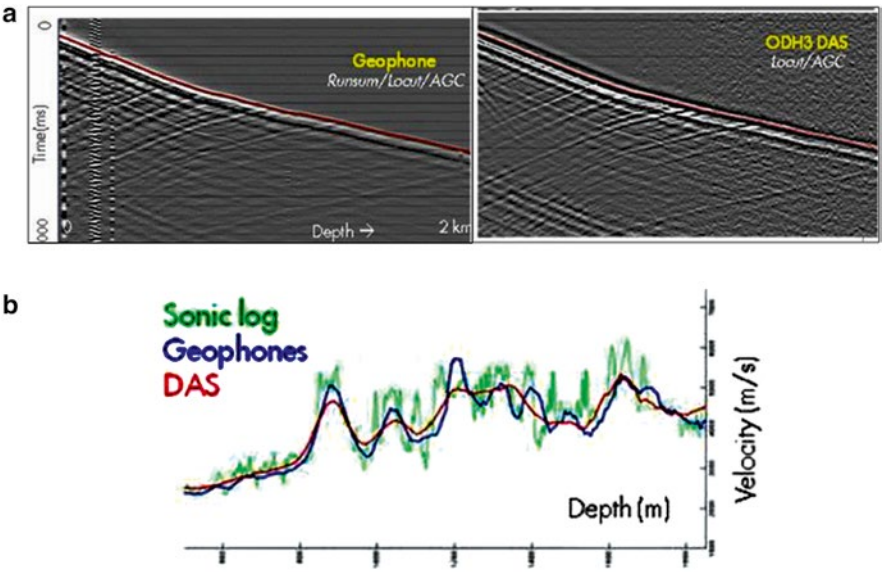

Fig. 14.15 (**a**) *Left*: VSP recorded using a geophone array. *Right*: VSP recorded using the DAS array. (**b**) Comparison of velocity profiles obtained from (borehole) sonic log (*green*), geophones (*blue*), and DAS (*red*). Courtesy SPE 150203

Thermocouple vs. DTS Measurements

An older technology used wired thermocouples placed at strategic points along a wellbore in order to monitor temperature changes with time or as a result of production, injection, or other stimulation or treatment. While such measurements are accurate and are fairly inexpensive to install the results can sometimes be misleading, as illustrated in Fig. 14.16. In a SAGD well both DTS and thermocouple (TC) temperature measurements are available. There are three TC measurements available along the horizontal portion of the well marked on the figure with red dots. Taken on their own they suggest a temperature gradient as shown by the straight red line. However a DTS continuous temperature profile paints a different picture as shown by the continuous blue line. The black line shows the wellbore path (changing from vertical to horizontal going from left to right).

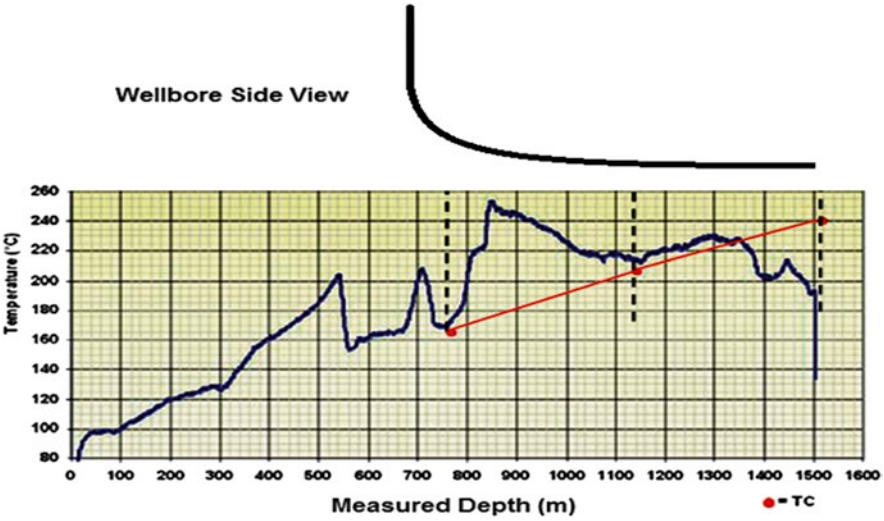

Fig. 14.16 DTS vs. TC temperature distribution in a SAGD well. Courtesy SPE 117206

Bibliography

Feng M, Lufan Z, Michio I. Detection of ceramic cracks using a distributed high-resolution Brillouin fiber optic sensor. SICE J Control Meas Syst Integrat. 2010;3(4):279–84.

Holley EH, et al. Interpreting uncemented multistage hydraulic-fracturing completion effectiveness by use of fiber-optic DTS injection data. SPE Drill Completion. 2013;28(03):243–53.

Holley EH, et al. Integrated analysis combining microseismic mapping and fiber-optic distributed temperature sensing (DTS). In: Paper 136565 presented at the Canadian unconventional resources & international petroleum conference, Calgary, Alberta, Canada; 19–21 Oct 2010.

Huckabee P. Optic fiber distributed temperature for fracture stimulation diagnostics and well performance evaluation. In: Paper 118831 presented at the SPE hydraulic fracturing technology conference, The Woodlands, Texas; 19–21 Jan 2009.

Hudon C, et al. Determination of stator temperature profile using distributed sensing. In: Published in the proceeding at the electrical insulation conference (EIC), Ottawa, Canada; 2–5 June 2013. p. 191–5.

Kaura JD, Sierra JR. Successful field application in continuous DTS monitoring under harsh environment of SAGD wells using improved optical fiber technology—case study from Canada. In: Paper 117206 presented at the international thermal operations and heavy oil symposium, Calgary, Alberta, Canada; 20–23 Oct 2008.

Koelman JMVA, Lopez JL, Potters JHHM. Optical fibers: the neurons for future intelligent wells. In: Paper 150203 presented at the SPE intelligent energy international, Utrecht, The Netherlands; 27–29 Mar 2012.

MacPhail WFP, Lisoway B, Banks K. Fiber optic distributed acoustic sensing of multiple fractures in a horizontal well. In: Paper 152422 presented at the SPE hydraulic fracturing technology conference, The Woodlands, Texas; 6–8 Feb 2012.

Zou L, Sezerman O, Revie W. Pipeline corrosion monitoring by fiber optics distributed strain and temperature sensors. In: NACE international corrosion conference and expo. 2008. Ozoptics.com

ERRATUM TO

Cased-Hole Log Analysis and Reservoir Performance Monitoring

2nd Edition

Richard M. Bateman

R.M. Bateman, *Cased-Hole Log Analysis and Reservoir Performance Monitoring*,
DOI 10.1007/978-1-4939-2068-6

DOI 10.1007/978-1-4969-2068-6_15

On Page 47, Line 2 currently reads $\gamma_o = 450°$ API should read $\gamma_o = 45°$ API.

Appendix A Table:
On Page 263, Column 5, Line 5 change "3-oct liters" to "10^{-3} liters"
On Page 265, column 2, Line 6 change "3-oct kg" to "10^{-3} kg"
On Page 265, column 5, Line 19 change "4-oct m^2" to "10^{-4} m^2"
The entire "Appendix A Table" format has been altered in Alphabetical order.

The online version of the original book can be found at
http://dx.doi.org/10.1007/978-1-4969-2068-6

R.M. Bateman, *Cased-Hole Log Analysis and Reservoir Performance Monitoring*,
DOI 10.1007/978-1-4939-2068-6_15

Appendices: Production Logging—Charts and Tables

Appendix A: Conversion Factors Between Metric, API, and US Measures

R.M. Bateman, *Cased-Hole Log Analysis and Reservoir Performance Monitoring*,
DOI 10.1007/978-1-4939-2068-6

Multiply	by	to find	Multiply	by	to find
acres	0.4047	hectares	cubic centimeters	3.531×10^{-3}	cu ft
"	43,560	sq ft	"	6.102×10^{-2}	cu in.
acre-feet	4,047	m^2	"	10^{-4}	m^3
"	7,758	bbl[a]	"	2.642×10^{-4}	gal
"	43,560	cu ft	"	10^{-3}	liters
atmospheres	3.259×10^{5}	gal	"	6.2897×10^{-6}	bbl[a]
"	76	cm Hg	cubic feet	0.1781	bbl[a]
"	29.92	in. Hg	"	2.832×10^{4}	cc[b]
"	33.93	ft of water	"	7.481	gal
"	1.033	kg/cm^3	"	1,728	cu in.
barrels (API)	14.7	psi	"	0.02832	m^3
"	1.289×10^{-4}	acre-ft	"	28.32	liters
"	158,987	cc[b]	cubic feet/day	1.18	liters/hr
"	5.615	cu ft	"	1.18×10^{-3}	c m/hr
"	42	gal	"	0.02832	m^3/ day
"	9,702	cu in.	"	0.1781	bbl/day[a]
"	1,590	liters	cubic feet/minute	10.686	bbl/ hr[a]
barrels/day[a]	0.159	m^3	"	256.5	B/D[a]
"	5.615	cu ft/D	"	472	cc/s
"	0.02917	gal/min	"	7.481	gal/min
"	6.625	liters/hr	"	0.472	liters/s
"	0.159	m^3/d	cubic inches	16.39	cc[b]
barrels/hour[a]	0.006625	m^3/hr	"	5.787×10^{-4}	cu ft
"	0.0936	cu ft/min	"	1.639×10^{-3}	m^3
"	0.7	gal/min	"	4.329×10^{-3}	gal
bars	2.695	cu in. /s	"	$1.639\ 10^{-2}$	liters
"	0.9869	atm	cubic meters	6.2897	bbl[a]
"	1.02	kg/cm^3	"	106	cc[b]
British thermal units	14.5	psi	"	264.2	gal
"	778.57	ft-lb	"	6.102×10^{4}	cu in.
"	0.252	kcal	"	35.31	cu ft
	0.293	W-hr	"	103	liters
Btu/minute	0.02357	hp	cubic meters/hour	151.0	B/D[a]
"	0.01758	kW	"	847.8	cu ft/D
"	12.97	ft-lb/s	"	103	liters/hr
centimeters	3.281×10^{-2}	ft	cubic meters/day	0.2621	bbl/hr[a]
"	0.3937	in.	"	6.2897	B/D[a]
"	0.01	m	"	1.471	cu ft/hr
"	10	mm	"	35.31	cu ft/D
cm of mercury	0.01316	atm	"	41.67	liters/hr
"	0.4461	ft H_2O	"	0.04167	m^3/hr
"	0.0136	kg/cm^2	days	1,440	min
cm per second	0.1934	psi	"	86,400	s
"	1.969	ft/min	feet	30.48	cm
"	0.03281	ft/s	"	12	in
"	0.6	m/min	"	0.3048	m

Multiply	by	to find	Multiply	by	to find
feet of water	0.0295	atm	"	0.01	km^2
"	0.8826	in. Hg	horsepower	42.4	Btu/min
"	0.03048	kg/cm^2	"	33,000	ft-lb/ min
"	62.43	lb/sq ft	"	550	ft-lb/s
"	0.4335	psi	"	1.014	metric hp
feet/hour	0.008467	cm/s	"	10.68	kcal/min
"	5.086×10^{-3}	m/min	"	0.7457	kW
"	0.01667	ft/min	"	745.7	watts
feet/minute	0.508	cm/s	horsepower-hour	2,544	Btu
"	0.01667	ft/s	"	641.1	kcal
"	0.01829	km/hr	"	2.737×10^3	kg-m
"	0.3048	m/min	"	0.7455	kW-hr
feet/second	30.48	cm/s	inches	2.54	cm
"	18.29	m/min	"	8.333×10^{-2}	ft
foot-pounds	1.285×10^{-3}	Btu	in. of mercury	0.03342	atm
"	3.238×10^{-4}	kcal	"	1.133	ft H_2O
foot-pounds/minute	3.030×10^{-3}	hp	"	0.03453	kg/cm^2
"	2.260×10^{-3}	kW	"	0.4912	psi
foot-pounds/second	1.818×10^{-3}	hp	in. of water	0.002458	atm
"	1.356×10^{-3}	kW	"	0.07349	in. Hg
gallons (U.S.)	0.02381	bbl[a]	"	0.002538	kg/cm^3
"	3,785	cc[b]	"	0.03609	psi
"	0.1337	cu ft	kilograms	10^3	g
"	231	cu in.	"	2.205	lb
"	3.785×10^{-3}	m^4	"	1.102×10^{-3}	tons (short)
"	3.785	liters	kilogram-calories	3.986	Btu
gallons (imperial)	1.2009	gal (U.S.)	"	3,088	ft-lb
gallons/minute	1.429	bbl/hr[a]	"	1.560×10^{-3}	hp-hr
"	34.286	B/D	"	427	kg-m
"	0.1337	cu ft/min	"	1.163×10^{-3}	kW-hrs
"	192.5	cu ft/D	kg-calories/min	0.09358	hp
"	3.785	liters/min	"	0.06977	kW
"	90.84	liters/hr	kg/cubic meter	10^{-3}	g/cc[b]
grain (avoir)	0.0648	g	kg/square cm	0.9678	atm
grains/gal	17.12	ppm	"	0.9807	bars
"	142.9	lb/10^4 gal	"	32.84	ft H_2O
"	0.01714	g/liter	"	28.96	in. Hg
"			"	14.22	psi
grams	15.432	grains	kilowatts	56.88	Btu/min
"	10^{-3}	kg	"	4.427×10^4	ft-lb/min
"	0.3125	oz	"	737.8	ft-lb/s
"	2.205×10^{-3}	lb	"	1.341	hp
grams/cc[b]	62.43	lb/cu ft	"	103	watts
"	8.344	lb/gal	kilowatt-hours	3,413	Btu
"	0.03613	lb/cu in.	"	2.656×10^6	ft-lb
grams/liter	58.42	grains/gal	"	1.341	hp-hr
hectares	2.471	acres	"	860	kcal
"	1.076×10^5	sq ft	"	3.672×10^5	kg-m

Multiply	by	to find	Multiply	by	to find
liters	10^3	cc[b]	"	144	lb/cu ft
"	6.2897×10^{-3}	bbl[a]	seconds	1.157×10^{-3}	days
"	0.03531	cu ft	"	2.778×10^{-4}	hr
"	0.2642	gal	"	1.667×10^{-3}	min
"	61.02	cu in.	square cm	1.076×10^{-3}	sq ft
"	10^{-3}	m^3	"	0.155	sq in.
liters/hour	0.1509	B/D	"	10^{-4}	m^2
"	6.289×10^{-3}	bbl/hr[a]	"	100	mm^2
"	5.885×10^{-4}	cu ft/min	square feet	2.296×10^{-5}	acres
"	0.8475	cu ft/d	"	929	cm^2
"	10^{-3}	m^3/hr	"	144	sq in.
"	0.024	m^3/d	"	0.0929	m^2
meters	3.281	ft	square inches	6.452	cm^2
"	39.37	in.	"	6.944×10^{-3}	sq ft
"	103	mm	"	645.2	mm^2
"	6.214×10^{-4}	mile	square meters	10.76	sq ft
meters/minute	1.667	cm/s	"	2.471×10^{-4}	acres
"	3.281	ft/min	"	1,550	sq in.
"	1.969	ft/hr	°Cent. + 273	1	°K (abs)
"	0.05468	ft/s	°Fahr. + 460	1	°R (abs)
mile	5,280	ft	°Cent. + 17.8	1.8	°F
"	1.609	km	°Fahr. – 32	5/9	°C
miles/hour	44.7	cm/s	°Cent./100 meters	0.5486	°F/100 ft
"	88	ft/min	°F/100 ft	1.823	°C/100 ft
"	26.82	m/min	tons (long)	1,016	kg
millimeters	0.1	cm	"	2,240	lb
"	3.281×10^{-3}	ft	tons (metric)	103	kg
"	0.03937	in.	"	2,205	lb
minutes	6.944×10^{-4}	days	tons (short)	2,000	lb
"	1.667×10^{-3}	hrs	viscosity, lb-s/sq in.	6.895×10^6	viscosity, cp
parts/million	0.05835	grains/gal	viscosity, lb-s/sq ft	4.78×10^4	viscosity, cp
"	8.337	lb/10^6 gal	viscosity, centistokes	density	viscosity, cp
pound	7,000	grains	watts	0.05688	Btu/min
"	453.6	g	"	44.27	ft-lb/min
"	0.4536	kg	"	0.7378	ft-lb/s
pounds/cubic ft	0.1337	lb/gal	"	1.341×10^{-3}	hp
"	0.01602	g/cc[b]	"	0.01433	kcal/min
"	16.02	kg/m^3	"	10^{-3}	kW
"	5.787×10^{-4}	lb/m^4	watt-hours	3.413	Btu
pounds/square in.	0.06805	atm	"	2,656	ft-lb
"	2.309	ft H_2O	"	1.341×10^{-3}	hp-hr
"	2.036	in. Hg	"	0.86	kcal
"	51.7	mm Hg	"	367.2	kg-m
"	0.07031	kg/cm^2	"	10^{-3}	kW-hr

Volume Capacity of Pipes[a]

Gallons per 1,000 ft = 40.3 × (ID in inches)^2
Cubic feet per 1,000 ft = 5.454 × (ID in inches)^2
Barrels per 1,000 ft = 0.9714 × (ID in inches)^2
Gallons per mile = 215.4240 × (ID in inches)^2
Barrels per 1,000 ft = approximately (ID in inches)^2
Barrels per mile = 5.1291 × (ID in inches)^2

Velocity[a]

Feet per minute = 0.127324 (cubic feet per day)/(ID in inches)^2
Feet per minute = 1,029.42 (barrels per minute)/(ID in inches)^2
Feet per second = 0.4085 (gallons per minute)/(ID in inches)^2

Tank Volumes[a]

Barrels per foot in round tank = (diameter, in feet)^2/7.14
Barrels per inch in round tank = (diameter, in feet)^2/85.7
Barrels per inch in square tank = 0.0143 (length, in feet) × (width, in feet)
Cubic feet per inch in square tank = 0.0833 (length, in feet) × (width, in feet)

Oil Gravity

$$\text{sp.gr.@}\,60°\text{F} = \frac{141.5}{131.5 + \text{API gravity}}$$

$$\text{API gravity} = \frac{141.5}{\text{sp.gr.@}\,60°\text{F}} - 131.5$$

Gas Gravity[c]

$$\text{Gas specific gravity} = \frac{\text{Density of gas at sc}(\text{g/cc})}{0.00122} = \frac{\text{Density of gas at sc}(\text{lb/cuft})}{0.0762}$$

$$\text{Gas specific gravity} = \frac{\text{density of gas}}{\text{desnsity of air at same temp. and press.}} = \frac{\text{molecular weight of gas}}{28.966}$$

[b]The metric symbol, cc, for cubic centimeters has been replaced by the SI symbol cm^3, but it is still widely used.

[c]sc (standard conditions) = 60 °F (15.56 °C) and 14.7 psia (one atmosphere).

Appendix B: Average Fluid Velocity Versus Tubing Size

Description				Fluid Velocity for Flow Rate of:											
Nom. OD	Wt.	Int. Diameter		1000 B/D			10 m^3 / hr			100 m^3 / d			1000 cu ft / D		
in. (mm)	lb/ft	in.	mm	m/min	cm/s	ft/min	m/min	cm/s	ft/min	m/min	cm/s	ft/min	m/min	cm/s	ft/min
1.9 (48.3)	2.75	1.610	40.89	84.54	140.9	276	127.11	211.8	417.0	52.9	88.11	173.5	15.0	25.0	49.12
2 1/8 (60.3)	4.00	2.041	51.84	52.56	87.6	172	79.00	131.7	259.2	32.8	54.79	107.8	9.31	15.5	30.56
	4.60	1.995	50.67	55.02	91.7	180	82.70	137.8	271.3	34.4	57.32	112.8	9.75	16.3	31.99
	5.80	1.867	47.42	62.82	104.7	205	94.42	157.4	309.8	39.3	65.47	128.9	11.1	18.6	36.53
2 7/8 (73.0)	6.40	2.441	62.00	36.78	61.3	120	55.28	92.1	181.4	22.9	38.31	75.5	6.51	10.9	21.37
	8.60	2.259	57.38	42.90	71.5	140	64.48	107.5	211.5	26.8	44.72	87.9	7.60	12.7	24.95
3 1/2 (88.9)	7.70	3.068	77.93	23.28	38.8	76.0	34.99	58.3	114.8	14.5	24.25	47.7	4.12	6.87	13.53
	9.20	2.992	76.00	24.48	40.8	79.8	36.79	61.3	120.7	15.3	25.50	50.2	4.33	7.22	14.22
	10.20	2.922	74.22	25.68	42.8	83.7	38.60	64.3	126.6	16.1	26.75	52.7	4.54	7.57	14.91
	12.70	2.750	69.85	28.98	48.3	94.5	43.56	72.6	142.9	18.1	30.20	59.4	5.13	8.55	16.84
4 (101.6)	9.50	3.548	90.12	17.40	29.0	56.7	26.15	43.6	85.8	10.9	18.14	35.7	3.08	5.14	10.11
4 1/2 (114.3)	12.6	3.958	100.53	13.98	23.3	45.6	21.01	35.0	68.9	8.7	14.56	28.7	2.48	4.13	8.128
API upset tubing															
1.05 (26.67)	1.20	0.824	20.93	322.62	537.7	1053	484.90	808.2	1590.9	201.71	336.21	661.81	57.2	95.3	187.5
1.315 (33.40)	1.80	1.049	26.64	199.14	331.9	650	299.31	498.8	982.0	124.51	207.50	408.51	35.3	58.8	115.7
1.660 (42.16)	2.40	1.380	35.05	115.02	191.7	375	172.88	288.1	567.2	71.92	119.85	235.95	20.4	34.0	66.86
1.9 (48.26)	2.90	1.610	40.89	84.54	140.9	276	127.11	211.8	417.0	52.88	88.11	173.47	15.0	25.0	49.12
2-1/8 (60.32)	4.70	1.995	50.67	55.02	91.7	180	82.70	137.8	271.3	34.40	57.32	112.86	9.75	16.3	31.99
	5.95	1.867	47.42	62.82	104.7	205	94.42	157.4	309.8	39.28	65.48	128.88		18.6	36.53
2-7/8 (73.02)	6.50	2.441	62.00	36.78	61.3	120	55.28	92.1	181.4	22.99	38.31	75.46	11.1	10.9	21.37
	8.70	2.259	57.38	42.90	71.5	140	64.48	107.5	211.6	26.82	44.72	88.02	7.60	12.7	24.95
3½ (88.9)	9.30	2.992	76.00	24.48	40.8	79.8	36.79	61.3	120.7	15.30	25.50	50.21	4.33	7.22	14.22
	12.95	2.750	69.85	28.98	48.3	94.5	43.56	72.6	142.9	18.12	30.20	58.45	5.13	8.55	16.84
4 (101.6)	11.00	3.476	88.29	18.12	30.2	59.2	27.23	45.4	89.3	11.32	18.89	38.15	3.21	5.35	10.54
4½ (114.3)	12.75	3.958	100.53	13.98	23.3	45.6	21.01	35.0	68.9	8.74	14.56	28.66	2.48	4.13	8.128

Appendix C: Average Fluid Velocity Versus Casing Size

Description				Fluid Velocity for Flow Rate of:											
Nom. OD	Wt.	Int. Diameter		1000 B/D			10 m^3/ hr			100 m^3 / d			1000 cu ft/D		
in. (mm)	lb/ft	in.	mm	m/min	cm/s	ft/min	m/min	cm/s	ft/min	m/min	cm/s	ft/min	m/min	cm/s	ft/min
4 1/2 (114.3)	9.50	4.090	103.9	13.08	21.80	42.70	19.74	32.90	64.80	8.21	13.70	26.90	2.320	3.867	7.613
	11.60	4.000	101.6	13.44	22.40	44.70	20.40	34.00	66.90	8.49	14.10	27.80	2.426	4.043	7.958
	13.50	3.920	99.6	14.22	23.70	46.60	21.48	35.80	70.50	8.94	14.90	29.30	2.530	4.216	8.299
	15.10	3.826	97.2	15.00	25.00	48.80	22.50	37.50	73.80	9.36	15.60	30.70	2.651	4.419	8.698
5 (127.0)	11.50	4.560	115.8	10.50	17.50	34.40	15.84	26.40	52.00	6.59	11.00	21.60	1.866	3.110	6.123
	13.00	4.494	114.2	10.80	18.00	35.40	16.26	27.10	53.40	6.76	11.30	22.20	1.921	3.202	6.304
	15.00	4.408	112.0	11.28	18.80	36.80	16.98	28.30	55.70	7.06	11.80	23.20	1.997	3.329	6.553
	18.00	4.276	108.6	11.88	19.80	39.10	17.94	29.90	58.90	7.46	12.40	24.50	2.123	3.538	6.964
5 1/2 (139.7)	13.00	5.044	128.1	8.64	14.40	28.10	12.96	21.60	42.50	5.39	8.90	17.70	1.525	2.542	5.004
	14.00	5.012	127.3	8.70	14.50	28.50	13.08	21.80	42.90	5.44	9.10	17.80	1.545	2.575	5.069
	15.50	4.950	125.7	8.94	14.90	29.20	13.44	22.40	44.10	5.59	9.30	18.30	1.584	2.640	5.196
	17.00	4.892	124.3	9.12	15.20	29.90	13.74	22.90	45.10	5.72	9.50	18.70	1.622	2.703	5.320
	20.00	4.778	121.4	9.60	16.00	31.30	14.40	24.00	47.30	5.99	9.90	19.70	1.700	2.833	5.577
	23.00	4.670	118.6	10.02	16.70	32.80	15.12	25.20	49.60	6.29	10.50	20.60	1.780	2.966	5.838
6 5/8 (168.3)	17.00	6.135	155.8	5.82	9.70	19.00	8.76	14.60	28.70	3.64	6.10	11.90	1.031	1.719	3.383
	20.00	6.049	153.6	5.94	9.90	19.50	9.00	15.00	29.50	3.74	6.20	12.30	1.061	1.768	3.480
	24.00	5.921	150.5	6.24	10.40	20.40	9.42	15.70	30.90	3.92	6.50	12.80	1.107	1.845	3.632
	28.00	5.791	147.1	6.54	10.90	21.30	9.90	16.50	32.50	4.12	6.80	13.50	1.157	1.929	3.797
	32.00	5.675	144.1	6.78	11.30	22.20	10.20	17.00	33.50	4.24	7.10	13.90	1.205	2.008	3.953
7 (177.8)	17.00	6.538	166.1	5.10	8.50	16.70	7.68	12.80	25.20	3.19	5.30	10.50	0.908	1.513	2.979
	20.00	6.456	164.0	5.22	8.70	17.20	7.86	13.10	25.80	3.27	5.40	10.70	0.931	1.552	3.055
	23.00	6.366	161.7	5.40	9.00	17.60	8.16	13.60	26.80	3.39	5.60	11.10	0.958	1.596	3.142
	26.00	6.276	159.4	5.52	9.20	18.20	8.34	13.90	27.40	3.47	5.80	11.40	0.985	1.642	3.233
	29.00	6.184	157.1	5.70	9.50	18.70	8.64	14.40	28.40	3.51	6.00	11.80	1.015	1.691	3.329
	32.00	6.094	154.8	5.88	9.80	19.30	8.88	14.80	29.10	3.69	6.20	12.10	1.045	1.745	3.429
	35.00	6.004	152.5	6.06	10.10	19.80	9.12	15.20	29.90	3.79	6.30	12.40	1.077	1.794	3.532
	38.00	5.920	150.4	6.24	10.40	20.40	9.42	15.70	30.90	3.92	6.50	12.80	1.107	1.846	3.633
7 3/8 (193.7)	20.00	7.125	181.0	4.32	7.20	14.10	6.48	10.80	21.30	2.69	4.40	8.86	0.764	1.274	2.508
	24.00	7.052	178.4	4.44	7.40	14.50	6.54	10.90	21.50	2.72	4.50	8.94	0.786	1.310	2.580
	26.40	6.969	177.0	4.50	7.50	14.70	6.78	11.30	22.20	2.82	4.70	9.23	0.799	1.332	2.622
	29.70	6.875	174.6	4.62	7.70	15.10	6.96	11.60	22.80	2.90	4.80	9.48	0.821	1.369	2.694
	33.70	6.765	171.8	4.80	8.00	15.60	7.20	12.00	23.60	2.99	4.90	9.81	0.848	1.413	2.782
	39.00	6.625	168.3	4.92	8.20	16.30	7.44	12.40	24.40	3.09	5.20	10.20	0.884	1.474	2.901
8 5/8 (219.1)	24.00	8.097	205.7	3.33	5.55	10.90	5.02	8.38	16.50	2.09	3.50	6.86	0.592	0.987	1.942
	28.00	8.017	203.6	3.39	5.66	11.10	5.13	8.55	16.80	2.13	3.60	6.98	0.604	1.006	1.981
	32.00	7.921	201.2	3.48	5.81	11.40	5.25	8.75	17.20	2.18	3.60	7.15	0.618	1.031	2.029
	36.00	7.825	198.8	3.55	5.92	11.70	5.35	8.93	17.60	2.23	3.70	7.32	0.634	1.056	2.079
	40.00	7.725	196.2	3.63	6.05	12.00	5.46	9.10	17.90	2.27	3.80	7.44	0.650	1.084	2.134
	44.00	7.625	193.7	3.75	6.25	12.30	5.64	9.40	18.50	2.35	3.90	7.69	0.668	1.113	2.190
	49.00	7.511	190.8	3.87	6.45	12.70	5.82	9.70	19.10	2.42	4.00	7.94	0.688	1.147	2.257
9 5/8 (244.5)	29.30	9.063	230.2	2.66	4.44	8.70	4.00	6.68	13.10	1.66	2.77	5.45	0.472	0.787	1.550
	32.30	9.001	228.6	2.69	4.49	8.83	4.05	6.75	13.30	1.68	2.80	5.53	0.479	0.799	1.572
	36.00	8.921	226.6	2.74	4.58	8.98	4.17	6.95	13.70	1.73	2.89	5.69	0.488	0.813	1.600
	40.00	8.835	224.4	2.80	4.67	9.16	4.23	7.05	13.90	1.76	2.93	5.78	0.497	0.829	1.631
	43.50	8.755	222.4	2.85	4.75	9.33	4.29	7.15	14.10	1.78	2.97	5.86	0.506	0.844	1.661
	47.00	8.681	220.5	2.88	4.81	9.49	4.35	7.25	14.30	1.81	3.02	5.95	0.515	0.859	1.690
	53.50	8.535	216.8	3.00	5.00	9.81	4.51	7.53	14.80	1.88	3.13	6.16	0.533	0.888	1.748

Appendix C (continued)

10 3/4 (273.0)	32.75	10.192	258.9	2.10	3.50	6.88	3.17	5.28	10.40	1.32	2.19	4.33	0.374	0.623	1.226
	40.50	10.050	255.3	2.16	3.60	7.08	3.25	5.42	10.70	1.35	2.25	4.45	0.384	0.641	1.261
	45.50	9.950	252.7	2.20	3.68	7.22	3.33	5.55	10.90	1.39	2.31	4.53	0.392	0.653	1.286
	51.00	9.850	250.2	2.25	3.75	7.37	3.39	5.65	11.10	1.41	2.35	4.61	0.400	0.666	1.312
	55.50	9.760	247.9	2.29	3.82	7.51	3.45	5.75	11.30	1.44	2.39	4.70	0.408	0.679	1.337
	60.70	9.660	245.4	2.34	3.91	7.66	3.52	5.88	11.50	1.46	2.44	4.78	0.416	0.693	1.364
	65.70	9.560	242.8	2.40	4.00	7.82	3.60	6.00	11.80	1.50	2.49	4.91	0.425	0.708	1.393
11 3/4 (298.5)	38.00	11.150	283.2	1.76	2.94	5.75	2.64	4.41	8.66	1.10	1.83	3.60	0.312	0.520	1.024
	42.00	11.084	281.5	1.77	2.96	5.82	2.67	4.45	8.76	1.11	1.85	3.64	0.316	0.526	1.036
	47.00	11.000	279.4	1.81	3.02	5.91	2.73	4.55	8.96	1.14	1.89	3.73	0.321	0.534	1.052
	54.00	10.880	276.4	1.84	3.08	6.04	2.79	4.65	9.15	1.16	1.93	3.81	0.328	0.547	1.076
	60.00	10.772	273.6	1.88	3.14	6.16	2.83	4.73	9.29	1.18	1.97	3.86	0.334	0.557	1.097
13 3/8 (339.7)	48.00	12.715	323.0	1.35	2.25	4.42	2.04	3.40	6.69	0.85	1.41	2.78	0.240	0.400	0.788
	54.50	12.615	320.4	1.37	2.29	4.49	2.07	3.46	6.79	0.86	1.44	2.82	0.244	0.406	0.800
	61.00	12.515	317.9	1.39	2.33	4.56	2.11	3.52	6.92	0.88	1.46	2.87	0.248	0.413	0.813
	68.00	12.415	315.3	1.41	2.36	4.64	2.13	3.53	6.99	0.89	1.48	2.91	0.252	0.420	0.826
	72.00	12.347	313.6	1.43	2.39	4.69	2.16	3.60	7.09	0.90	1.49	2.95	0.255	0.424	0.835
16 (406.4)	55.00	15.376	390.6	0.92	1.54	3.02	1.39	2.32	4.56	0.58	0.86	1.90	0.164	0.274	0.539
	65.00	15.250	387.4	0.93	1.56	3.07	1.41	2.36	4.63	0.59	0.91	1.92	0.167	0.278	0.548
	75.00	15.124	384.2	0.95	1.59	3.13	1.44	2.40	4.72	0.60	0.99	1.96	0.170	0.283	0.557
	84.00	15.010	381.3	0.97	1.62	3.17	1.46	2.44	4.79	0.61	1.02	1.99	0.172	0.287	0.565
20 (508.0)	94.00	19.124	485.8	0.60	1.00	1.95	0.90	1.50	2.96	0.37	0.62	1.23	0.106	0.177	0.348

Appendix D: Average Fluid Velocity

When a production logging tool is present in the casing or tubing, the average fluid velocity in the tool/pipe annulus may be determined from the following charts.

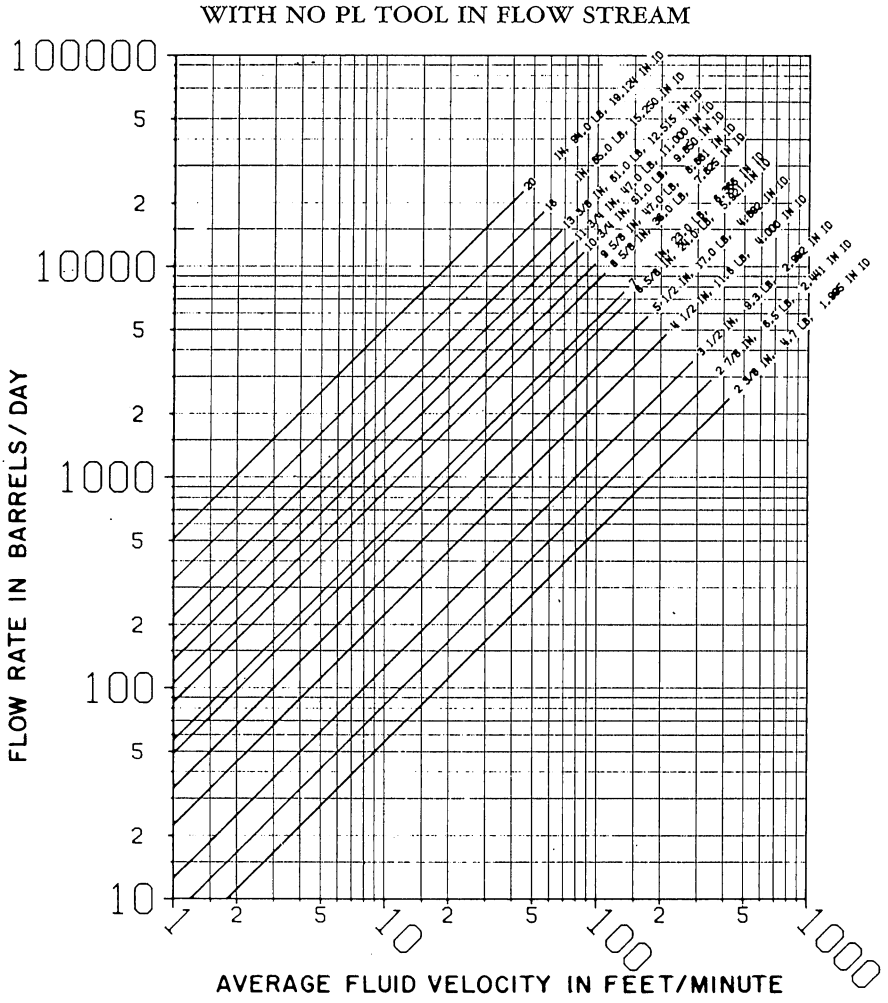

Courtesy Schlumberger, from "Fluid Conversions in Production Log Interpretation" (1974) 54–56.

WITH 1½-IN. PL TOOL IN FLOW STREAM

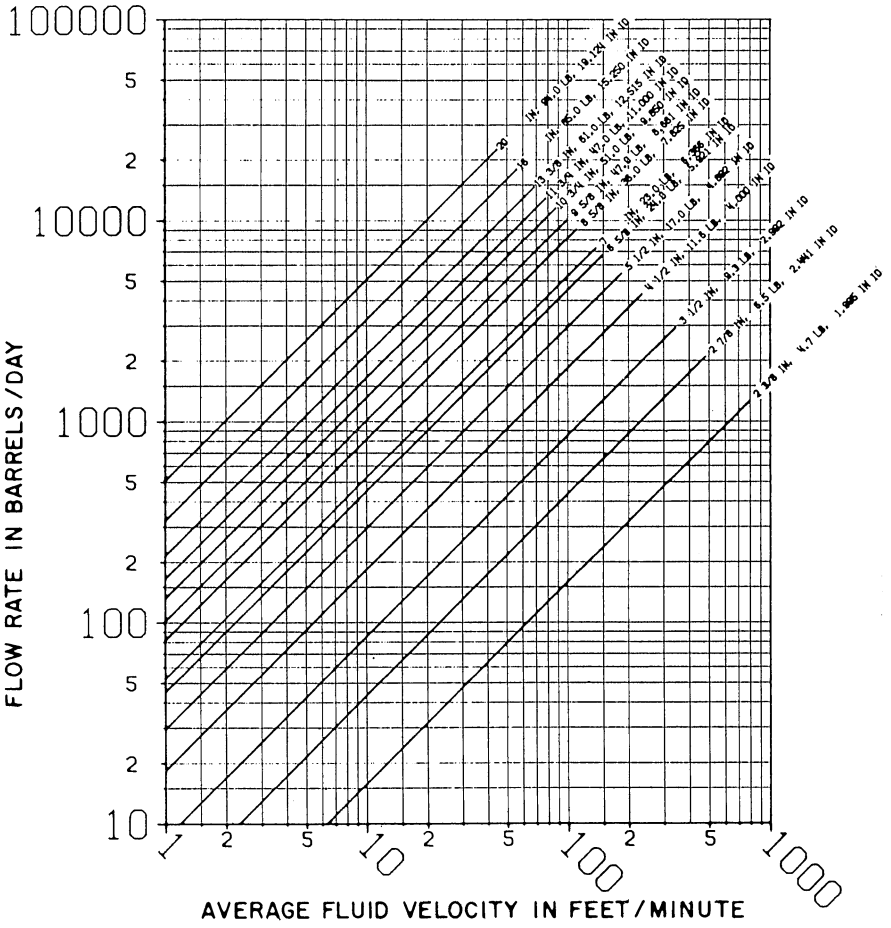

WITH 2⅛-IN. PL TOOL IN FLOW STREAM

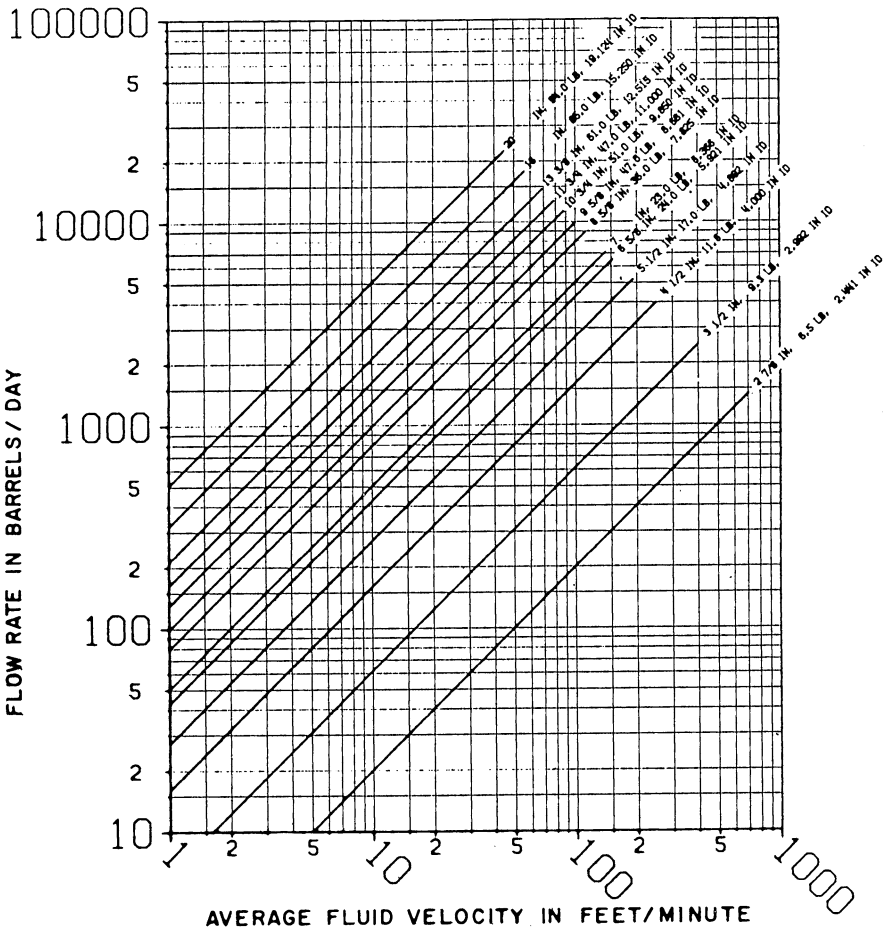

Appendix E: Quick Guide to Biphasic Flow Interpretation

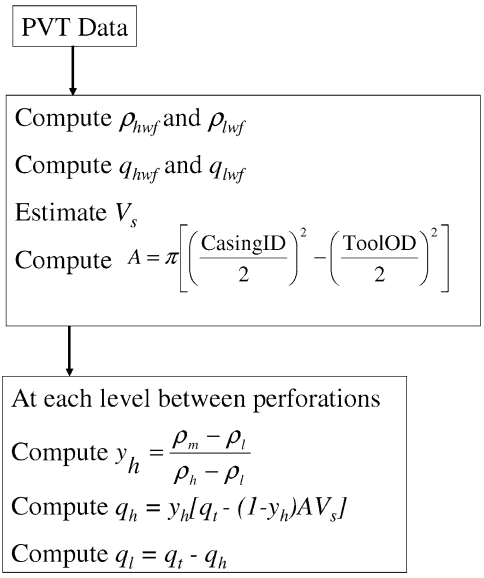

Where: h is for heavy phase
l is for light phase
m is for mixture

General Bibliography

Peng DY, Robinson DB. A new two-constant equation of state. Ind Eng Chem Fundam. 1976;15:59.

Standing MB. Volumetric and phase behavior of oil field hydrocarbon systems. New York: Reinhold Publishing Corporation; 1952.

Standing MB, Katz DL. Density of natural gases. Trans AIME. 1942;146:140–9.

Dresser Atlas

Carbon/oxygen log (1981).

Casing evaluation services (1983).

Interpretative methods for production well logs. Second edition (1982).

Production services (1981).

Spectralog (1981).

Wireline services catalog (1982).

DIA-LOG
Borehole sound survey.
General catalog.

N.L. McCullough
Noise logging service (1976).

Petroleum Extension Service, The University of Texas at Austin
Lesson 6—well cementing (1983).

Schlumberger
Services catalog (1970).
Production log interpretation (1970 and 1973).
Fluid conversions in production logging (1974).
Production services (March 1975).
The essentials of cement evaluation (1976).
Reservoir and production fundamentals (1980).
Well evaluation developments-continental Europe (1982).
Fundamental of formation testing (2006)—06-FE-014.

Index

R.M. Bateman, *Cased-Hole Log Analysis and Reservoir Performance Monitoring*,
DOI 10.1007/978-1-4939-2068-6